Universidade do Minho
Escola de Engenharia

Ana Catarina Saraiva Almeida

Multifunctional Mussel Inspired Coatings for Orthopaedic Applications

Dissertação de Mestrado

Mestrado em Engenharia Biomédica

Trabalho efetuado sob a orientação de:

Professora Doutora Natália Maria de Araújo Alves

Dezembro de 2017

DECLARAÇÃO

Nome: Ana Catarina Saraiva Almeida

Endereço eletrónico: a75959@alunos.uminho.pt

Bilhete de Identidade: 14370272

Título da dissertação: Multifunctional Mussel Inspired Coatings for Orthopaedic Applications

Orientador(es): Professora Doutora Natália Maria de Araújo Alves

Ano de conclusão: 2017

Designação do Mestrado: Mestrado Integrado em Engenharia Biomédica

Ramo: Biomateriais, Reabilitação e Biomecânica

É AUTORIZADA A REPRODUÇÃO INTEGRAL DESTA DISSERTAÇÃO APENAS PARA EFEITOS DE INVESTIGAÇÃO, MEDIANTE DECLARAÇÃO ESCRITA DO INTERESSADO, QUE A TAL SE COMPROMETE.

Universidade do Minho, _____/_____/_____

Assinatura:

“Science without religion is lame, religion without science is blind.”

Albert Einstein

ACKNOWLEDGMENTS

Em primeiro lugar, gostaria de agradecer especialmente à professora doutora Natália pela oportunidade de trabalhar numa área de investigação que sempre me cativou. Agradeço toda a sua disponibilidade, orientação e entusiasmo que foram muito importantes para a realização deste trabalho.

Em segundo lugar, gostaria de agradecer à investigadora Catarina Vale por todo o apoio durante este trabalho. Foste uma pessoa que esteve sempre pronta a ajudar e a compartilhar conhecimentos e experiências, que foram de extrema importância para a execução deste trabalho. Nunca esquecerei todos os momentos que passamos juntas, todas as conversas intermináveis, conselhos e gargalhadas.

Gostaria também de agradecer a todos os investigadores e staff do grupo 3B's que de alguma forma contribuíram para a concretização deste trabalho. Os 3B´s foram uma experiência enriquecedora tanto a nível profissional como pessoal, que será sem dúvida importante para o meu futuro.

Quero agradecer à minha amiga Patrícia por todo o apoio incondicional durante todos estes anos. Obrigada por sempre acreditares nas minhas capacidades. Sem ti, teria sido mais difícil.

Ao meu namorado Carlos um obrigada muito especial por todo o apoio, compreensão e carinho. Foste tu quem me deu a força necessária nos momentos mais difíceis. Obrigada por estares sempre do meu lado e por me ajudares sempre. Sabes que te serei sempre grata.

Finalmente, um grande obrigado à minha família por todo o amor e apoio durante todo o meu percurso académico. Um obrigado muito especial aos meus pais, Sérgio e Lúcia, pois sem eles nada disto teria sido possível. Obrigada por acreditarem sempre em mim. Serei eternamente grata a vocês por fazerem de mim quem eu sou hoje! É a vocês a quem eu dedico esta dissertação.

ABSTRACT

Currently, there is still a significant rate of implant failures in clinical practice. Current solutions would consist of the development of robust, biocompatible, biodegradable coatings with enhanced adhesive and bioactive properties. So, in this work the development of multifunctional coatings inspired by adhesive properties of mussels and the robust nacre structure were proposed. Based on the configuration of the 3,4-dihydroxy-L-phenylalanine (DOPA) amino-acid of the mussel's adhesive proteins, catechol groups were conjugated to chitosan (CHT) and hyaluronic acid (HA). Layer-by-layer (LbL) assembly was used to mimic the nacre structure, where the organic phase consisted of both polymers and the inorganic phase of bioactive glass nanoparticles (BGNPs). In parallel, polymeric LbL coatings were constructed for the sake of comparison.

The modified polymers were characterized by ultraviolet-visible (UV-Vis) spectroscopy. The construction of various LbL configurations was monitored by quartz crystal microbalance and the adhesive properties were evaluated by lap shear adhesive tests. The bioactivity and the *in-vitro* cell behaviour were analysed for the coatings with and without BGNPs. *In-vitro* tests were conducted using the cell line L929. Hydroxyapatite deposition was evaluated by scanning electron microscopy (SEM) coupled with energy dispersive X-ray spectroscopy (EDS) and X-ray powder diffraction (XRD). Since the structure and topography play an important role in the functional performance of the films, two LbL assembly methods, dip- and spin-coating, were compared using three different substrates: glass, stainless steel, and titanium. The coatings were characterized by SEM, Fourier transform infrared spectroscopy (FT-IR), atomic force microscopy (AFM) and water contact angle (WCA).

Given the enhanced adhesion and bioactivity of the developed films, they could be used as coatings of a variety of implants. In addition, spin-coating was found to be a particularly suitable method for the build-up, since films with smoother and more uniform surfaces were produced.

RESUMO

Atualmente, ainda há uma percentagem significativa de falhas dos implantes na prática clínica. Soluções atuais envolveriam o desenvolvimento de revestimentos robustos, biocompatíveis, biodegradáveis, com propriedades adesivas e bioativas melhoradas. Assim, neste trabalho foi proposto o desenvolvimento de revestimentos multifuncionais inspirados nas propriedades adesivas dos mexilhões e na estrutura robusta do nácar. Baseado na configuração do aminoácido 3,4-dihidroxi-ʟ-fenilalanina (DOPA) das proteínas adesivas dos mexilhões, foram conjugados grupos catecóis ao quitosano (CHT) e ao ácido hialurónico (HA). A montagem camada-a-camada (LbL) foi utilizada para mimetizar a estrutura do nácar, onde a fase orgânica consistiu em ambos os polímeros e a fase inorgânica nas nanopartículas de vidro bioativas (BGNPs). Paralelamente, foram construídos revestimentos LbL poliméricos para fins de comparação.

Os polímeros modificados foram caracterizados por espectroscopia ultravioleta-visível (UV-Vis). A construção das várias configurações LbL foi monitorizada através da microbalança de cristal de quartzo e as suas propriedades adesivas avaliadas através de testes adesivos sob tensão de corte. A bioatividade e o comportamento celular *in-vitro* foram analisados para os revestimentos com e sem BGNPs. Os testes *in-vitro* foram realizados usando a linha celular L929. A deposição de hidroxiapatita foi avaliada por microscopia eletrónica de varrimento (SEM) acoplada com espectroscopia de energia dispersiva de raios-X (EDS) e por difração de raios-X (XRD). Uma vez que a estrutura e topografia apresentam um papel importante no desempenho funcional dos filmes, dois métodos de montagem LbL, revestimento por imersão e por rotação, foram comparados usando três substratos diferentes: vidro, aço inoxidável e titânio. Os revestimentos foram caracterizados por SEM, espectroscopia de infravermelho por transformada de Fourier (FT-IR), microscopia de força atómica (AFM) e ângulo de contacto da água (WCA).

Dado à adesão e bioatividade melhoradas dos filmes desenvolvidos, estes poderiam ser utilizados como revestimentos para uma variedade de implantes. Além disso, verificou-se que o revestimento por rotação foi um método particularmente adequado para a construção, uma vez que foram produzidos filmes com superfícies mais lisas e uniformes.

CONTENTS

Acknowledgments v
Abstract vii
Resumo ix
List of Abbreviations xv
List of Figures xix
List of Tables xxiii
1. Chapter 1 - General Introduction 1
1.1 Motivation 1
1.2 Implantable Orthopaedic Devices: Biocompatibility Issues 3
1.2.1 Inflammatory Response to Orthopaedic Implants 4
1.3 Coatings for Orthopaedic Implants: Current Trends 5
1.3.1 Calcium Phosphate-like and Bioactive Glass Coatings 6
1.3.2 Biomolecules-containing Coatings 6
1.4 Tissue Adhesives 8
1.5 Bioinspired Underwater Adhesives 11
1.5.1 Marine Mussel Adhesive Properties 11
1.6 Catechols as Versatile Platforms for Bioinspired Polymer Adhesives 13
1.6.1 Catechol-Conjugated Chitosan 14
1.6.2 Catechol-Conjugated Hyaluronic Acid 16
1.7 Nanoparticles for Biomedical Applications 18
1.7.1 Bioactive Glass Nanoparticles 18
1.8 Layer-by-Layer Assembly Method 19
1.9 Nacre: Definition and Structure 22
1.9.1 Bioinspired Nacre-like Coatings for Biomedical Implants and Scaffolds 24
1.10 References 24
2. Chapter 2 – Materials and Methods 51
2.1 Materials 51

2.1.1 Chitosan 51
2.1.2 Hyaluronic Acid 52
2.1.3 Dopamine 54
2.1.4 Hydrocaffeic Acid 55
2.1.5 Bioactive Glass Nanoparticles 56
2.1.6 Substrates 58
2.1.7 Chitosan Purification 60
2.1.8 Synthesis of the Catechol-Conjugated Hyaluronic Acid 60
2.1.9 Synthesis of the Catechol-Conjugated Chitosan 61
2.1.10 Bioactive Glass Nanoparticles Production 62
2.1.11 LbL Assembly – Production of Multifunctional LbL Coatings 63
2.2 Characterization Techniques 69
2.2.1 Ultraviolet-Visible Spectroscopy 69
2.2.2 Rheological measurements 70
2.2.3 Zeta Potential Measurements 72
2.2.4 Quartz Crystal Microbalance with Dissipation Monitoring: Multilayer Films Modelling 73
2.2.5 Fourier Transform Infrared Spectroscopic Imaging Analysis 75
2.2.6 X-Ray Diffraction Analysis 77
2.2.7 Water Contact Angle Measurements 79
2.2.8 Scanning Electron Microscopy coupled with Energy Dispersive X-Ray Spectroscopy 80
2.2.9 Adhesion Tests 81
2.2.10 Atomic Force Microscopy Analysis 83
2.2.11 In-Vitro Bioactivity Studies 86
2.2.12 In-vitro Biological Studies 87
2.2.13 Statistical Analysis 89
2.3 References 89
3. Chapter 3 – Thin LbL Coatings with Superior Adhesive and Bioactive Properties 109
3.1 Introduction 110
3.2 Materials and Methods 111
3.2.1 Materials 111
3.2.2 HA-DN Synthesis 112

3.2.3 CHT-C Synthesis 113
3.2.4 BGNPs Production 113
3.2.5 UV-Vis Spectroscopy Characterization 114
3.2.6 Rheological Characterization 114
3.2.7 Zeta Potential (ζ) Characterization 114
3.2.8 Quartz Crystal Microbalance with dissipation (QCM-D) Monitoring: Multilayer Films Modelling 115
3.2.9 Adhesion Tests 117
3.2.10 In-Vitro Bioactivity Studies 118
3.2.11 In-Vitro Biological Studies 119
3.2.12 Statistical Analysis 120
3.3 Results and Discussion 120
3.3.1 Synthesis and Characterization of HA-DN and CHT-C conjugates 120
3.3.2 Rheological Characterization of the PE used 122
3.3.3 Zeta Potential (ζ) Characterization of PE used 123
3.3.4 QCM-D Monitoring of the LbL Films Construction 124
3.3.5 Adhesion tests 130
3.3.6 In-Vitro Bioactivity Analysis 131
3.3.7 In-Vitro Biological Analysis 134
3.4 Conclusions 137
Acknowledgements 137
3.5 References 137
4. Chapter 4 – New Adhesive LbL Coatings Produced by Dip- and Spin-Coating 145
4.1 Introduction 146
4.2 Materials and Methods 148
4.2.1 Materials 148
4.2.2 HA-DN Synthesis 149
4.2.3 Catechol-conjugated chitosan (CHT-C) Synthesis 149
4.2.4 BGNPs Production 150
4.2.5 UV-Vis Characterization of HA-DN and CHT-C 150
4.2.6 LBL Assembly of the Coatings 150

4.2.7 Surface Characterization 152
4.2.8 Statistical Analysis 153
4.3 Results and Discussion 153
4.3.1 HA-DN and CHT-C Modified Polymers: DS (%) Analysis 153
4.3.2 SEM and FT-IR Analysis 154
4.3.3 AFM Analysis 159
4.3.4 WCA Analysis 162
4.4 Conclusions 166
Acknowledgements 167
4.5 References 167
5. Chapter 5 – General Conclusions and Future Work 175
5.1 General Conclusions 175
5.2 Future Work 177
Appendix I – HA modification with catechol groups 178
Appendix II – CHT modification with catechol groups 182
Appendix III – Optimization work on Spin Coater 186

LIST OF ABBREVIATIONS

A

Abs: Absorbance

AFM: Atomic Force Microscope

Ag: Silver

Al: Aluminium

ASTM D1002: Apparent Shear Strength of Single-Lap-Joint Adhesively Bonded Metal Specimens by Tension Loading

ATR: Attenuated Total Reflectance

B

BG: Bioactive Glass

BGNPs: Bioactive Glass Nanoparticles

BMP: Bone Morphogenetic Protein

C

CaP: Calcium Phosphate

CHT: Chitosan

CHT-C: Catechol-conjugated Chitosan

CoCr: Cobalt-Chromium

D

DAC: Defensive Antibacterial Coating

DAPI: 4',6-diami-dino-2-phenylindole

D-MEM: Dulbecco's Modified Minimum Essential Medium

DN: Dopamine

DOPA: 3,4-dihydroxyphenyl-L-alanine

DS: Substitution Degree

E

E: Elastic Modulus

ECACC: European Collection of Authenticated Cell Cultures

ECM: Extracellular Matrix

EDC: N-(3-(dimethylamino)propyl)-N′-ethylcarbodiimide hydrochloride

EDS: Energy Dipersive X-ray Spectroscopy

EO: Ethylene Oxide

F

FBS: Fetal Bovine Serum

FT-IR: Fourier Transform Infrared

H

HA: Hyaluronic Acid

HA-DN: Catechol-conjugated Hyaluronic Acid

hADSC: Human Adipose-derived Stem Cell

HCl: Hydrochloric acid

hMSC: Human Bone Marrow-derived Mesenchymal Stem Cell

I

ICDD: International Centre for Diffraction Data

IR: Infrared

L

LbL: Layer-by-Layer

M

MAPs: Mussel's Adhesive Proteins

Mefp: Mytilus edulis foot proteins

MTS: 3-(4,5-dimethylthiazol-2-yl)-5-(3-carboxymethoxyphenyl)-2-(4-sulfophenyl)-2H-tetrazolium

MSC: Mesenchymal Stem Cell

MW: Molecular Weight

N

NaCl: Sodium Chloride

NaOH: Sodium Hydroxide

NP: Nanoparticle

O

OD: Optical Density

P

PBS: Phosphate Buffered Saline

PCL: poly(ε-caprolactone)

PDGF-AA: Platelet-derived Growth Factor-AA

PE: Polyelectrolyte

PEI: Poly(ethylenimine)

PEG: Poly(ethylene glycol)

PEM: Polyelectrolyte Multilayer

Q

QCM-D: Quartz Crystal Microbalance with Dissipation Monitoring

R

Ra: Average Roughness

ROS: Reactive Oxygen Species

Rq: Root Mean Square Roughness

S

SBF: Simulated Body Fluid

SD: Standard Deviation

SEM: Scanning Electron Microscopy

Si: Silicon

Sr: Strontium

SS: Stainless Steel

SSZ: Sulfasalazine

T

TCP: Tissue Culture Polystyrene

TEOS: Tetraethyl orthosilicate

Ti: Titanium

U

UV-Vis: Ultraviolet-Visible

V

VEGF: Vascular Endothelial Growth Factor

W

WCA: Water Contact Angle

X

XRD: X-ray Diffraction

LIST OF FIGURES

Figure 1.1 – a) BGNPs-containing coatings and b) Polymeric coatings for orthopaedic implants. Adapted from [39,40]. 3

Figure 1.2 – Underwater adhesion of some marine creatures. Left to right: mussels, barnacles, tube worms and starfish [24]. 11

Figure 1.3 – Adhesive plaques of a marine mussel connected by threads to a glass sheet (left) and Teflon (polytetrafluoroethylene, right) [24]. 11

Figure 1.4 – Illustration of a DOPA unit. Adapted from [28]. 12

Figure 1.5 – Illustration of a polymer-catechol system mimicking MAPs. Adapted from [154]. 13

Figure 1.6 – Schematics illustration of the LbL deposition process: A - Steps 1 and 3 represent the immersion of the substrate in a polyanionic and polycationic solution, respectively. Steps 2 and 4 represent the washing steps. This cyclic process represents the formation of one bilayer, and can be repeated as many times as intended; B - Representation of the LbL deposition process at a molecular level. Adapted from [244]. 20

Figure 1.7 – Schematics illustration of the adsorption and interlayer diffusion during the LbL deposition process. Adapted from [253]. 21

Figure 1.8 – Schematic illustration of the brick-and-mortar microstructure for (A) columnar nacre and (B) sheet nacre [36]. 23

Figure 2.1 – Chemical structures of N-acetyl-D-glucosamine residues (chitin) and D-glucosamine residues (chitosan) during deacetylation process. Adapted from [3]. 51

Figure 2.2 – Chemical structure of hyaluronic acid [49]. 53

Figure 2.3 – DOPA decarboxylation into dopamine. Adapted from [77]. 54

Figure 2.4 – Chemical structures of HCA. Adapted from [90]. 55

Figure 2.5 – Scheme of HA-DN synthesis. Adapted from [152]. 61

Figure 2.6 – Scheme of CHT-C synthesis. Adapted from [153]. 62

Figure 2.7 – Scheme of BGNPs production. 63

Figure 2.8 – Schematic representation of LbL assembly by the dip-coating method. Adapted from [159]. 64

Figure 2.9 – Schematic representation of LbL assembly by the spin-coating method. 65

Figure 2.10 – Spin coater instrument. 68

Figure 2.11 – Schematic illustration of the different multifunctional (MF) and control (CTR) LbL coatings. 68

Figure 2.12 – (Left) Variable pathlength in a microplate well. (Right) Fix pathlength in a cuvette (1cm). 70

Figure 2.13 – (Left) Kinexus Pro Rheometer. (Right) Cone-plate geometry. 72

Figure 2.14 – Schematic representation of the zeta potential of a negatively charged particle. Adapted from [175]. 73

Figure 2.15 – a) and b) QCM-D system. c) Schematic representation of the mounting and the physical parts of the QCM-D system: flow modules, sensor crystals and flow chamber system. 74

Figure 2.16 – Perkin-Elmer Spectrum Spotlight 300 FT-IR Microscope System. 77

Figure 2.17 – Illustration of Bragg's Law [186]. 78

Figure 2.18 – Schematic representation of WCA measurements on a solid surface: (a) hydrophobic surface; (b) and (c) hydrophilic surfaces [192]. 79

Figure 2.19 – Scheme showing the optical system of SEM. Adapted from [194]. 81

Figure 2.20 – Schematic representation of a single-lap-joint (dimensions in mm). Adapted from [196,197]. 82

Figure 2.21 – a) Frontal and b) lateral view of a single-lap-joint used in this study. c) Schematic representation of single-lap-joint using a mechanical testing machine. Adapted from [198]. 83

Figure 2.22 – a) Illustration of AFM work principle. Representation of different AFM operating modes: b) contact mode and c) tapping mode. Adapted from [200]. 85

Figure 2.23 – Representation of a surface profile ($\boldsymbol{Z(x)}$) showing the $\boldsymbol{Ra}$ and $\boldsymbol{Rq}$ parameters based on the mean line [203]. 85

Figure 3.1 – Schematic illustration of the different multifunctional (MF) and control (CTR) LbL coatings. 116

Figure 3.2 – UV-Vis spectra for different concentrations of HA-DN*$_{4h}$ and HA-DN*$_{36h}$. 121

Figure 3.3 – UV-Vis spectra for different concentrations of CHT-C*$_{18h}$. 121

Figure 3.4 – Trend line of HA, HA-DN*$_{4h}$, HA-DN*$_{36h}$, CHT and CHT-C*$_{18h}$ solutions at different concentrations. Data are presented by means ± standard deviation (n = 3). 122

Figure 3.5 – QCM-D results representing the $\Delta f/\upsilon$ and ΔD variations, as a mean of the 7th, 9th and 11th overtones, and as a function of the deposited layers in the build-up of polymeric films (CTR). 126

Figure 3.6 – QCM-D results representing the $\Delta f/\upsilon$ and ΔD variations, as a mean of the 7th, 9th and 11th overtones, and as a function of the deposited layers in the build-up of the MF LbL coatings containing the BGNPs. 127

Figure 3.7 – Cumulative thickness evolution of the multilayered films constructed, as a function of the number of deposited layers. 128

Figure 3.8 – Adhesion strength values (MPa) measured for each LbL coating. Data are presented by means ± standard deviation (n = 5; **** p<0.0001; *** p<0.001, ** p<0.01; * p<0.05) [One-way ANOVA with Turkey's Multiple comparison test]. 130

Figure 3.9 – In-vitro bioactivity studies. Representative SEM images and respective quantitative EDS analysis of four LbL coatings configurations (see Figure 3.1), before and after SBF immersion for 7 and 14 days. The scale bar represents 5 μm. 132

Figure 3.10 – XRD diffractograms obtained for each LbL coating configuration before and after immersion in SBF for 14 days. 133

Figure 3.11– L929 viability results obtained through: a) MTS assay for 1, 3 and 7 days, where absorbance was read at 490 nm. Statistically significant differences between distinct samples by each time point were marked with ** and ***, which represents p<0.01 and p<0.001, respectively. Data are presented by means ± standard deviation (n = 3) [One-way ANOVA with Turkey's Multiple comparison test]; b) Fluorescence images of cells stained with DAPI (blue) and phalloidin (red) at 1, 3 and 7 days of culture on the different multilayer coatings (CTR5: $[CHT^*_{18h}/HA\text{-}DN^*_{4h}]_{11}$, MF5: $[CHT^*_{18h}/HA\text{-}DN^*_{4h}/CHT^*_{18h}/BGNPs]_5+CHT^*_{18h}/HA\text{-}DN^*_{4h}]$, CTR6: $[CHT^*_{18h}/HA\text{-}DN^*_{36h}]_{11}$, MF6: $[CHT^*_{18h}/HA\text{-}DN^*_{36h}/CHT^*_{18h}/BGNPs]_5+CHT^*_{18h}/HA\text{-}DN^*_{36h}]$): the nuclei of the cells were stained with blue and their cytoskeleton with red. All images are representative for each condition and time point. Scale bar represents 50 μm. 135

Figure 4.1 – Schematic illustration of the multifunctional (MF) and control (CTR) coatings. 151

Figure 4.2 – UV-Vis spectra for $HA\text{-}DN^*_{36h}$ and $CHT\text{-}C^*_{18h}$..... 153

Figure 4.3 – SEM images of the two LbL coatings configurations (Figure 4.1) obtained by dip- and spin-coating methods, using glass as substrate. The scale bar of the main images represents 500 μm and the secondary ones 10 μm. 154

Figure 4.4 – SEM images of the two LbL coatings configurations (Figure 4.1) obtained by dip- and spin-coating methods, using 316L SS as substrate. The scale bar of the main images represents 500 μm and the secondary ones 10 μm. 155

Figure 4.5 – SEM images of the two LbL coatings configurations (Figure 4.1) obtained by dip- and spin-coating methods, using Ti as substrate. The scale bar of the main images represents 500 μm and the secondary ones 10 μm..... 155

Figure 4.6 – Chemical maps of the two LbL coatings configurations (Figure 4.1) obtained by dip- and spin-coating methods, using glass as substrate. For the chemical map, red indicates the presence of CHT, green the presence of HA, blue the presence of catechol groups and cyan corresponds to the BGNPs. Note that the existence of regions with different intensities can be an indication of differences in thickness. 156

Figure 4.7 – Chemical maps of the two LbL coatings configurations (Figure 4.1) obtained by dip- and spin-coating methods, using 316L SS as substrate. For the chemical map, red indicates the presence of CHT, green the presence of HA, blue the presence of catechol groups and cyan corresponds to the BGNPs. Note that the existence of regions with different intensities can be an indication of differences in thickness. 157

Figure 4.8 – Chemical maps of the two LbL coatings configurations (Figure 4.1) obtained by dip- and spin-coating methods, using Ti as substrate. For the chemical map, red indicates the presence of CHT, green the presence of HA, blue the presence of catechol groups and cyan corresponds to the BGNPs. Note that the existence of regions with different intensities can be an indication of differences in thickness. 158

Figure 4.9 – a) Ra and Rq roughness values (nm) measured for the two LbL coatings configurations (Figure 4.1) produced on glass by dip- and spin-coating. Data are presented by means ± standard deviation (n = 3). Statistical differences were represented for Rq roughness values, where rows plus "*" indicate differences between the various conditions, and "+" (at the top of each bar) indicate their differences compared to the uncoated glass substrate (glass control) [++++/**** p<0.0001; ** p<0.01; * p<0.05; One-way ANOVA with Turkey's Multiple comparison test]. b) Representative AFM images for each LbL coating condition, with a scanned surface area of 20×20 μm^2. 160

Figure 4.10 – a) Ra and Rq roughness values (nm) measured for the two LbL coatings configurations (Figure 4.1) produced on 316L SS by dip- and spin-coating methods. Data are presented by means ± standard deviation (n = 3) [One-way ANOVA with Turkey's Multiple comparison test]. b) Representative AFM images for each LbL coating condition, with a scanned surface area of 20×20 μm^2. 160

Figure 4.11 – a) Ra and Rq roughness values (nm) measured for the two LbL coatings configurations (Figure 4.1) produced on Ti by dip- and spin-coating methods. Data are presented by means ± standard deviation (n = 3) [One-way ANOVA with Turkey's Multiple comparison test]. b) Representative AFM images for each LbL coating condition, with a scanned surface area of 20×20 μm^2. 161

Figure 4.12 – a) WCA (°) values measured for the two LbL coatings configurations (Figure 4.1) produced on glass by dip- and spin-coating methods. Statistical differences between the various configurations are indicated by the rows plus "*", while their comparisons with the uncoated glass substrate (glass control) are indicated by "+" (at the top of each bar). Data are presented by means ± standard deviation (n = 3; ++++/**** p<0.0001; * p<0.05) [One-way ANOVA with Turkey's Multiple comparison test]; b) Representative image of water drops for each multilayered film surface..... 163

Figure 4.13 – a) WCA (°) values measured for the two LbL coatings configurations (Figure 4.1) produced on 316L SS by dip- and spin-coating methods. Statistical differences between the various configurations are indicated by the rows plus "*", while their comparisons with the uncoated SS substrate (SS control) are indicated by "+" (at the top of each bar). Data are presented by means ± standard deviation (n = 3; ++++/**** p<0.0001; ++ p<0.01; * p<0.05) [One-way ANOVA with Turkey's Multiple comparison test]; b) Representative image of water drops for each multilayered film surface..... 163

Figure 4.14 – a) WCA (°) values measured for the two LbL coatings configurations (Figure 4.1) produced on Ti by dip- and spin-coating methods. Statistical differences between the various configurations are indicated by the rows plus "*", while their comparisons with the uncoated Ti substrate (Ti control) are indicated by "+" (at the top of each bar). Data are presented by means ± standard deviation (n = 3; ++++/**** p<0.0001; ++ p<0.01) [One-way ANOVA with Turkey's Multiple comparison test]; b) Representative image of water drops for each multilayered film surface. 164

Figure I.1 – UV-Vis spectra for different concentrations of HA-DN_{4h} and HA-DN_{36h}. 180

Figure I.2 – UV-Vis spectra for different concentrations of HA-DN^*_{4h} and HA-DN^*_{36h}. 181

Figure II.1 – UV-Vis spectra for different concentrations of CHT-C_{18h} and CHT-C_{36h}. 184

Figure II.2 – UV-Vis spectra for different concentrations of CHT-C^*_{18h}. 185

LIST OF TABLES

Table 1.1 – Natural and synthetic tissue adhesives commercially available. Adapted from [5,6,88]. 9
Table 1.2 – Summary of the intended applications of catechol-functionalized CHT adhesive polymer. 14
Table 1.3 – Summary of the intended applications of catechol-functionalized HA adhesive polymer.... 16
Table 2.1 – PE and respective concentration and function for the LbL assembly. 66
Table 2.2 – Ion concentrations of SBF and human blood plasma. Adapted from [204]..... 87
Table 3.1 – Zeta potential values for each PE solution with 0.5 mg.mL^{-1} concentration. 123
Table I.1 – UV-Vis characterization of different concentrations of DN. 179
Table I.2 – UV-Vis characterization of different concentrations of HA-DN$_{4h}$ and HA-DN$_{36h}$. 180
Table I.3 – UV-Vis characterization of different concentrations of HA-DN*$_{4h}$ and HA-DN*$_{36h}$. 181
Table II.1– UV-Vis characterization of different concentrations of HCA. 183
Table II.2– UV-Vis characterization of different concentrations of CHT-C$_{18h}$ and CHT-C$_{36h}$. 184
Table II.3– UV-Vis characterization of different concentrations of CHT-C*$_{18h}$. 185

1. CHAPTER 1 - GENERAL INTRODUCTION

1.1 Motivation

Although biomedical metals have been widely used in orthopaedic applications, few of these have reported good biocompatibility and successfully used in clinic [1,2]. In many cases, after their implantation in the host bone, fibrous encapsulation occurs on the implant surface [3,4]. Since supporting and fixation are the most common basic functions of the biomedical metals, other functions such as bioadhesiveness, bioactivity, biocompatibility are required [2]. Current trends in surface modifications on orthopaedic implants still have significant limitations and drawbacks. They generally exhibit poor robustness, low bioabsortion and metabolic rates, low adherence to substrate surface, poor tissue-bonding properties, poor biomolecules loading efficiency, poor mechanical stability after implantation into bone defects, and most often present some cytotoxicity and trigger inflammatory reactions due to the release of degradation products or to the presence of proteins in their composition, among others [5–8].

Currently, biomedical coatings research is focused on designing multifunctional nanostructured approaches to act as an interface between the material and the host tissue, being able to trigger several biologic processes, from the inflammatory reaction to the tissue remodelling [9,10]. Layer-by-layer (LbL) deposition approach has been proven to be an ideal method for the construction of such coatings, due to its simplicity and versatility in merging different functionalities from different materials into a single composite and its ability to produce films with nanoscale-controlled thickness [11–13].

Therefore, inspired by this new focus of biomedical coatings for orthopaedic applications, multifunctional LbL coatings containing natural polymers and nanoparticles were produced in the present work. In parallel, polymeric coatings were produced for the sake of comparison. Biopolymers such as chitosan (CHT) and hyaluronic acid (HA) have received much attention from researchers, due their numerous interesting properties as example biocompatibility, biodegradability, availability, processing, modification flexibilities, among others [14–16]. Its assembly in polyelectrolyte multilayer (PEM) systems onto a huge diversity of substrates has already been reported in literature [17–19]. Based on previous studies [20–23], both polysaccharides were used in this work with their further modification with catechol groups to improve the adhesive properties of LbL coatings [20–23]. Conjugation with catechol groups was inspired by the underwater adhesive properties of marine mussels, which are attributed to the ortho-dihydroxyphenyl (catechol) moiety of amino-acid 3,4-dihydroxyphenyl-L-alanine (DOPA) present in the

mussel's adhesive proteins (MAPs) [24–26]. Their strong adhesive properties to different substrates in wet environments make them potential bioadhesives for diverse applications [27,28]. So far, the previous works of our group [18,29], has only studied the modification of HA with catechol groups. They used it in combination with CHT to build multilayer coatings demonstrating a positive effect on their adhesive properties. Thus, we hypothesize that modification of both polysaccharides could further improve the adhesive ability of previously developed LbL coatings. Furthermore, based on the interesting osteoconductive properties of the bioactive glass nanoparticles (BGNPs) in the orthopaedic field [30–32], they were used in this work as an inorganic phase of the coatings. Due to their bioactive properties, they can bind to bone stimulating new tissue growth by the precipitation of a calcium phosphate (CaP) layer on their surface while dissolving over time [33,34]. The BGNPs inorganic phase was added to the organic phase of polysaccharides to develop multifunctional LbL coatings. Such strategy was inspired by the layered structure of nacre, which is present in the shell of some molluscs. This structure combines resistance to fracture provided by inorganic matrix of aragonite nanoplatelets and toughness conferred by organic matrix surrounding the inorganic materials [35,36]. However, it is important to highlight that unlike the nacre structure, in this study the content of inorganic phase was lower than the organic phase to develop flexible coatings. Previous studies have also been inspired by this strategy using the BGNPs in combination with CHT and HA biopolymers to develop biomimetic and coatings [29,37,38]. They already evidenced that, when BGNPs were in contact with simulated body fluid (SBF) solution, they induce the deposition of a CaP layer that would be identical to that produced when in contact with bone.

Therefore, the present work will be focused on the production of nature-inspired multilayered coatings with enhanced biocompatibility and tissue adhesion properties, and with and without bioactivity properties. We hypothesized that the presence of catechol groups on both modified natural polymers could improve the implant-tissue adhesion, as well as the cellular response of distinct coated materials, which is extremely important for orthopaedic purposes [20]. In addition, it is also expected that the BGNPs-containing coatings will provide bioactive properties. So far, it will the first time that both CHT and HA modified polymers will be combined with BGNPs for LbL constructions. Thus, two multilayered strategies will be developed to cover a wide range of applications: the BGNPs-containing coatings (multifunctional coatings, Figure 1.1-a) could be used to promote bone-implant interaction, as an alternative option of bone cements; on the other hand, polymeric coatings (control coatings, Figure 1.1-b) which could be used to improve the adhesion between distinct implants and other tissues where the bioactivity is not a requirement, as an alternative for synthetic tissue adhesives.

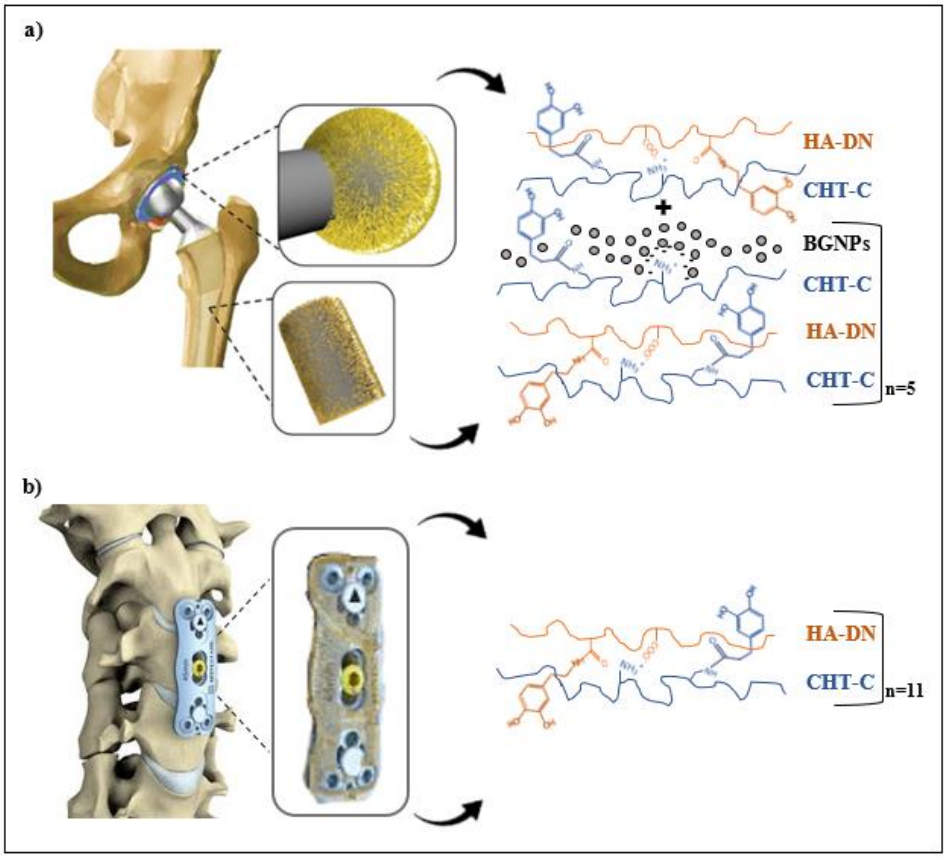

Figure 1.1 – a) BGNPs-containing coatings and b) Polymeric coatings for orthopaedic implants. Adapted from [39,40].

1.2 Implantable Orthopaedic Devices: Biocompatibility Issues

Worldwide, orthopaedic implants are used routinely for fixation of long bone fractures and non-unions, for correction and stabilization of spinal fractures and deformities, for replacement of arthritic joints, and for other orthopaedic and maxillofacial applications [7].

Around 70–80% of orthopaedic implants are made of metallic biomaterials. Metallic biomaterials are remarkably important for the reconstruction of failed tissue, specially failed hard tissue. The main purpose of these implants is to provide mechanical stabilization so that optimal alignment and function of bone can be maintained during physiologic loading of bones and joints, thus promoting healing and return of bone function [7,41].

Commercial metallic biomaterials used for orthopaedic implant manufacture are titanium (Ti) and its alloys, stainless steel 316L (SS) and cobalt-chromium (CoCr) alloys. Among these, Ti and its alloys are generally preferred owing to their high mechanical strength, low density, corrosion resistance, and superior biocompatibility [42,43]. On the other hand, SS has properties such as ductility and cyclic twist strength that are higher in comparison to Co–Cr and Ti alloys [42].

However, since the mechanical and biological aspects of bone healing are closely interrelated, it is not enough to focus solely on the mechanical properties and function of the implant [7]. For example, cementless joint replacements do not always osseointegrate with the surrounding bone, which may result in implant migration and loosening [44]. In fact, in the USA, there are approximately 600,000 cases of late union fractures and 100,000 non-union fractures each year [45]. Besides that, infections of orthopaedic fractures and reconstructive devices occur in approximately 5% of cases and total about 100,000 cases per year in the USA alone, which is a substantial cause of morbidity and even mortality [46,47].

Therefore, despite the advantages of metallic biomaterials in the orthopaedic field, other biofunctionalities such as biological and mechanical biocompatibility must be achieved to improve the implant function and to mitigate potentially serious systemic side effects [7,42]. Through surface modifications, it is possible to enhance the osseointegration, osteoconductivity and bioactivity of orthopaedic devices as well as mitigate adverse events associated with the foreign body response or infection [7,42].

1.2.1 Inflammatory Response to Orthopaedic Implants

Often, implantation of an orthopaedic device lead to host reactions including acute and chronic inflammation, granulation tissue development, foreign body reaction, and fibrosis/fibrous capsule development [3,4].

When an orthopaedic implant is used, wear and corrosion debris are generated, which are usually attributed to local inflammatory responses leading to aseptic failure and osteolysis [48,49]. Common types of corrosion debris formation have been found in metallic implants, such are pitting corrosion, crevice corrosion, fretting corrosion, fatigue and fatigue corrosion [41]. Moreover, bearing surfaces of joint replacements, and non-articulating implant surfaces that impinge or fret, for example screws in a plate for fracture fixation or spinal stabilization, have been identified as the main causes of formation of wear debris and other by-products [7].

Implant infections are potential dreaded complications that may necessitate further surgery and are considered a substantial cause of morbidity and even mortality [47]. The acute and chronic inflammation to orthopaedic implants has been characterized and occurs sequentially [7]. Acute inflammatory response is characterized by the release of cytokines, chemokines and pro-inflammatory molecules at the implant interface by polymorphonuclear leukocytes, macrophages, activated fibroblasts and other cells, disturbing normal homeostatic mechanisms [50–52]. Thus, if this process continues

without resolution, it results in chronic inflammation and osteolysis, compromising the long-term stability of the implant [7]. Chronic inflammation is characterized by the presence of mononuclear cells, i.e. monocytes and lymphocytes, at the implant site [53].

Following the recovery of acute and chronic inflammatory responses, a formation of a granulation tissue at the implant interface occurs, composed by macrophages, fibroblasts and neovascularization of the new healing tissue [53]. This granulation tissue is the precursor to the fibrous capsule formation which is separated from the implant by one- to two-layer of cellular components belonging to the foreign body reaction, namely monocytes, macrophages, and foreign body giant cells [53].

Therefore, the research has focused on methods to stimulate the migration of osteoprogenitor cells to the implant site and to mitigate the systemic reaction of the foreign body [7,42].

1.3 Coatings for Orthopaedic Implants: Current Trends

Supporting and fixation are the most common basic functions of the biomedical devices, being need other functions such as bioadhesiveness, bioactivity, biocompatibility and other like anticorrosion properties, anti-inflammation, anti-microbial and anti-tumour properties [2]. Thus, development of new functions on biomedical metals to enhance bone bonding between the metal implants and the host bone, besides stimulating the immature cells to differentiate into preosteoblasts, has a promising future [2].

The induction of the bone-like apatite layer *in-vivo* might be the key to increase bioactivity [2]. The hydroxyapatite layer formation on biomedical metal surfaces is a typical heterogeneous nucleation process that is influenced by the morphology and chemical composition of the surface [2]. For example, implant surfaces that provide active sites for bonding of Ca^{2+} ions can, in turn, provide binding sites for the PO_4^{3-} ions, resulting in the formation of hydroxyapatite [54]. On the other hand, the higher surface roughness of the implant surfaces provides large specific surface area which offers more nucleation sites to the hydroxyapatite crystal formation [2].

The physiological environment of the human body has also an important role in the bioactivity of the biomedical metals, since that when they are implanted *in-vivo*, the adsorption of biomolecules like proteins and collagen occurs. Cells can respond to those biomolecules and modulate the microenvironment, i.e. the extracellular matrix (ECM), which serves as the bridge between materials and the cells. Thus, if the material influence the proliferation and the activity of the osteogenic cells, those cells might change the microenvironment around implants and modulate the formation of hydroxyapatite [2].

1.3.1 Calcium Phosphate-like and Bioactive Glass Coatings

Calcium phosphate-like coatings such as hydroxyapatite have been demonstrated to enhance osseointegration of metallic prothesis within bone [55,56]. Recently, hydroxyapatite coatings have been used not only for their osteoconductive properties, but as a method for delivery of growth factors, such as bone morphogenetic proteins (BMPs), bioactive molecules, DNA and small peptides as RGD peptides for improve mesenchymal stem cells (MSCs) adhesion [57–59].

Although, hydroxyapatite coatings can form tight bonds with living bone, its suboptimal fatigue properties, and low robustness to withstand physiological loads without fragmentation and problems related to third body wear by hydroxyapatite particles limit its more widespread use [7,60].

Bioactive glasses (BGs) are highly attractive ceramic materials for use as coatings onto orthopaedic implants, since they can bind to hard and soft tissues stimulating new tissue growth while dissolving over time [33,34]. Bone binding is evidenced by the precipitation of a layer of calcium–deficient carbonated apatite on the BG surface when *in-vivo* applications or in contact with physiological fluid [61,62].

The commercial product 45S5 Bioglass®, was reported in 1971 by Larry Hench and colleagues [63], and is one of the more widely used surface coatings for the modification of metal implants with great potential for bone regeneration. 45S5 Bioglass® is composed by 45% SiO_2, 24.5% Na_2O, 24.5% CaO, 5% P_2O_5 (wt.%) [64]. However, there are other BGs, having variations in the elemental composition to that of Bioglass®, that are not only biocompatible but also possess bioactive properties leading to enhanced cellular activity on the implant's surface [65,66].

BG coatings have been applied by several techniques including enamelling, electrophoresis, sol-gel, and plasma spraying [64]. Recently, nanostructured multilayered coatings have been developed via LbL assembly, combining BG nanoparticles with polysaccharides, which can be modified with catechol groups to improve coating adhesion on both substrate surface and osteoblastic cells [29,37,38,67].

1.3.2 Biomolecules-containing Coatings

A wide range of biomolecules may be incorporated into coatings of orthopaedic implants to promote their osseointegration. Examples of these are large proteins, for instance collagen, and polysaccharides such as chondroitin sulphate, CHT and HA, that have demonstrated to provide a biomimetic coating promoting the osteogenic differentiation of human bone marrow-derived mesenchymal stem cells (hMSCs) [68]. Another type of biomolecules widely used are growth factors due to their ability to modulate cellular functions such as reducing inflammation, enhancing stem cell differentiation, inducing blood vessel formation, or acting as chemoattractants for osteoprogenitor cells [69–75]. In addition, small

peptides derived from protein molecules may also be used to enhance desirable cellular functions of coatings such as adhesion or bone formation from local osteoblasts [76,77]. As an alternative, DNA molecules have also been incorporated into coatings to be subsequently released and translocated into the cell nucleus expressing sequence specific mRNAs [78,79].

Some of these biomolecules have been widely incorporated in hydrogel coatings to provide a variety of biomolecular cues that can regulate proliferation, differentiation and migration of osteoblasts leading to improved adhesion at the bone-implant interface [7,80]. Subramani *et al.* [80], have reported poly(ethylene glycol) (PEG) hydrogel coatings incorporating vascular endothelial growth factors (VEGF). The results shown that incorporating VEGF in the hydrogel produced micropatterns that dramatically altered rat osteoblast behaviour proving that this system could be applied for guided tissue bone regeneration orthopaedic applications. In addition, drug-eluting hydrogel coatings have been used onto orthopaedic implants to prevent infections related to orthopaedic surgeries [81–84]. The commercially available hydrogel DAC® (Defensive Antibacterial Coating; Novagenit Srl, Mezzolombardo, Italy) is a fast-resorbable hydrogel coating, composed of covalently linked hyaluronan and poly-D,L-lactide, which is spread onto cementless hip prothesis [83,84]. Hydrogel DAC® is loaded intra-operatively with one or more antibiotics, for example, vancomycin, gentamicin, or N-acetylcysteine, which are released within 48 to 72h, providing antibacterial and antibiofilm protection to the implant [83,84]. Moreover, this hydrogel coating has been shown to be capable of resisting removal during implant insertion when used as a press-fit implant coating on uncemented femoral stems [85].

Although hydrogel coatings are easy to apply, by simply immersing implants into hydrogel solutions, and being able to coat implants with complex geometries, there is minimal control of their loading efficiency or release kinetics, as well as batch-to-batch variability [7]. Thus, recent studies have demonstrated that LbL assembly is quite promising in the orthopaedic area for the effective loading and controlled release of multiple types of biomolecules from coatings. For example, Crouzier *et al.* [70] shown that crosslinked poly(L-lysine)/hyaluronan LbL films can serve as a reservoir for rhBMP-2 delivery to myoblasts and induce their differentiation into osteoblasts in a dose-dependent manner. La *et al.* [74] have also described a Ti implant coated with graphene oxide by LbL assembly of positively and negatively charged graphene oxide sheets and loaded with BMP-2 at the outermost coating layer. They demonstrated that the *in-vitro* osteogenic differentiation of hMSCs, is enhanced and found that after implantation in mouse models of calvarial defects robust new bone formation occurred [74]. Also, Lee *et al.* [75], reported a novel surface functionalization approach with Ti-adhesive nanoparticles prepared by LbL assembly of a catechol-functionalized poly(amino acid) diblock copolymer, that can load and controllably release BMP-

2. They demonstrated that the Ti substrate functionalized with BMP-2-incorporated nanoparticles significantly promoted attachment, proliferation, spreading and alkaline phosphatase activity of human adipose-derived stem cells (hADSC) [75].

1.4 Tissue Adhesives

The structural and functional restoration of an injured tissue requires its surgical reconnection. To this end, mechanical fasteners such as sutures, staples and wires, have been used for years for joining tissues. Despite their common clinic use, these mechanical methods still have some drawbacks [5].

Tissue adhesives have emerged as attractive alternatives as they are able to join tissues or tissues to non-tissues, such as prostheses, allowing adequate tissue healing, while also interrupting the leakage of biological fluids and resisting tensile loads. In addition, they exhibit some advantageous features, such as reduction of surgery time, mitigation of surgical complications (e.g. infection), easy application, and no removal requirements [86,87].

Currently there are several types of commercially available tissue adhesives, which are traditionally classified into two main categories: natural and synthetic adhesives [5]. Table 1.1 summarizes the main tissue adhesive types commercially available as well as their applications [5,6,88]. Despite natural tissue adhesives are effective in some applications, they are quite expensive and have limited availability because they are derived from autologous tissue. In addition, they often exhibit relatively poor mechanical and tissue-bonding properties, and are potentially pro-inflammatory because most of them are based on proteins [5,6]. On the other hand, synthetic tissue adhesives present several disadvantages such as low bioabsortion and metabolic rates, cytotoxicity, low adherence to wet surfaces and chronic inflammation induced by the release of some degradation products [5,6]. Therefore, it is pertinent to develop improved adhesives and methods of tissue adhesion for use in connection with living tissues, since the currently available tissue adhesives still have significant limitations and drawbacks [5,88]. Recently, an active area of research is related to the development of mimicking adhesive materials found in mussels, due to their outstanding adhesion properties presented in wet environments [27,28].

Table 1.1 – Natural and synthetic tissue adhesives commercially available. Adapted from [5,6,88].

Adhesive Type	Commercial Product	Approved indications	Constituents	Ref.
		Natural Adhesives		
Polysaccharides-based	HemCon® Bandage Pro	• Haemostasis • Antibacterial barrier	CHT	[89]
	Actamax	• Adhesion prevention • Tissue sealing	Dextran aldehyde, 8-arm PEG amine functionalized with tris(2-aminoethyl)amine	[90,91]
Proteins-based	Tisseel (Baxter)	• Haemostasis during cardio bypass surgery • Treatment of splenic injuries • Adjunct in colonic anastomosis	Human fibrinogen, human fibronectin, human thrombin, human Factor XIII, bovine aprotinin, calcium chloride	[92,93]
	Evicel (Ethicon)	• General haemostasis in surgery	Human fibrinogen, human thrombin, human factor XIII, calcium chloride	[92,94]
	CryoSeal (Thermogen)	• Haemostasis in liver resection surgery	Human fibrinogen, human thrombin, human fibronectin, human Factor XIII, human Factor VIII, human vWF, human thrombin from individual units of plasma	[95,96]
	Hemaseel (Haemacure Corp.)	• Used in surgical procedures to arrest bleeding and as an adjunct to wound healing	Human fibrinogen, human fibronectin, human factor XIII, bovine thrombin, calcium chloride	[93]
	Crosseal® (Omrix)	• Adjunct to haemostasis in liver surgery	Human fibrinogen, human thrombin, human fibronectin, human factor XIII, calcium chloride	[94,97]
	TachoSil® (Pharmaceuticals International GmbH)	• Haemostatic agent and tissue sealant	Equine collagen patch, human fibrinogen, human thrombin	[98,99]
	Vitagel™ (Stryker) replaced CoStasis Surgical Haemostat	• Surgical procedures (other than neurological and ophthalmic) as adjunct to haemostasis	Bovine collagen, bovine thrombin, patients own plasma	[100,101]
	GRF® Biological Glue (Microval)	• Thoracic aortic dissections and haemostasis	Gelatin, resorcinol, formaldehyde, glutaraldehyde	[102,103]
	BioGlue® (CryoLife)	• Adjunct to achieve haemostasis and in open surgical repair of large vessels	Albumin, glutaraldehyde	[104,105]
	ProGel® (NeoMend)	• Sealing air leaks on lung tissue after surgery	Human Serum Albumin, PEG di NHS	[106,107]

Synthetic Adhesives				
Cyanoacrylates	Histoacryl® and Histoacryl® Blue	• Closure of superficial skin wound and lacerations	n-Butyl-2-cyanoacrylate	[108]
	Dermabond®	• Closure of superficial skin wound and lacerations • Microbial barrier	2-Octyl-2-cyanoacrylate	[108,109]
	Indermil®	• Closure of superficial skin wound and lacerations • Microbial barrier	n-Butyl-2-cyanoacrylate	[108]
	Omnex®	• Blocking passage of blood, body fluids or air	n-Octyl-2-cyanoacrylate/butyl lactoyl-2-cyano acrylate	[108]
	Glubran® and Glubran2®	• Surgical glue for internal and external use • Haemostatic, adhesive, sealer, and bacteriostatic properties	n-Butyl-2-cyanoacrylate/methacryloxysulpholane	[110]
	IFABond®	• Implantable device alternative to staples and sutures (mesh)	N-Hexyl-2-cyanoacrylate	[88]
PEG derivatives	FocalSeal-L® (Focal Inc.), replaced AdvaSeal	• Sealing lung air leaks	Photopolymerizable PEG-co-poly(lactic acid)/poly(trimethylene carbonate)	[111,112]
	DuraSeal™ (Covidien), DuraSeal Xact	• Adjunct to sutures for dural repair • Retina reattachment • Nerve sciatic anastomosis • Vascular closure	Tetra-NHS-derivatized PEG and trilysine	[113,114]
	CoSeal® (Cohesion Technologies)	• Adjunct haemostasis in vascular surgery; inhibiting suture line bleeding	Tetra-NHS-derivatized PEG and tetra-thiol-derivatized PEG	[115]
	SprayGel® (Covidien)	• Adhesion barrier in gynaecological and colorectal procedures	Tetra-NHS-derivatized PEG and tetra-amine-derivatized PEG	[116,117]
Polyesters	TissuePatch™ (TissueMed)	• Air leakage in thoracic surgery • Sealing and reinforcing soft tissues adjunct to sutures • Dural repair in cranial surgery, adjunct to sutures	poly-((N-vinylpyrrolidone)$_{40}$-co-(acrylic acid)$_{25}$-co-(acrylic acid N-hydroxysuccinimide ester)$_{25}$)	[118,119]
Dendrimers and hyperbranched polymers	OcuSeal (Hyperbranch Medical Technology)	• Dressing for corneal lacerations and bandage for corneal transplants	poly(glycerol succinic acid) and PEG-aldehyde	[120,121]
	Adherus™ (Hyperbranch)	• Surgical sealant for dural repair, hernia mesh fixation, spinal and cardiovascular applications	Activated PEG and branched poly(ethylene imine)	[122]
Polyurethanes	TissuGlu®	• Preventing the seroma formation in abdominoplasty	Lysine di/tri isocyanate-PEG prepolymers	[123]

1.5 Bioinspired Underwater Adhesives

Wet environments created by body fluids are a considerable challenge for tissue adhesives, since the intersurface physical adhesive forces may be weakened and the chemical bonds altered in the presence of water [124]. Although synthetic reactive glues like cyanoacrylate [125] or bioderived glues like fibrin [126] give an effective wet adhesion, they present some disadvantages [124]. Other alternatives are the bioinspired underwater adhesives such as glues and cements inspired by marine creatures such as mussels, barnacles, tube worms, algae, and starfish, as depicted in Figure 1.2 [24,127,128].

Figure 1.2 – Underwater adhesion of some marine creatures. Left to right: mussels, barnacles, tube worms and starfish [24].

Concerning the biomimetic polymers, mussels and barnacles have become the main target for marine adhesion studies [5]. However, unlike the barnacle adhesion that still presents pioneering studies [119,129], the biochemical knowledge on mussel adhesions has been accumulated during the over past 30 years [5,130,131].

1.5.1 Marine Mussel Adhesive Properties

Blue mussels (*Mytilus edulis*) adhere themselves to surfaces through byssal (or "byssus" or "beard") adhesive assembly, consisting of a series of small deposited adhesive plaques, each connected to the mussel by a long thread as shown in Figure 1.3 [5,24].

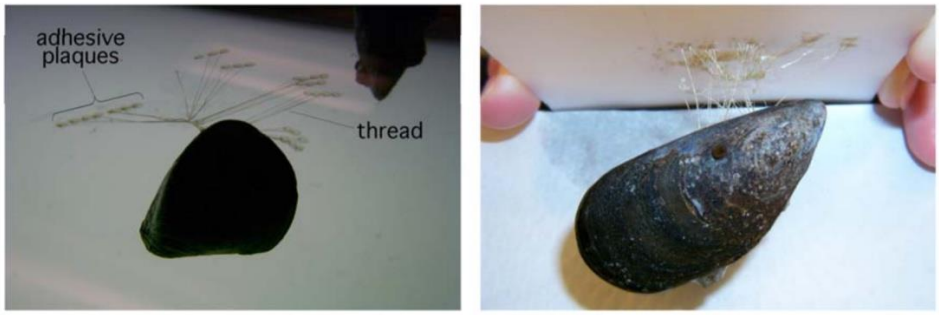

Figure 1.3 – Adhesive plaques of a marine mussel connected by threads to a glass sheet (left) and Teflon (polytetrafluoroethylene, right) [24].

The main element responsible for the adhesion of mussels has been determined to be the post-translationally modified amino acid, DOPA, as represented in Figure 1.4 [28,132]. The *Mytilus edulis* foot proteins (Mefp), in the mussel adhesive plaque were largely characterized and six of them were identified

to present a DOPA content ranging from 3 mol% (Mefp-2) to 30 mol% (Mefp-5) [133]. The excellent underwater adhesive properties of Mefps have recently attracted much attention [134–136].

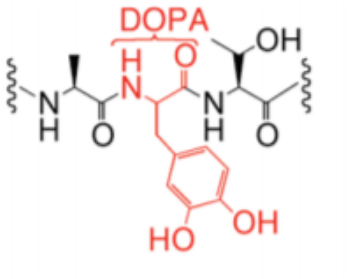

Figure 1.4 – Illustration of a DOPA unit. Adapted from [28].

It has been confirmed that the ortho-dihydroxyphenyl (catechol) moiety of DOPA present in secreted MAPs is responsible for the strong adhesion between adhesive pads of mussels and opposing surfaces [26,134,135,137,138]. The adhesion of MAPs, extracted and recombinant, to various solid materials [25,139,140] and mammalian cells [140–142] has already been verified. However, the specific adhesion mechanism of these small molecules is still not completely understood [143]. Although several proposals of interaction modes can be found in the literature, it is well accepted that catechol groups are particularly susceptible to oxidation under neutral to alkaline pH conditions, such as in seawater, and this fact is thought to provide the water-resistance characteristics of mussel adhesion [135]. Thus, under oxidative conditions, DOPA residues are converted to DOPA-quinone, which are capable of many different types of chemical interactions, giving rise to a highly cross-linked three-dimensional matrix that quickly solidifies [132,144]. In fact, MAPs allow mussels to adhere to and maintain functional adhesion even in harsh marine environments over a wide temperature range (-40 °C to 40 °C), fluctuating salinity and humidity [24,25].

As such, water-resistant adhesives based on marine mussels are the most exploited biomimetic approaches in recent years, due to their many fascinating features [134–136]. Mussel-based adhesives can potentially be used as surgical adhesives or as orthopaedic cements, since they are flexible, elastic, and much stronger than other polymer-based adhesives such as epoxy and phenolic resins [5,25]. In addition, they have proved to be environmentally friendly, as they are biodegradable [145] and apparently harmless to the human body because do not impose immunogenicity, which indicates their potential use for *in-vivo* applications [146,147].

1.6 Catechols as Versatile Platforms for Bioinspired Polymer Adhesives

As said before, catechol groups are responsible for the versatile adhesion of mussels under very harsh and wet conditions. In fact, they had an extremely strong affinity to various organic/inorganic surfaces such as metal, metal oxide, polymer surfaces, and even biomacromolecules [26,148]. Thus, researchers have used catechol chemistry to modify several types of substrates [20,149], particles [150,151] and to improve the mechanical properties of polymer composites [28,152].

Chemical incorporation of DOPA and analogous reactive groups, such as catechol groups into a variety of polymer backbones, Figure 1.5, is being pursued to enhance their adhesive strength [28,153,154]. Such unique and robust chemistry of catechol provides scientists a tool to design various bioadhesive materials for a wide range of biomedical applications [143].

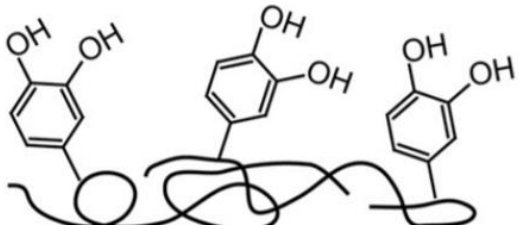

Figure 1.5 – Illustration of a polymer-catechol system mimicking MAPs. Adapted from [154].

Bio-inspired synthetic polymers containing catechol groups are being generated from poly(peptides) [25,155,156], poly(amides) [157], poly(N-isopropylacrylamides) [158,159], poly(allylamines) [160], poly(acrylates) [161–163], poly(acrylic acids) [40,136], poly(ethylene glycols) [164–166], poly(styrenes) [28,167,168], poly(vinyl alcohols) [169,170], poly(ethylenimines) [20,40,171], and poly(urethanes) [172].

Natural polymers have also been conjugated to catechol groups. Examples of these systems are HA [18,29,20,38,173,137,174–185], dextran [186,187], alginate [188–191], CHT [21,22,153,192–206], gelatin [207–209] and heparin [210–214].

These catechol-functionalized polymers are enabling the development of nanoparticle shells [171,199,200], elastomers [162,168], resins [167], hydrogels [22,137,159,160,172,175,178,180,183,188,191,192,197,198,205], surface treatments [18,29,20,38,156,169,181,182,185,190,196,203], antibacterial coverings [215], drug delivery systems [22,40,179,184], membranes [136,176,189], and antifouling coatings [163,165,186,187,214].

Indeed, the field of catechol-containing polymers, owing to their fascinating intrinsic chemical properties and their practical applications, has greatly expanded over the past decade [143].

1.6.1 Catechol-Conjugated Chitosan

Since there is an amount very limited of polycationic polysaccharides, CHT has received much attention from researchers [181].

This polysaccharide is the de-acetylated form of chitin and is by far the most widespread biopolymer used in PEM films for many biomedical applications [181,216]. This is due to its ability to bind to anionic polymers, via LbL self-assembly, giving rise to multilayered structures [217,218], and to its numerous interesting properties, [216] as biodegradability, biocompatibility, bioadhesivity, and haemostatic and antibacterial properties [14,89,217]. For example, CHT has received attention as a potential coating material for orthopaedic and dental/craniofacial implants due to its osteogenic and biodegradable/drug delivery properties, ability to accelerate wound healing, and processing and modification flexibilities [14,15,29,37,38].

However, CHT has poor mechanical properties [219,220] and is soluble only under acidic conditions, which may limit its performance during the LbL assembly process [220]. Thus, many researchers have described new approaches to overcome them, either by chemical modification or by covalent and ionic cross-linking of CHT [220].

CHT can be functionalized with hydrocaffeic acid to obtain water-soluble catechol-conjugated CHT (CHT-C). Table 1.2 summarizes several biomedical applications reported in the literature using CHT-C.

Table 1.2 – Summary of the intended applications of catechol-functionalized CHT adhesive polymer.

Catechol-functionalized Polymer	Intended Applications	Ref.
Chitosan–Catechol	• LbL Coatings for Tissue Adhesion	[196]
	• Haemostatic Coatings with Adhesive Properties and Prevent Bleeding	[195,203]
	• Nanocomposites for Biosensor Applications	[194]
	• Nanoparticle Shells for Drug Delivery	[199]
	• Nanoparticle Shells for Antibacterial Applications	[200,206]
	• Adhesive Gel Patches for Drug Delivery	[202]
	• Adhesive Platform for Bio-macromolecules Immobilization	[204]
	• Hydrogels for Tissue Adhesion	[192,197,205]
	• Haemostatic Hydrogels for Antibleeding Applications	[192]
	• Hydrogels for Drug Delivery	[22,198]

Functionalization of CHT with catechol groups was first proposed by Ryu and co-workers [192]. They reported an injectable and thermosensitive composite hydrogel composed of CHT-C cross-linked with terminally thiolated Pluronic F-127 triblock copolymer, for tissue adhesives and haemostatic materials [192]. The composite hydrogels showed strong adhesiveness to soft tissues and mucous layers, and superior haemostatic properties, demonstrating that they could be potentially used for injectable drug delivery depots, tissue engineering hydrogels, tissue adhesives, and antibleeding materials [192].

Kim *et al.* [193], described that chemical modification of CHT with catechol groups dramatically increased their solubility in water (to 60 $mg.mL^{-1}$ at pH 7.0) and its adhesive properties compared to unmodified CHT. The fact of CHT-C being soluble in water, in neutral buffer solutions, allowed them to directly form a CHT hydrogel [193].

Stabilization of silver-core nanoparticle shells with the assistance of CHT-C was reported by Cu and co-workers [206]. They confirmed that even at a very low concentration of silver nanoparticles, the nanoparticle shells exhibited a strong antibacterial activity against *E. coli* and *S. aureus*, offering this system a novel method for antibacterial applications [206].

Lee *et al.* [202], reported a water-resistant CHT-C adhesive gel patch for cartilage repair model. The adhesive barrier exhibited directional release of platelet-derived growth factor-AA (PDGF-AA) only toward the marrow cavity defect areas, leading to effective recruitment of hMSCs [202]. A significant improvement of cartilage tissue was demonstrated by *in-vivo* imaging and macroscopic histological assessments, suggesting that the directional controlled release trough this concept could be a strategy for the improvement of tissue regeneration in general [202].

Xu and co-workers [22], developed a buccal drug delivery system using a novel CHT-C hydrogel crosslinked with genipin. They showed that the novel hydrogels systems significantly increased mucoadhesion to the porcine mucosal membrane *in-vitro*, and sustained the release of lidocaine for about 3 h, *in-vivo*, using the rabbit buccal mucosa as test model. The results indicated that the proposed CHT-C hydrogel is a promising mucoadhesive and biocompatible system for mucosal drug delivery. In another study, Xu and co-workers [198], used the same hydrogel system for the efficient rectal administration of sulfasalazine (SSZ) to treat ulcerative colitis in a mouse model. Results have shown that SSZ/CHT-C rectal hydrogels are more effective and safer formulations for ulcerative colitis treatment than oral SSZ, exhibiting their potential as drug delivery systems for treating a generalized disease [198].

Recently, Chen *et al.* [196], proposed a surface functionalization of Ti implants with CHT-C for suppression of the oxidative stress induced by reactive oxygen species (ROS), which would hinder the bone healing process. Surface functionalization consisted of the construction of a multilayered structure

composed of CHT-C, gelatin, and hydroxyapatite nanofibers on Ti substrates [196]. The results showed that this multilayer effectively protected osteoblasts from ROS damage, besides promoting osteoblasts differentiation, collagen secretion, ECM mineralization and osteogenesis-related genes expression *in-vitro* [196].

1.6.2 Catechol-Conjugated Hyaluronic Acid

HA polysaccharide is an integral component of ECM that promotes tissue hydration, making ECM an ideal environment for cellular activity such as proliferation, differentiation, and tissue repair [221]. Therefore, its wide availability, ease processing, low toxicity, viscoelastic and rheological properties make HA a polymer attractive for the construction of new biocompatible and biodegradable materials for tissue engineering and drug delivery applications [16,222].

HA has been used in several biomedical applications such as wound healing, tissue regeneration, drug delivery and post-surgical anti-adhesion [137]. Among the polysaccharides, HA is the most studied as biofilm repelling coating [223,224].

Beyond that, it has proved to be an effective polyanion capable of complexing with cationic polymers such as CHT [17,18,29,38,173,225–227], providing opportunities to generate LbL systems. CHI/HA multilayers have been built up onto a huge diversity of substrates such as glass [228], Ti [173,229–232] or poly(propylene) [233].

HA can react with dopamine to obtain catechol-conjugate HA (HA-DN) [29,38], Table 1.3 summarizes several biomedical applications reported in the literature using HA-DN.

Table 1.3 – Summary of the intended applications of catechol-functionalized HA adhesive polymer.

Catechol-functionalized Polymer	Intended Applications	Ref.
Hyaluronic Acid–Catechol	• LbL Coatings for Tissue adhesion	[18,29,20,38,173,181]
	• Coatings for improve Hemocompatibility and Re-endothelization of Endovascular Stents	[182,185]
	• Coatings to support cell cultures	[175]
	• Hydrogels for Tissue Adhesion	[137,175,178,180,183]
	• Nanogels for Drug Delivery	[184]
	• LbL Membranes for Tissue Adhesion	[176]
	• Hollow Particles for Drug Delivery	[179]

Functionalization of HA with catechol groups was first proposed by Lee and co-workers [174]. They reported an immobilization of a homogeneous and robust coating of HA-DN on monodisperse magnetite nanocrystals, for their stabilization in aqueous solution and to be applied *in-vivo* targeted-cancer imaging [174]. Lee and co-workers [137] also developed lightly cross-linked hydrogels containing HA-DN and thiol end-capped Pluronic F127 copolymer. They demonstrated that *in-situ* formed hydrogels exhibited excellent tissue adhesion properties with superior *in-vivo* gel stability [137].

Both adhesive and cohesive properties of HA-DN were first confirmed by Hong *et al.* [175]. They have shown that these properties are mainly pH-dependent, in which alkaline solutions (pH 8 to 9) favour the cohesive state of HA-DN polymer [175]. In this way, HA-DN can exhibit either adhesiveness, functionalizing the surface of materials, or cohesiveness, building 3D hydrogels [175]. They also proved that HA-DN hydrogels are highly cell compatible, showing better viability (greater than 80%) compared to other HA-based hydrogels (less than 50%) [175].

Zhang and co-workers [173], constructed a multilayer coating of HA-DN/CHT through LbL self-assembly on Ti alloy. They have proved that the fabricated coating can serve as potential modification in orthopaedic applications, demonstrating that the proposed technique improves the biocompatibility of the Ti alloy with a significant increase of the proliferation of osteoblasts compared to uncoated Ti alloy [173]. Neto *et al.* [18], have also developed CHT/HA-DN multilayer coatings through LbL methodology, but using glass as substrate. They showed that the adhesion strength of multilayer coatings containing HA-DN was significantly higher than multilayer coatings containing unmodified HA [18]. In addition, they reported enhanced *in-vitro* cell adhesion, proliferation, and viability for biomimetic films with catechol groups, demonstrating their potential to be used in various biomedical applications [18]. Rego and co-workers [29], constructed for the first time organic-inorganic multilayered films, with a nacre-like architecture based on BGNPs, CHT and HA-DN. They found that the multifunctional LbL films exhibited both improved adhesion and bioactivity, promoting the formation of bone-like apatite *in-vitro*, and thus could be used as coatings on implants for orthopaedic applications [29].Carvalho *et al.* [38], produced LbL films combining the adhesive properties of HA-DN and the bioactivity and bactericidal properties of silver doped BGNPs. They also found that the LbL films displayed improved adhesion, promoting cell adhesion, proliferation, and viability *in-vitro*, and bioactivity, contributing for the formation of a bone-like apatite layer *in-vitro* [38]. Besides that, they confirmed the remarkable antibacterial effect against *Staphylococcus aureus* and *Escherichia coli* cultures, provided by silver doped nanoparticles [38]. In this way, they evidenced the great potential of the antibacterial bioadhesive films to be used as coatings for orthopaedic implants [38].

1.7 Nanoparticles for Biomedical Applications

In recent years, significant interest has arisen in the research of nanoparticles (NPs), in particular for biomedical applications [234]. The integration of nanotechnology into the field of medical science has opened new possibilities, among them, the potential of providing novel methods for the treatment of diseases that present size restrictions [234].

Due to their unique properties, synthesis, and applications, several biomedical fields have studied sub 100 nm materials like NPs [235]. The possibility of creating new strategies that can act *in situ* at a sub-cellular level, have led NPs to be applied in a wide range of applications, such as imaging agents, drug delivery systems, diagnostic tools, bioactivity enablers/improvers, biofunctionalization agents, among others [235,236]. Furthermore, its high surface-to-volume ratio provides a high surface area allowing it to be suitable modified to improve characteristics that are essential for biomedical applications, such as its pharmacokinetic properties, vascular circulation life-time and bioavailability [235]. NPs also have other advantages, such as their extremely high surface energy, and optical, magnetic and electronic properties that can be exploited in areas like biosensors and medic imaging [235,236].

1.7.1 Bioactive Glass Nanoparticles

Since their discovery in 1971, BGs have been used to improve the bond between bone and orthopaedic implants [33,237,31]. In particular, BGNPs obtained from sol-gel routes have been used in several studies not only to confer bioactivity to various composite systems, but also to improve their mechanical properties [238–243]. For instance, Luz and Mano [238], developed biomimetic osteoconductive membranes by combining BGNPs with a polymeric matrix of CHT. The BGNPs size around 50 nm allowed their uniform dispersion in the CHT membrane [238]. These membranes also demonstrated bioactivity potential by forming a dense apatite layer on the surface of the composite, after being immersed for seven days in a SBF solution [238]. Misra *et al.* [240], compared the effects of introducing micro-sized BGs and BGNPs on various properties (thermal, mechanical and microstructural) of poly(3-hydroxybutyrate). When compared with micro-sized BGs, the composite films containing BGNPs exhibited increased stiffness, wettability, protein adsorption and a great level of bioactivity [240].Couto and co-workers [241], proposed a novel injectable thermo-responsive hydrogel, combining CHT–β-glycerophosphate salt and BGNPs for orthopaedic applications. After immersing the hydrogel formulations in SBF, they observed a bone-like apatite formation indicating that the proposed hydrogels are bioactive [241]. Also, the rheological characterization of the developed hydrogels revealed that they have adequate

characteristics for intracorporal injection [241]. These results confirmed that the stimuli-responsive hydrogels could be potentially used as temporary injectable scaffolds in bone tissue engineering applications [241]. Mota *et al.* [243], produced a novel membrane composed by CHT and BGNPs for periodontal and bone regeneration. They showed that the composite membranes were bioactive, inducing the precipitation of bone-like apatite in SBF [243]. In addition, biological tests using human periodontal ligament cells and human bone marrow stromal cells demonstrated that the composite membranes promoted cell metabolic activity and mineralization [243]. Thus, this strategy could be potentially used as a temporary guided tissue regeneration membrane in periodontal regeneration, with the possibility to induce bone regeneration [243].

Recently, nanostructured multilayers coatings inspired by the adhesive properties of mussels, combining an inorganic matrix of BGNPs with an organic matrix of CHT and HA-DN were developed for the first time [29]. This study showed that the bioinspired coatings not only exhibited ability to induce the apatite formation, after immersion in a SBF solution for 7 days, but also present an improved adhesive strength conferred by catechol groups of HA-DN [29]. Thus, these mussels inspired coatings could be potentially used as coatings of a variety of implants for orthopaedic applications [29]. Both CHT and HA-DN polysaccharides and BGNPs have been also used to produce composite membranes for guided tissue regeneration [176]. These biomimetic membranes showed a bioactive behaviour necessary for the formation of new bone, tunable properties and enhanced adhesion [176].

1.8 Layer-by-Layer Assembly Method

Since its inception in 1990s [244], the LbL assembly approach has been proven to be an ideal method for construction of multifunctional nanostructured materials. Through this approach, almost any types of charged species such as polysaccharides, polypeptides, enzymes, nucleic acids, viruses, colloids, nanoparticles, clays, dyes, and metal oxides, can be used into multilayer films with promising applications in emerging areas such as medicine, sensing, biosensing, bioelectronics, separation, tissue engineering, drug delivery, catalysis, energy storage and conversion, electronics, and optics [12,13,40,245–250].

Contrary to other preparation techniques, the LbL approach is a relatively simple and highly versatile way for merging different functionalities into a single composite, while maintaining bulk properties [11,251]. It relies on the sequential adsorption of solutions of oppositely charged polymers, polyelectrolytes, mainly via electrostatic interactions, onto bulk surfaces generally negatively charged due to surface oxidation and hydrolysis, Figure 1.6. The cyclic process of immersing the charge substrate into

oppositely charged polyelectrolyte solutions, can be repeated as many times as intended, giving rise to complex multilayered films [11,20,252,244]. From this method, it is possible to have an extensive control over the properties, composition, structure, and thickness of the multilayer films, varying both the properties of the adsorbed species (charge density, concentration, molecular weight) and the liquid medium (salt/buffer composition, solvent quality, ionic strength, pH), as well as external parameters (temperature, exposure to light, mechanical stress, electrical field, adsorption time, number of layers) during the LbL assembly process [12,13,36]. Therefore, the multilayered structure can be simply functionalized by the incorporation of active compounds and their properties adjusted by the deposition conditions and the choice of the outermost layer (anionic or cationic) [225]. In addition, the film thickness can generally be well-controlled at the molecular level, increasing with the decrease in charge density and with the increase in ionic strength, temperature, and number of layers deposited [12].

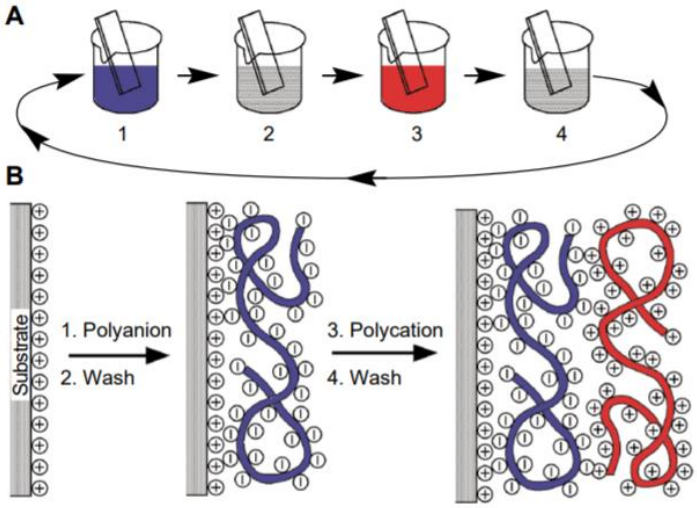

Figure 1.6 – Schematics illustration of the LbL deposition process: A - Steps 1 and 3 represent the immersion of the substrate in a polyanionic and polycationic solution, respectively. Steps 2 and 4 represent the washing steps. This cyclic process represents the formation of one bilayer, and can be repeated as many times as intended; B - Representation of the LbL deposition process at a molecular level. Adapted from [244].

During the growth of the multilayers, there are two possible steps, which may dominate, the adsorption and the interlayer diffusion of the polyelectrolytes, as shown in Figure 1.7. Adsorption is characterized by the movement of the polyelectrolyte molecules from the solution to the film surface. On the other hand, interlayer diffusion occurs when the polyelectrolyte molecules move from the surface into the film [253]. Based on these two steps, two types of multilayer growth behaviours have been reported so far, linear and exponential growth. Linear growth, is characterized by an adsorption controlled of the polyelectrolytes in the solution, interacting only with the oppositely charged polyelectrolytes on the film surface. Usually, it is observed in films comprising strong polyelectrolyte pairs and is due to the charge overcompensation that is required for the build-up of the multilayers. It is associated with a linear increase

in the thickness or mass of the film with the number of bilayers [12,254,255]. Exponential growth, is based on the interlayer diffusion within the film, which always occurs in weak polyelectrolyte systems consisting of at least one polypeptide or polysaccharide, such as CHT/HA. Thus, it is related to the exponential increase in film thickness with the number of bilayers [12,256,257]. Generally, linear regimes lead to thinner films compared to exponential regimes [12].

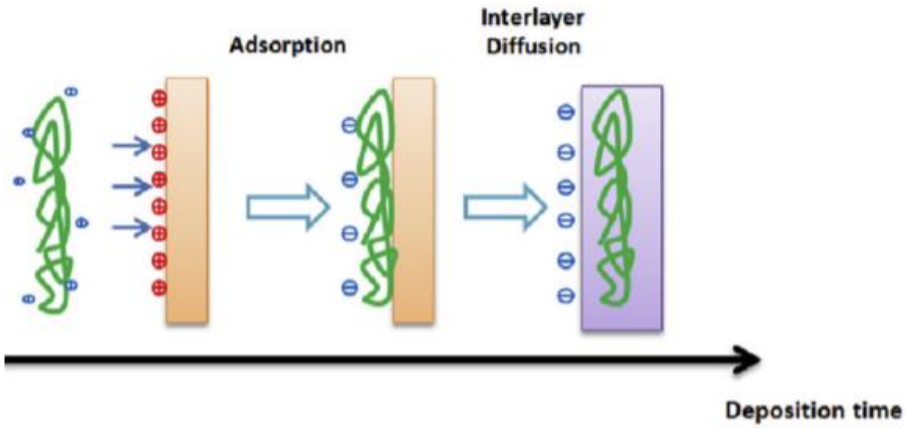

Figure 1.7 – Schematics illustration of the adsorption and interlayer diffusion during the LbL deposition process. Adapted from [253].

Multilayer films may also undergo a transition between these growth types, depending on the strength of the polyelectrolyte intermolecular interactions, the molecular weight of polyelectrolytes and the experimental deposition conditions [12]. Recent studies have demonstrated that the tendency of the polyelectrolytes to diffuse throughout films during the LbL process is believed to be due to a mismatch of the charge density between oppositely charged polyelectrolytes [258,259], and/or the enhanced mobility of polymers with low molecular weight, or low charge densities [256,260]. The deposition time is another parameter related to interlayer diffusion [12,13,254]. Typically, increasing the deposition time leads to the construction of thicker films, i.e., with exponential growth, since during short deposition times, interlayer diffusion is limited translating into linear growth behaviour [12].

Often the interlayer diffusion phenomenon represents a problem for certain systems that should provide delivery functions of bioactive molecules and polyelectrolyte components in the presence of external stimuli, such as changes in pH or ionic strength [40]. Therefore, to enhance the stability of LbL films, thermal [261], chemical [262,263] and photoreactive [264] routes have been employed. However, the use of such routes can be detrimental when fragile and sensitive biomolecules are incorporated into the LbL films [40]. As such, there is a growing demand for the development of alternative non-destructive strategies to improve the stability of LbL films and, eventually, to achieve a long-term biomolecules delivery [40]. Min and co-workers [40] developed chemically and mechanically stable LbL films inspired

by the adhesive properties of catechol groups, largely present in MAPs. They used the carbodiimide strategy to conjugate catechol groups onto branched poly(ethyleneimine) and poly(acrylic acid). They demonstrated that the incorporation of catechol groups led to a doubling of the average film thickness and a linear film growth, which contributed to improve both film stability and mechanical properties. In addition, they showed that the LbL films with catechol modifications can been used for the controlled release of biomolecules [40].

The LbL processing method is not only limited to electrostatics interactions, but can also be performed trough hydrogen-bonding, charge transfer, covalent bonding, biological recognition and hydrophobic interactions [12]. As result of all potentialities of the LbL technique, several different types of films and structures with different functional properties have been produced for various biomedical applications [13,265]. These applications include fabrication of scaffolds, medical adhesives, stents, wound healing systems and coatings for implants with complex geometries [13,265].

1.9 Nacre: Definition and Structure

Nacre can be found in the inner layer of hard shells of most molluscs of the bivalve and gastropods classes. It is composed of 95% (wt.) of aragonite, which is a crystallographic form of $CaCO_3$, and 5% (wt.) of organic materials, such as proteins and polysaccharides [35]. This organic matrix plays an important role in spatial and chemical control of the crystal nucleation and growth, microstructure, and toughness enhancement [35,266].

Nacre structure, called brick-and-mortar like structure, is composed by hard aragonite platelets connected through organic materials, as shown in Figure 1.8 [36]. Although the nacre is composed of a hierarchy of structures ranging from the nano to the macro-scale, similarly to bone structure, it is possible to distinguish two different nacre types structures, columnar and sheet nacre [35,36]. In the columnar nacre (Figure 1.8 A), found in gastropods, platelets are stacked in columns with clear core and overlap regions, while the sheet nacre (Figure 1.8 B), found in bivalves, exhibits a more random staggered arrangement without well-defined cores and overlap regions [36]. In both nacres, the arrangement and size of the platelets are highly uniform and compact, as well as showing an obvious waviness [36].

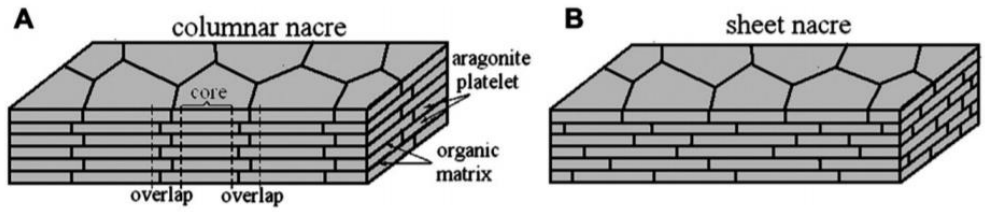

Figure 1.8 – Schematic illustration of the brick-and-mortar microstructure for (A) columnar nacre and (B) sheet nacre [36].

At nanoscale, the polygonal aragonite nanograins of the building blocks of nacre are connected by mineral bridges, which are embedded in biopolymer layers, forming nanoplatelets (first level) [36,267]. These mineral bridges allow continuous mineralization in the organic layers, and play an important role in improving mechanical properties and in preventing crack extension on nacre [35] The nanoplatelets are staggered into a brick-and-mortar structure, also, enveloped by biopolymer (second level) [36,267].

Under mechanical deformation, the nanograins of the nanoplatelets suffer rotation and deformation, owing to its capability for undergoing large inelastic deformations. This fact allows to dissipate the mechanical energy, providing a ductile nature to aragonite nanoplatelet, which, in turn, is relevant for nacre's high fracture toughness [35].

According to the findings of Jackson *et al.* [268], nacre from the shell of a bivalve mollusc, *Pinctada imbricate*, have shown a value of elastic modulus (E) of approximately 70 GPa (dry) and 60 GPa (wet), and tensile strength of approximately 170 MPa (dry) and 130 MPa (wet). These findings have shown that the hydration effect is particularly important for the toughness of nacre [266]. Barthelat *et al.* [269] reported that the E value of a single nanoplatelet was 79 GPa, which is close to the monolithic aragonite (81 GPa). Moreover, organic phase of nacre has displayed E values between 2.84 and 15 GPa [35]. These results suggest that both the softer organic matrix and the structure of aragonite nanoplatelets influence the overall properties of nacre [35].

These outstanding mechanical and structural properties of nacre have inspired many researchers to fabricate novel materials and structures [35,266], such as biomimetic coatings [29,37,38,67,270], free standing films [176,271–273], and composite materials [274–282]. Among the different processing techniques that have been proposed to develop nacre-like composites, LbL deposition appears as one of the most attractive methods. This technique allows the development of nanostructured layered structures with thickness controlled at the nanoscale level, using a wide range of different materials [13,36,252]. In particular, LbL deposition enables the combination of organic and inorganic materials to obtain nacre-like structures [13,36].

1.9.1 Bioinspired Nacre-like Coatings for Biomedical Implants and Scaffolds

Biomedical coatings have been designed to act as an interface between the material and the host tissue to trigger several biologic processes from the inflammatory reaction to ultimate tissue remodelling [9,10]. Their main applications have been based on improving the *in-vivo* integration of various implants [173,231,232,283–285], and for enhancing cell adhesion in scaffolds for tissue engineering [286], among others [287].

Currently, researchers have relied on the composition and structure of the nacre for the construction of LbL coatings for the same applications believing that they offer other structural and functional advantages [29,37]. Recent studies have demonstrated that LbL coatings, inspired by the layered structure of nacre [29,37], containing an organic matrix of polysaccharides and an inorganic matrix of BGNPs can be potentially used onto orthopaedic implants and scaffolds due to their mechanical performance, toughness, and bioactivity [35,36]. Their bioactive properties were confirmed by the presence of a bone-like apatite layer onto the coatings, after immersion in SBF. In fact, for the proper integration of orthopaedic implants *in-vivo* and for the formation of new bone, the development of this bone-like apatite layer is vital [287]. In addition, both studies showed that the LbL coatings produced had viscoelastic properties similar to nacre [29,37]. Thus, such multilayers coatings could avoid the typical use of bone cements and thus could be used on a variety of implants for orthopaedic applications [39,40].

1.10 References

[1] M.P. Staiger, A.M. Pietak, J. Huadmai, G. Dias, Magnesium and its alloys as orthopedic biomaterials: A review, Biomaterials. 27 (2006) 1728–1734. doi:10.1016/j.biomaterials.2005.10.003.

[2] M. Xiao, Y.M. Chen, M.N. Biao, X.D. Zhang, B.C. Yang, Bio-functionalization of biomedical metals, Mater. Sci. Eng. C. 70 (2017) 1057–1070. doi:10.1016/j.msec.2016.06.067.

[3] C. Gretzer, L. Emanuelsson, E. Liljensten, P. Thomsen, The inflammatory cell influx and cytokines changes during transition from acute inflammation to fibrous repair around implanted materials., J. Biomater. Sci. Polym. Ed. 17 (2006) 669–687.

[4] D.T. Luttikhuizen, M.C. Harmsen, M.J.A. Van Luyn, Cellular and molecular dynamics in the foreign body reaction., Tissue Eng. 12 (2006) 1955–1970. doi:10.1089/ten.2006.12.1955.

[5] A.P. Duarte, J.F. Coelho, J.C. Bordado, M.T. Cidade, M.H. Gil, Surgical adhesives: Systematic review of the main types and development forecast, Prog. Polym. Sci. 37 (2012) 1031–1050.

doi:https://doi.org/10.1016/j.progpolymsci.2011.12.003.

[6] M. Mehdizadeh, J. Yang, Design Strategies and Applications of Tissue Bioadhesives, Macromol. Biosci. 13 (2013) 271–288. doi:10.1002/mabi.201200332.

[7] S.B. Goodman, Z. Yao, M. Keeney, F. Yang, The future of biologic coatings for orthopaedic implants., Biomaterials. 34 (2013) 3174–3183. doi:10.1016/j.biomaterials.2013.01.074.

[8] R. Teghil, L. D'Alessio, D. Ferro, S.M. Barinov, Hardness of bioactive glass film deposited on titanium alloy by pulsed laser ablation, J. Mater. Sci. Lett. 21 (2002) 379–382. doi:10.1023/A:1014903117057.

[9] V. Gribova, R. Auzely-Velty, C. Picart, Polyelectrolyte Multilayer Assemblies on Materials Surfaces: From Cell Adhesion to Tissue Engineering, Chem. Mater. 24 (2012) 854–869. doi:10.1021/cm2032459.

[10] N.M. Alves, I. Pashkuleva, R.L. Reis, J.F. Mano, Controlling cell behavior through the design of polymer surfaces., Small. 6 (2010) 2208–2220. doi:10.1002/smll.201000233.

[11] G. Decher, J. Hong, Buildup of ultrathin multilayer films by a self-assembly process, 1 consecutive adsorption of anionic and cationic bipolar amphiphiles on charged surfaces, in: Macromol. Symp., Wiley Online Library, 1991: pp. 321–327.

[12] J. Borges, J.F. Mano, Molecular interactions driving the layer-by-layer assembly of multilayers., Chem. Rev. 114 (2014) 8883–8942. doi:10.1021/cr400531v.

[13] Z. Tang, Y. Wang, P. Podsiadlo, N.A. Kotov, Biomedical Applications of Layer-by-Layer Assembly: From Biomimetics to Tissue Engineering, Adv. Mater. 18 (2006) 3203–3224. doi:10.1002/adma.200600113.

[14] I.-Y. Kim, S.-J. Seo, H.-S. Moon, M.-K. Yoo, I.-Y. Park, B.-C. Kim, C.-S. Cho, Chitosan and its derivatives for tissue engineering applications, Biotechnol. Adv. 26 (2008) 1–21. doi:10.1016/j.biotechadv.2007.07.009.

[15] A. Di Martino, M. Sittinger, M. V. Risbud, Chitosan: A versatile biopolymer for orthopaedic tissue-engineering, Biomaterials. 26 (2005) 5983–5990. doi:10.1016/j.biomaterials.2005.03.016.

[16] G. Kogan, L. Šoltés, R. Stern, P. Gemeiner, Hyaluronic acid: A natural biopolymer with a broad range of biomedical and industrial applications, Biotechnol. Lett. 29 (2007) 17–25. doi:10.1007/s10529-006-9219-z.

[17] T.I. Croll, A.J. O'Connor, G.W. Stevens, J.J. Cooper-White, A blank slate? Layer-by-layer deposition of hyaluronic acid and chitosan onto various surfaces, Biomacromolecules. 7 (2006) 1610–1622. doi:10.1021/bm060044l.

[18] A.I. Neto, A.C. Cibrão, C.R. Correia, R.R. Carvalho, G.M. Luz, G.G. Ferrer, G. Botelho, C. Picart, N.M. Alves, J.F. Mano, Nanostructured polymeric coatings based on chitosan and dopamine-modified hyaluronic acid for biomedical applications, Small. 10 (2014) 2459–2469. doi:10.1002/smll.201303568.

[19] B. Thierry, F.M. Winnik, Y. Merhi, M. Tabrizian, Nanocoatings onto arteries via layer-by-layer deposition: toward the in vivo repair of damaged blood vessels., J. Am. Chem. Soc. 125 (2003) 7494–7495. doi:10.1021/ja034321x.

[20] H. Lee, Y. Lee, A.R. Statz, J. Rho, T.G. Park, P.B. Messersmith, Substrate-independent layer-by-layer assembly by using mussel-adhesive-inspired polymers, Adv. Mater. 20 (2008) 1619–1623. doi:10.1002/adma.200702378.

[21] K. Kim, K. Kim, J.H. Ryu, H. Lee, Chitosan-catechol: A polymer with long-lasting mucoadhesive properties, Biomaterials. 52 (2015) 161–170. doi:10.1016/j.biomaterials.2015.02.010.

[22] J. Xu, S. Strandman, J.X.X. Zhu, J. Barralet, M. Cerruti, Genipin-crosslinked catechol-chitosan mucoadhesive hydrogels for buccal drug delivery, Biomaterials. 37 (2015) 395–404. doi:10.1016/j.biomaterials.2014.10.024.

[23] A. Ghadban, A.S. Ahmed, Y. Ping, R. Ramos, N. Arfin, B. Cantaert, R. V. Ramanujan, A. Miserez, Bioinspired pH and magnetic responsive catechol-functionalized chitosan hydrogels with tunable elastic properties, Chem. Commun. 52 (2016) 697–700. doi:10.1039/C5CC08617E.

[24] J.J. Wilker, Marine bioinorganic materials: mussels pumping iron, Curr. Opin. Chem. Biol. 14 (2010) 276–283. doi:https://doi.org/10.1016/j.cbpa.2009.11.009.

[25] M. Yu, T.J. Deming, Synthetic Polypeptide Mimics of Marine Adhesives, Macromolecules. 31 (1998) 4739–4745. doi:10.1021/ma980268z.

[26] H. Lee, N.F. Scherer, P.B. Messersmith, Single-molecule mechanics of mussel adhesion, Proc. Natl. Acad. Sci. 103 (2006) 12999–13003. doi:10.1073/pnas.0605552103.

[27] H.J. Cha, D.S. Hwang, S. Lim, Development of bioadhesives from marine mussels., Biotechnol. J. 3 (2008) 631–638. doi:10.1002/biot.200700258.

[28] C.R. Matos-Pérez, J.D. White, J.J. Wilker, Polymer Composition and Substrate Influences on the Adhesive Bonding of a Biomimetic, Cross-Linking Polymer, J. Am. Chem. Soc. 134 (2012) 9498–9505. doi:10.1021/ja303369p.

[29] S.J. Rego, A.C. Vale, G.M. Luz, J.F. Mano, N.M. Alves, Adhesive Bioactive Coatings Inspired by Sea Life, Langmuir. 32 (2016) 560–568. doi:10.1021/acs.langmuir.5b03508.

[30] M. MačKović, A. Hoppe, R. Detsch, D. Mohn, W.J. Stark, E. Spiecker, A.R. Boccaccini, Bioactive

glass (type 45S5) nanoparticles: In vitro reactivity on nanoscale and biocompatibility, J. Nanoparticle Res. 14 (2012). doi:10.1007/s11051-012-0966-6.

[31] A.R. Boccaccini, M. Erol, W.J. Stark, D. Mohn, Z. Hong, J.F. Mano, Polymer/bioactive glass nanocomposites for biomedical applications: A review, Compos. Sci. Technol. 70 (2010) 1764–1776. doi:10.1016/j.compscitech.2010.06.002.

[32] M. De, P.S. Ghosh, V.M. Rotello, Applications of Nanoparticles in Biology, Adv. Mater. 20 (2008) 4225–4241. doi:10.1002/adma.200703183.

[33] J.R. Jones, Review of bioactive glass: from Hench to hybrids., Acta Biomater. 9 (2013) 4457–4486. doi:10.1016/j.actbio.2012.08.023.

[34] F. Baino, G. Novajra, V. Miguez-Pacheco, A.R. Boccaccini, C. Vitale-Brovarone, Bioactive glasses: Special applications outside the skeletal system, J. Non. Cryst. Solids. 432, Part (2016) 15–30. doi:http://dx.doi.org/10.1016/j.jnoncrysol.2015.02.015.

[35] J. Sun, B. Bhushan, Hierarchical structure and mechanical properties of nacre: a review, RSC Adv. 2 (2012) 7617–7632. doi:10.1039/C2RA20218B.

[36] J. Wang, Q. Cheng, Z. Tang, Layered nanocomposites inspired by the structure and mechanical properties of nacre, Chem. Soc. Rev. 41 (2012) 1111–1129. doi:10.1039/C1CS15106A.

[37] D.S. Couto, N.M. Alves, J.F. Mano, Nanostructured multilayer coatings combining chitosan with bioactive glass nanoparticles., J. Nanosci. Nanotechnol. 9 (2009) 1741–1748.

[38] A.L. Carvalho, A.C. Vale, M. Sousa, A.M. Barbosa, E. Torrado, J. Mano, N.M. Alves, Antibacterial bioadhesive layer-by-layer coatings for orthopedic applications, J. Mater. Chem. B. 4 (2016) 5385–5393. doi:10.1039/C6TB00841K.

[39] Nanolayer film adheres biomedical implants to bone, Nanotchecweb. (2013). http://nanotechweb.org/ (accessed September 10, 2017).

[40] Y. Min, P.T. Hammond, Catechol-Modified Polyions in Layer-by-Layer Assembly to Enhance Stability and Sustain Release of Biomolecules: A Bioinspired Approach, Chem. Mater. 23 (2011) 5349–5357. doi:10.1021/cm201801n.

[41] M. Sivakumar, S. Rajeswari, Investigations of failures in stainless orthopeadic implants devices: Pit induced stress corrosion cracking., J Mater Sci. 11 (1992) 1039–1042. doi:10.1007/BF00729754.

[42] M. Niinomi, M. Nakai, J. Hieda, Development of new metallic alloys for biomedical applications, Acta Biomater. 8 (2012) 3888–3903. doi:https://doi.org/10.1016/j.actbio.2012.06.037.

[43] Y.F. Ding, R.W. Li, M. Nakai, T. Majumdar, D.H. Zhang, M. Niinomi, N. Birbilis, P.N. Smith, X.B.

Chen, Osteoanabolic Implant Materials for Orthopedic Treatment, Adv. Healthc. Mater. 5 (2016) 1740–1752. doi:10.1002/adhm.201600074.

[44] H.T. Aro, J.J. Alm, N. Moritz, T.J. Makinen, P. Lankinen, Low BMD affects initial stability and delays stem osseointegration in cementless total hip arthroplasty in women: a 2-year RSA study of 39 patients., Acta Orthop. 83 (2012) 107–114. doi:10.3109/17453674.2012.678798.

[45] J.A. Bishop, A.A. Palanca, M.J. Bellino, D.W. Lowenberg, Assessment of compromised fracture healing., J. Am. Acad. Orthop. Surg. 20 (2012) 273–282. doi:10.5435/JAAOS-20-05-273.

[46] T.F. Moriarty, U. Schlegel, S. Perren, R.G. Richards, Infection in fracture fixation: can we influence infection rates through implant design?, J. Mater. Sci. Mater. Med. 21 (2010) 1031–1035. doi:10.1007/s10856-009-3907-x.

[47] R.O. Darouiche, Treatment of infections associated with surgical implants., N. Engl. J. Med. 350 (2004) 1422–1429. doi:10.1056/NEJMra035415.

[48] S.B. Goodman, Wear Particles, Periprosthetic Osteolysis and the Immune System, Biomaterials. 28 (2007) 5044–5048. doi:10.1016/j.biomaterials.2007.06.035.

[49] N.J. Hallab, J.J. Jacobs, Biologic effects of implant debris., Bull. NYU Hosp. Jt. Dis. 67 (2009) 182–188.

[50] J. Zdolsek, J.W. Eaton, L. Tang, Histamine release and fibrinogen adsorption mediate acute inflammatory responses to biomaterial implants in humans, J. Transl. Med. 5 (2007) 31. doi:10.1186/1479-5876-5-31.

[51] L. Tang, T.A. Jennings, J.W. Eaton, Mast cells mediate acute inflammatory responses to implanted biomaterials, Proc. Natl. Acad. Sci. U. S. A. 95 (1998) 8841–8846. http://www.ncbi.nlm.nih.gov/pmc/articles/PMC21164/.

[52] J. Gallo, S.B. Goodman, Y.T. Konttinen, M. Raska, Particle disease: biologic mechanisms of periprosthetic osteolysis in total hip arthroplasty., Innate Immun. 19 (2013) 213–224. doi:10.1177/1753425912451779.

[53] J.M. Anderson, A. Rodriguez, D.T. Chang, FOREIGN BODY REACTION TO BIOMATERIALS, Semin. Immunol. 20 (2008) 86–100. doi:10.1016/j.smim.2007.11.004.

[54] P. Zhang, Z. Zhang, W. Li, M. Zhu, Effect of Ti-OH groups on microstructure and bioactivity of TiO2 coating prepared by micro-arc oxidation, Appl. Surf. Sci. 268 (2013) 381–386. doi:https://doi.org/10.1016/j.apsusc.2012.12.105.

[55] R.J. Talib, M.R.M. Toff, Plasma-sprayed coating of hydroxyapatite on metal implants-a review., Med. J. Malaysia. 59 Suppl B (2004) 153–154.

[56] R.G. Geesink, K. de Groot, C.P. Klein, Chemical implant fixation using hydroxyl-apatite coatings. The development of a human total hip prosthesis for chemical fixation to bone using hydroxyl-apatite coatings on titanium substrates., Clin. Orthop. Relat. Res. (1987) 147–170.

[57] J. He, T. Huang, L. Gan, Z. Zhou, B. Jiang, Y. Wu, F. Wu, Z. Gu, Collagen-infiltrated porous hydroxyapatite coating and its osteogenic properties: in vitro and in vivo study., J. Biomed. Mater. Res. A. 100 (2012) 1706–1715. doi:10.1002/jbm.a.34121.

[58] S. Choi, W.L. Murphy, Sustained plasmid DNA release from dissolving mineral coatings, Acta Biomater. 6 (2010) 3426–3435. doi:10.1016/j.actbio.2010.03.020.

[59] N. Saran, R. Zhang, R.E. Turcotte, Osteogenic Protein-1 Delivered by Hydroxyapatite-coated Implants Improves Bone Ingrowth in Extracortical Bone Bridging, Clin. Orthop. Relat. Res. 469 (2011) 1470–1478. doi:10.1007/s11999-010-1573-4.

[60] P. Laquerriere, A. Grandjean-Laquerriere, E. Jallot, G. Balossier, P. Frayssinet, M. Guenounou, Importance of hydroxyapatite particles characteristics on cytokines production by human monocytes in vitro., Biomaterials. 24 (2003) 2739–2747.

[61] L.L. Hench, Bioceramics, J. Am. Ceram. Soc. 81 (1998) 1705–1728. doi:10.1111/j.1151-2916.1998.tb02540.x.

[62] P. Ducheyne, Bioglass coatings and bioglass composites as implant materials, J. Biomed. Mater. Res. 19 (1985) 273–291. doi:10.1002/jbm.820190309.

[63] L.L. Hench, The story of Bioglass®, J. Mater. Sci. Mater. Med. 17 (2006) 967–978. doi:10.1007/s10856-006-0432-z.

[64] E.J. Szili, S. Kumar, R.S.C. Smart, N.H. Voelcker, Generation of a stable surface concentration of amino groups on silica coated onto titanium substrates by the plasma enhanced chemical vapour deposition method, Appl. Surf. Sci. 255 (2009) 6846–6850. doi:https://doi.org/10.1016/j.apsusc.2009.02.092.

[65] H. Oonishi, S. Kushitani, E. Yasukawa, H. Iwaki, L.L. Hench, J. Wilson, E. Tsuji, T. Sugihara, Particulate bioglass compared with hydroxyapatite as a bone graft substitute., Clin. Orthop. Relat. Res. (1997) 316–325.

[66] L.L. Hench, J. Wilson, Surface-active biomaterials., Science. 226 (1984) 630–636.

[67] J.R. Rodrigues, N.M. Alves, J.F. Mano, Nacre-inspired nanocomposites produced using layer-by-layer assembly: Design strategies and biomedical applications, Mater. Sci. Eng. C. 76 (2017) 1263–1273. doi:https://doi.org/10.1016/j.msec.2017.02.043.

[68] S. Mathews, R. Bhonde, P.K. Gupta, S. Totey, A novel tripolymer coating demonstrating the

synergistic effect of chitosan, collagen type 1 and hyaluronic acid on osteogenic differentiation of human bone marrow derived platelets., Biochem. Biophys. Res. Commun. 414 (2011) 270–276. doi:10.1016/j.bbrc.2011.09.071.

[69] M.L. Macdonald, R.E. Samuel, N.J. Shah, R.F. Padera, Y.M. Beben, P.T. Hammond, Tissue integration of growth factor-eluting layer-by-layer polyelectrolyte multilayer coated implants., Biomaterials. 32 (2011) 1446–1453. doi:10.1016/j.biomaterials.2010.10.052.

[70] T. Crouzier, K. Ren, C. Nicolas, C. Roy, C. Picart, Layer-by-layer films as a biomimetic reservoir for rhBMP-2 delivery: controlled differentiation of myoblasts to osteoblasts., Small. 5 (2009) 598–608. doi:10.1002/smll.200800804.

[71] Y. Liu, K. de Groot, E.B. Hunziker, BMP-2 liberated from biomimetic implant coatings induces and sustains direct ossification in an ectopic rat model., Bone. 36 (2005) 745–757. doi:10.1016/j.bone.2005.02.005.

[72] N.J. Shah, M.L. Macdonald, Y.M. Beben, R.F. Padera, R.E. Samuel, P.T. Hammond, Tunable dual growth factor delivery from polyelectrolyte multilayer films., Biomaterials. 32 (2011) 6183–6193. doi:10.1016/j.biomaterials.2011.04.036.

[73] N.J. Shah, J. Hong, M.N. Hyder, P.T. Hammond, Osteophilic Multilayer Coatings for Accelerated Bone Tissue Growth, Adv. Mater. 24 (2012) 1445–1450. doi:10.1002/adma.201104475.

[74] W.-G. La, S. Park, H.-H. Yoon, G.-J. Jeong, T.-J. Lee, S.H. Bhang, J.Y. Han, K. Char, B.-S. Kim, Delivery of a Therapeutic Protein for Bone Regeneration from a Substrate Coated with Graphene Oxide, Small. 9 (2013) 4051–4060. doi:10.1002/smll.201300571.

[75] H.J. Lee, A.N. Koo, S.W. Lee, M.H. Lee, S.C. Lee, Catechol-functionalized adhesive polymer nanoparticles for controlled local release of bone morphogenetic protein-2 from titanium surface., J. Control. Release. 170 (2013) 198–208. doi:10.1016/j.jconrel.2013.05.017.

[76] J. Auernheimer, D. Zukowski, C. Dahmen, M. Kantlehner, A. Enderle, S.L. Goodman, H. Kessler, Titanium implant materials with improved biocompatibility through coating with phosphonate-anchored cyclic RGD peptides., Chembiochem. 6 (2005) 2034–2040. doi:10.1002/cbic.200500031.

[77] A.M. Wojtowicz, A. Shekaran, M.E. Oest, K.M. Dupont, K.L. Templeman, D.W. Hutmacher, R.E. Guldberg, A.J. Garcia, Coating of biomaterial scaffolds with the collagen-mimetic peptide GFOGER for bone defect repair., Biomaterials. 31 (2010) 2574–2582. doi:10.1016/j.biomaterials.2009.12.008.

[78] K.M. Dupont, J.D. Boerckel, H.Y. Stevens, T. Diab, Y.M. Kolambkar, M. Takahata, E.M. Schwarz,

R.E. Guldberg, Synthetic scaffold coating with adeno-associated virus encoding BMP2 to promote endogenous bone repair., Cell Tissue Res. 347 (2012) 575–588. doi:10.1007/s00441-011-1197-3.

[79] H. Ito, M. Koefoed, P. Tiyapatanaputi, K. Gromov, J.J. Goater, J. Carmouche, X. Zhang, P.T. Rubery, J. Rabinowitz, R.J. Samulski, T. Nakamura, K. Soballe, R.J. O'Keefe, B.F. Boyce, E.M. Schwarz, Remodeling of cortical bone allografts mediated by adherent rAAV-RANKL and VEGF gene therapy., Nat. Med. 11 (2005) 291–297. doi:10.1038/nm1190.

[80] K.S. and M.A. Birch, Fabrication of poly(ethylene glycol) hydrogel micropatterns with osteoinductive growth factors and evaluation of the effects on osteoblast activity and function, Biomed. Mater. 1 (2006) 144. http://stacks.iop.org/1748-605X/1/i=3/a=009.

[81] E. De Giglio, S. Cometa, M.A. Ricci, D. Cafagna, A.M. Savino, L. Sabbatini, M. Orciani, E. Ceci, L. Novello, G.M. Tantillo, M. Mattioli-Belmonte, Ciprofloxacin-modified electrosynthesized hydrogel coatings to prevent titanium-implant-associated infections, Acta Biomater. 7 (2011) 882–891. doi:https://doi.org/10.1016/j.actbio.2010.07.030.

[82] F. Ordikhani, E. Tamjid, A. Simchi, Characterization and antibacterial performance of electrodeposited chitosan–vancomycin composite coatings for prevention of implant-associated infections, Mater. Sci. Eng. C. 41 (2014) 240–248. doi:https://doi.org/10.1016/j.msec.2014.04.036.

[83] W. Boot, D. Gawlitta, P.G.J. Nikkels, B. Pouran, M.H.P. van Rijen, W.J.A. Dhert, H.C. Vogely, Hyaluronic Acid-Based Hydrogel Coating Does Not Affect Bone Apposition at the Implant Surface in a Rabbit Model, Clin. Orthop. Relat. Res. 475 (2017) 1911–1919. doi:10.1007/s11999-017-5310-0.

[84] C.L. Romano, S. Scarponi, E. Gallazzi, D. Romano, L. Drago, Antibacterial coating of implants in orthopaedics and trauma: a classification proposal in an evolving panorama., J. Orthop. Surg. Res. 10 (2015) 157. doi:10.1186/s13018-015-0294-5.

[85] L. Drago, W. Boot, K. Dimas, K. Malizos, G.M. Hansch, J. Stuyck, D. Gawlitta, C.L. Romano, Does implant coating with antibacterial-loaded hydrogel reduce bacterial colonization and biofilm formation in vitro?, Clin. Orthop. Relat. Res. 472 (2014) 3311–3323. doi:10.1007/s11999-014-3558-1.

[86] J.C. Dumville, P. Coulthard, H. V Worthington, P. Riley, N. Patel, J. Darcey, M. Esposito, M. van der Elst, O.J.F. van Waes, Tissue adhesives for closure of surgical incisions., Cochrane Database Syst. Rev. (2014) CD004287. doi:10.1002/14651858.CD004287.pub4.

[87] M. Ryou, C.C. Thompson, Tissue Adhesives: A Review, Tech. Gastrointest. Endosc. 8 (2006) 33–37. doi:https://doi.org/10.1016/j.tgie.2005.12.007.

[88] P.J.M. Bouten, M. Zonjee, J. Bender, S.T.K. Yauw, H. van Goor, J.C.M. van Hest, R. Hoogenboom, The chemistry of tissue adhesive materials, Prog. Polym. Sci. 39 (2014) 1375–1405. doi:https://doi.org/10.1016/j.progpolymsci.2014.02.001.

[89] R. Jayakumar, M. Prabaharan, P.T. Sudheesh Kumar, S. V. Nair, H. Tamura, Biomaterials based on chitin and chitosan in wound dressing applications, Biotechnol. Adv. 29 (2011) 322–337. doi:10.1016/j.biotechadv.2011.01.005.

[90] S.K. Bhatia, S.D. Arthur, H.K. Chenault, G.K. Kodokian, Interactions of polysaccharide-based tissue adhesives with clinically relevant fibroblast and macrophage cell lines., Biotechnol. Lett. 29 (2007) 1645–1649. doi:10.1007/s10529-007-9465-8.

[91] G.H. Trew, G.A. Pistofidis, S.Y. Brucker, B. Krämer, N.M. Ziegler, M. Korell, H. Ritter, A. McConnachie, I. Ford, A.M. Crowe, T.D. Estridge, M.P. Diamond, R.L. De Wilde, A first-in-human, randomized, controlled, subject- and reviewer-blinded multicenter study of Actamax™ Adhesion Barrier, Arch. Gynecol. Obstet. 295 (2017) 383–395. doi:10.1007/s00404-016-4211-x.

[92] S. Patel, E.C. Rodriguez-Merchan, F.S. Haddad, The use of fibrin glue in surgery of the knee., J. Bone Joint Surg. Br. 92 (2010) 1325–1331. doi:10.1302/0301-620X.92B10.24828.

[93] L.J. Currie, J.R. Sharpe, R. Martin, The use of fibrin glue in skin grafts and tissue-engineered skin replacements: a review., Plast. Reconstr. Surg. 108 (2001) 1713–1726.

[94] S. Dhillon, Fibrin Sealant (Evicel® [Quixil®/Crosseal™]), Drugs. 71 (2011) 1893–1915. doi:10.2165/11207700-000000000-00000.

[95] W.D. Spotnitz, Fibrin sealant: past, present, and future: a brief review., World J. Surg. 34 (2010) 632–634. doi:10.1007/s00268-009-0252-7.

[96] A. Kouketsu, S. Nogami, M. Yamada-Fujiwara, H. Nagai, K. Yamauchi, S. Mori, H. Miyashita, T. Kawai, A. Matsui, Y. Kataoka, N. Satomi, Y. Ezoe, S. Abe, Y. Takeda, T. Tone, B. Hirayama, T. Kurobane, K. Tashiro, Y. Yanagisawa, T. Takahashi, Clinical evaluations of complete autologous fibrin glue, produced by the CryoSeal® FS system, and polyglycolic acid sheets as wound coverings after oral surgery, J. Cranio-Maxillofacial Surg. 45 (2017) 1458–1463. doi:https://doi.org/10.1016/j.jcms.2017.06.004.

[97] S. Lee, A.M. Pham, S.G. Pryor, T. Tollefson, J.M. Sykes, Efficacy of Crosseal fibrin sealant (human) in rhytidectomy., Arch. Facial Plast. Surg. 11 (2009) 29–33. doi:10.1001/archfacial.2008.511.

[98] M.C. Parker, U. Pohlen, I.H.M. Borel Rinkes, T. Delvin, The application of TachoSil(R) for sealing

colorectal anastomosis: a feasibility study., Colorectal Dis. 15 (2013) 252–257. doi:10.1111/j.1463-1318.2012.03144.x.

[99] A. Berghaus, M. San Nicoló, C. Jacobi, Use of a fibrinogen-thrombin sponge in rhinoplasty, HNO. (2017). doi:10.1007/s00106-017-0414-0.

[100] W.D. Spotnitz, R. Prabhu, Fibrin sealant tissue adhesive-review and update., J. Long. Term. Eff. Med. Implants. 15 (2005) 245–270.

[101] H. Seyednejad, M. Imani, T. Jamieson, A.M. Seifalian, Topical haemostatic agents, Br. J. Surg. 95 (2008) 1197–1225. doi:10.1002/bjs.6357.

[102] H.-W. Sung, D.-M. Huang, W.-H. Chang, R.-N. Huang, J.-C. Hsu, Evaluation of gelatin hydrogel crosslinked with various crosslinking agents as bioadhesives: In vitro study, J. Biomed. Mater. Res. 46 (1999) 520–530. doi:10.1002/(SICI)1097-4636(19990915)46:4<520::AID-JBM10>3.0.CO;2-9.

[103] H. Nomori, H. Horio, K. Suemasu, The efficacy and side effects of gelatin-resorcinol formaldehyde-glutaraldehyde (GRFG) glue for preventing and sealing pulmonary air leakage., Surg. Today. 30 (2000) 244–248. doi:10.1007/s005950050053.

[104] E. Raanani, D.A. Latter, L.E. Errett, D.B. Bonneau, Y. Leclerc, G.C. Salasidis, Use of “BioGlue” in aortic surgical repair, Ann. Thorac. Surg. 72 (2001) 638–640. doi:https://doi.org/10.1016/S0003-4975(01)02663-7.

[105] Z. Bahouth, S. Halachmi, S. Shprits, Y. Burbara, O. Avitan, I. Masarwa, B. Moskovitz, O. Nativ, The use of bovine serum albumin-glutaraldehyde tissue adhesive (BioGlue®) for tumor bed closure following open partial nephrectomy, Actas Urológicas Españolas (English Ed. 41 (2017) 511–515. doi:https://doi.org/10.1016/j.acuroe.2017.07.005.

[106] K. Mortman, M. Corral, X. Zhang, I. Berhane, M. Bourque, N. Ferko, A Retrospective Premier Database Study to Evaluate Differences Between Progel(TM) Pleural Air Leak Sealant As Compared with Other Sealants in The Inpatient Surgical Setting, Value Heal. 19 (2017) A691. doi:10.1016/j.jval.2016.09.1980.

[107] A. Assmann, A. Vegh, M. Ghasemi-Rad, S. Bagherifard, G. Cheng, E.S. Sani, G.U. Ruiz-Esparza, I. Noshadi, A.D. Lassaletta, S. Gangadharan, A. Tamayol, A. Khademhosseini, N. Annabi, A highly adhesive and naturally derived sealant, Biomaterials. 140 (2017) 115–127. doi:https://doi.org/10.1016/j.biomaterials.2017.06.004.

[108] S.K. Bhatia, Biomaterials for clinical applications, 1st ed., Springer Science & Business Media, New York, 2010. doi:https://doi.org/10.1007/978-1-4419-6920-0.

[109] A. Dragu, F. Unglaub, S. Schwarz, J.P. Beier, U. Kneser, A.D. Bach, R.E. Horch, Foreign body reaction after usage of tissue adhesives for skin closure: a case report and review of the literature., Arch. Orthop. Trauma Surg. 129 (2009) 167–169. doi:10.1007/s00402-008-0643-5.

[110] L. Montanaro, C.R. Arciola, E. Cenni, G. Ciapetti, F. Savioli, F. Filippini, L.A. Barsanti, Cytotoxicity, blood compatibility and antimicrobial activity of two cyanoacrylate glues for surgical use., Biomaterials. 22 (2001) 59–66.

[111] A.S. Sawhney, C.P. Pathak, J.A. Hubbell, Bioerodible hydrogels based on photopolymerized poly(ethylene glycol)-co-poly(.alpha.-hydroxy acid) diacrylate macromers, Macromolecules. 26 (1993) 581–587. doi:10.1021/ma00056a005.

[112] A.M. Gillinov, B.W. Lytle, A novel synthetic sealant to treat air leaks at cardiac reoperation., J. Card. Surg. 16 (2001) 255–257.

[113] M.C. Preul, W.D. Bichard, R.F. Spetzler, Toward optimal tissue sealants for neurosurgery: use of a novel hydrogel sealant in a canine durotomy repair model., Neurosurgery. 53 (2003) 1189.

[114] G.R. Cosgrove, J.B. Delashaw, J.A. Grotenhuis, J.M. Tew, H. Van Loveren, R.F. Spetzler, T. Payner, G. Rosseau, M.E. Shaffrey, L.N. Hopkins, R. Byrne, A. Norbash, Safety and efficacy of a novel polyethylene glycol hydrogel sealant for watertight dural repair., J. Neurosurg. 106 (2007) 52–58. doi:10.3171/jns.2007.106.1.52.

[115] D.G. Wallace, G.M. Cruise, W.M. Rhee, J.A. Schroeder, J.J. Prior, J. Ju, M. Maroney, J. Duronio, M.H. Ngo, T. Estridge, G.C. Coker, A tissue sealant based on reactive multifunctional polyethylene glycol., J. Biomed. Mater. Res. 58 (2001) 545–555.

[116] R. Dunn, M.D. Lyman, P.G. Edelman, P.K. Campbell, Evaluation of the SprayGel adhesion barrier in the rat cecum abrasion and rabbit uterine horn adhesion models., Fertil. Steril. 75 (2001) 411–416.

[117] D.A. Johns, R. Ferland, R. Dunn, Initial feasibility study of a sprayable hydrogel adhesion barrier system in patients undergoing laparoscopic ovarian surgery., J. Am. Assoc. Gynecol. Laparosc. 10 (2003) 334–338.

[118] C. von der Brelie, M. Soehle, H.R. Clusmann, Intraoperative sealing of dura mater defects with a novel, synthetic, self adhesive patch: application experience in 25 patients., Br. J. Neurosurg. 26 (2012) 231–235. doi:10.3109/02688697.2011.619597.

[119] P. Ferroli, F. Acerbi, M. Broggi, M. Schiariti, E. Albanese, G. Tringali, A. Franzini, G. Broggi, A novel impermeable adhesive membrane to reinforce dural closure: a preliminary retrospective study on 119 consecutive high-risk patients., World Neurosurg. 79 (2013) 551–557.

doi:10.1016/j.wneu.2011.09.022.

[120] A.M. Oelker, J.A. Berlin, M. Wathier, M.W. Grinstaff, Synthesis and characterization of dendron cross-linked PEG hydrogels as corneal adhesives., Biomacromolecules. 12 (2011) 1658–1665. doi:10.1021/bm200039s.

[121] V. AJ, C. MA, J. Kristinsson, S. Stinnett, G. MW, T. Kim, New dendritic adhesives for sutureless ophthalmic surgical procedures: In vitro studies of corneal laceration repair, Arch. Ophthalmol. 122 (2004) 867–870. http://dx.doi.org/10.1001/archopht.122.6.867.

[122] C. Zoia, D. Bongetta, F. Lombardi, V.M. Custodi, R. Pugliese, P. Gaetani, First impressions about Adherus, a new dural sealant., J. Appl. Biomater. Funct. Mater. 13 (2015) e372–e375. http://10.0.20.181/jabfm.5000241.

[123] T.W. Gilbert, S.F. Badylak, J. Gusenoff, E.J. Beckman, D.M. Clower, P. Daly, J.P. Rubin, Lysine-derived urethane surgical adhesive prevents seroma formation in a canine abdominoplasty model., Plast. Reconstr. Surg. 122 (2008) 95–102. doi:10.1097/PRS.0b013e31817743b8.

[124] A. Majumder, A. Sharma, A. Ghatak, A Bioinspired Wet/Dry Microfluidic Adhesive for Aqueous Environments, Langmuir. 26 (2010) 521–525. doi:10.1021/la9021849.

[125] J.L. Maw, J. V Quinn, G.A. Wells, Y. Ducic, P.F. Odell, A. Lamothe, P.J. Brownrigg, T. Sutcliffe, A prospective comparison of octylcyanoacrylate tissue adhesive and suture for the closure of head and neck incisions., J. Otolaryngol. 26 (1997) 26–30.

[126] B. Petersen, A. Barkun, S. Carpenter, P. Chotiprasidhi, R. Chuttani, W. Silverman, N. Hussain, J. Liu, G. Taitelbaum, G.G. Ginsberg, Tissue adhesives and fibrin glues., Gastrointest. Endosc. 60 (2004) 327–333.

[127] J.H. Waite, Mussel glue from Mytilus californianus Conrad: a comparative study., J. Comp. Physiol. B. 156 (1986) 491–496.

[128] K. Kamino, Underwater adhesive of marine organisms as the vital link between biological science and material science., Mar. Biotechnol. (NY). 10 (2008) 111–121. doi:10.1007/s10126-007-9076-3.

[129] X. Liu, C. Liang, X. Zhang, J. Li, J. Huang, L. Zeng, Z. Ye, B. Hu, W. Wu, Amyloid fibril aggregation: An insight into the underwater adhesion of barnacle cement, Biochem. Biophys. Res. Commun. (2017). doi:https://doi.org/10.1016/j.bbrc.2017.08.136.

[130] J.H. WAITE, ADHESION IN BYSSALLY ATTACHED BIVALVES, Biol. Rev. 58 (1983) 209–231. doi:10.1111/j.1469-185X.1983.tb00387.x.

[131] K. Zhang, F. Zhang, Y. Song, J.-B. Fan, S. Wang, Recent Progress of Mussel-Inspired Underwater

Adhesives, Chinese J. Chem. 35 (2017) 811–820. doi:10.1002/cjoc.201600778.

[132] M. Yu, J. Hwang, T.J. Deming, Role of l-3,4-Dihydroxyphenylalanine in Mussel Adhesive Proteins, J. Am. Chem. Soc. 121 (1999) 5825–5826. doi:10.1021/ja990469y.

[133] H. Zhao, J.H. Waite, Linking adhesive and structural proteins in the attachment plaque of Mytilus californianus., J. Biol. Chem. 281 (2006) 26150–26158. doi:10.1074/jbc.M604357200.

[134] S.K. Madhurakkat Perikamana, J. Lee, Y. Bin Lee, Y.M. Shin, E.J. Lee, A.G. Mikos, H. Shin, Materials from Mussel-Inspired Chemistry for Cell and Tissue Engineering Applications, Biomacromolecules. 16 (2015) 2541–2555. doi:10.1021/acs.biomac.5b00852.

[135] H. Lee, S.M. Dellatore, W.M. Miller, P.B. Messersmith, Mussel-Inspired Surface Chemistry for Multifunctional Coatings, Science (80-.). 318 (2007) 426–430. doi:10.1126/science.1147241.

[136] J. Wu, L. Zhang, Y. Wang, Y. Long, H. Gao, X. Zhang, N. Zhao, Y. Cai, J. Xu, Mussel-Inspired Chemistry for Robust and Surface-Modifiable Multilayer Films, Langmuir. 27 (2011) 13684–13691. doi:10.1021/la2027237.

[137] Y. Lee, H.J. Chung, S. Yeo, C.-H. Ahn, H. Lee, P.B. Messersmith, T.G. Park, Thermo-sensitive, injectable, and tissue adhesive sol–gel transition hyaluronic acid/pluronic composite hydrogels prepared from bio-inspired catechol-thiol reaction, Soft Matter. 6 (2010) 977–983. doi:10.1039/b919944f.

[138] Q. Lin, D. Gourdon, C. Sun, N. Holten-Andersen, T.H. Anderson, J.H. Waite, J.N. Israelachvili, Adhesion mechanisms of the mussel foot proteins mfp-1 and mfp-3, Proc. Natl. Acad. Sci. U. S. A. 104 (2007) 3782–3786. doi:10.1073/pnas.0607852104.

[139] D.R. Filpula, S.M. Lee, R.P. Link, S.L. Strausberg, R.L. Strausberg, Structural and functional repetition in a marine mussel adhesive protein., Biotechnol. Prog. 6 (1990) 171–177. doi:10.1021/bp00003a001.

[140] D.S. Hwang, Y. Gim, H.J. Yoo, H.J. Cha, Practical recombinant hybrid mussel bioadhesive fp-151., Biomaterials. 28 (2007) 3560–3568. doi:10.1016/j.biomaterials.2007.04.039.

[141] D.S. Hwang, S.B. Sim, H.J. Cha, Cell adhesion biomaterial based on mussel adhesive protein fused with RGD peptide, Biomaterials. 28 (2007) 4039–4046. doi:https://doi.org/10.1016/j.biomaterials.2007.05.028.

[142] D.S. Hwang, Y. Gim, D.G. Kang, Y.K. Kim, H.J. Cha, Recombinant mussel adhesive protein Mgfp-5 as cell adhesion biomaterial, J. Biotechnol. 127 (2007) 727–735. doi:https://doi.org/10.1016/j.jbiotec.2006.08.005.

[143] E. Faure, C. Falentin-Daudré, C. Jérôme, J. Lyskawa, D. Fournier, P. Woisel, C. Detrembleur,

Catechols as versatile platforms in polymer chemistry, Prog. Polym. Sci. 38 (2013) 236–270.

[144] K. Yamada, T. Chen, G. Kumar, O. Vesnovsky, L.D. Topoleski, G.F. Payne, Chitosan based water-resistant adhesive. Analogy to mussel glue., Biomacromolecules. 1 (2000) 252–258.

[145] J.H. Waite, Adhesion a la moule., Integr. Comp. Biol. 42 (2002) 1172–1180. doi:10.1093/icb/42.6.1172.

[146] J. Dove, P. Sheridan, Adhesive protein from mussels: possibilities for dentistry, medicine, and industry., J. Am. Dent. Assoc. 112 (1986) 879.

[147] D.A. Grande, M.I. Pitman, The use of adhesives in chondrocyte transplantation surgery. Preliminary studies, Bull. Hosp. Jt. Dis. Orthop. Inst. 48 (1988) 140–148. http://europepmc.org/abstract/MED/2854480.

[148] J.H. Waite, M.L. Tanzer, Polyphenolic Substance of Mytilus edulis: Novel Adhesive Containing L-Dopa and Hydroxyproline., Science. 212 (1981) 1038–1040. doi:10.1126/science.212.4498.1038.

[149] J.H. An, N.T. Huynh, Y. Sil Jeon, J.-H. Kim, Surface modification using bio-inspired adhesive polymers based on polyaspartamide derivatives, Polym. Int. 60 (2011) 1581–1586. doi:10.1002/pi.3116.

[150] C.J. Ochs, T. Hong, G.K. Such, J. Cui, A. Postma, F. Caruso, Dopamine-Mediated Continuous Assembly of Biodegradable Capsules, Chem. Mater. 23 (2011) 3141–3143. doi:10.1021/cm201390e.

[151] E. Amstad, T. Gillich, I. Bilecka, M. Textor, E. Reimhult, Ultrastable Iron Oxide Nanoparticle Colloidal Suspensions Using Dispersants with Catechol-Derived Anchor Groups, Nano Lett. 9 (2009) 4042–4048. doi:10.1021/nl902212q.

[152] P. Podsiadlo, Z. Liu, D. Paterson, P.B. Messersmith, N.A. Kotov, Fusion of Seashell Nacre and Marine Bioadhesive Analogs: High-Strength Nanocomposite by Layer-by-Layer Assembly of Clay and L-3,4-Dihydroxyphenylalanine Polymer, Adv. Mater. 19 (2007) 949–955. doi:10.1002/adma.200602706.

[153] J.H. Ryu, S. Hong, H. Lee, Bio-inspired adhesive catechol-conjugated chitosan for biomedical applications: A mini review, Acta Biomater. 27 (2015) 101–115. doi:10.1016/j.actbio.2015.08.043.

[154] S.H. Ku, J. Ryu, S.K. Hong, H. Lee, C.B. Park, General functionalization route for cell adhesion on non-wetting surfaces., Biomaterials. 31 (2010) 2535–2541. doi:10.1016/j.biomaterials.2009.12.020.

[155] J. Wang, C. Liu, X. Lu, M. Yin, Co-polypeptides of 3,4-dihydroxyphenylalanine and l-lysine to mimic marine adhesive protein, Biomaterials. 28 (2007) 3456–3468. doi:https://doi.org/10.1016/j.biomaterials.2007.04.009.

[156] S. Saxer, C. Portmann, S. Tosatti, K. Gademann, S. Zürcher, M. Textor, Surface Assembly of Catechol-Functionalized Poly(l-lysine)-graft-poly(ethylene glycol) Copolymer on Titanium Exploiting Combined Electrostatically Driven Self-Organization and Biomimetic Strong Adhesion, Macromolecules. 43 (2010) 1050–1060. doi:10.1021/ma9020664.

[157] L. Li, Y. Li, X. Luo, J. Deng, W. Yang, Helical poly(N-propargylamide)s with functional catechol groups: Synthesis and adsorption of metal ions in aqueous solution, React. Funct. Polym. 70 (2010) 938–943. doi:https://doi.org/10.1016/j.reactfunctpolym.2010.09.006.

[158] J.S. Kim, T.G. Kim, W.H. Kong, T.G. Park, Y.S. Nam, Thermally controlled wettability of a nanoporous membrane grafted with catechol-tethered poly(N-isopropylacrylamide)., Chem. Commun. (Camb). 48 (2012) 9227–9229. doi:10.1039/c2cc32233a.

[159] G. Marcelo, M. López-González, F. Mendicuti, M.P. Tarazona, M. Valiente, Poly(N-isopropylacrylamide)/Gold Hybrid Hydrogels Prepared by Catechol Redox Chemistry. Characterization and Smart Tunable Catalytic Activity, Macromolecules. 47 (2014) 6028–6036. doi:10.1021/ma501214k.

[160] M. Krogsgaard, M.A. Behrens, J.S. Pedersen, H. Birkedal, Self-Healing Mussel-Inspired Multi-pH-Responsive Hydrogels, Biomacromolecules. 14 (2013) 297–301. doi:10.1021/bm301844u.

[161] H. Shao, R.J. Stewart, Biomimetic Underwater Adhesives with Environmentally Triggered Setting Mechanisms, Adv. Mater. 22 (2010) 729–733. doi:10.1002/adma.200902380.

[162] H. Chung, P. Glass, J.M. Pothen, M. Sitti, N.R. Washburn, Enhanced Adhesion of Dopamine Methacrylamide Elastomers via Viscoelasticity Tuning, Biomacromolecules. 12 (2011) 342–347. doi:10.1021/bm101076e.

[163] C. Gao, G. Li, H. Xue, W. Yang, F. Zhang, S. Jiang, Functionalizable and ultra-low fouling zwitterionic surfaces via adhesive mussel mimetic linkages, Biomaterials. 31 (2010) 1486–1492. doi:https://doi.org/10.1016/j.biomaterials.2009.11.025.

[164] M.B. and L.V. and J.L.M. and F.X. and A.L. and W.D.L. and B.P. Lee, Biomechanical properties of Achilles tendon repair augmented with a bioadhesive-coated scaffold, Biomed. Mater. 6 (2011) 15014. http://stacks.iop.org/1748-605X/6/i=1/a=015014.

[165] H. Lee, K.D. Lee, K.B. Pyo, S.Y. Park, H. Lee, Catechol-Grafted Poly(ethylene glycol) for PEGylation on Versatile Substrates, Langmuir. 26 (2010) 3790–3793. doi:10.1021/la904909h.

[166] B.P. Lee, J.L. Dalsin, P.B. Messersmith, Synthesis and gelation of DOPA-modified poly(ethylene glycol) hydrogels, Biomacromolecules. 3 (2002) 1038–1047. doi:10.1021/bm025546n.

[167] J. Bernard, C. Branger, I. Beurroies, R. Denoyel, A. Margaillan, Catechol immobilized on crosslinked polystyrene resins by grafting or copolymerization: Incidence on metal ions adsorption, React. Funct. Polym. 72 (2012) 98–106. doi:https://doi.org/10.1016/j.reactfunctpolym.2011.11.001.

[168] X.-D. Pan, Z. Qin, Y.-Y. Yan, P. Sadhukhan, Elastomers with chain-end mussel-mimetic modification for nanocomposites: Strong modifications to reinforcement and viscoelastic properties, Polymer (Guildf). 51 (2010) 3453–3461. doi:https://doi.org/10.1016/j.polymer.2010.05.031.

[169] H.Y. Son, J.H. Ryu, H. Lee, Y.S. Nam, Bioinspired Templating Synthesis of Metal–Polymer Hybrid Nanostructures within 3D Electrospun Nanofibers, ACS Appl. Mater. Interfaces. 5 (2013) 6381–6390. doi:10.1021/am401550p.

[170] Z. Wu, L. Li, Y. Mu, X. Wan, Synthesis and Adhesive Property Study of a Mussel-Inspired Adhesive Based on Poly(vinyl alcohol) Backbone, Macromol. Chem. Phys. 218 (2017) 1700206–n/a. doi:10.1002/macp.201700206.

[171] C. Kim, Y. Lee, S.H. Lee, J.S. Kim, J.H. Jeong, T.G. Park, Self-crosslinked polyethylenimine nanogels for enhanced intracellular delivery of siRNA, Macromol. Res. 19 (2011) 166–171. doi:10.1007/s13233-011-0207-3.

[172] P. Sun, J. Wang, X. Yao, Y. Peng, X. Tu, P. Du, Z. Zheng, X. Wang, Facile Preparation of Mussel-Inspired Polyurethane Hydrogel and Its Rapid Curing Behavior, ACS Appl. Mater. Interfaces. 6 (2014) 12495–12504. doi:10.1021/am502106e.

[173] X. Zhang, Z. Li, X. Yuan, Z. Cui, X. Yang, Fabrication of dopamine-modified hyaluronic acid/chitosan multilayers on titanium alloy by layer-by-layer self-assembly for promoting osteoblast growth, Appl. Surf. Sci. 284 (2013) 732–737. doi:10.1016/j.apsusc.2013.08.002.

[174] Y. Lee, H. Lee, Y.B. Kim, J. Kim, T. Hyeon, H. Park, P.B. Messersmith, T.G. Park, Bioinspired Surface Immobilization of Hyaluronic Acid on Monodisperse Magnetite Nanocrystals for Targeted Cancer Imaging, Adv. Mater. 20 (2008) 4154–4157. doi:10.1002/adma.200800756.

[175] S. Hong, K. Yang, B. Kang, C. Lee, I.T. Song, E. Byun, K.I. Park, S.-W. Cho, H. Lee, Hyaluronic Acid Catechol: A Biopolymer Exhibiting a pH-Dependent Adhesive or Cohesive Property for Human Neural Stem Cell Engineering, Adv. Funct. Mater. 23 (2013) 1774–1780. doi:10.1002/adfm.201202365.

[176] J.R. Rodrigues, N.M. Alves, J.F. Mano, Biomimetic polysaccharide/bioactive glass nanoparticles multilayer membranes for guided tissue regeneration, RSC Adv. 6 (2016) 75988–75999.

[177] Y. Lee, H. Lee, P.B. Messersmith, T.G. Park, A Bioinspired Polymeric Template for 1D Assembly of Metallic Nanoparticles, Semiconductor Quantum Dots, and Magnetic Nanoparticles, Macromol. Rapid Commun. 31 (2010) 2109–2114. doi:10.1002/marc.201000423.

[178] T. Sato, T. Aoyagi, M. Ebara, R. Auzély-Velty, Catechol-modified hyaluronic acid: in situ-forming hydrogels by auto-oxidation of catechol or photo-oxidation using visible light, Polym. Bull. 74 (2017) 4069–4085. doi:10.1007/s00289-017-1937-y.

[179] J. Lee, K.C. Yoo, J. Ko, B. Yoo, J. Shin, S.-J. Lee, D. Sohn, Hollow hyaluronic acid particles by competition between adhesive and cohesive properties of catechol for anticancer drug carrier, Carbohydr. Polym. 164 (2017) 309–316. doi:https://doi.org/10.1016/j.carbpol.2017.02.009.

[180] H.-J. Park, Y. Jin, J. Shin, K. Yang, C. Lee, H.S. Yang, S.-W. Cho, Catechol-Functionalized Hyaluronic Acid Hydrogels Enhance Angiogenesis and Osteogenesis of Human Adipose-Derived Stem Cells in Critical Tissue Defects, Biomacromolecules. 17 (2016) 1939–1948. doi:10.1021/acs.biomac.5b01670.

[181] A.I. Neto, N.L. Vasconcelos, S.M. Oliveira, D. Ruiz-Molina, J.F. Mano, High-Throughput Topographic, Mechanical, and Biological Screening of Multilayer Films Containing Mussel-Inspired Biopolymers, Adv. Funct. Mater. 26 (2016) 2745–2755. doi:10.1002/adfm.201505047.

[182] E. Lih, S.G. Choi, D.J. Ahn, Y.K. Joung, D.K. Han, Optimal conjugation of catechol group onto hyaluronic acid in coronary stent substrate coating for the prevention of restenosis, J. Tissue Eng. 7 (2016) 1–11. doi:10.1177/2041731416683745.

[183] J. Shin, J.S. Lee, C. Lee, H.-J. Park, K. Yang, Y. Jin, J.H. Ryu, K.S. Hong, S.-H. Moon, H.-M. Chung, H.S. Yang, S.H. Um, J.-W. Oh, D.-I. Kim, H. Lee, S.-W. Cho, Tissue Adhesive Catechol-Modified Hyaluronic Acid Hydrogel for Effective, Minimally Invasive Cell Therapy, Adv. Funct. Mater. 25 (2015) 3814–3824. doi:10.1002/adfm.201500006.

[184] D.D. Gurav, A.S. Kulkarni, A. Khan, V.S. Shinde, pH-responsive targeted and controlled doxorubicin delivery using hyaluronic acid nanocarriers, Colloids Surfaces B Biointerfaces. 143 (2016) 352–358. doi:https://doi.org/10.1016/j.colsurfb.2016.03.049.

[185] D.H. Choi, S.N. Kang, S.M. Kim, S. Gobaa, B.J. Park, I.H. Kim, Y.K. Joung, D.K. Han, Growth factors-loaded stents modified with hyaluronic acid and heparin for induction of rapid and tight re-endothelialization, Colloids Surfaces B Biointerfaces. 141 (2016) 602–610. doi:https://doi.org/10.1016/j.colsurfb.2016.01.028.

[186] J.Y. Park, J. Yeom, J.S. Kim, M. Lee, H. Lee, Y.S. Nam, Cell-repellant dextran coatings of porous titania using mussel adhesion chemistry., Macromol. Biosci. 13 (2013) 1511–1519. doi:10.1002/mabi.201300224.

[187] J.Y. Park, J.S. Kim, Y.S. Nam, Mussel-inspired modification of dextran for protein-resistant coatings of titanium oxide., Carbohydr. Polym. 97 (2013) 753–757. doi:10.1016/j.carbpol.2013.05.064.

[188] A. Cholewinski, F.K. Yang, B. Zhao, Underwater Contact Behavior of Alginate and Catechol-Conjugated Alginate Hydrogel Beads, Langmuir. 33 (2017) 8353–8361. doi:10.1021/acs.langmuir.7b00795.

[189] F. Ponzio, V. Le Houerou, S. Zafeiratos, C. Gauthier, T. Garnier, L. Jierry, V. Ball, Robust Alginate-Catechol@Polydopamine Free-Standing Membranes Obtained from the Water/Air Interface, Langmuir. 33 (2017) 2420–2426. doi:10.1021/acs.langmuir.6b04435.

[190] J. V Alegre-Requena, M. Haring, R.P. Herrera, D. Diaz Diaz, Regulatory parameters of self-healing alginate hydrogel networks prepared via mussel-inspired dynamic chemistry, New J. Chem. 40 (2016) 8493–8501. doi:10.1039/C6NJ02367C.

[191] J. Hou, C. Li, Y. Guan, Y. Zhang, X.X. Zhu, Enzymatically crosslinked alginate hydrogels with improved adhesion properties, Polym. Chem. 6 (2015) 2204–2213. doi:10.1039/C4PY01757A.

[192] J.H. Ryu, Y. Lee, W.H. Kong, T.G. Kim, T.G. Park, H. Lee, Catechol-functionalized chitosan/pluronic hydrogels for tissue adhesives and hemostatic materials, Biomacromolecules. 12 (2011) 2653–2659. doi:10.1021/bm200464x.

[193] K. Kim, J.H. Ryu, D.Y. Lee, H. Lee, Bio-inspired catechol conjugation converts water-insoluble chitosan into a highly water-soluble, adhesive chitosan derivative for hydrogels and LbL assembly, Biomater. Sci. 1 (2013) 783–790. doi:Doi 10.1039/C3bm00004d.

[194] P. Sobolewski, A. Goszczynska, M. Aleksandrzak, K. Urbas, J. Derkowska, A. Bartoszewska, J. Podolski, E. Mijowska, M. El Fray, A biofunctionalizable ink platform composed of catechol-modified chitosan and reduced graphene oxide/platinum nanocomposite., Beilstein J. Nanotechnol. 8 (2017) 1508–1514. doi:10.3762/bjnano.8.151.

[195] M. Shin, S.-G. Park, B.-C. Oh, K. Kim, S. Jo, M.S. Lee, S.S. Oh, S.-H. Hong, E.-C. Shin, K.-S. Kim, S.-W. Kang, H. Lee, Complete prevention of blood loss with self-sealing haemostatic needles, Nat Mater. 16 (2017) 147–152. http://dx.doi.org/10.1038/nmat4758.

[196] W. Chen, X. Shen, Y. Hu, K. Xu, Q. Ran, Y. Yu, L. Dai, Z. Yuan, L. Huang, T. Shen, K. Cai, Surface functionalization of titanium implants with chitosan-catechol conjugate for suppression of ROS-induced cells damage and improvement of osteogenesis, Biomaterials. 114 (2017) 82–96.

doi:http://dx.doi.org/10.1016/j.biomaterials.2016.10.055.

[197] J.H. Ryu, Y. Lee, M.J. Do, S.D. Jo, J.S. Kim, B.S. Kim, G. Il Im, T.G. Park, H. Lee, Chitosan-g-hematin: Enzyme-mimicking polymeric catalyst for adhesive hydrogels, Acta Biomater. 10 (2014) 224–233. doi:10.1016/j.actbio.2013.09.014.

[198] J. Xu, M. Tam, S. Samadei, S. Lerouge, J. Barralet, M.M. Stevenson, M. Cerruti, Mucoadhesive chitosan hydrogels as rectal drug delivery vessels to treat ulcerative colitis, Acta Biomater. 48 (2016) 247–257. doi:10.1016/j.actbio.2016.10.026.

[199] D. Nayak, A.P. Minz, S. Ashe, P.R. Rauta, M. Kumari, P. Chopra, B. Nayak, Synergistic combination of antioxidants, silver nanoparticles and chitosan in a nanoparticle based formulation: Characterization and cytotoxic effect on MCF-7 breast cancer cell lines., J. Colloid Interface Sci. 470 (2016) 142–152. doi:10.1016/j.jcis.2016.02.043.

[200] V.A. Ho, P.T. Le, T.P. Nguyen, C.K. Nguyen, V.T. Nguyen, N.Q. Tran, Silver Core-shell Nanoclusters Exhibiting Strong Growth Inhibition of Plant-pathogenic Fungi, J. Nanomater. 16 (2015) 13:13–13:13. doi:10.1155/2015/241614.

[201] J.H. Ryu, S. Jo, M.-Y. Koh, H. Lee, Bio-Inspired, Water-Soluble to Insoluble Self-Conversion for Flexible, Biocompatible, Transparent, Catecholamine Polysaccharide Thin Films, Adv. Funct. Mater. 24 (2014) 7709–7716. doi:10.1002/adfm.201402250.

[202] J.M. Lee, J.H. Ryu, E.A. Kim, S. Jo, B.-S. Kim, H. Lee, G.-I. Im, Adhesive barrier/directional controlled release for cartilage repair by endogenous progenitor cell recruitment., Biomaterials. 39 (2015) 173–181. doi:10.1016/j.biomaterials.2014.11.006.

[203] H. Wei, L. Han, J. Ren, L. Jia, Anticoagulant Surface Coating Using Composite Polysaccharides with Embedded Heparin-Releasing Mesoporous Silica, ACS Appl. Mater. Interfaces. 5 (2013) 12571–12578. doi:10.1021/am403882x.

[204] K. Ni, X. Zhou, L. Zhao, H. Wang, Y. Ren, D. Wei, Magnetic Catechol-Chitosan with Bioinspired Adhesive Surface: Preparation and Immobilization of ω-Transaminase, PLoS One. 7 (2012) e41101. https://doi.org/10.1371/journal.pone.0041101.

[205] J.H. Ryu, Y. Lee, W.H. Kong, T.G. Kim, T.G. Park, Bio-inspired tissue adhesive chitosan/pluronic composite hydrogel, J. Control. Release. 152 (2011) e236–e237. doi:http://dx.doi.org/10.1016/j.jconrel.2011.09.033.

[206] T.S. Cu, V. Du Cao, C.K. Nguyen, N.Q. Tran, Preparation of silver core-chitosan shell nanoparticles using catechol-functionalized chitosan and antibacterial studies, Macromol. Res. 22 (2014) 418–423. doi:10.1007/s13233-014-2054-5.

[207] X. Yang, L. Zhu, S. Tada, D. Zhou, T. Kitajima, T. Isoshima, Y. Yoshida, M. Nakamura, W. Yan, Y. Ito, Mussel-inspired human gelatin nanocoating for creating biologically adhesive surfaces, Int. J. Nanomedicine. 9 (2014) 2753–2765. doi:10.2147/IJN.S60624.

[208] Y.J. Xu, K. Wei, P. Zhao, Q. Feng, C.K.K. Choi, L. Bian, Preserving the adhesion of catechol-conjugated hydrogels by thiourea-quinone coupling., Biomater. Sci. 4 (2016) 1726–1730. doi:10.1039/c6bm00434b.

[209] C. Fan, J. Fu, W. Zhu, D.-A. Wang, A mussel-inspired double-crosslinked tissue adhesive intended for internal medical use, Acta Biomater. 33 (2016) 51–63. doi:https://doi.org/10.1016/j.actbio.2016.02.003.

[210] L. Ma, H. Qin, C. Cheng, Y. Xia, C. He, C. Nie, L. Wang, C. Zhao, Mussel-inspired self-coating at macro-interface with improved biocompatibility and bioactivity via dopamine grafted heparin-like polymers and heparin, J. Mater. Chem. B. 2 (2014) 363–375. doi:10.1039/C3TB21388A.

[211] Y. Yang, P. Qi, F. Wen, X. Li, Q. Xia, M.F. Maitz, Z. Yang, R. Shen, Q. Tu, N. Huang, Mussel-inspired one-step adherent coating rich in amine groups for covalent immobilization of heparin: hemocompatibility, growth behaviors of vascular cells, and tissue response., ACS Appl. Mater. Interfaces. 6 (2014) 14608–14620. doi:10.1021/am503925r.

[212] I. You, S.M. Kang, Y. Byun, H. Lee, Enhancement of blood compatibility of poly(urethane) substrates by mussel-inspired adhesive heparin coating., Bioconjug. Chem. 22 (2011) 1264–1269. doi:10.1021/bc2000534.

[213] M. Lee, Y. Kim, J.H. Ryu, K. Kim, Y.-M. Han, H. Lee, Long-term, feeder-free maintenance of human embryonic stem cells by mussel-inspired adhesive heparin and collagen type I, Acta Biomater. 32 (2016) 138–148. doi:https://doi.org/10.1016/j.actbio.2016.01.008.

[214] S. Kim, S. Ko, S.M. Kang, Adhesive heparin coating for marine antifouling applications, Macromol. Res. 24 (2016) 645–649. doi:10.1007/s13233-016-4091-8.

[215] S. Yuan, D. Wan, B. Liang, S.O. Pehkonen, Y.P. Ting, K.G. Neoh, E.T. Kang, Lysozyme-Coupled Poly(poly(ethylene glycol) methacrylate)–Stainless Steel Hybrids and Their Antifouling and Antibacterial Surfaces, Langmuir. 27 (2011) 2761–2774. doi:10.1021/la104442f.

[216] C.J. Detzel, A.L. Larkin, P. Rajagopalan, Polyelectrolyte multilayers in tissue engineering., Tissue Eng. Part B. Rev. 17 (2011) 101–113. doi:10.1089/ten.TEB.2010.0548.

[217] N. Bhattarai, J. Gunn, M. Zhang, Chitosan-based hydrogels for controlled, localized drug delivery, Adv. Drug Deliv. Rev. 62 (2010) 83–99. doi:10.1016/j.addr.2009.07.019.

[218] J.A. Lichter, K.J. Van Vlietpa, M.F. Rubner, Design of antibacterial surfaces and interfaces:

Polyelectrolyte multilayers as a multifunctional platform, Macromolecules. 42 (2009) 8573–8586. doi:10.1021/ma901356s.

[219] C. Pandis, S. Madeira, J. Matos, A. Kyritsis, J.F. Mano, J.L.G. Ribelles, Chitosan-silica hybrid porous membranes, Mater. Sci. Eng. C. 42 (2014) 553–561. doi:10.1016/j.msec.2014.05.073.

[220] M. Vakili, M. Rafatullah, B. Salamatinia, A.Z. Abdullah, M.H. Ibrahim, K.B. Tan, Z. Gholami, P. Amouzgar, Application of chitosan and its derivatives as adsorbents for dye removal from water and wastewater: A review, Carbohydr. Polym. 113 (2014) 115–130. doi:10.1016/j.carbpol.2014.07.007.

[221] M. Viola, D. Vigetti, A. Genasetti, M. Rizzi, E. Karousou, P. Moretto, M. Clerici, B. Bartolini, F. Pallotti, G. De Luca, A. Passi, Molecular Control of the Hyaluronan Biosynthesis, Connect. Tissue Res. 49 (2008) 111–114. doi:10.1080/03008200802148405.

[222] P. Prehm, Release of hyaluronate from eukaryotic cells, Biochem. J. 267 (1990) 185–189. http://www.pubmedcentral.nih.gov/articlerender.fcgi?artid=1131262&tool=pmcentrez&rendertype=abstract.

[223] L.G. Harris, R.G. Richards, Staphylococcus aureus adhesion to different treated titanium surfaces, J. Mater. Sci. Mater. Med. 15 (2004) 311–314. doi:10.1023/B:JMSM.0000021093.84680.bb.

[224] X. Hu, K.G. Neoh, Z. Shi, E.T. Kang, C. Poh, W. Wang, An in vitro assessment of titanium functionalized with polysaccharides conjugated with vascular endothelial growth factor for enhanced osseointegration and inhibition of bacterial adhesion, Biomaterials. 31 (2010) 8854–8863. doi:10.1016/j.biomaterials.2010.08.006.

[225] L. Richert, P. Lavalle, E. Payan, X.Z. Shu, G.D. Prestwich, J.-F. Stoltz, P. Schaaf, J.-C. Voegel, C. Picart, Layer by Layer Buildup of Polysaccharide Films: Physical Chemistry and Cellular Adhesion Aspects, Langmuir. 20 (2004) 448–458. doi:10.1021/la035415n.

[226] H. Hartmann, S. Hossfeld, B. Schlosshauer, U. Mittnacht, A.P. P??go, M. Dauner, M. Doser, D. Stoll, R. Krastev, Hyaluronic acid/chitosan multilayer coatings on neuronal implants for localized delivery of siRNA nanoplexes, J. Control. Release. 168 (2013) 289–297. doi:10.1016/j.jconrel.2013.03.026.

[227] G.A. Junter, P. Thébault, L. Lebrun, Polysaccharide-based antibiofilm surfaces, Acta Biomater. 30 (2016) 13–25. doi:10.1016/j.actbio.2015.11.010.

[228] K. Mulligan, Z.J. Jakubek, L.J. Johnston, Supported lipid bilayers on biocompatible polysaccharide multilayers, Langmuir. 27 (2011) 14352–14359. doi:10.1021/la203207p.

[229] J. Zhan, Q.J. Luo, Y. Huang, X.D. Li, Cellular response to titanium discs coated with polyelectrolyte

multilayer films, Int. J. Miner. Metall. Mater. 21 (2014) 925–933. doi:10.1007/s12613-014-0991-9.

[230] S. Zankovych, J. Bossert, M. Faucon, U. Finger, K.D. Jandt, Selectively promoting or preventing osteoblast growth on titanium functionalized with polyelectrolyte multilayers, Adv. Eng. Mater. 13 (2011) 454–461. doi:10.1002/adem.201180020.

[231] S. Zankovych, M. Diefenbeck, J. Bossert, T. Mückley, C. Schrader, J. Schmidt, H. Schubert, S. Bischoff, M. Faucon, U. Finger, K.D. Jandt, The effect of polyelectrolyte multilayer coated titanium alloy surfaces on implant anchorage in rats, Acta Biomater. 9 (2013) 4926–4934. doi:10.1016/j.actbio.2012.08.013.

[232] P.H. Chua, K.G. Neoh, E.T. Kang, W. Wang, Surface functionalization of titanium with hyaluronic acid/chitosan polyelectrolyte multilayers and RGD for promoting osteoblast functions and inhibiting bacterial adhesion, Biomaterials. 29 (2008) 1412–1421. doi:10.1016/j.biomaterials.2007.12.019.

[233] A.L. Larkin, R.M. Davis, P. Rajagopalan, Biocompatible, detachable, and free-standing polyelectrolyte multilayer films, Biomacromolecules. 11 (2010) 2788–2796. doi:10.1021/bm100867h.

[234] C. Blanco-Andujar, L.D. Tung, N.T.K. Thanh, Synthesis of nanoparticles for biomedical applications, Annu. Reports Sect. "A" (Inorganic Chem. 106 (2010) 553–568. doi:10.1039/B920666N.

[235] K. Chatterjee, S. Sarkar, K. Jagajjanani Rao, S. Paria, Core/shell nanoparticles in biomedical applications, Adv. Colloid Interface Sci. 209 (2014) 8–39. doi:https://doi.org/10.1016/j.cis.2013.12.008.

[236] G. Schmid, Nanoparticles: from theory to application, John Wiley & Sons, 2011.

[237] G. Kaur, O.P. Pandey, K. Singh, D. Homa, B. Scott, G. Pickrell, A review of bioactive glasses: Their structure, properties, fabrication and apatite formation., J. Biomed. Mater. Res. A. 102 (2014) 254–274. doi:10.1002/jbm.a.34690.

[238] G.M. Luz, J.F. Mano, Preparation and characterization of bioactive glass nanoparticles prepared by sol–gel for biomedical applications, Nanotechnology. 22 (2011) 494014. doi:10.1088/0957-4484/22/49/494014.

[239] G.M. Luz, J.F. Mano, Nanoengineering of bioactive glasses: hollow and dense nanospheres, J. Nanoparticle Res. 15 (2013) 1457. doi:10.1007/s11051-013-1457-0.

[240] S.K. Misra, D. Mohn, T.J. Brunner, W.J. Stark, S.E. Philip, I. Roy, V. Salih, J.C. Knowles, A.R.

Boccaccini, Comparison of nanoscale and microscale bioactive glass on the properties of P(3HB)/Bioglass composites., Biomaterials. 29 (2008) 1750–1761. doi:10.1016/j.biomaterials.2007.12.040.

[241] D.S. Couto, Z. Hong, J.F. Mano, Development of bioactive and biodegradable chitosan-based injectable systems containing bioactive glass nanoparticles, Acta Biomater. 5 (2009) 115–123. doi:https://doi.org/10.1016/j.actbio.2008.08.006.

[242] G.M. Luz, J.F. Mano, Chitosan/bioactive glass nanoparticles composites for biomedical applications, Biomed. Mater. 7 (2012) 1–9. doi:10.1088/1748-6041/7/5/054104.

[243] J. Mota, N. Yu, S.G. Caridade, G.M. Luz, M.E. Gomes, R.L. Reis, J.A. Jansen, X.F. Walboomers, J.F. Mano, Chitosan/bioactive glass nanoparticle composite membranes for periodontal regeneration, Acta Biomater. 8 (2012) 4173–4180. doi:https://doi.org/10.1016/j.actbio.2012.06.040.

[244] G. Decher, Fuzzy Nanoassemblies: Toward Layered Polymeric Multicomposites, Science (80-.). 277 (1997) 1232–1237. doi:10.1126/science.277.5330.1232.

[245] J.L. Dalsin, P.B. Messersmith, Bioinspired antifouling polymers, Mater. Today. 8 (2005) 38–46. doi:https://doi.org/10.1016/S1369-7021(05)71079-8.

[246] L. Chen, H. Therien-Aubin, M.C.Y. Wong, E.M. V Hoek, C.K. Ober, Improved antifouling properties of polymer membranes using a {'}layer-by-layer{'} mediated method, J. Mater. Chem. B. 1 (2013) 5651–5658. doi:10.1039/C3TB20916D.

[247] P. Wilke, N. Helfricht, A. Mark, G. Papastavrou, D. Faivre, H.G. Börner, A Direct Biocombinatorial Strategy toward Next Generation, Mussel-Glue Inspired Saltwater Adhesives, J. Am. Chem. Soc. 136 (2014) 12667–12674. doi:10.1021/ja505413e.

[248] A. Wu, D. Yoo, J.-K. Lee, M.F. Rubner, Solid-state light-emitting devices based on the tris-chelated ruthenium (II) complex: 3. High efficiency devices via a layer-by-layer molecular-level blending approach, J. Am. Chem. Soc. 121 (1999) 4883–4891.

[249] T. Boudou, T. Crouzier, K. Ren, G. Blin, C. Picart, Multiple functionalities of polyelectrolyte multilayer films: New biomedical applications, Adv. Mater. 22 (2010) 441–467. doi:10.1002/adma.200901327.

[250] B.B. Hsu, S.R. Hagerman, K. Jamieson, J. Veselinovic, N. O'Neill, E. Holler, J.Y. Ljubimova, P.T. Hammond, Multilayer Films Assembled from Naturally-Derived Materials for Controlled Protein Release, Biomacromolecules. 15 (2014) 2049–2057. doi:10.1021/bm5001839.

[251] P. Podsiadlo, S. Paternel, J.-M. Rouillard, Z. Zhang, J. Lee, J.-W. Lee, E. Gulari, N.A. Kotov, Layer-

by-layer assembly of nacre-like nanostructured composites with antimicrobial properties, Langmuir. 21 (2005) 11915–11921.

[252] G. Decher, J.D. Hong, J. Schmitt, Buildup of ultrathin multilayer films by a self-assembly process: III. Consecutively alternating adsorption of anionic and cationic polyelectrolytes on charged surfaces, Thin Solid Films. 210–211 (1992) 831–835. doi:https://doi.org/10.1016/0040-6090(92)90417-A.

[253] J. Yu, B.M. Meharg, I. Lee, Adsorption and interlayer diffusion controlled growth and unique surface patterned growth of polyelectrolyte multilayers, Polymer (Guildf). 109 (2017) 297–306. doi:https://doi.org/10.1016/j.polymer.2016.12.055.

[254] G. Ladam, P. Schaad, J.C. Voegel, P. Schaaf, G. Decher, F. Cuisinier, In Situ Determination of the Structural Properties of Initially Deposited Polyelectrolyte Multilayers, Langmuir. 16 (2000) 1249–1255. doi:10.1021/la990650k.

[255] Z. Sui, D. Salloum, J.B. Schlenoff, Effect of Molecular Weight on the Construction of Polyelectrolyte Multilayers: Stripping versus Sticking, Langmuir. 19 (2003) 2491–2495. doi:10.1021/la026531d.

[256] N.S. Zacharia, M. Modestino, P.T. Hammond, Factors Influencing the Interdiffusion of Weak Polycations in Multilayers, Macromolecules. 40 (2007) 9523–9528. doi:10.1021/ma071828+.

[257] S.S. Shiratori, M.F. Rubner, pH-Dependent Thickness Behavior of Sequentially Adsorbed Layers of Weak Polyelectrolytes, Macromolecules. 33 (2000) 4213–4219. doi:10.1021/ma991645q.

[258] P. Bieker, M. Schönhoff, Linear and Exponential Growth Regimes of Multilayers of Weak Polyelectrolytes in Dependence on pH, Macromolecules. 43 (2010) 5052–5059. doi:10.1021/ma1007489.

[259] C. Picart, J. Mutterer, L. Richert, Y. Luo, G.D. Prestwich, P. Schaaf, J.-C. Voegel, P. Lavalle, Molecular basis for the explanation of the exponential growth of polyelectrolyte multilayers, Proc. Natl. Acad. Sci. . 99 (2002) 12531–12535. doi:10.1073/pnas.202486099.

[260] N.S. Zacharia, D.M. DeLongchamp, M. Modestino, P.T. Hammond, Controlling Diffusion and Exchange in Layer-by-Layer Assemblies, Macromolecules. 40 (2007) 1598–1603. doi:10.1021/ma061080f.

[261] J.J. Harris, P.M. DeRose, M.L. Bruening, Synthesis of Passivating, Nylon-Like Coatings through Cross-Linking of Ultrathin Polyelectrolyte Films, J. Am. Chem. Soc. 121 (1999) 1978–1979. doi:10.1021/ja9833467.

[262] B. Li, D.T. Haynie, Multilayer Biomimetics: Reversible Covalent Stabilization of a Nanostructured

Biofilm, Biomacromolecules. 5 (2004) 1667–1670. doi:10.1021/bm0496155.

[263] L. Richert, F. Boulmedais, P. Lavalle, J. Mutterer, E. Ferreux, G. Decher, P. Schaaf, J.-C. Voegel, C. Picart, Improvement of Stability and Cell Adhesion Properties of Polyelectrolyte Multilayer Films by Chemical Cross-Linking, Biomacromolecules. 5 (2004) 284–294. doi:10.1021/bm0342281.

[264] S.Y. Yang, M.F. Rubner, Micropatterning of Polymer Thin Films with pH-Sensitive and Cross-linkable Hydrogen-Bonded Polyelectrolyte Multilayers, J. Am. Chem. Soc. 124 (2002) 2100–2101. doi:10.1021/ja017681y.

[265] R.R. Costa, J.F. Mano, Polyelectrolyte multilayered assemblies in biomedical technologies., Chem. Soc. Rev. 43 (2014) 3453–3479. doi:10.1039/c3cs60393h.

[266] G.M. Luz, J.F. Mano, Biomimetic design of materials and biomaterials inspired by the structure of nacre, Philos. Trans. R. Soc. London A Math. Phys. Eng. Sci. 367 (2009) 1587–1605. doi:10.1098/rsta.2009.0007.

[267] H.D. Espinosa, J.E. Rim, F. Barthelat, M.J. Buehler, Merger of structure and material in nacre and bone – Perspectives on de novo biomimetic materials, Prog. Mater. Sci. 54 (2009) 1059–1100. doi:https://doi.org/10.1016/j.pmatsci.2009.05.001.

[268] A.P. Jackson, J.F. V Vincent, R.M. Turner, The Mechanical Design of Nacre, Proc. R. Soc. London. Ser. B. Biol. Sci. 234 (1988) 415–440. http://rspb.royalsocietypublishing.org/content/234/1277/415.abstract.

[269] F. Barthelat, C.-M. Li, C. Comi, H.D. Espinosa, Mechanical properties of nacre constituents and their impact on mechanical performance, J. Mater. Res. 21 (2006) 1977–1986. doi:DOI: 10.1557/jmr.2006.0239.

[270] A. Sellinger, P.M. Weiss, A. Nguyen, Y. Lu, R.A. Assink, W. Gong, C.J. Brinker, Continuous self-assembly of organic-inorganic nanocomposite coatings that mimic nacre, Nature. 394 (1998) 256–260. http://dx.doi.org/10.1038/28354.

[271] Z. Tang, N.A. Kotov, S. Magonov, B. Ozturk, Nanostructured artificial nacre, 2 (2003) 413. http://dx.doi.org/10.1038/nmat906.

[272] H. Wei, N. Ma, F. Shi, Z. Wang, X. Zhang, Artificial Nacre by Alternating Preparation of Layer-by-Layer Polymer Films and CaCO3 Strata, Chem. Mater. 19 (2007) 1974–1978. doi:10.1021/cm062898i.

[273] H.-B. Yao, H.-Y. Fang, Z.-H. Tan, L.-H. Wu, S.-H. Yu, Biologically Inspired, Strong, Transparent, and Functional Layered Organic–Inorganic Hybrid Films, Angew. Chemie Int. Ed. 49 (2010) 2140–2145. doi:10.1002/anie.200906920.

[274] C. Wang, Y. Huang, Q. Zan, H. Guo, S. Cai, Biomimetic structure design — a possible approach to change the brittleness of ceramics in nature, Mater. Sci. Eng. C. 11 (2000) 9–12. doi:https://doi.org/10.1016/S0928-4931(00)00133-8.

[275] G. Mayer, Rigid Biological Systems as Models for Synthetic Composites, Science (80-.). 310 (2005) 1144 LP-1147. http://science.sciencemag.org/content/310/5751/1144.abstract.

[276] E. Munch, M.E. Launey, D.H. Alsem, E. Saiz, A.P. Tomsia, R.O. Ritchie, Tough, Bio-Inspired Hybrid Materials, Science (80-.). 322 (2008) 1516 LP-1520. http://science.sciencemag.org/content/322/5907/1516.abstract.

[277] M.E. Launey, E. Munch, D.H. Alsem, E. Saiz, A.P. Tomsia, R.O. Ritchie, A novel biomimetic approach to the design of high-performance ceramic–metal composites, J. R. Soc. Interface. 7 (2010) 741–753. doi:10.1098/rsif.2009.0331.

[278] D. Zhu, F. Barthelat, A Novel Biomimetic Material Duplicating the Structure and Mechanics of Natural Nacre BT - Mechanics of Biological Systems and Materials, Volume 2: Proceedings of the 2011 Annual Conference on Experimental and Applied Mechanics, in: T. Proulx (Ed.), Springer New York, New York, NY, 2011: pp. 181–187. doi:10.1007/978-1-4614-0219-0_25.

[279] S.M. Waraich, B. Hering, Z. Burghard, J. Bill, P. Behrens, H. Menzel, Fabrication and characterization of biocompatible nacre-like structures from α-zirconium hydrogen phosphate hydrate and chitosan, J. Colloid Interface Sci. 367 (2012) 74–82. doi:https://doi.org/10.1016/j.jcis.2011.10.042.

[280] H. Cao, X. Chen, J. Yao, Z. Shao, Fabrication of an alternative regenerated silk fibroin nanofiber and carbonated hydroxyapatite multilayered composite via layer-by-layer, J. Mater. Sci. 48 (2013) 150–155. doi:10.1007/s10853-012-6722-6.

[281] J. Li, D. Liu, B. Li, J. Wang, S. Han, L. Liu, H. Wei, A bio-inspired nacre-like layered hybrid structure of calcium carbonate under the control of carboxyl graphene, CrystEngComm. 17 (2015) 520–525. doi:10.1039/C4CE01632G.

[282] W. Hao, L. Zhang, X. Wang, J. Wang, Z. Hu, W. Yang, Tough and strong nacre-like composites from hyperbranched poly(amido amine) and clay nanosheets cross-linked by genipin, RSC Adv. 6 (2016) 1415–1421. doi:10.1039/C5RA21580C.

[283] T.G. Kim, H. Lee, Y. Jang, T.G. Park, Controlled Release of Paclitaxel from Heparinized Metal Stent Fabricated by Layer-by-Layer Assembly of Polylysine and Hyaluronic Acid-g-Poly(lactic-co-glycolic acid) Micelles Encapsulating Paclitaxel, Biomacromolecules. 10 (2009) 1532–1539. doi:10.1021/bm900116r.

[284] S. Schweizer, T. Schuster, M. Junginger, G. Siekmeyer, A. Taubert, Surface modification of nickel/titanium alloy and titanium surfaces via a polyelectrolyte multilayer/calcium phosphate hybrid coating, Macromol. Mater. Eng. 295 (2010) 535–543. doi:10.1002/mame.200900347.

[285] H. Ao, Y. Xie, H. Tan, S. Yang, K. Li, X. Wu, X. Zheng, T. Tang, Fabrication and in vitro evaluation of stable collagen/hyaluronic acid biomimetic multilayer on titanium coatings., J. R. Soc. Interface. 10 (2013) 1–9. doi:10.1098/rsif.2013.0070.

[286] C.A. Custódio, R.L. Reis, J.F. Mano, Engineering Biomolecular Microenvironments for Cell Instructive Biomaterials, Adv. Healthc. Mater. 3 (2014) 797–810. doi:10.1002/adhm.201300603.

[287] N.M. Alves, I.B. Leonor, H.S. Azevedo, R.L. Reis, J.F. Mano, Designing biomaterials based on biomineralization of bone, J. Mater. Chem. 20 (2010) 2911. doi:10.1039/b910960a.

2. CHAPTER 2 – MATERIALS AND METHODS

This chapter describes all the materials and methods carried out to achieve the experimental results presented in this dissertation. In addition, all the characterization techniques that were used are also described.

2.1 Materials

2.1.1 Chitosan

Medium molecular weight chitosan (CHT) was purchased from Sigma-Aldrich (ref. 448877, Brookshield viscosity 200–800 cP, molecular weight 190–310 kDa) and purified by a series of filtering steps and precipitation in water and ethanol, followed by the freeze-drying process.

CHT (1-4, 2-amino-2-deoxy-β-D-glucan) is a natural linear polysaccharide obtained by deacetylation of chitin (1-4, 2-acetoamino-2-deoxy-β-D-glucan) composed by N-acetyl-D-glucosamine and D-glucosamine units, as represented in Figure 2.1 [1–3]. It is a copolymer present in the exoskeletons of arthropods (crustaceans and insects), being the second most abundant polysaccharide found in nature after cellulose [1]. Unlike chitin which is generally insoluble in aqueous solutions, CHT is soluble in dilute acids at pH<6 due to protonation of amino groups [2]. In fact, when the acetylation degree (expressed as molar percentage), which differentiates chitin from CHT, is lower than 50 mol%, the product is named CHT and it becomes soluble in acidic aqueous solutions [3].

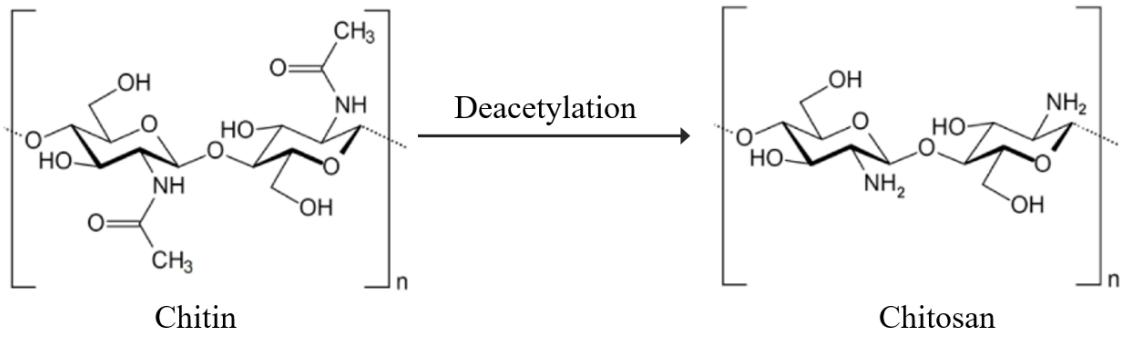

Figure 2.1 – Chemical structures of N-acetyl-D-glucosamine residues (chitin) and D-glucosamine residues (chitosan) during deacetylation process. Adapted from [3].

During the deacetylation process, acetyl groups are removed and the depolymerization reaction takes place leading to changes in molecular weight (MW), crystallinity, solubility, mechanical

strength and biological properties of CHT [3,4]. Within the body, the enzymatic degradation of CHT leads to the release of amino sugars, including saccharides and glucosamines, which can be easily processed and released through the metabolic system [2,5].

CHT offers excellent biocompatibility, biodegradability, bioadhesivity, non-toxicity and processability properties, allowing a wide range of applications in the biomedical area [6–9]. Also, CHT demonstrates attractive biological activities such as antimicrobial, antioxidant, antitumor actions [3] and lower toxicity towards mammalian cells [10]. Due to its similarity to hyaluronic acid HA and glycosaminoglycan extracellular matrix (ECM) molecules, it's considered biocompatible [11] and, thanks to its polycationic nature, it also displays antimicrobial properties [1,12–14]. Recent studies explain the extensive use of this polysaccharide and its derivatives in antimicrobial coatings for implant materials due to its antibiofilm effects [15–17]. In addition, the positive charge of CHT allows it to have establish electrostatic interactions with negatively charged molecules such as cytokines, growth factors which are correlated with enhanced cell attachment, growth and proliferation [5]. Also, CHT has received attention as a potential coating material for orthopaedic and dental/craniofacial implants due to its osteogenic and biodegradable/drug delivery properties, ability to accelerate wound healing, and flexibility in its processing and modification [6,18–22]. Likewise, as a cationic polyelectrolyte, it has been combined with anionic polymers via layer-by-layer (LbL) self-assembly [23,24], giving rise to multilayered structures. Beyond that, owing to its well-known properties, CHT is probably the most widely used polysaccharide in LbL films [7]. However, CHT has weak mechanical properties [4,25], solubility only under acidic conditions and low surface area, which may limit its performance during the adsorption process [25] in the LbL assembly of multilayer films. Thus, many researchers have described new approaches to overcome these drawbacks, either by chemical modification or by covalent and ionic cross-linking of CHT [25].

CHT is also used in various types of biomedical applications such as drug and gene delivery, wound healing, tissue engineering, and stem cell technology [26]. It can be easily processed into various products, including hydrogels [27–29], membranes [30], fibers [30], films [31,32], coatings [31,33], nanofibers [34–36], beads [37], micro/nanoparticles [38–41], scaffolds [42,43], and sponges [44–46].

2.1.2 Hyaluronic Acid

Hyaluronic acid sodium salt from Streptococcus equi (HA) was purchased from Sigma (ref. 53747, molecular weight 1500–1800 kDa).

HA is a linear and high-molecular-mass anionic biopolymer composed of repeating disaccharide units of β–(1,4)-D-glucuronic acid and β–(1,3)–N–acetyl-D-glucosamine, as shown in Figure 2.2 [47–49]. Among the glycosaminoglycans family, it is a mucopolysaccharide like other commonly known compounds, such as chondroitin sulfate, keratan sulfate I and II, heparin, heparan sulfate, and dermatan sulfate [47]. The individual portions of HA are synthesized by HA synthases, located on the inner side of the cell membrane, emerging towards outside the cell [50].

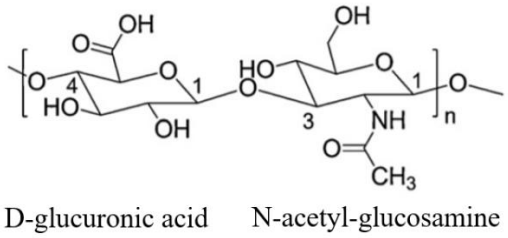

Figure 2.2 – Chemical structure of hyaluronic acid [49].

Its wide availability, ease processing, fully biodegradability *in-vivo*, biocompatibility, low toxicity, hydration of tissues, non-adhesive nature, viscoelastic and rheological properties make it an attractive biomaterial for various medical applications [50,51]. It can also influence the cell activity, namely proliferation, differentiation, and tissue repair [51].

Naturally present in the human body, HA is mostly found on the skin (about 50 % of the total HA) [52], synovial fluid [53], the vitreous body [54], and the umbilical cord [55] as well as in friction zones (joints, tendons, sheaths, pleura, and pericardium) [50]. In addition, HA is involved in numerous processes that occur in the body such as wound healing, ovulation, fertilization, signal transduction and tumour physiology [53,56]. HA is also present in the capsules of some bacteria, like the strains of Streptococci, but is absent in fungi, plants, and insects [51]. Its structure is identical in both vertebrates and bacteria, and can be obtained from bacteria fermentation [47,50,57].

To overcome problems with HA degradation, chemical modifications by crosslinking, wherein different HA chains are linked together by two or more bonds, or conjugations, in which a compound is grafted onto an HA chain by a single bond, have been exploited in the preparation of medical grade HA-materials [49,58].

HA is commonly used in biomedicine for ophthalmology, orthopaedics, aesthetic dermatology, wound healing, drug delivery and as a diagnostic marker for many diseases including cancer, rheumatoid arthritis and liver pathologies [51]. It is also used for supplementation of impaired synovial fluid in arthritic patients through intra-articular injections and reconstruction of soft tissue [51].

Its biocompatibility and therefore negligible side effects make it one of the most used compounds in many fields of medicine in the 21st century [51]. Among the polysaccharides, HA is the most studied as a biofilm repelling coating [59–61]. It has proven to be an effective polyanion able to complex with cationic polymers such as CHT [24,62–68], providing for opportunities to generate polyelectrolyte multilayers (PEMs) systems. CHI/HA multilayers have been built up onto a huge diversity of substrates like, glass [69], Ti [64,70–73], detachable poly(propylene) [74], poly(ethylene terephthalate) [75], among other ones.

2.1.3 Dopamine

Dopamine hydrochloride, 3,4-dihydroxyphenethylamine hydrochloride (DN), (ref. H8502, molecular weight 189,64 Da) was purchased from Sigma.

DN is commonly known as a hormone and neurotransmitter, which consists in a catecholamine that mimics the 3,4-dihydroxyphenyl-L-alanine (DOPA) responsible for the exceptional adhesive characteristics of the mussel's adhesive proteins (MAPs) [76–78]. It is formed by decarboxylation of DOPA, as shown in Figure 2.3 [77]. Similarly to DOPA, DN has a catechol and amine group that gives it the ability to interact with organic surfaces and adhesion to a wide spectrum of materials [79]. Several authors [65,80,81] demonstrated the enhancement of the cellular behaviour with the presence of DN functional group and they have correlated with the fact of DN can act as an active anchor between the material surface and the cells, allowing the formation of covalent and non-covalent bonds.

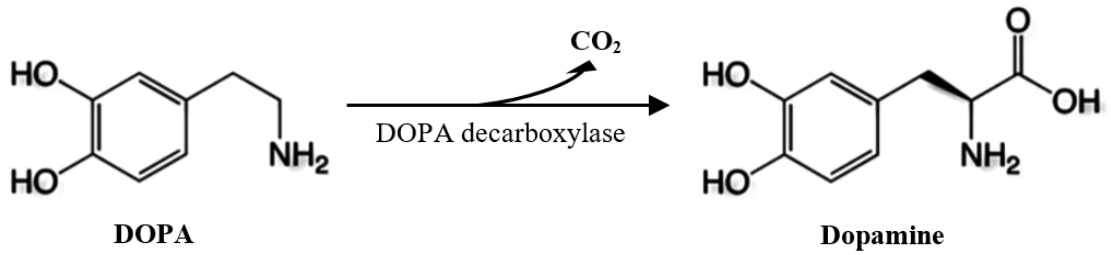

Figure 2.3 – DOPA decarboxylation into dopamine. Adapted from [77]**.**

Under defined conditions, alkaline solutions, DN undergoes to oxidative self-polymerization creating a strongly adhesive polydopamine layer on almost all type of material, including metal, ceramics, and macromolecular polymers [82–84], regardless of its surface chemistry, with the accompanied oxidation of catechol groups to the quinone form [78,80]. Therefore, DN is becoming a versatile and attractive polymer to form coatings for surface modification of different materials [82].

By a simple dip-coating method it is possible to modify the surface of a given material by forming bonds between thiol- or amine- containing molecules and the DN coating layer [82,85,86]. In addition, the use of DN as a coating can improve the hydrophilicity, adhesion or ion exchange performances of many surfaces, therefore extending the use of inert and hydrophobic surfaces in further applications [82]. Xi *et al.* [82], used the coating and polymerization of DOPA and DN to perform a surface hydrophilic modification of poly(ethylene), poly(vinylidene fluoride) and polytetrafluoroethylene porous membranes. They found that the water contact angle of the modified membranes was reduced in comparison with to the corresponding original membranes, suggesting that the membrane hydrophilicity was significantly improved. They also showed that the polymer layers containing carboxyl, hydroxyl and amino groups were substantially attached onto the membranes by the strong interaction between poly(DOPA)/poly(DN) and membrane surfaces. Moreover, HA-DN conjugate has been used in coatings to modify the surface of biomedical devices and to develop a cell-supporting matrix in various fields of biomedical research [87,88].

2.1.4 Hydrocaffeic Acid

Hydrocaffeic acid, 3,4-dihydroxyhydrocinnamic acid (HCA), (98%, ref. 102601, molecular weight 182.17 Da) was purchased from Sigma.

HCA is a nonflavonoid catecholic compound which is present in distinct plants, Figure 2.4 [89,90]. It has demonstrated low cytotoxicity, non-immunogenicity and high-affinity anchors for coordination and nanocomplex stabilization [91,92]. It has also been reported the multiple biological and pharmacological properties of HCA, such as anti-inflammatory, antimutagenic, antioxidant, and anticarcinogenic activities [89]. In addition, many studies have reported that the conjugation of catechol moieties of HCA onto CHT backbone significantly increases its water solubility, adhesiveness on tissue surfaces, biocompatibility and mechanical properties [93–97].

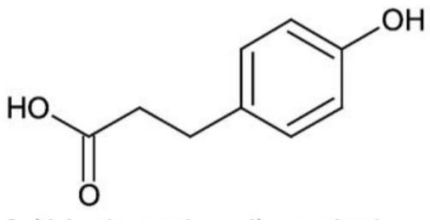

Figure 2.4 – Chemical structures of HCA. Adapted from [90].

Catechol groups of the MAPs have been known to be responsible for the strong underwater adhesion [98,99]. Therefore, to enhance the adhesion strength, catechol derivatives as DN and HCA

have been introduced into the polymers backbone [100]. Zhou *et al.* [100] reported an *in situ* forming nerve adhesive hydrogel composed of CHT and ε-polylysine-catechol conjugate, which mimics the polysaccharides/protein structure of natural epineurium matrices. Catechol groups conjugated onto ε-polylysine molecules were demonstrated to reinforce both the bulk cohesive force of the hydrogel and the interfacial adhesive force between the hydrogel and epineurium. After 8 weeks, the morphology of the repaired nerve fiber coated by the hydrogel was very close to the morphology of normal nerve. Qiao *et al.* [91] designed a kidney-specific nanocomplex by forming coordination-driven assembly from catechol-derived CHT, metal ions and active drug molecules. The nanocomplex demonstrated satisfactory stability under normal physiological conditions and pH-responsive drug release in acidic environments. Lee *et al.* [101] tested a water-resistant catechol-conjugated CHT adhesive gel patch in a cartilage repair model which plays a role in releasing the encapsulated platelet-derived growth factor-AA (PDGF-AA) to maximize the mesenchymal stem cell (MSC) migration from the bone marrow. The results showed a directional PDGF-AA release which promoted effective recruitment of human mesenchymal stem cell (hMSCs) and prevention of its further migration and dispersion. Ryu *et al.* [95] synthesized an injectable and thermosensitive CHT/Pluronic composite hydrogel for tissue adhesives and haemostatic materials. CHT was conjugated with catechol groups in the backbone and cross-linked with terminally thiolated Pluronic F-127 triblock copolymer. The injectable hydrogels showed superior haemostatic properties and strong adhesiveness to soft tissues and mucous layers. Soliman *et tal.* [102] studied HCA–CHT nanoparticles prepared by ionic gelation with sodium tripolyphosphate to enhance CHT mucoadhesion and stabilize it in nanoparticulate form. Nanoparticles showed stability without aggregation or precipitation, maintained their size and mucoadhesion to rabbit intestine. Xu *et al.* [103], proposed an injectable mucoadhesive hydrogel based on catechol modified-CHT crosslinked by genipin to improve the efficacy of rectal sulfasalazine administration for colitis in mice. Rectal treatment showed better therapeutic effects than the oral treatment and reduced the risk of side effects.

2.1.5 Bioactive Glass Nanoparticles

Ternary bioactive glass nanoparticles (BGNPs) were produced by a sol-gel methodology in which precursors of various chemicals elements that constitutes the bioactive glass (BG). Tetraethyl orthosilicate (TEOS, 99.90%) was purchased by Merck Chemicals. Ammonium phosphate dibasic (≥98%), citric acid monohydrate (99%), calcium nitrate tetrahydrate (99%), ethanol absolute, and ammonium hydroxide solution (30-33% of NH_3) were purchased from Sigma-Aldrich.

The first bioactive material was reported by Larry Hench and colleagues, in 1971, having developed what is nowadays termed 45S5 Bioglass® with great potential for bone regeneration [104]. BGs are highly attractive materials for healthcare and regenerative medicine, since they can bind to hard and soft tissues stimulating new tissue growth while dissolving over time [105,106]. Bone binding is evidenced by the precipitation of a layer of calcium–deficient carbonated apatite on the BG surface when *in-vivo* applications or in contact with physiological fluid [107,108].

BGNPs consists of a silicate network incorporating sodium, calcium and phosphorus in different relative proportions and have recently gained attention due to their size, easy dispersability, mechanical properties, bioactivity, ability to work as nanocarriers, osteoconductivity and cytocompatibility [109–111]. Moreover, its high specific surface area allows a faster release of ions and greater protein adsorption [112]. BGNPs have been used in combination with polymeric matrixes to obtain nanofiber composites, LbL coatings, scaffolds, and injectable materials with enhanced mechanical properties [113]. Its smaller particle size, when compared to the microparticles, makes them ideal candidates for injectable carriers, as well as accelerate their interaction with tissue and improve mechanical properties of composites [110]. Among the various techniques for its synthesis, sol-gel method stands out due to its low processing temperatures, easy control of the final product form as well as high purity, high specific area, high osteoconductivity properties and high degradability [114,115].

To improve the BGNPs properties, some works have shown that doping BGs with different ions can improve their biological performance. For example, by adding magnesium, one of the main substitutes of calcium in biological apatite, to the BGs formulation, osteoblastic adhesion can be enhanced [116]. Other elements have also been used to dope BG, such as strontium (Sr) which promotes osteoblastic differentiation [116,117] and silver (Ag) that confers bacteriostatic and bactericidal properties [66,118,119].

Very recently, adhesive and bioactive coatings inspired by the structure of nacre using BGNPs have been developed [66,67]. Carvalho *et al.* [66] reported antibacterial and bioactive coatings with a nacre-like architecture using Ag doped BGNPs, CHT and HA modified with catechol groups through layer-by-layer deposition. Rego *et al.* [67] also performed bioactive coatings inspired by the structure of nacre using BGNPs, CHT and HA modified with catechol groups through layer-by-layer deposition. These coatings have shown excellent adhesive properties and good bioactivity, and they could thus be used as a coating of a variety of implants for orthopaedic applications [66,67].

2.1.6 Substrates

Glass, titanium (Ti) and 316L stainless steel (SS) substrates were used for the deposition of LbL coatings by dip- and spin-coating methods. Borosilicate glass was used as plates of 3 mm thickness, and round coverglasses with 18 mm diameter. 99.6 % purity Ti (Goodfellow Metals Ltd, Cambridge, UK) was used as disks of 3 mm thickness and 18 mm diameter. Also, 316L SS (Goodfellow Metals Ltd, Cambridge, UK) was used as disks of 3 mm thickness and 18 mm diameter. Prior to use, Ti disks were manually polished with abrasive discs of P180, P320, P600 and P800 (Struers, France). In addition, prior to coating deposition, all the substrates were cleaned in sequential ultrasonic baths to remove surface impurities: 1º - 15 minutes with acetone; 2º - 15 minutes with ethanol; 3º - 15 minutes in osmotized water; and finally, they were dried with a nitrogen flow.

Glass

Borosilicate glass was used in this work, since in previous works [65–67] was also used for LbL deposition of multilayer films based on CHT, HA, catechol-conjugated HA, and BGNPs through the dip-coating technique.

In addition, borosilicate glass is the most similar substrate, in terms of contact angle, to gold-coated quartz crystals used for quartz crystal microbalance measurements.

Titanium

Most procedures for restoring bone and joint function in orthopaedics and to replace missing bones and teeth in dental/craniofacial applications involve the use of Ti and Ti-based alloy implants [2,120]. Due to their excellent biocompatibility, good mechanical properties, low density, and anticorrosion properties, Ti and its alloys have been recommended as the ultimate choice for hard tissue replacement [121]. Ti owes its good biocompatibility to a dense surface oxide layer which forms spontaneously in the presence of oxygen [122].

The success of these implant therapies is related to the ability of Ti and its alloys to the osseointegration, i.e., becoming well integrated into the surrounding bone [2]. However, as the Ti and its alloys are bioinert materials, after their implantation, a fibrous encapsulation occurs on surface of these materials [120]. Some studies have demonstrated that these implants have expectable long-term clinical success of 72-92% at 10 years for total joint devices, and 81-91% for dental implants at up to 15 years [123–128]. However, given the younger patient population and increased life expectancies, the demand for longer functional lifetime service of these implant devices is increasing.

So, implant designers and engineers have been focused on improving osseointegration of implants through new approaches, such as, surface modifications and coatings [64,70,129–136].

Covering Ti surfaces by one or more layers of polymers creates new perspectives for Ti-biological environment interfaces. Several authors have studied the use of polyelectrolytes films for covering strategy based on electrostatic interactions. However, the strength of these interactions against the stress applied to the biomaterial may be insufficient [137,138].

Different types of grafting methods are available to anchor onto the Ti surface a film of synthetic or natural polyelectrolytes. One way to perform grafting on a Ti surface is to use catechols groups. Dalsin *et al.* [139] were inspired by MAPs to anchor poly(ethylene glycol) (PEG), using catechol groups, onto Ti and gold surfaces for antifouling purposes. They demonstrated that the use of a natural adhesive protein conjugated to PEG readily adsorbs onto gold and Ti surfaces, rendering these surfaces resistant to cell attachment for up to 2 weeks. In addition, Hu and co-workers [140] reported Ti surfaces functionalized by covalently grafting either with DN followed by carboxymethyl CHT or HA-catechol. They showed that the polysaccharide-modified substrates significantly decrease bacterial adhesion.

316L Stainless Steel

316L biomedical SS has been widely applied in biomedical applications, such as bone implants and vascular stents, owing to its favourable mechanical properties, corrosion resistance and low manufacturing cost [141,142]. Despite its corrosion resistance conferred by the thin protective chromium-enriched oxide layer on its surface, several kinds of corrosion mechanisms have been observed in biological environments [143]. The localized attack through chloride-containing environments that occurs on the SS surface leads to the release of metal ions such as iron, chromium and nickel from the alloy resulting in a decreased biocompatibility [143]. Thus, many researchers have focused on different ways to improve its corrosion resistance, through surface modification and coatings approaches [144].

Polymeric coatings have shown to have an effective protection role against the corrosion of metallic implants. Different polymers have been used as coatings for load-bearing bone implants and cardiovascular stents consisting of poly(L-lactic acid), poly(ε–caprolactone) (PCL) and poly(glycolic acid) [145–147]. Currently, nanocomposite coatings of polymers, such as PCL, poly(D,L-lactic-co-glycolic), poly(methylmethacrylate), poly(D,L)lactide) and bioactive ceramics, such as hydroxyapatite and bioglass, have been established with the aim of improving bone-tissue interaction and

osseointegration as well as corrosion resistance [142,146,148].In addition, polymeric coatings have been used on SS substrates to improve their biocompatibility and to provide an antimicrobial role [149,150].

Feng *et al.* [149] prepared coatings based on HA and DN onto 316L SS via chemical conjugation to enhance biocompatibility of cardiovascular implanted devices. It was shown that HA/DN coatings presented better hemocompatibility compared with the bare 316L SS. Also, Charlot *et al.* [150] developed robust antimicrobial films on SS based on the LbL deposition of polyelectrolytes containing DOPA. A polycationic copolymer bearing DOPA units was synthesized and co-deposited with precursors of Ag nanoparticles as the first layer. Multilayer films were obtained by alternating the nanoparticle-loaded polycationic copolymer with polystyrene sulfonate, a commercial polyanion, resulting in SS with high antibacterial activity against E. coli bacteria [150].

2.1.7 Chitosan Purification

The procedure to obtain a pure CHT from a CHT commercial product was based on the one already optimized by 3B's group. Thus, by dissolving CHT in acetic acid solution followed by precipitation, many impurities resulting from the chitin deacetylation process can be removed. To this end, CHT medium molecular weight was added to acetic acid solution (2wt%, v/v) to obtain (1wt%, w/v) CHT solution followed by stirring at room temperature overnight. After that, the final solution was filtered thrice using a nylon filter to remove the sludges. The purification of CHT in the neutralized form was attained by carefully adding of 2M NaOH to the filtered solution until the pH reached 8, promoting the precipitation of the polymer. After this step, the polysaccharide's precipitate, was filtered and exhaustively washed with osmotized water until its neutrality. Then, ethanol-water solutions (80/20, 50/50, 90/10) were added to the CHT precipitate to gradually be forced to dehydrate the sample, followed by filtration. The final product was frozen at -80 °C overnight and then, freeze-dried (at least 4 days). The purified CHT powder is soluble in diluted acetic and hydrochloric acids.

2.1.8 Synthesis of the Catechol-Conjugated Hyaluronic Acid

The synthesis results of catechol-conjugated hyaluronic acid (HA-DN) was shown in Appendix I. HA-DN polymers with the highest degree of substitution (DS, %) of catechol groups were chosen.

Therefore, HA-DN was synthesized from the procedure proposed by Lee and co-workers [151], with some modifications. HA modification with catechol groups was performed by the carbodiimide chemistry using *N*-(3-(dimethylamino)propyl)-*N'*-ethylcarbodiimide hydrochloride (EDC) as an

activation agent of the carboxyl groups on HA chains. This activation allowed the coupling between the carboxyl groups of HA to primary amines of DN as shown in Figure 2.5 [152].

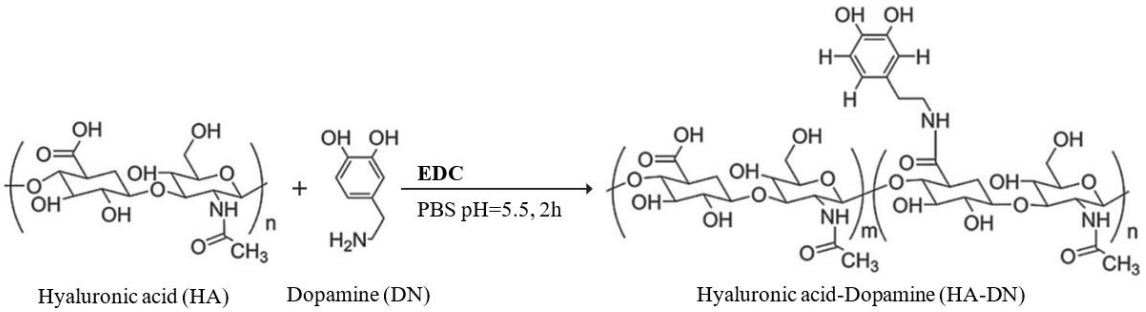

Figure 2.5 – Scheme of HA-DN synthesis. Adapted from [152]**.**

Briefly, a HA solution (10 mg.mL^{-1}) was prepared in phosphate buffered saline (PBS) solution and the pH was adjusted to 5.5 using 0.5M hydrochloric acid (HCl) or 0.5M sodium hydroxide (NaOH) aqueous solution under magnetic stirring. To limit the oxygen interaction with the solution, it was purged with nitrogen for 30 min. Then, 338 mg of EDC and 474 mg of DN were added to the previous solution and the pH was maintained at 5.5 at 4 °C. The resulting solution was divided in two different solution with different reaction times i.e. HA-DN*$_{4h}$ and HA-DN*$_{36h}$. Unreacted chemicals and urea byproducts were removed by dialysis against a pH 5.0 HCl solution for 4 days and osmotized water for 1 day, using a dialysis membrane tube, at 4°C. Finally, the HA-DN conjugates were freeze-dried for 4 days and stored at -20°C. The entire procedure and storage of the produced HA-DN was performed at 4°C and protected from light to prevent the DN oxidation.

2.1.9 Synthesis of the Catechol-Conjugated Chitosan

The catechol-conjugated chitosan (CHT-C) synthesis was based on the results presented in Appendix II, in which it was noticed that the first approach proposed by Xu and co-workers [153], although having a DS (%) of catechol group slightly superior to the second one, did not show a total dissolution in aqueous solutions as expected. Therefore, the CHT-C synthesis was based on procedure proposed by Kim *et al.* [154], Xu *et al.* [153] and Ghadban *et al.* [155].

As in the HA-DN synthesis, the CHT modification with catechol groups was accomplished by the carbodiimide chemistry using EDC as an activation agent. Thus, the coupling between the amine groups of the CHT and the carboxyl groups of the HCA was achieved, as shown in Figure 2.6.

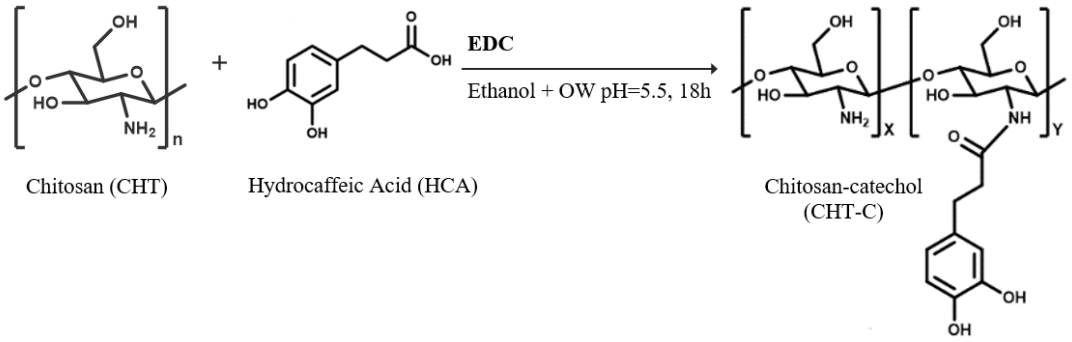

Figure 2.6 – Scheme of CHT-C synthesis. Adapted from [153].

So, 1% (w/v) medium molecular weight CHT solution was prepared in HCl solution at pH 2.5. Then, a HCA solution (59 mg.mL^{-1}) was prepared in osmotized water and an EDC solution (119 mg.mL^{-1}) was prepared in a mixture of osmotized water and ethanol. These two previous solutions were mixed and added to CHT solution, under stirring at 4° C, followed by the addition of 1M NaOH solution to obtain a final pH of 4.8. The reaction was allowed to continue for 18 h, CHT-C*$_{18h}$, under nitrogen atmosphere for 30 min. After that, the product was purified by dialysis against an acidic osmotized water solution (pH 5.0, HCL solution) for 3 days and osmotized water for 4 hours, using a dialysis membrane tube, at 4°C and protected from the light. The resulting product was freeze-dried and stored at -20°C.

2.1.10 Bioactive Glass Nanoparticles Production

The procedure to obtain the ternary system of BGNPs with the composition SiO_2:CaO:P_2O_5 (mol.%) = 50:45:5 was based on the sol-gel method already optimized by two previous works [156,157].

First, a "solution A" was prepared through a mixture of precursor´s solutions. So, 6% (w/v) of calcium nitrate tetrahydrate ($Ca(NO_3)_2{\cdot}4H_2O$), calcium precursor, was dissolved in osmotized water at room temperature. Then, 9.8353 mL of tetraethyl orthosilicate (TEOS), silica precursor, together with 60 mL of ethanol absolute was added to the previous solution. The pH of solution A was adjusted to 2 with citric acid solution (10 % (w/v)), under stirring for 3 hours. After that, a "solution B" was also prepared by adding 0.07% (w/v) of diammonium hydrogenophosphate (ammonium phosphate dibasic, $(NH_4)_2HPO_4$), phosphorus precursor, to osmotized water. The pH of solution B was adjusted to 11.5 with ammonia hydroxide solution. Under stirring, the solution A was slowly added, drop-by-drop, to solution B and the pH was maintained at 11.5 by continuous supplement of ammonia hydroxide solution. This reaction mixture was left under stirring during 48 h and then, under resting

for 24 h to occur the gel particle precipitation. Afterwards, the gel precipitate was washed tree times with osmotized water and stored during 24 h at -80°C to be subsequently freeze-dried for 7 days. The obtained white gel powder was calcinated at 700°C for 3 h to get the BGNPs with improved bioactivity. The procedure described above is shown in Figure 2.7.

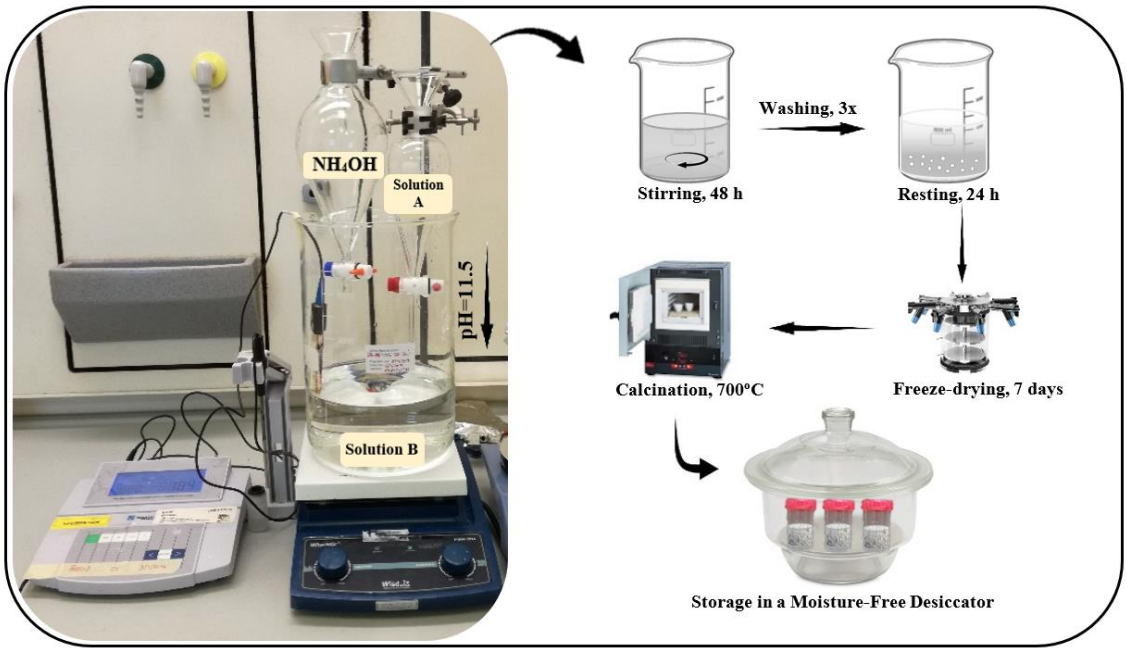

Figure 2.7 – Scheme of BGNPs production.

2.1.11 LbL Assembly – Production of Multifunctional LbL Coatings

Among the several techniques to for the thin film deposition, LbL assembly is an extremely versatile technique for the production of nanostructured polymeric multilayer thin films with well-tailored thickness, composition, structure, properties, and functions over different types of substrate. As previously described, LbL assembly is based on sequential adsorption of complementary multivalent molecules on a substrate surface, occurring either via electrostatic or nonelectrostatic interactions. Through this approach, it is possible to build an effective and reproducible film by the deposition of alternate layers with oppositely charged materials [158]. A multilayer assembly is reached by repeating the deposition cycles that produce the desired number of layers. A variety of deposition methods for the LbL build-up of multilayer assembly have been already reported in the literature, including dip-coating, spin-coating, spraying and perfusion. Among these, dip-coating has been definitely the LbL deposition technique most widely used [158,159].

Dip-coating is a LbL assembly method based on electrostatic interactions, which consists in the vertical alternate dipping of a charged substrate into diluted solutions of oppositely charged molecules. In this process, a washing step between the deposition of each polyelectrolyte (PE) is required to

remove the unbounded materials and stabilizes weakly adsorbed layers [160]. The process is repeated the times intended until achieving the desired layers number, as depicted in Figure 2.8 [159]. Crucial parameters for the control of the properties and thickness of the film are the concentration, pH, ionic strength, viscosity of the PE solutions, and the deposition time (immersion time). Dip-coating method presents advantages compared to other deposition techniques, such as the simplicity and low-cost of the LbL process and equipment, as well as its suitability to coating substrates with complex geometries. However, the need of a relatively large amount of materials for each deposition step and the time-consuming leads to choose alternative methods, such as the spin-coating [159,161]. Therefore, the spin-coating method appears as a good alternative to produce low-cost, rapid, and uniform LbL films using the same materials of the dip-coating and allowing the electrostatic self-assembly [159].

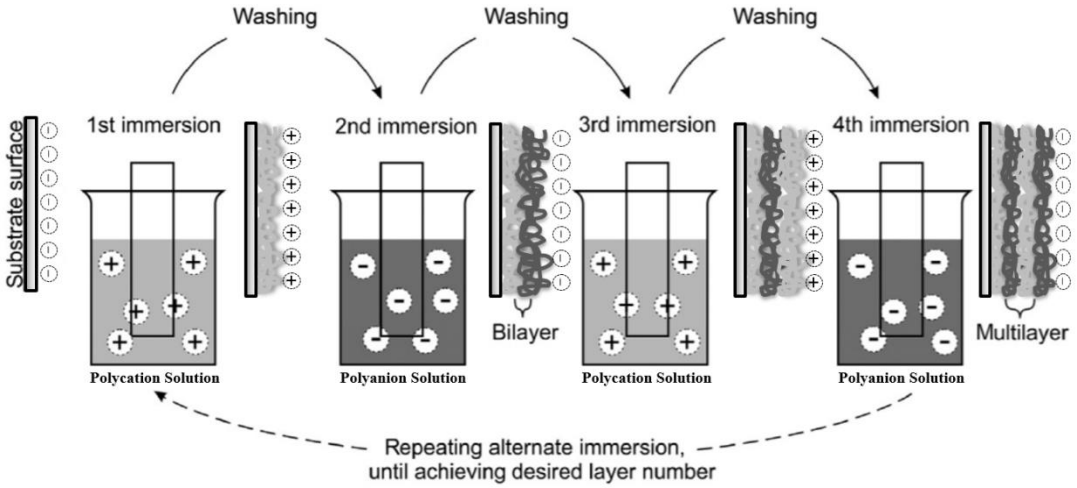

Figure 2.8 – Schematic representation of LbL assembly by the dip-coating method. Adapted from [159].

In the spin-coating method, a spin coater is required to perform the LbL assembly, which comprises four main steps, as shown in Figure 2.9. The first step, the deposition, consists in depositing an excess amount of a charged solution onto a substrate to ensure full coverage of the substrate during the high-speed spinning step. The second stage, spin-up, occurs when the substrate is accelerated up to the desired spinning speed, usually around 3000 rpm. This stage is generally characterised by aggressive fluid expulsion (radial flow) from the substrate surface by the rotational motion. The fast spinning generates centrifugal forces that enable the spread of the solution and the quickly development, in seconds, of the first molecular layer on the full substrate area. The combination of spinning speed and time selected for this stage greatly contribute to tune the film thickness. The third step, spin-off, is characterised by gradual fluid thinning at a constant rate. In this stage, the rotation is continued until the desired thickness of the film is achieved. The uniformity of

the coating is mainly improved at this stage, due to the centrifugal forces from the rotational motion and the air shear forces from the air flow surrounding the sample. Finally, the fourth stage, evaporation, is represented by the loss of volatile species, while the substrate spins at constant rate. In fact, at this point, the solvent evaporation dominates the coating thinning behaviour, causing an increase of the solution concentration, which in turn leads to the fluid thickness reaching a point where the viscosity effects increase effectively freezing the coating in place. Subsequently, these cascade effects results in the formation of a dry thin film on the substrate [159,162–164]. The process above described is repeated until the desired number of layers was achieved. Similarly with the dip-coating procedure, between each PE deposition, it is performed a rising cycle to remove the surplus coating solution [159].

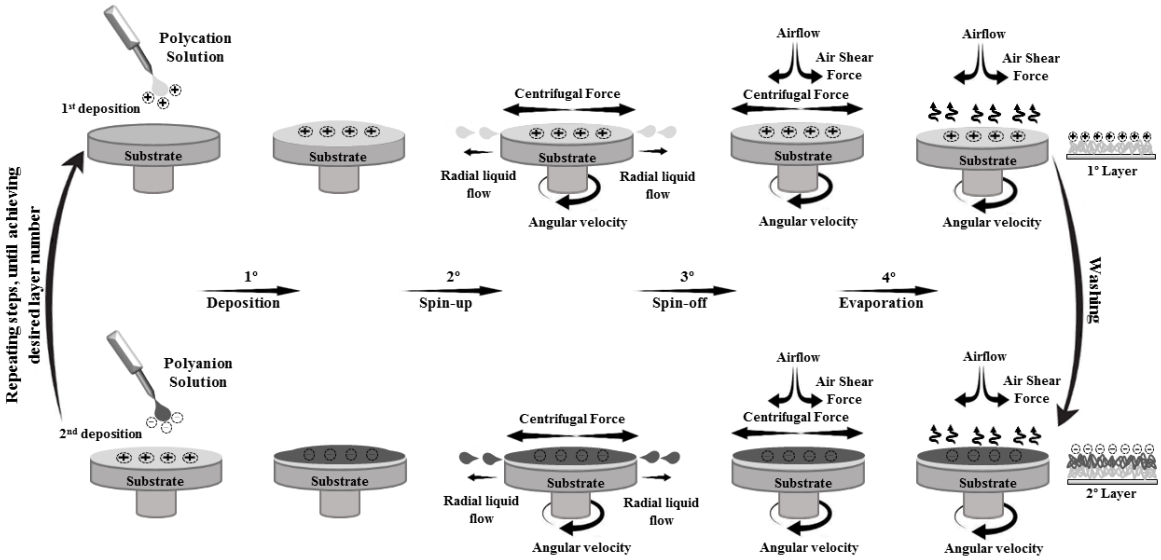

Figure 2.9 – Schematic representation of LbL assembly by the spin-coating method.

The third and fourth stages describe two processes that have the most impact on the final coating thickness, respectively viscous flow, and evaporation. Although these occur simultaneously through all times, at an engineering level, the viscous flow effects are considered to dominate first, while the evaporation processes dominate later [163,164].

The parameters chosen for the spin process, such as spinning speed, spinning time and acceleration, as well as other parameters, greatly depends on the nature of the PE solutions (concentration, viscosity, surface tension, and drying rate). Specifically, for higher polymer viscosity or the substrate area, a higher polymer volume will be needed to be dispensed. Also, higher spin speeds and longer spin times could generate thinner films. In addition, higher acceleration rate values may reduce coating coverage, as well as high drying rate values may reduce thickness uniformity [180], [181].

The spin-coating method has remarkable advantages comparatively to the dip-coating one. It can reduce both the polymer required for the deposition of each layer and the cost of LbL production, promoting also the increase of the film quality. Spin-assisted LbL films have demonstrated a more highly ordered coating structure and therefore, more uniform smooth surfaces, and higher biaxial strength and toughness [165,166]. Additionally, films produced by this method have shown less PE interpenetration between the layers yielding a linear growth of the thickness, rather than the exponential growth which is common in the LbL assembly by dip-coating [166].

Although spin-coating is a very promising method, it can only use flat planar substrates with nonporous or complex geometries. In addition, it is not applicable to construct LbL coatings onto very large surfaces, specially due to the difficulty of producing uniform films using aqueous solutions [166,167].

The LbL assembly of different multifunctional LbL coatings was carried out using the two previously described methods, dip-coating, and spin-coating.

Seven different PE solutions, containing CHT, HA, CHT-C*$_{18h}$, HA-DN*$_{4h}$, HA-DN*$_{36h}$, BGNPs and poly(ethylenimine) (PEI), were prepared. The concentration and function of each PE is shown in Table 2.1. All PE solutions were prepared in a 0.15 M sodium chloride (NaCl) solution. For the CHT solution, 2% (v/v) of acetic acid was added to the NaCl solution, since CHT is soluble only under acidic conditions. The PE solutions were prepared under stirring and allowed to dissolve overnight. Except for PEI, the pH of the PE solutions was adjusted to 5.5 using 0.5 M NaOH or 0.5 M HCl aqueous solutions under magnetic stirring. To avoid BGNPs agglomeration, the solutions containing the nanoparticles were kept under magnetic stirring and, periodically, subjected to an ultrasonic treatment during 10 – 15 minutes.

Table 2.1 – PE and respective concentration and function for the LbL assembly.

PE	[PE] (mg.mL^{-1})	Function
CHT	1 mg.mL^{-1}	Polycation
HA	0.5 mg.mL^{-1}	Polyanion
CHT-C*$_{18h}$	1 mg.mL^{-1}	Polycation
HA-DN*$_{4h}$	0.5 mg.mL^{-1}	Polyanion
HA-DN*$_{36h}$	0.5 mg.mL^{-1}	Polyanion
BGNPs	2.5 mg.mL^{-1}	Polyanion
PEI	5 mg.mL^{-1}	Initial precursor

As described in Table 2.1, HA, HA-DN*$_{4h,}$ HA-DN*$_{36h}$ and BGNPs were used as polyanion, while CHT and CHT-C*$_{18h}$ were used as polycation. PEI was used as an initial layer precursor, by immersing

each substrate for 20 min, prior to multilayer deposition. Therefore, after immersion in PEI, a polycation was used to initiate alternating deposition between oppositely charged PE. All substrates used in the experiments were rinsed with acetone, ethanol and osmotized water and, then, dried with a nitrogen flow before each use.

So, for the dip-coating technique, glass plates (3 mm thickness), round coverglasses (18 mm diameter) and SS and Ti disks (18 mm diameter and 3 mm thickness) were used as substrates. The substrates were alternately dipped in the oppositely-charged PE solutions with the pH adjusted to 5.5, to produce LbL coatings with 11 bilayers, i.e. 22 layers, and to be able to compare the results with those obtained in previous works [65,67]. The dipping time for CHT, HA and their respective conjugates (CHT-C and HA-DN) was 10 minutes, whereas for the BGNPs suspension it was 20 minutes. These dipping times were established after an optimization process in the two previously mentioned works [65,67], where it was verified by a quartz crystal microbalance (QCM) study that these corresponded to the moment when the PE adsorption reached equilibrium. In addition, a rinsing step was included for 5 min with 0.15 M NaCl solution, between the adsorptions of each PE.

For the spin-coating technique, round coverglasses (18 mm diameter) and SS and Ti disks (18 mm diameter and 3 mm thickness) were used as substrates. Spin-assisted LbL films were prepared using a spin-coater (WS-650Hzb-23NPPB-UD-3, LAURELL, USA), Figure 2.10, and following an optimization procedure described in appendix III. A 300 µL PE solution was dropped for the first bilayer, 200 µL for the second bilayer and 100 µL for the remaining bilayers, so that the entire surface area of substrate was covered. PE solutions were alternatively spin-coated at 3000 rpm spinning speed, 10 sec spinning time and 1300 rmp^2 acceleration, onto the substrates. Additional rising steps between the layer depositions were excluded, since the concentration of PE solutions used was low and the SEM analysis results showed no significant difference in the uniformity of the LbL coatings, using or not rising steps for these specific conditions.

Figure 2.10 – Spin coater instrument.

All experiments were performed at 25°C and distinct films were developed, as shown in Figure 2.11: the multifunctional LbL coatings containing $[CHT/HA/CHT/BGNPs]_5$ + [CHT/HA], $[CHT\text{-}C^*_{18h}/HA/CHT\text{-}C^*_{18h}/BGNPs]_5$ + $[CHT\text{-}C^*_{18h}/HA]$, $[CHT/HA\text{-}DN^*_{4h}/CHT/BGNPs]_5$ + $[CHT/HA\text{-}DN^*_{4h}]$, $[CHT/HA\text{-}DN^*_{36h}/CHT/BGNPs]_5$ + $[CHT/HA\text{-}DN^*_{36h}]$, $[CHT\text{-}C^*_{18h}/ HA\text{-}DN^*_{4h} /CHT\text{-}C^*_{18h}/BGNPs]_5$ + $[CHT\text{-}C^*_{18h}/ HA\text{-}DN^*_{4h}]$, $[CHT\text{-}C^*_{18h}/ HA\text{-}DN^*_{36h} /CHT\text{-}C^*_{18h}/BGNPs]_5$ + $[CHT\text{-}C^*_{18h}/ HA\text{-}DN^*_{36h}]$, and respective controls containing $[CHT/HA]_{11}$, $[CHT\text{-}C^*_{18h}/HA]_{11}$, $[CHT/HA\text{-}DN^*_{4h}]_{11}$, $[CHT/HA\text{-}DN^*_{36h}]_{11}$, $[CHT\text{-}C^*_{18h}/HA\text{-}DN^*_{4h}]_{11}$, $[CHT\text{-}C^*_{18h}/HA\text{-}DN^*_{36h}]_{11}$. These configurations were used to study the effect of the presence of BGNPs on multilayer films compared to polymeric films, both with or without conjugates (CHT-C or HA-DN), on the adhesive properties and bioactivity.

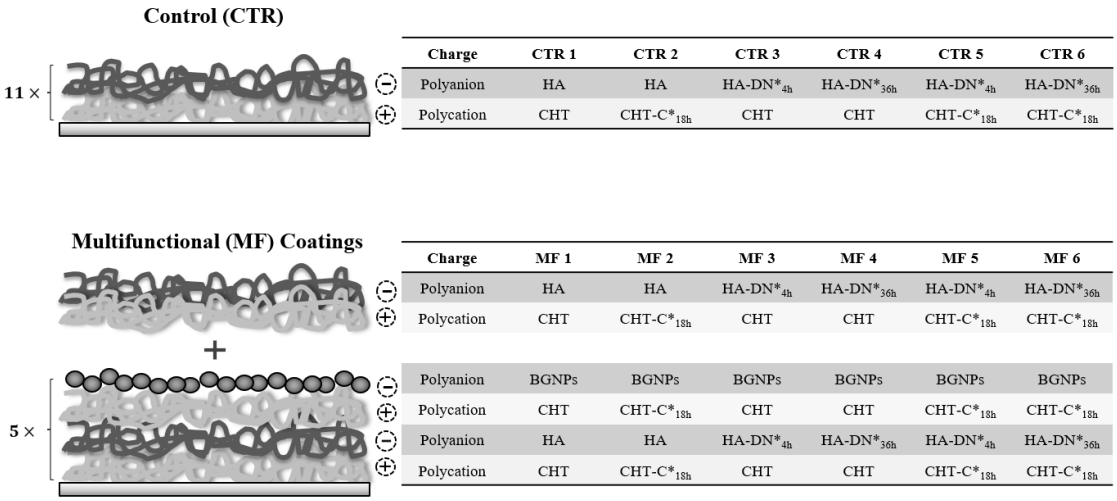

Charge	CTR 1	CTR 2	CTR 3	CTR 4	CTR 5	CTR 6
Polyanion	HA	HA	$HA\text{-}DN^*_{4h}$	$HA\text{-}DN^*_{36h}$	$HA\text{-}DN^*_{4h}$	$HA\text{-}DN^*_{36h}$
Polycation	CHT	$CHT\text{-}C^*_{18h}$	CHT	CHT	$CHT\text{-}C^*_{18h}$	$CHT\text{-}C^*_{18h}$

Charge	MF 1	MF 2	MF 3	MF 4	MF 5	MF 6
Polyanion	HA	HA	$HA\text{-}DN^*_{4h}$	$HA\text{-}DN^*_{36h}$	$HA\text{-}DN^*_{4h}$	$HA\text{-}DN^*_{36h}$
Polycation	CHT	$CHT\text{-}C^*_{18h}$	CHT	CHT	$CHT\text{-}C^*_{18h}$	$CHT\text{-}C^*_{18h}$
Polyanion	BGNPs	BGNPs	BGNPs	BGNPs	BGNPs	BGNPs
Polycation	CHT	$CHT\text{-}C^*_{18h}$	CHT	CHT	$CHT\text{-}C^*_{18h}$	$CHT\text{-}C^*_{18h}$
Polyanion	HA	HA	$HA\text{-}DN^*_{4h}$	$HA\text{-}DN^*_{36h}$	$HA\text{-}DN^*_{4h}$	$HA\text{-}DN^*_{36h}$
Polycation	CHT	$CHT\text{-}C^*_{18h}$	CHT	CHT	$CHT\text{-}C^*_{18h}$	$CHT\text{-}C^*_{18h}$

Figure 2.11 – Schematic illustration of the different multifunctional (MF) and control (CTR) LbL coatings.

Multifunctional films ending with an adhesive layer were chosen since in a previous work [67], they were shown to have higher adhesive strength when, compared to the multifunctional films ending in BGNPs.

At the end of each procedure, the LbL coatings were subjected to 3 rising steps in ultrapure water to remove any salt deposition derived from the LbL deposition process. The LbL were then allowed to dry at room temperature, overnight.

2.2 Characterization Techniques

2.2.1 Ultraviolet-Visible Spectroscopy

The DS (%) of catechol groups in the conjugates were determined by ultraviolet-visible (UV-Vis) Spectroscopy, in a quartz microplate with 96 wells, using a Synergy HT Multi-Mode Microplate Reader (BioTek Instruments, U.S.A.) for measuring the absorbance (Abs) between 200 and 350 nm. Solutions of HA-DN and CHT-C with different concentrations, 0.5, 1, 2, 3, 4, 5 $mg.mL^{-1}$ in 0.15 M NaCl, were prepared for the UV-Vis analysis. 100 μl of test solution was used in each well and NaCl was used as blank.

The Synergy HT Multi-detection reader is a robotic-compatible microplate reader that can measure Abs, fluorescence, and luminescence. Microplate-based assays make determinations on large numbers of samples, any plate format up to 384-well, and provides temperature control up to 50° C and shaking as standard features. The Abs measurements are given in a single-channel system that measures Abs from the UV to the near IR range. The monochromator-based Abs optics, illuminated by a xenon-flash lamp, has a wavelength range of 200-999 nm and can perform spectral scans in increments of 1 nm. The monochromatic light is split into an experimental and a reference channel. The experimental channel is focused onto the microplate well sample and the reference channel is directed to the reference detector. The unabsorbed light is then focused onto a detector, located opposite the light source, on the other side of the microplate well [168].

The light detector measures the intensity of the transmitted light through the wells, aiming to quantify the Abs, A, given by equation (2.1) [169].

$$A = \log_{10} \frac{I_0}{I} \tag{2.1}$$

Where I_0 is the intensity of the incident light and I is the intensity of light transmitted through the wells containing the sample [169].

Unlike UV/VIS spectrophotometers, where samples are read through cuvettes or tubes with a horizontal (cross-sectional) light path, the microplate readers use a vertical light beam that results in a pathlength dependent on the volume of fluid in each well [168], Figure 2.12.

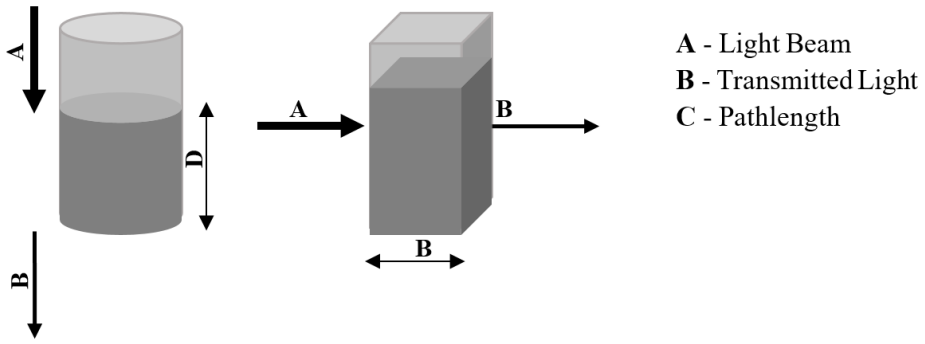

Figure 2.12 – **(**Left) Variable pathlength in a microplate well. (Right) Fix pathlength in a cuvette (1cm).

2.2.2 Rheological measurements

The Kinexus Rheometer is a rotational rheometer system that applies controlled shear deformation to a sample under test, to enable measurement of various rheological characteristics. Here, rheology represents an ideal tool for discerning structural and compositional changes of materials, as well as enabling to engineer its rheological properties to achieve the desired performance responses. Common test modes are rotational (or flow) to measure shear viscosity, and oscillation to measure dynamic material properties such as viscoelastic modulus and phase angle. It also allows the evaluation of other rheological properties, including yield stress, thixotropy, creep and recovery and stress relaxation [170,171].

The sample is placed into a gap between two geometries, interchangeable by concentric cylinder, cone-plate, and parallel plate, specially designed to impose simple shear flow when rotated. The choice of the appropriate geometries is made considering the material properties and the ideal conditions of a process or in situ application [170–172].

In the cone-plate geometry, torque is measured as a consequence of the drag of fluid on the cone. This system allows a constant shear rate across the entire measuring gap, the use of small sample quantities, and the study of a wide viscosity range with high shear rates. The cone angle is chosen such that for each point on the cone surface, the ratio of angular speed and distance to the

plate is constant. For low viscous samples, a cone with an angle between 0.5 ° and 1.0 ° and diameter between 50 mm and 60 mm is generally used [170–172].

In the cone-plate measuring system, viscosity (η, Pa.s^{-1}) is given by equation (2.2), where shear stress (τ, Pa) and shear rate (γ, s^{-1}) values are obtained through the torque (T, N.m^{-1}) and rotor speed (n, min^{-1}) measurements [171].

$$\eta = \frac{\tau}{\gamma} \tag{2.2}$$

In addition, τ and γ are given by equations (2.3) and (2.4), respectively [171]:

$$\tau = \frac{3}{2\pi r_c^3} * T \tag{2.3}$$

$$\gamma = \frac{1}{\theta} * \Omega \tag{2.4}$$

Where r_c (m) is the cone radius, θ (rad) is the cone angle and Ω (rad.s^{-1}) is the angular velocity. In turn, Ω is given by equation (2.5) [171].

$$\Omega = \frac{2\pi}{60} * n \tag{2.5}$$

The rheological properties of the different polymers used were characterized on a Kinexus Pro Rheometer (Malvern Instruments Ltd, UK) fitted with cone-plate geometry, Figure 2.13. This geometry was chosen due to the possibility of studying polymers with wide viscosity range. Other geometries can be used on a Kinexus Pro Rheometer, such as plate-plate, which is normally used in oscillatory tests or tests at low shear rates, and concentric cylinder, which is ideal for dispersed systems and low viscous samples [170–172]. A cone with 40 mm diameter and 4° angle (CP4/40: SR 1772SS) and a plate with 65 mm diameter (PL65: S1425SS) were used.

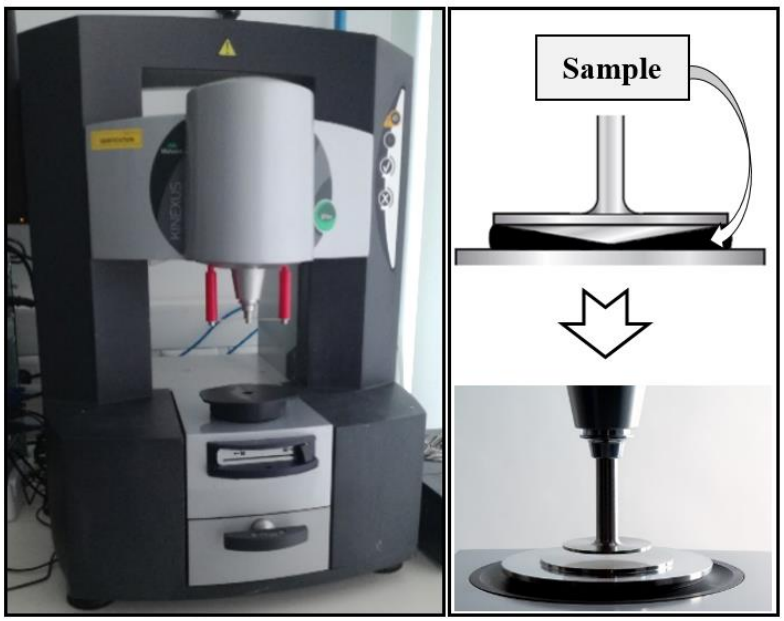

Figure 2.13 – **(**Left) Kinexus Pro Rheometer. (Right) Cone-plate geometry.

Rotational measurements of CHT, HA, CHT-C*$_{18h}$, HA-DN*$_{4h}$ and HA-DN*$_{36h}$ solutions at different concentrations of 0.5, 1, 2, 3 mg.mL^{-1}, in 0.15 M NaCl, were made. The steady-state flow measurements were performed under controlled-stress conditions where the torque amplitude was imposed by using a logarithmic ramp of shear rate ranging from 10 to 100 s^{-1}. All experiments were performed at a controlled temperature of 25 °C, and results represent the average of three measurements. Measured data were registered with rSpace for Kinexus Pro 1.7 software.

2.2.3 Zeta Potential Measurements

When particles are in contact with aqueous solutions an interfacial charge is formed, which leads to the rearrangement of the free ions in the solution. The existence of an electric charge on the particles surfaces attracts oppositely charged ions giving rise to an ionic atmosphere called electrical double layer. Thus, the electrical double layer comprises two regions of charge. The first one refers to an immobile layer of ions, compact layer or Stern layer, which adhere to the particle surface, and the second one to a mobile layer of oppositely charged ions, diffuse layer, which are attracted by the immobile layer [173,174].

Within the diffuse layer there is a point called as shear level or slip plane, where the electrical potential difference between the dispersion medium and the Stern layer is called the zeta potential, ζ Figure 2.14 represents the zeta potential of a negatively charged particle [175]. Zeta potential in the diffuse layer decreases exponentially approaching zero with increasing of the distance from the particle

surface. As this potential approaches to zero, the particles tend to aggregate giving an indication of system stability [175].

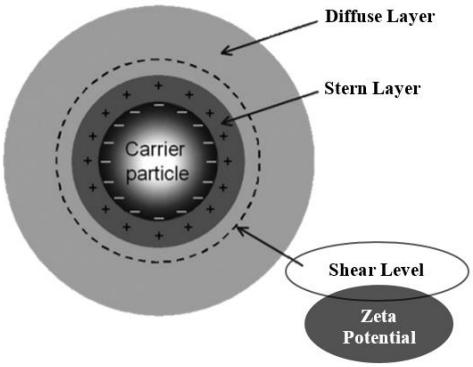

Figure 2.14 – Schematic representation of the zeta potential of a negatively charged particle. Adapted from [175].

A value of 25 mV (positive or negative) can be taken as the arbitrary value to indicate whether a surface has low or high charge. Thus, if the zeta potential (negative or positive) is higher than 25 mV, the particles tend to repel and the dispersion will be stable. On the other hand, if the zeta potential (negative or positive) is lower than 25 mV, the attraction forces are stronger than the repulsion ones, leading to the particle aggregation [176].

The zeta potential of natural polymers and nanoparticles were measured to confirm the success of multilayer films construction. For this, it is expected that polyelectrolytes such as CHT and its derivates (CHT-C*$_{18h}$) have a positive charge, and HA and its derivates (HA-DN*$_{4h}$ and HA-DN*$_{36h}$), as well as BGNPs have a negative charge, in the same order of magnitude. These measurements were performed by a Zetasizer equipment (Nano ZS, Malvern, UK), at 25°C, and the results were given as an average of 3 measurements for each 0.5 mg.mL^{-1} solution in 0.15M NaCl solution. Immediately prior to measurement, the BGNPs solution was dispersed for 15 minutes in the ultrasonic equipment to prevent nanoparticle agglomeration.

2.2.4 Quartz Crystal Microbalance with Dissipation Monitoring: Multilayer Films Modelling

Quartz crystal microbalance with dissipation monitoring (QCM-D), Figure 2.15, is an accurate technique which make use of piezoelectric quartz crystals to detect adsorption of molecules, at nanoscale, by measuring frequency changes [177]. Each side of the quartz crystals is coated by gold electrodes which are excited at multiple overtones, 1, 3, 5, 7, 9, 11, and 13, corresponding respectively, to 5, 15, 25, 35, 45, 55, and 65 MHz fundamental resonant f [178]. According to Sauerbrey equation, in vacuum, when a thin and rigid mass is deposited onto the crystal surface, there is a decrease in resonant frequency change [179]. However, in the case of viscoelastic materials, the adsorbed mass does not fully couple the crystal's oscillation and dampens the oscillation. Thus,

from the decay monitoring of the crystal's oscillation is quantified the dissipation which represents the viscoelastic properties of the adsorbed mass [178].

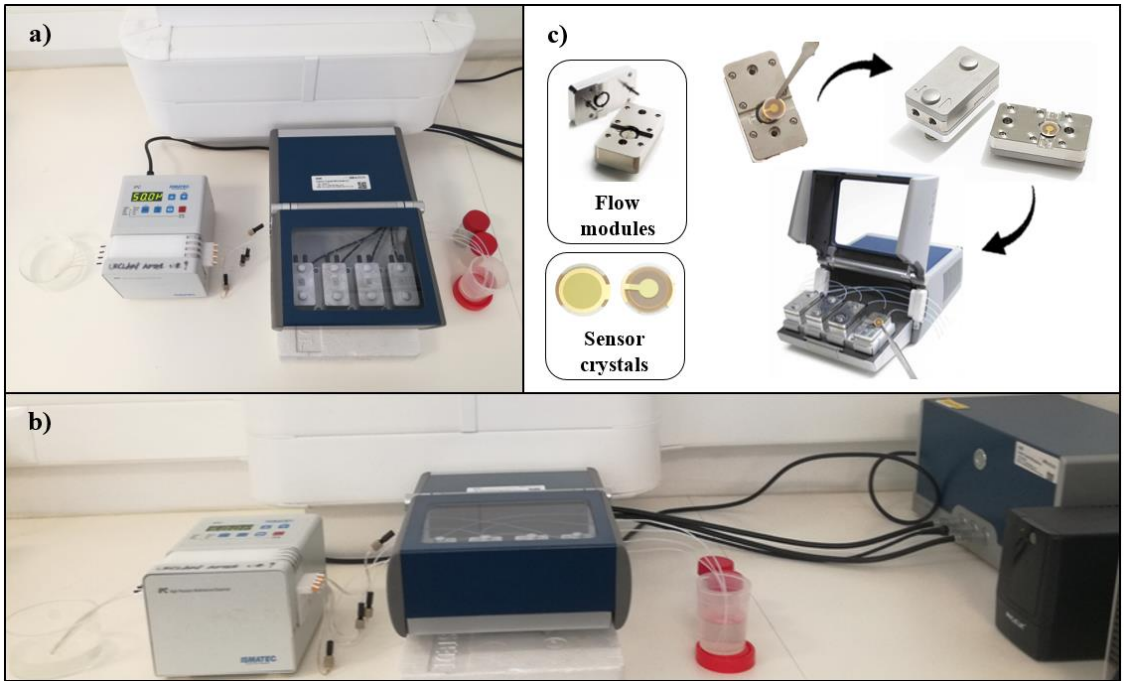

Figure 2.15 – a) and b) QCM-D system. c) Schematic representation of the mounting and the physical parts of the QCM-D system: flow modules, sensor crystals and flow chamber system.

So, through the QCM-D monitoring, it is possible to simultaneously measure the adsorbed amount, given by the normalized resonance frequency ($\Delta f/\nu$) of each overtone to the fundamental resonant, and the variation of the viscoelastic properties, given by energy dissipation (ΔD), of the multilayer film in real time [178].

The build-up of multilayered films with different materials was monitored in situ by QCM-D (Q-sense, E4 system, Sweden) onto gold-coated quartz crystals. The quartz crystals were previously cleaned in an ultrasound bath with sequential sonication for 5-10 min in: 2% (v/v) acetic acid solution, mixture of osmotized water, ammonia hydroxide and hydrogen peroxide at 75° C, acetone, isopropanol, ethanol, and ultrapure water. The crystals were then dried with flowing nitrogen gas and treated with UV/Ozone cleaner (Bioforce Nanoscience, ProCleaner 220) for 10 min.

To ensure that the crystals are perfectly clean (null frequency), all experiments started with a 0.15M NaCl baseline. Adsorption took place at 25 °C, pH 5.5 and at a constant flow rate of 50 µL.min^{-1} using a peristaltic pump. LbL coatings were produced using fresh solutions prepared in 0.15 M NaCl and starting with injection of CHT (1 mg.mL^{-1} with 2% (v/v) of acetic acid) or CHT-C*$_{18h}$ (1 mg.mL^{-1}) used as polycations, while HA (0.5 mg.mL^{-1}), HA-DN$_{4h}$* (0.5 mg.mL^{-1}), HA-DN$_{36h}$* (0.5 mg.mL^{-1}), and BGNPs (2.5 mg.mL^{-1}) acted as polyanions and were used as ended-polymer layer. Before the QCM

experiments, the BGNPs suspension was dispersed in an ultrasonic water bath (25°C) for 15 to 20 minutes to avoid agglomeration and the precipitation of nanoparticles.

The injection of the polymers was standing for 10 min and the nanoparticles for 20 min to allow the adsorption until the equilibrium was achieved in QCM-D monitoring. A rising step of 5 min, with 0.15M NaCL solution, between the polyelectrolyte adsorptions was include. These steps were repeated to form a total of 20 layers. The thickness of the multilayer films was estimated using the Voigt model in the Q-Tools software (Q-Sense). According to this model, the Δf and ΔD are given by equations (2.6) and (2.7), respectively [180]:

$$\Delta f \approx -\frac{1}{2\pi\rho_0 h_0}\left\{\frac{\eta_B}{\delta_B}+h_L\rho_L\omega-2h_L\left(\frac{\eta_B}{\delta_B}\right)^2\frac{\eta_L\omega^2}{\mu_L^2+\omega^2\eta_L^2}\right\} \quad (2.6)$$

$$\Delta D \approx \frac{1}{\pi f\rho_0 h_0}\left\{\frac{\eta_B}{\delta_B}+2h_L\left(\frac{\eta_B}{\delta_B}\right)^2\frac{\mu_L\omega}{\mu_L^2+\omega^2\eta_L^2}\right\} \quad (2.7)$$

Where ω is the angular frequency of the oscillation, ρ_0 and h_0 are the density and thickness of the crystal, respectively, η_B the solution viscosity, δ_B ($=(2\eta_B/\rho_B\omega)^{1/2}$) the viscous penetration depth of the shear wave in the solution, ρ_B the solution density, and h_L, ρ_L, η_L and μ_L the thickness, density, viscosity and elastic shear modulus of the adsorbed layer, respectively [178,180].

From the modelled results obtained by the previous presented equations, the QTools software compared them with Δf and ΔD experimental values and it found the best fitting using a Simplex algorithm (Total ChiSqr) through the minimum in the sum of the squares of the scaled errors. For this, ρ_B, η_B and ρ_L should be changed to get the lower error possible [178]. In this study, a fluid density of 1000 kg.m^{-3}, a fluid viscosity of 1 mPa.s and a layer density of 1200 kg.m^{-3} was assumed. In addition, Δf and ΔD were fitted for three overtones, in which the 1st and 13th overtones were disregarded since the first one is very sensible to the piezoelectric effect and the second one departs from the fundamental frequency having more associated error.

2.2.5 Fourier Transform Infrared Spectroscopic Imaging Analysis

Fourier transform infrared (FT-IR) spectroscopy is a quick and easy technique for analysing materials that provides qualitative information about the atom vibration in a compound. The vibrational mode is a characteristic of each molecular group and is caused by the transitions between vibrational energy levels of the molecules, by stretching or bending of bonds. These transitions cause the

appearance of bands at a specific frequency ranging from 4000-400 cm^{-1} in the infrared (IR) spectrum, which depends on the relative masses of the atoms, bond strength, atom geometry and dipole moment of the molecule [169].

In the FT-IR equipment a single pulse of IR radiation is transmitted by a source to an interferometer, which interacts with the sample and reaches a detector that measures the energy absorbed by the molecules at each frequency. The interferometer is an optical device that has a semi-transparent moving mirror (beam splitter) which separates a single light beam into two light beams, one directed to the sample and another to the system, where it is then recombined in a single beam leaving the interferometer. The obtained attenuation beam is converted into frequency domain using the Fourier transform algorithm, causing corresponding peaks to appear in a specific position of the absorption spectrum [181,182].

Since a single beam is used in modern IR spectrometers, the analysis begins by collecting a background spectrum which is then subtracted to the sample spectrum to remove, for example, the contribution of carbon dioxide and atmospheric water [169].

FTIR analysis can be performed by three different modes, namely transmittance, reflectance and attenuated total reflectance (ATR). In the transmittance mode, a transparent matrix to the IR beam, usually KBr, is used to attenuate the transmitted beam after passing the sample. The obtained spectrum is an absorption pattern for the entire volume of the sample. The reflectance mode is useful for *in situ* analysis of materials that strongly absorb IR radiation and when the surface of the sample needs to be analysed. On the other hand, ATR uses the total reflection angle to further investigate the chemical composition of smooth surfaces [181,182].

The main disadvantage of this type of spectroscopy is the water content of samples, which is revealed by wide and intense peaks, that could hide peaks of dissolved solutes. Also, the presence of mixtures may cause difficulty in analysis due to overlapping of specific bands resulting in a complex spectrum [181].

FT-IR imaging analysis was performed using a Perkin-Elmer Spectrum Spotlight 300 FT-IR Microscope System, Figure 2.16, in the reflectance mode for surface analysis of distinct LbL coatings onto different substrates.

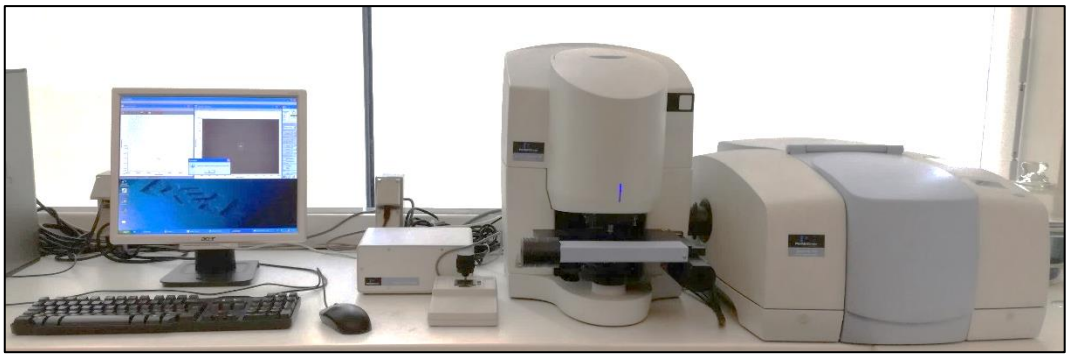

Figure 2.16 – Perkin-Elmer Spectrum Spotlight 300 FT-IR Microscope System.

FT-IR maps were constructed by a spectrum collected in the continuous scan mode for a spectral range 4000–720 cm^{-1} and sample areas of 500×500 μm^2. Each spectrum was collected with an average of 15 repetitive scans with a spectral resolution of 16 cm^{-1}. Spectra were integrated by taking the areas under the curve between the limits of the peaks of interest. The chosen region for CHT identification corresponds to C=O stretching of amide I centred at approximately 1650 cm^{-1} and the C=O stretching of carboxylic acid at about 1730 cm^{-1} was chosen for HA [183,184]. The characteristic peak of CHT corresponding to the amine deformation vibration, N–H bending vibration, centred at 1590 cm^{-1} could not be used due to overlapping with a peak of the amide II present in both polysaccharides [185]. On the other hand, the chosen region for catechol group identification corresponds to out-of-plane C–H bending vibration centred at 740 cm^{-1} and C–H stretching vibration centred at 3052 cm^{-1}, both belonging to the aromatic C–H group. The C=C vibrations peaks of the aromatic ring, approximately between 1466 and 1515 cm^{-1}, were not chosen due to overlapping with characteristic peaks of the polysaccharides. Furthermore, for the BGNPs identification the chosen region was the silicate absorption bands, Si–O–Si, assigned to the peaks 1085 and 800 cm^{-1} corresponding to asymmetric stretching and symmetric stretching vibration, respectively [157].

2.2.6 X-Ray Diffraction Analysis

X-ray diffraction (XRD) is a microstructural characterization technique based on the observation of the scattered intensity of an X-ray beam on a sample providing detailed information about the chemical composition and crystallographic structure of the materials. It is primarily used for identification of phases, amorphous or crystalline, identification of polymorphic forms (“fingerprints”), determination of the lattice parameter, determination of the orientation, shape, size, and internal stress of crystals, as well as for quantification of crystallinity percentage of a sample [186].

X-rays are electromagnetic waves with high energy, ranging from 100 eV to 100 keV, and very short wavelength, which are found in the electromagnetic spectrum between γ-rays and ultraviolet

radiation. They are formed when an interaction between an electrons external beam and electrons belonging to shells of an atom occurs [186,187].

An X-ray diffractometer generates X-rays when an electron beam, produced by a voltage difference between two electrodes, is accelerated towards the metallic target (anode) from a heated tungsten filament (cathode) inside a vacuum tube. So, as the electrons collide with the atoms of the metal, a deceleration occurs that leads to the beam diffraction generating consequently the X-rays [186,187].

Once the X-rays are scattered, the propagation of the electromagnetic wave, reemitted by the electron, in different directions depends on the crystalline structure and the radiation wavelength. Bragg's law describes this condition, Figure 2.17.

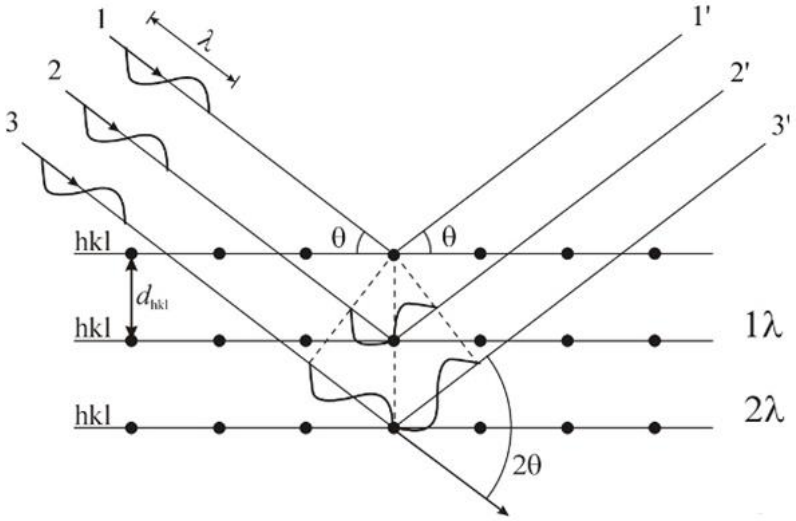

Figure 2.17 – Illustration of Bragg's Law [186]**.**

Bragg's law is represented by equation (2.8) relating the X-rays wavelength, λ, and the diffraction order, n, to the diffraction angle, θ, and the spacing between atomic planes of a unit cell (lattice spacing, d_{hkl}) in a crystalline sample. The Miller indices, *hkl*, characterize the orientation of the atomic planes and are associated with the unit cell dimension [187].

$$n\lambda = 2d_{hkl}sin\theta \tag{2.8}$$

The XRD analysis provides a plot with a series of peaks representing a diffracted X-ray from a set of planes, with different intensities. When properly interpreted, by comparison with standard reference patterns and measurements, the peaks positions allow the identification of the crystalline form [187].

The crystalline structure of the LbL coatings was determined by XRD experiments on a Bruker AXS D8 Discover operated at 40 kV and 40 mA using Cu Kαradiation (λ = 1.54060 Å). The detector

was scanned over a range of 2θ angles from 15° to 60° at a speed of 0.04°/1s. The identification of crystalline phases was achieved using an analytical software EVA and they were indexed using the ICDD database (International Centre for Diffraction Data).

2.2.7 Water Contact Angle Measurements

Coatings must provide a suitable surface for the apposition and growth of bone tissue. Thus, coating topography has an important effect on cellular response and depends both on physical and chemical characteristics of the surface. Surface chemical characteristics such as wettability have been linked to changes in protein adsorption and cell growth *in-vitro* [188,189]. One of the most widely used techniques for assessing the wettability of a material is by measuring the water contact angle (WCA). This analysis is given by Young's equation, which assuming a perfectly flat surface, calculates the angle between the material surface and the line tangent to the radius of a dispensed water drop [188,190]. Depending on the WCA, the surfaces are characterized by their hydrophilicity (WCA<90°) and hydrophobicity (WCA>90°), Figure 2.18.

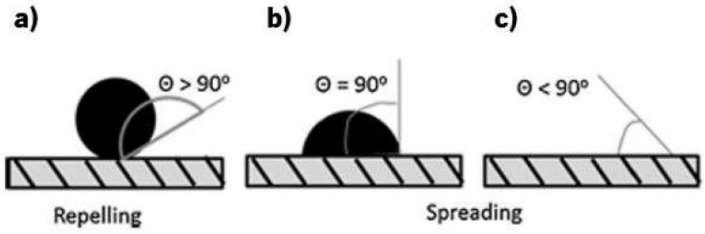

Figure 2.18 – Schematic representation of WCA measurements on a solid surface: (a) hydrophobic surface; (b) and (c) hydrophilic surfaces [192].

Some studies have shown that more hydrophilic coatings have better ability to support the formation of an apatite-like layer upon its surface [188]. However, it is now been well accepted in biomaterial community that very hydrophilic or hydrophobic surfaces are not good for cell attachment, rather, surfaces with moderate wettability are able to adsorb a proper amount of proteins while preserving their natural conformation, resulting in higher cell responses [189,191].

The wettability of the coatings was assessed by the sessile drop method using an OCA15plus Goniometer equipment (DataPhysics, Germany). For each coating surface, 3 measurements were made, using 3 μL droplets of osmotized water dispensed by a motor-driven syringe. The measurements were performed at room temperature and the pictures were taken immediately after the drop contacted the surface. The results were treated using the SCA20 software.

2.2.8 Scanning Electron Microscopy coupled with Energy Dispersive X-Ray Spectroscopy

The scanning electron microscopy (SEM) is a non-destructive equipment that can be used to analyse several materials on a nanometer-to-micrometer scale. The fact that it has a large depth of field makes the SEM a high resolution electronic microscope, which is essential for obtaining topographic images with a 3D aspect and with a large magnification range [193]. Besides the topography, SEM allows to obtain information about the morphology, composition and crystallographic nature of the analysed specimens [194]. Although several materials can be studied using this microscopy technique, polymers and biological samples have low conductivity and may degrade chemically due to electron-induced reactions. Thus, in these cases, a thin conducting layer of carbon, gold, or platinum is required [193].

SEM have two main components, the electron column and the control console or electronics console. The first one contains an electron gun and electron lens working in a vacuum, while the control console has the electron beam control and other electronic elements [193]. In SEM, Figure 2.19, a highly energetic electron beam, created by the electron gun, is focused by a series of condenser lenses and an objective lens to scan the sample and form a high-resolution image by the interaction between the electron beam and the electrons in the sample. The three-dimensional interaction volume, resulting from the interaction of the electron beam with the specimen atoms, is influenced by the electron beam energy, specimen nature, composition, and sample preparation. The imaging process is performed using the electrons emitted from the sample, where different signals can be collected by different types of detectors giving rise to different information. Among them, the secondary electrons provide information about the topography of the sample, and backscattered electrons give information about the atomic number [193,194]. Also analytical X-rays, provided by SEM, can be analysed by energy dispersive X-ray spectroscopy (EDS) providing qualitative and quantitative information on specimen composition [194]. In this analysis, each element has its own characteristic X-ray peaks (qualitative analysis), which in turn are more intense the higher its concentration (quantitative analysis) [193,195].

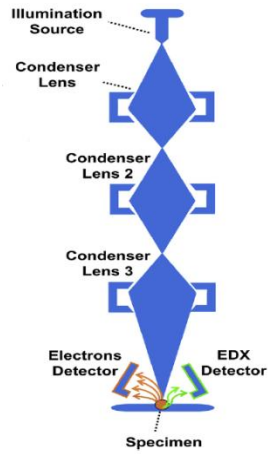

Figure 2.19 – Scheme showing the optical system of SEM. Adapted from [194].

SEM (JSM-6010 LV, JEOL, Japan) equipment was used to evaluate the surface topography of the LbL coatings. Before analysis, the samples were sputtered with a thin platinum layer, using a sputter coater EM ACE600 (Leica Microsystems, Germany). SEM is equipped with EDS (INCAx-Act, PentaFET Precision, Oxford Instruments), which was used to detect the chemical elements present on the surface of coatings, during *in-vitro* bioactivity tests.

2.2.9 Adhesion Tests

The adhesive strength of LbL coatings using glass plates as the substrate was evaluated following the ASTM D1002 standard, "Apparent Shear Strength of Single-Lap-Joint Adhesively Bonded Metal Specimens by Tension Loading". ASTM D1002 is a standard test method widely used to determine the apparent shear strengths of adhesives for bonding metals when tested on a standard single-lap-joint specimen [196].

According to ASTM D1002 standard, the dimensions and form of the specimens should follow specific conditions of preparation and test as shown in Figure 2.20 [196,197]. The recommended thickness of the substrates is 1.62 ± 0.125 mm with a corresponding overlap length of 12.7 ± 0.25 mm. In some cases, the overlap length values can be changed according to the thickness and type of substrate [196].

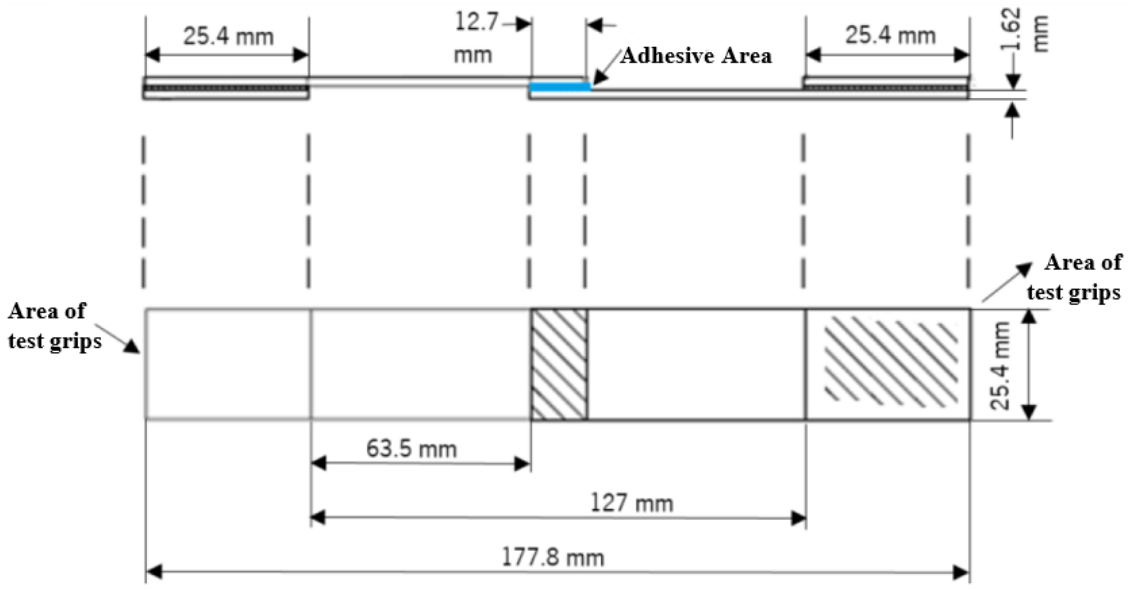

Figure 2.20 – Schematic representation of a single-lap-joint (dimensions in mm). Adapted from [196,197].

To measure the adhesive strength of the LbL coatings on glass substrates, adhesion tests were performed using a universal mechanical testing machine (Instron 5543, USA) with a 1 kN load cell. Lap shear tests were accomplished following an adaptation of the procedure described in the ASTM D1002 standard.

Immediately after the LbL deposition by dip coating method, pairs of glass plates were put in contact with an overlapping area of $15 \times 20\ mm^2$. The specimens were tightly clamped using metal binder clips, Figure 2.21 (a), and maintained at 37°C overnight. To perform the adhesion experiments, each end of the specimens was placed in the grips of the mechanical testing machine, as shown in Figure 2.21 (b). At the upper specimen edge an axial tensile load was applied, at a constant cross-head speed of 5 $mm.min^{-1}$ to be pulled until the detachment of the specimens. Five specimens of each condition were tested to calculate the mean and standard deviation (SD) values of the adhesion strength.

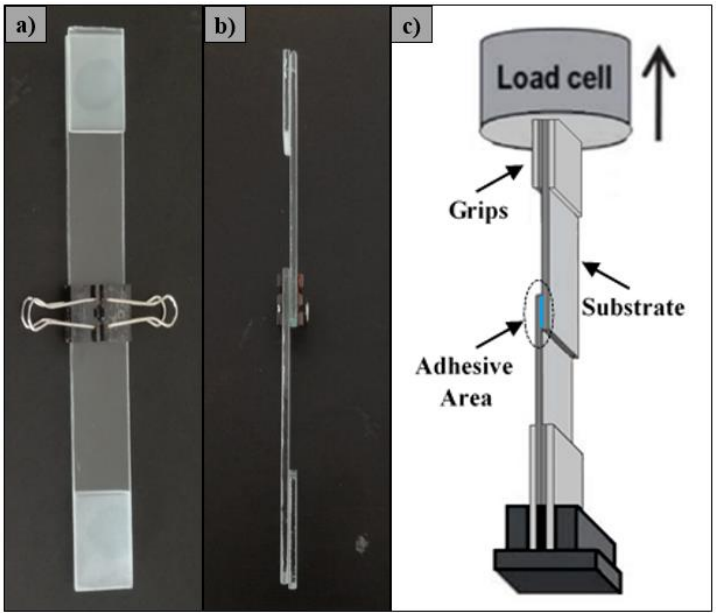

Figure 2.21 – a) Frontal and b) lateral view of a single-lap-joint used in this study. c) Schematic representation of single-lap-joint using a mechanical testing machine. Adapted from [198].

The testing software used was the Bluehill2 (INSTRON Corporation), and stress-strain curves was obtained for each testing condition from the maximum tensile stress (σ_{Tmax}) and the maximum tensile strain (ε_{Tmax}) calculations. The σ_{Tmax} is the maximum stress that the film can support without detachment, being obtained from the load applied (F) data, acquired during the test, and the overlapping area (A_0), equation (2.9). The ε_{Tmax} corresponds to the strain value reached for the σ_{Tmax} and is obtained from the length change (ΔL) data, acquired during the test, and the initial length (L_0), equation (2.10) [67].

$$\sigma_{Tmax} = \frac{F(N)}{A_0\ (m^2)} \tag{2.9}$$

$$\varepsilon_{Tmax} = \frac{\Delta L(m)}{L_0\ (m)} \tag{2.10}$$

2.2.10 Atomic Force Microscopy Analysis

Atomic Force Microscopy (AFM) a three-dimensional topographic technique used to measure local surface properties such as roughness, friction, adhesion, viscoelasticity, and stiffness at nanoscale [199]. This topographic analysis is based on the detection of forces acting between a sharp tip and the surface of the sample, Figure 2.22 (a). The tip is attached to a flexible cantilever, which acts as a spring, and is mounted on a piezoelectric scanner. The piezoelectric scanner can move in

all three-dimensions, providing local scanning with good resolution of the sample surface. Topography mapping and surface-tip interactions monitoring are acquired by measuring the magnitude of laser-beam deflection changes. In this way, a laser-beam is focused on the cantilever causing its deflection. The resulting reflected laser-beam is detected by position-sensitive detectors (photodiodes) that converts these deflections into continuously recorded voltages signals and, then, it can be visualized on the computer in real time [199–201].

AFM can be divided into two operational modes, static and dynamic. The static mode is characterized by quasi-static oscillation of the cantilever and includes contact mode and friction force microscopy. On the other hand, the dynamic mode is characterized by the oscillation of the cantilever near or at its resonance frequency and is categorized in terms of cantilever deflection and excitation mechanism including tapping mode, non-contact, force modulation mode, atomic force acoustic microscopy mode, torsional resonance mode, lateral excitation mode and combined normal and lateral excitation mode [202].

The most commonly used AFM imaging modes include contact mode and tapping mode. In contact mode, the tip maintains constant contact with the sample surface, during the scan, Figure 2.22 (b), to generate a topographical image. In contrast, in tapping mode the cantilever oscillates continuously, translating into intermittent contact of the tip with the sample surface. Thus, as the height of the sample changes, the amplitude of the cantilever oscillations changes, Figure 2.22 (c). In addition, of obtaining a topographical image, this method allows the monitoring of the oscillation phase to acquire changes in the mechanical properties of the sample, such as friction, adhesion, and stiffness. Furthermore, it is more suitable for samples that can be damaged or deformed using the contact mode [200,201].

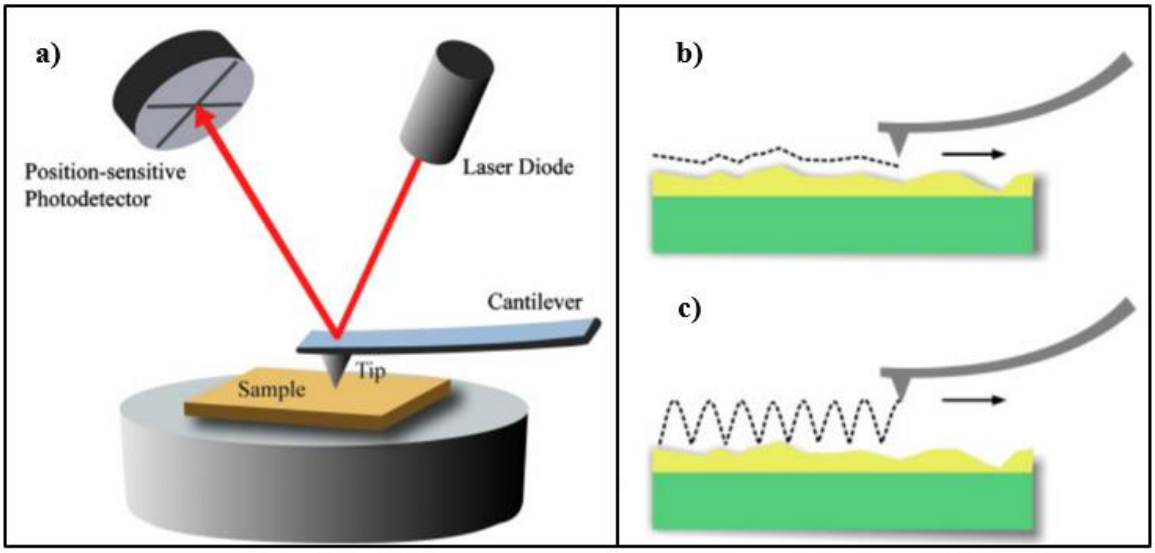

Figure 2.22 – a) Illustration of AFM work principle. Representation of different AFM operating modes: b) contact mode and c) tapping mode. Adapted from [200].

Amplitude parameters are the main parameters that can be obtained from the AFM analysis to characterize the surface topography of a sample. Among these, the average roughness (R_a) and the root mean square roughness (R_q) are the most widely used, being shown in the equations (2.11) and (2.12), respectively [203].

$$R_a = \frac{1}{L}\int_0^L |Z(x)|dx \tag{2.11}$$

$$R_q = \sqrt{\frac{1}{L}\int_0^L |Z^2(x)|dx} \tag{2.12}$$

Where $Z(x)$ is the function that describes the surface profile in terms of height (Z) and position (x) of the sample over the evaluation length (L), Figure 2.23. R_a represents the arithmetic mean absolute values of height of the surface profile $Z(x)$, while R_q is a function that describes the mean squared absolute values of surface profile making it a more sensitive parameter [203].

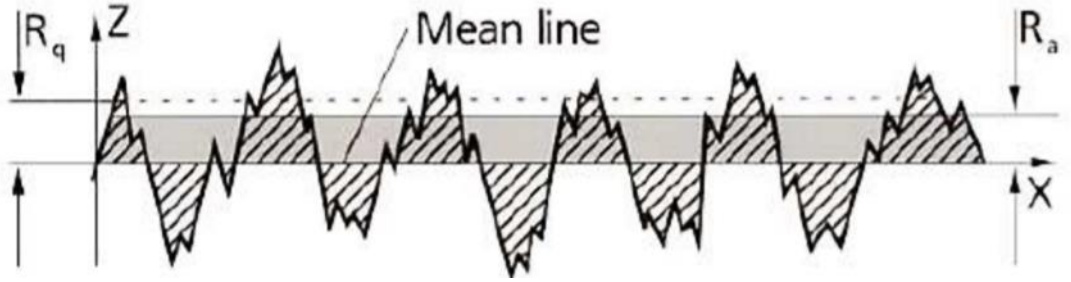

Figure 2.23 – Representation of a surface profile ($\boldsymbol{Z(x)}$) showing the $\boldsymbol{R_a}$ and $\boldsymbol{R_q}$ parameters based on the mean line [203].

The surface roughness of the LbL coatings in dried state was examined using a bio-AFM. All AFM images were acquired with a JPK NanoWizard III AFM system (JPK Instruments AG, Berlin, Germany), in tapping mode (AC mode) AFM operated in air. A commercial silicon (Si) probe (Acta probe) with aluminium (Al) coating on the cantilever backside, and with a spring constant of 40 N/m was used. The topography of the LbL coatings was analysed with a resolution of 512 x 512 pixels, at line rates of 0.5 to 1 Hz, and resonance frequency around 300 kHz. AFM images with 20 x 20 μm^2 were obtained and at least three measurements of the surface roughness were performed, followed by R_q and R_a calculations.

2.2.11 *In-Vitro* Bioactivity Studies

Bioactivity is defined as the ability of an implanted material to create a bond with living tissues. BGs, as already mentioned, are materials with great potential for bone regeneration due to their ability to naturally bond to living bone, without the development of fibrous tissue, and to induce the precipitation of a bone-like apatite layer on their surface. This precipitation can be observed when BGs are used in *in-vivo* applications or when in contact with physiological fluid [104,107,108,113]. In fact, the presence of this apatite layer is crucial for any implanted material to form a bond with the living bone [105,113].

The bone-bonding ability of a material can be asserted *in-vitro* by evaluating the formation of apatite on its surface, when immersed in simulated body fluid (SBF). In 2003, conventional SBF with the refined recipe was proposed to the Technical Committee ISO/TC150 of International Organization for Standardization as a solution for *in-vitro* measurement of apatite-forming ability of implant materials. This solution contains ionic concentrations nearly equal to those of human blood plasma, as shown in Table 2.2 [204].

Table 2.2 – Ion concentrations of SBF and human blood plasma. Adapted from [204]

Ion	Ion concentration (mM)	
	Human blood plasma	SBF
Na^+	142.0	142.0
K^+	5.0	5.0
Mg^{2+}	1.5	1.5
Ca^{2+}	2.5	2.5
Cl^-	103.0	147.8
HCO_3^-	27.0	4.2
HPO_4^{2-}	1.0	1.0
SO_4^{2-}	0.5	0.5

This method can be used for screening bioactivity of materials prior to animal testing. Thus, the number of animals used and the duration of animal experiments can be remarkably reduced by using this method [204].

Standard *in-vitro* bioactivity studies were performed by immersing the LbL coatings in a pH adjusted SBF solution to 7.4, which was prepared by following the Kokubo and Takadama procedure [204], in order to simulate the concentration of ionic species and pH present in human blood plasma. Each dip-coated coverglass (18 mm diameter) was immersed for 7 days in 13 mL of SBF solution at 37°C. Likewise, dip-coated coverglass pieces, with the same LbL coatings, were immersed for 14 days in 13 mL of SBF solution at 37°C. The LbL conditions used for these bioactivity studies were the formulations containing both conjugates (CHT-C and HA-DN) and BGNPs and their respective controls, namely MF5, MF6, CTR5, CTR6. After removing from SBF, these coverglass were cleaned three times with ultrapure water and, then, dried at room temperature. The bone-like apatite layer formation was characterized by a surface analysis using the SEM/EDS and XRD technologies.

2.2.12 *In-vitro* Biological Studies

Studies of cells morphology, and activity were performed with the aim of evaluating the *in-vitro* biological performance of the developed dip-coated LbL conditions. Dip-coated coverglasses with the formulations containing both conjugates (CHT-C and HA-DN) and BGNPs and their respective controls, namely MF5, MF6, CTR5, CTR6, were used.

The mouse fibroblast cell line L929, from European Collection of cell cultures (ECACC, UK), was chosen to perform direct contact tests with the developed LbL coatings. Before cell seeding, the samples were sterilized by ethylene oxide sterilization (EO) which takes approximately 12h, with 3h of EO exposure at 42°C and, then, they were washed twice with sterile PBS. Cells were cultured with Dulbecco's modified minimum essential medium (D-MEM) supplemented with 10% fetal bovine serum (FBS) and 1% antibiotic. The cultures were then incubated at 37°C, in humidified air atmosphere of 5% CO_2, and placed to grow until confluence. The culture medium was replaced every 2 days. When 90% of confluence was reached, the cells were seeded onto the LbL coatings, using 3 replicates (n=3), at a density of 1×10^4 cells per sample and then incubated at 37°C for one, three and seven days. After 4 hours, supplemented D-MEM was added to each well to nourish the adhered cells.

MTS Assays

MTS assays were performed to evaluate the cytotoxicity of the dip-coated LbL conditions, and to determine their relative cellular viability (%).

MTS (3-(4,5-dimethylthiazol-2-yl)-5-(3-carboxymethoxyphenyl)-2-(4-sulfophenyl)-2H-tetrazolium) assay is a colorimetric method based on the quantification of a coloured formazan product obtained by the reduction of tetrazolium products. This reduction reaction is performed by mitochondrial activity of viable cells at 37°C, and therefore can be directly correlated with the number of viable cells in culture and quantified by measuring the Abs at 490 nm [205].

The MTS test (Promega) was done after immersing LbL coatings in a MTS solution and after each time point of 1, 3 and 7 days of culture. The MTS solution was prepared using 1:5 ratio of MTS reagent and D-MEM culture medium without phenol red or FBS, and then incubated for 3 hours at 37°C. Relative cellular viability (%) of each condition was obtained and compared with tissue culture polystyrene (TCPS), used as positive control of cell viability. All cytotoxicity tests were conducted using three replicates (n=3), and optical density (OD) was read at 490 nm on a multiwell microplate reader (Synergy HT, BioTek Instruments, U.S.A.).

Phalloidin/DAPI Analysis

Phalloidin/DAPI fluorescent assays were performed at each time culture period, 1, 3 and 7 days, to obtain fluorescence images.

Briefly, for each time point, the culture medium was removed and 10% formalin was added to each well in three replicates (n=3) for 30 minutes. Then, formalin was removed and the wells of the plate were washed with PBS. The samples were labelled with fluorescent stains: Phalloidin (phalloidin-

tetramethylrhodamine B isothiocyanate), which binds to actin filaments staining the cytoskeleton of the cells in red, and DAPI (4',6-diamidino-2-phenylindole), which binds to DNA regions staining cell nuclei in blue. For this, first, phalloidin was incubated with samples at 1:200 in PBS for 30 min and then, DAPI was added at 1:1000 in PBS for 5 min. This procedure was done at room temperature and protected from light. Finally, the samples were washed twice with PBS, left overnight and then visualized in the dark using a fluorescence microscope (Transmitted and Reflected Light Microscope with Apotome 2, Zeiss, Germany). The images were acquired and processed using AxioVision software version: Zeiss 2012 (Zeiss, Germany).

2.2.13 Statistical Analysis

The results of all experiments were carried out at least in three replicates (n=3) and were presented as mean ± standard deviation (SD).

Statistical significance between groups was determined by One-way ANOVA with Turkey's Multiple comparison test, using Graph Pad Prism version 6.0 (GraphPad software, San Diego, CA). Statistical differences were represented and set to $p<0.05$(+/*), $p<0.01$(++/**), $p<0.001$(+++/***), and $p<0.0001$(++++/****).

2.3 References

[1] D. Raafat, H.G. Sahl, Chitosan and its antimicrobial potential - A critical literature survey, Microb. Biotechnol. 2 (2009) 186–201. doi:10.1111/j.1751-7915.2008.00080.x.

[2] M.R. Leedy, H.J. Martin, P.A. Norowski, J.A. Jennings, W.O. Haggard, J.D. Bumgardner, Use of Chitosan as a Bioactive Implant Coating for Bone-Implant Applications, in: R. Jayakumar, M. Prabaharan, R.A.A. Muzzarelli (Eds.), Chitosan Biomater. II, Springer Berlin Heidelberg, Berlin, Heidelberg, 2011: pp. 129–165. doi:10.1007/12.

[3] I. Younes, M. Rinaudo, Chitin and chitosan preparation from marine sources. Structure, properties and applications, Mar. Drugs. 13 (2015) 1133–1174. doi:10.3390/md13031133.

[4] C. Pandis, S. Madeira, J. Matos, A. Kyritsis, J.F. Mano, J.L.G. Ribelles, Chitosan-silica hybrid porous membranes, Mater. Sci. Eng. C. 42 (2014) 553–561. doi:10.1016/j.msec.2014.05.073.

[5] D.W. Lee, H. Lim, H.N. Chong, W.S. Shim, Advances in Chitosan Material and its Hybrid Derivatives: A Review, Open Biomater. J. 1 (2009) 10–20. doi:10.2174/1876502500901010010.

[6] I.-Y. Kim, S.-J. Seo, H.-S. Moon, M.-K. Yoo, I.-Y. Park, B.-C. Kim, C.-S. Cho, Chitosan and its derivatives for tissue engineering applications, Biotechnol. Adv. 26 (2008) 1–21. doi:10.1016/j.biotechadv.2007.07.009.

[7] N. Bhattarai, J. Gunn, M. Zhang, Chitosan-based hydrogels for controlled, localized drug delivery, Adv. Drug Deliv. Rev. 62 (2010) 83–99. doi:10.1016/j.addr.2009.07.019.

[8] R. Jayakumar, M. Prabaharan, P.T. Sudheesh Kumar, S. V. Nair, H. Tamura, Biomaterials based on chitin and chitosan in wound dressing applications, Biotechnol. Adv. 29 (2011) 322–337. doi:10.1016/j.biotechadv.2011.01.005.

[9] M. Garcia-Fuentes, M.J. Alonso, Chitosan-based drug nanocarriers: Where do we stand?, J. Control. Release. 161 (2012) 496–504. doi:10.1016/j.jconrel.2012.03.017.

[10] J. Synowiecki, N.A. Al-Khateeb, Production, properties, and some new applications of chitin and its derivatives., Crit. Rev. Food Sci. Nutr. 43 (2003) 145–171. doi:10.1080/10408690390826473.

[11] H. Tan, C.R. Chu, K.A. Payne, K.G. Marra, Injectable in situ forming biodegradable chitosan-hyaluronic acid based hydrogels for cartilage tissue engineering, Biomaterials. 30 (2009) 2499–2506. doi:10.1016/j.biomaterials.2008.12.080.

[12] E.I. Rabea, M.E.T. Badawy, C. V. Stevens, G. Smagghe, W. Steurbaut, Chitosan as antimicrobial agent: Applications and mode of action, Biomacromolecules. 4 (2003) 1457–1465. doi:10.1021/bm034130m.

[13] M. Kong, X.G. Chen, K. Xing, H.J. Park, Antimicrobial properties of chitosan and mode of action: A state of the art review, Int. J. Food Microbiol. 144 (2010) 51–63. doi:10.1016/j.ijfoodmicro.2010.09.012.

[14] Y. Chung, Y. Su, C. Chen, G. Jia, H. Wang, J.C.G. Wu, J. Lin, Relationship between antibacterial activity of chitosan and surface characteristics of cell wall, Acta Pharmacol. Sin. 25 (2004) 932–936.

[15] L.R. Martinez, M.R. Mihu, G. Han, S. Frases, R.J.B. Cordero, A. Casadevall, A.J. Friedman, J.M. Friedman, J.D. Nosanchuk, The use of chitosan to damage Cryptococcus neoformans biofilms, Biomaterials. 31 (2010) 669–679. doi:10.1016/j.biomaterials.2009.09.087.

[16] B. Orgaz, M.M. Lobete, C.H. Puga, C.S. Jose, Effectiveness of chitosan against mature biofilms formed by food related bacteria, Int. J. Mol. Sci. 12 (2011) 817–828. doi:10.3390/ijms12010817.

[17] E.M. Costa, S. Silva, F.K. Tavaria, M.M. Pintado, Study of the effects of chitosan upon

Streptococcus mutans adherence and biofilm formation, Anaerobe. 20 (2013) 27–31. doi:10.1016/j.anaerobe.2013.02.002.

[18] R. Jayakumar, M. Prabaharan, S. V. Nair, H. Tamura, Novel chitin and chitosan nanofibers in biomedical applications, Biotechnol. Adv. 28 (2010) 142–150. doi:10.1016/j.biotechadv.2009.11.001.

[19] Y. Yuan, B.M. Chesnutt, L. Wright, W.O. Haggard, J.D. Bumgardner, Mechanical property, degradation rate, and bone cell growth of chitosan coated titanium influenced by degree of deacetylation of chitosan, J. Biomed. Mater. Res. - Part B Appl. Biomater. 86 (2008) 245–252. doi:10.1002/jbm.b.31012.

[20] H.J. Martin, K.H. Schulz, J.D. Bumgardner, J.A. Schneider, Enhanced bonding of chitosan to implant quality titanium via four treatment combinations, Thin Solid Films. 516 (2008) 6277–6286. doi:10.1016/j.tsf.2007.12.001.

[21] J.D. Bumgardner, R. Wiser, P.D. Gerard, P. Bergin, B. Chestnutt, M. Marin, V. Ramsey, S.H. Elder, J. a Gilbert, Chitosan: potential use as a bioactive coating for orthopaedic and craniofacial/dental implants., J. Biomater. Sci. Polym. Ed. 14 (2003) 423–438. doi:10.1163/156856203766652048.

[22] A. Di Martino, M. Sittinger, M. V. Risbud, Chitosan: A versatile biopolymer for orthopaedic tissue-engineering, Biomaterials. 26 (2005) 5983–5990. doi:10.1016/j.biomaterials.2005.03.016.

[23] J.A. Lichter, K.J. Van Vlietpa, M.F. Rubner, Design of antibacterial surfaces and interfaces: Polyelectrolyte multilayers as a multifunctional platform, Macromolecules. 42 (2009) 8573–8586. doi:10.1021/ma901356s.

[24] L. Richert, P. Lavalle, E. Payan, X.Z. Shu, G.D. Prestwich, J.-F. Stoltz, P. Schaaf, J.-C. Voegel, C. Picart, Layer by Layer Buildup of Polysaccharide Films: Physical Chemistry and Cellular Adhesion Aspects, Langmuir. 20 (2004) 448–458. doi:10.1021/la035415n.

[25] M. Vakili, M. Rafatullah, B. Salamatinia, A.Z. Abdullah, M.H. Ibrahim, K.B. Tan, Z. Gholami, P. Amouzgar, Application of chitosan and its derivatives as adsorbents for dye removal from water and wastewater: A review, Carbohydr. Polym. 113 (2014) 115–130. doi:10.1016/j.carbpol.2014.07.007.

[26] K. Azuma, S. Ifuku, T. Osaki, Y. Okamoto, S. Minami, Preparation and biomedical applications of chitin and chitosan nanofibers, J. Biomed. Nanotechnol. 10 (2014) 2891–2920. doi:10.1166/jbn.2014.1882.

[27] L. Liu, Q. Gao, X. Lu, H. Zhou, In situ forming hydrogels based on chitosan for drug delivery and tissue regeneration, Asian J. Pharm. Sci. 11 (2016) 673–683.

[28] P.J. Kondiah, Y.E. Choonara, P.P.D. Kondiah, T. Marimuthu, P. Kumar, L.C. Du Toit, V. Pillay, A review of injectable polymeric hydrogel systems for application in bone tissue engineering, Molecules. 21 (2016). doi:10.3390/molecules21111580.

[29] R.A.A. Muzzarelli, M. El Mehtedi, C. Bottegoni, A. Aquili, A. Gigante, Genipin-Crosslinked Chitosan Gels and Scaffolds for Tissue Engineering and Regeneration of Cartilage and Bone, Mar. Drugs. 13 (2015) 7314–7338. doi:10.3390/md13127068.

[30] E. Salehi, P. Daraei, A. Arabi Shamsabadi, A review on chitosan-based adsorptive membranes, Carbohydr. Polym. 152 (2016) 419–432. doi:10.1016/j.carbpol.2016.07.033.

[31] G. Yuan, X. Chen, D. Li, Chitosan films and coatings containing essential oils: The antioxidant and antimicrobial activity, and application in food systems, Food Res. Int. 89 (2016) 117–128. doi:10.1016/j.foodres.2016.10.004.

[32] S. Karki, H. Kim, S.J. Na, D. Shin, K. Jo, J. Lee, Thin films as an emerging platform for drug delivery, Asian J. Pharm. Sci. 11 (2016) 559–574. doi:10.1016/j.ajps.2016.05.004.

[33] J. Carneiro, J. Tedim, M.G.S. Ferreira, Chitosan as a smart coating for corrosion protection of aluminum alloy 2024: A review, Prog. Org. Coatings. 89 (2015) 348–356. doi:10.1016/j.porgcoat.2015.03.008.

[34] M.Z. Elsabee, H.F. Naguib, R.E. Morsi, Chitosan based nanofibers, review, Mater. Sci. Eng. C. 32 (2012) 1711–1726. doi:10.1016/j.msec.2012.05.009.

[35] A.P. Martínez-Camacho, M.O. Cortez-Rocha, M.M. Castillo-Ortega, A. Burgos-Hernández, J.M. Ezquerra-Brauer, M. Plascencia-Jatomea, Antimicrobial activity of chitosan nanofibers obtained by electrospinning, Polym. Int. 60 (2011) 1663–1669. doi:10.1002/pi.3174.

[36] S. Ifuku, Chitin and chitosan nanofibers: Preparation and chemical modifications, Molecules. 19 (2014) 18367–18380. doi:10.3390/molecules191118367.

[37] Y. Hu, J. Peng, L. Ke, D. Zhao, H. Zhao, X. Xiao, Alginate/carboxymethyl chitosan composite gel beads for oral drug delivery, J. Polym. Res. 23 (2016) 129. doi:10.1007/s10965-016-1022-5.

[38] H. Onishi, Chitosan microparticles, J. Drug Deliv. Sci. Technol. 20 (2010) 15–22. doi:10.1016/S1773-2247(10)50002-9.

[39] A.D. Sezer, E. Cevher, Topical drug delivery using chitosan nano- and microparticles, Expert Opin. Drug Deliv. 9 (2012) 1129–1146.

[40] M. Prabaharan, Chitosan-based nanoparticles for tumor-targeted drug delivery, Int. J. Biol. Macromol. 72 (2015) 1313–1322. doi:10.1016/j.ijbiomac.2014.10.052.

[41] A. Landriscina, J. Rosen, A. Friedman, Biodegradable chitosan nanoparticles in drug delivery for infectious disease, Nanomedicine (Lond). 10 (2015) 1609–1619. doi:10.2217/nnm.15.7.

[42] P.R. Sivashankari, M. Prabaharan, Prospects of chitosan-based scaffolds for growth factor release in tissue engineering, Int. J. Biol. Macromol. 93 (2016) 1382–1389. doi:10.1016/j.ijbiomac.2016.02.043.

[43] S. Saravanan, R.S. Leena, N. Selvamurugan, Chitosan based biocomposite scaffolds for bone tissue engineering, Int. J. Biol. Macromol. 93 (2016) 1354–1365. doi:10.1016/j.ijbiomac.2016.01.112.

[44] F. Han, Y. Dong, Z. Su, R. Yin, A. Song, S. Li, Preparation, characteristics and assessment of a novel gelatin-chitosan sponge scaffold as skin tissue engineering material, Int. J. Pharm. 476 (2014) 124–133. doi:10.1016/j.ijpharm.2014.09.036.

[45] S. Jia, X. Yang, W. Song, L. Wang, K. Fang, Z. Hu, Z. Yang, C. Shan, D. Lei, B. Lu, Incorporation of osteogenic and angiogenic small interfering RNAs into chitosan sponge for bone tissue engineering, Int. J. Nanomedicine. 9 (2014) 5307–5316. doi:10.2147/IJN.S70457.

[46] G. Lan, B. Lu, T. Wang, L. Wang, J. Chen, K. Yu, J. Liu, F. Dai, D. Wu, Chitosan/gelatin composite sponge is an absorbable surgical hemostatic agent, Colloids Surfaces B Biointerfaces. 136 (2015) 1026–1034. doi:10.1016/j.colsurfb.2015.10.039.

[47] N.M. Salwowska, K.A. Bebenek, D.A. Żądło, D.L. Wcisło-Dziadecka, Physiochemical properties and application of hyaluronic acid: a systematic review, J. Cosmet. Dermatol. 15 (2016) 1–7. doi:10.1111/jocd.12237.

[48] T.C. Laurent, J.R. Fraser, Hyaluronan, FASEB J. 6 (1992) 2397–2404. doi:10.1016/S0140-6736(01)79484-6.

[49] C.E. Schanté, G. Zuber, C. Herlin, T.F. Vandamme, Chemical modifications of hyaluronic acid for the synthesis of derivatives for a broad range of biomedical applications, Carbohydr. Polym. 85 (2011) 469–489. doi:10.1016/j.carbpol.2011.03.019.

[50] P. Prehm, Release of hyaluronate from eukaryotic cells, Biochem. J. 267 (1990) 185–189. http://www.pubmedcentral.nih.gov/articlerender.fcgi?artid=1131262&tool=pmcentrez&rendertype=abstract.

[51] G. Kogan, L. Šoltés, R. Stern, P. Gemeiner, Hyaluronic acid: A natural biopolymer with a broad range of biomedical and industrial applications, Biotechnol. Lett. 29 (2007) 17–25.

doi:10.1007/s10529-006-9219-z.

[52] L. Juhlin, Hyaluronan in skin, J. Intern. Med. 242 (1997) 61–66. doi:10.1046/j.1365-2796.1997.00175.x.

[53] D. Hamerman, H. Schuster, Hyaluronate in normal human sinovial fluid, J Clin Invest. 37 (1957) 54–64.

[54] K. Meyer, J.W. Palmer, The polysaccharide of vitreous humor, J. Biol. Chem. 107 (1934) 629–634.

[55] B. Weissmann, K. Meyer, The Structure of Hyalobiuronic Acid and of Hyaluronic Acid from Umbilical Cord, J. Am. Chem. Soc. 76 (1954) 1753–1757. doi:10.1021/ja01636a010.

[56] B.P. Toole, Hyaluronan: from extracellular glue to pericellular cue, Nat Rev Cancer. 4 (2004) 528–539. http://dx.doi.org/10.1038/nrc1391.

[57] A.P. Maclennan, The Production of Capsules, Hyaluronic Acid and Hyaluronidase by 25 Strains of Group C Streptococci, J Gen Microbiol. 15 (1956) 485–491.

[58] M. Hemshekhar, R.M. Thushara, S. Chandranayaka, L.S. Sherman, K. Kemparaju, K.S. Girish, Emerging roles of hyaluronic acid bioscaffolds in tissue engineering and regenerative medicine, Int. J. Biol. Macromol. 86 (2016) 917–928. doi:10.1016/j.ijbiomac.2016.02.032.

[59] M. Morra, C. Cassineli, Non-fouling properties of polysaccharide-coated surfaces, J. Biomater. Sci. Polym. Ed. 10 (1999) 1107–1124. doi:10.1163/156856299X00711.

[60] L.G. Harris, R.G. Richards, Staphylococcus aureus adhesion to different treated titanium surfaces, J. Mater. Sci. Mater. Med. 15 (2004) 311–314. doi:10.1023/B:JMSM.0000021093.84680.bb.

[61] X. Hu, K.G. Neoh, Z. Shi, E.T. Kang, C. Poh, W. Wang, An in vitro assessment of titanium functionalized with polysaccharides conjugated with vascular endothelial growth factor for enhanced osseointegration and inhibition of bacterial adhesion, Biomaterials. 31 (2010) 8854–8863. doi:10.1016/j.biomaterials.2010.08.006.

[62] T.I. Croll, A.J. O'Connor, G.W. Stevens, J.J. Cooper-White, A blank slate? Layer-by-layer deposition of hyaluronic acid and chitosan onto various surfaces, Biomacromolecules. 7 (2006) 1610–1622. doi:10.1021/bm060044l.

[63] H. Hartmann, S. Hossfeld, B. Schlosshauer, U. Mittnacht, A.P. P??go, M. Dauner, M. Doser, D. Stoll, R. Krastev, Hyaluronic acid/chitosan multilayer coatings on neuronal implants for localized delivery of siRNA nanoplexes, J. Control. Release. 168 (2013) 289–297. doi:10.1016/j.jconrel.2013.03.026.

[64] X. Zhang, Z. Li, X. Yuan, Z. Cui, X. Yang, Fabrication of dopamine-modified hyaluronic acid/chitosan multilayers on titanium alloy by layer-by-layer self-assembly for promoting osteoblast growth, Appl. Surf. Sci. 284 (2013) 732–737. doi:10.1016/j.apsusc.2013.08.002.

[65] A.I. Neto, A.C. Cibrão, C.R. Correia, R.R. Carvalho, G.M. Luz, G.G. Ferrer, G. Botelho, C. Picart, N.M. Alves, J.F. Mano, Nanostructured polymeric coatings based on chitosan and dopamine-modified hyaluronic acid for biomedical applications, Small. 10 (2014) 2459–2469. doi:10.1002/smll.201303568.

[66] A.L. Carvalho, A.C. Vale, M. Sousa, A.M. Barbosa, E. Torrado, J. Mano, N.M. Alves, Antibacterial bioadhesive layer-by-layer coatings for orthopedic applications, J. Mater. Chem. B. 4 (2016) 5385–5393. doi:10.1039/C6TB00841K.

[67] S.J. Rego, A.C. Vale, G.M. Luz, J.F. Mano, N.M. Alves, Adhesive Bioactive Coatings Inspired by Sea Life, Langmuir. 32 (2016) 560–568. doi:10.1021/acs.langmuir.5b03508.

[68] G.A. Junter, P. Thébault, L. Lebrun, Polysaccharide-based antibiofilm surfaces, Acta Biomater. 30 (2016) 13–25. doi:10.1016/j.actbio.2015.11.010.

[69] K. Mulligan, Z.J. Jakubek, L.J. Johnston, Supported lipid bilayers on biocompatible polysaccharide multilayers, Langmuir. 27 (2011) 14352–14359. doi:10.1021/la203207p.

[70] J. Zhan, Q.J. Luo, Y. Huang, X.D. Li, Cellular response to titanium discs coated with polyelectrolyte multilayer films, Int. J. Miner. Metall. Mater. 21 (2014) 925–933. doi:10.1007/s12613-014-0991-9.

[71] S. Zankovych, J. Bossert, M. Faucon, U. Finger, K.D. Jandt, Selectively promoting or preventing osteoblast growth on titanium functionalized with polyelectrolyte multilayers, Adv. Eng. Mater. 13 (2011) 454–461. doi:10.1002/adem.201180020.

[72] S. Zankovych, M. Diefenbeck, J. Bossert, T. Mückley, C. Schrader, J. Schmidt, H. Schubert, S. Bischoff, M. Faucon, U. Finger, K.D. Jandt, The effect of polyelectrolyte multilayer coated titanium alloy surfaces on implant anchorage in rats, Acta Biomater. 9 (2013) 4926–4934. doi:10.1016/j.actbio.2012.08.013.

[73] P.H. Chua, K.G. Neoh, E.T. Kang, W. Wang, Surface functionalization of titanium with hyaluronic acid/chitosan polyelectrolyte multilayers and RGD for promoting osteoblast functions and inhibiting bacterial adhesion, Biomaterials. 29 (2008) 1412–1421. doi:10.1016/j.biomaterials.2007.12.019.

[74] A.L. Larkin, R.M. Davis, P. Rajagopalan, Biocompatible, detachable, and free-standing polyelectrolyte multilayer films, Biomacromolecules. 11 (2010) 2788–2796.

doi:10.1021/bm100867h.

[75] S. Del Hoyo-Gallego, L. Pérez-Álvarez, F. Gómez-Galván, E. Lizundia, I. Kuritka, V. Sedlarik, J.M. Laza, J.L. Vila-Vilela, Construction of antibacterial poly(ethylene terephthalate) films via layer by layer assembly of chitosan and hyaluronic acid, Carbohydr. Polym. 143 (2016) 35–43. doi:10.1016/j.carbpol.2016.02.008.

[76] L.Q. Xu, W.J. Yang, K.G. Neoh, E.T. Kang, G.D. Fu, Dopamine-induced reduction and functionalization of graphene oxide nanosheets, Macromolecules. 43 (2010) 8336–8339. doi:10.1021/ma101526k.

[77] R.B. Raffa, J. Danah, C.S. Tallarida, C. Zimmerman, G. Gill, S.J. Baron, S.M. Rawls, Potential of a planarian model to study certain aspects of anti-Parkinsonism drugs, Adv. Park. Dis. 2 (2013) 70–74. doi:10.4236/apd.2013.23014.

[78] S.-K. Hsu, J. Tian, W.-F. Ho, H.-C. Hsu, H.-J. Liao, Y.-F. Chen, S.-C. Wu, Enhancing the bioactivity of yttria-stabilized zirconia immobilized with adhesive peptide using l-dopa as cross-linker, Thin Solid Films. 620 (2016) 145–149. doi:10.1016/j.tsf.2016.07.083.

[79] S.K. Madhurakkat Perikamana, J. Lee, Y. Bin Lee, Y.M. Shin, E.J. Lee, A.G. Mikos, H. Shin, Materials from Mussel-Inspired Chemistry for Cell and Tissue Engineering Applications, Biomacromolecules. 16 (2015) 2541–2555. doi:10.1021/acs.biomac.5b00852.

[80] H. Lee, S.M. Dellatore, W.M. Miller, P.B. Messersmith, Mussel-Inspired Surface Chemistry for Multifunctional Coatings, Science (80-.). 318 (2007) 426–430. doi:10.1126/science.1147241.Mussel-Inspired.

[81] H. Lee, N.F. Scherer, P.B. Messersmith, Single-molecule mechanics of mussel adhesion, Proc. Natl. Acad. Sci. 103 (2006) 12999–13003. doi:10.1073/pnas.0605552103.

[82] Z.Y. Xi, Y.Y. Xu, L.P. Zhu, Y. Wang, B.K. Zhu, A facile method of surface modification for hydrophobic polymer membranes based on the adhesive behavior of poly(DOPA) and poly(dopamine), J. Memb. Sci. 327 (2009) 244–253. doi:10.1016/j.memsci.2008.11.037.

[83] C. Wu, W. Fan, J. Chang, Y. Xiao, Mussel-inspired porous SiO2 scaffolds with improved mineralization and cytocompatibility for drug delivery and bone tissue engineering, J. Mater. Chem. 21 (2011) 18300–18307. doi:10.1039/c1jm12770e.

[84] C.K. Poh, Z. Shi, X.W. Tan, Z.C. Liang, X.M. Foo, H.C. Tan, K.G. Neoh, W. Wang, Cobalt chromium alloy with immobilized BMP peptide for enhanced bone growth, J. Orthop. Res. 29 (2011) 1424–1430. doi:10.1002/jor.21409.

[85] M.J. LaVoie, B.L. Ostaszewski, A. Weihofen, M.G. Schlossmacher, D.J. Selkoe, Dopamine

covalently modifies and functionally inactivates parkin, Nat Med. 11 (2005) 1214–1221. doi:10.1038/nm1314.

[86] B.P. Lee, J.L. Dalsin, P.B. Messersmith, Synthesis and gelation of DOPA-modified poly(ethylene glycol) hydrogels, Biomacromolecules. 3 (2002) 1038–1047. doi:10.1021/bm025546n.

[87] E. Lih, S.G. Choi, D.J. Ahn, Y.K. Joung, D.K. Han, Optimal conjugation of catechol group onto hyaluronic acid in coronary stent substrate coating for the prevention of restenosis, J. Tissue Eng. 7 (2016) 1–11. doi:10.1177/2041731416683745.

[88] Y. Zhu, J. Wang, X. Li, D. Zhao, J. Sun, X. Liu, Self-assembly and emulsification of dopamine-modified hyaluronan, Carbohydr. Polym. 123 (2015) 72–79. doi:10.1016/j.carbpol.2015.01.030.

[89] M.Y. Moridani, H. Scobie, A. Jamshidzadeh, P.A.R. Salehi, P.J.O. Brien, Caffeic Acid, Chlorogenic Acid, and Dihydrocaffeic Acid Metabolism: Glutathione Conjugate Formation, Drug Metab. Dispos. 29 (2001) 1432–1439.

[90] A.M. Jenner, J. Rafter, B. Halliwell, Human fecal water content of phenolics: The extent of colonic exposure to aromatic compounds, Free Radic. Biol. Med. 38 (2005) 763–772. doi:10.1016/j.freeradbiomed.2004.11.020.

[91] H. Qiao, M. Sun, Z. Su, Y. Xie, M. Chen, L. Zong, Y. Gao, H. Li, J. Qi, Q. Zhao, X. Gu, Q. Ping, Kidney-specific drug delivery system for renal fibrosis based on coordination-driven assembly of catechol-derived chitosan, Biomaterials. 35 (2014) 7157–7171. doi:10.1016/j.biomaterials.2014.04.106.

[92] D. Ling, W. Park, Y. Il Park, N. Lee, F. Li, C. Song, S.G. Yang, S.H. Choi, K. Na, T. Hyeon, Multiple-interaction ligands inspired by mussel adhesive protein: Synthesis of highly stable and biocompatible nanoparticles, Angew. Chemie - Int. Ed. 50 (2011) 11360–11365. doi:10.1002/anie.201101521.

[93] E. Byun, J.H. Ryu, H. Lee, Catalyst-mediated yet catalyst-free hydrogels formed by interfacial chemical activation, Chem. Commun. 50 (2014) 2869–2872. doi:10.1039/c3cc49043b.

[94] J.H. Ryu, Y. Lee, M.J. Do, S.D. Jo, J.S. Kim, B.S. Kim, G. Il Im, T.G. Park, H. Lee, Chitosan-g-hematin: Enzyme-mimicking polymeric catalyst for adhesive hydrogels, Acta Biomater. 10 (2014) 224–233. doi:10.1016/j.actbio.2013.09.014.

[95] J.H. Ryu, Y. Lee, W.H. Kong, T.G. Kim, T.G. Park, H. Lee, Catechol-functionalized chitosan/pluronic hydrogels for tissue adhesives and hemostatic materials, Biomacromolecules. 12 (2011) 2653–2659. doi:10.1021/bm200464x.

[96] K. Kim, J.H. Ryu, D.Y. Lee, H. Lee, Bio-inspired catechol conjugation converts water-insoluble chitosan into a highly water-soluble, adhesive chitosan derivative for hydrogels and LbL assembly, Biomater. Sci. 1 (2013) 783–790. doi:Doi 10.1039/C3bm00004d.

[97] J.H. Ryu, S. Hong, H. Lee, Bio-inspired adhesive catechol-conjugated chitosan for biomedical applications: A mini review, Acta Biomater. 27 (2015) 101–115. doi:10.1016/j.actbio.2015.08.043.

[98] M. Guvendiren, P.B. Messersmith, K.R. Shull, Self-assembly and adhesion of DOPA-modified methacrylic triblock hydrogels, Biomacromolecules. 9 (2008) 122–128. doi:10.1021/bm700886b.

[99] Y. Lee, H.J. Chung, S. Yeo, C.-H. Ahn, H. Lee, P.B. Messersmith, T.G. Park, Thermo-sensitive, injectable, and tissue adhesive sol–gel transition hyaluronic acid/pluronic composite hydrogels prepared from bio-inspired catechol-thiol reaction, Soft Matter. 6 (2010) 977–983. doi:10.1039/b919944f.

[100] Y. Zhou, J. Zhao, X. Sun, S. Li, X. Hou, X. Yuan, X. Yuan, Rapid Gelling Chitosan/Polylysine Hydrogel with Enhanced Bulk Cohesive and Interfacial Adhesive Force: Mimicking Features of Epineurial Matrix for Peripheral Nerve Anastomosis, Biomacromolecules. 17 (2016) 622–630. doi:10.1021/acs.biomac.5b01550.

[101] J.M. Lee, J.H. Ryu, E.A. Kim, S. Jo, B.-S. Kim, H. Lee, G.-I. Im, Adhesive barrier/directional controlled release for cartilage repair by endogenous progenitor cell recruitment., Biomaterials. 39 (2015) 173–181. doi:10.1016/j.biomaterials.2014.11.006.

[102] G.M. Soliman, Y.L. Zhang, G. Merle, M. Cerruti, J. Barralet, Hydrocaffeic acid-chitosan nanoparticles with enhanced stability, mucoadhesion and permeation properties, Eur. J. Pharm. Biopharm. 88 (2014) 1026–1037. doi:10.1016/j.ejpb.2014.09.003.

[103] J. Xu, M. Tam, S. Samadei, S. Lerouge, J. Barralet, M.M. Stevenson, M. Cerruti, Mucoadhesive chitosan hydrogels as rectal drug delivery vessels to treat ulcerative colitis, Acta Biomater. 48 (2016) 247–257. doi:10.1016/j.actbio.2016.10.026.

[104] L.L. Hench, The story of Bioglass®, J. Mater. Sci. Mater. Med. 17 (2006) 967–978. doi:10.1007/s10856-006-0432-z.

[105] J.R. Jones, Review of bioactive glass: from Hench to hybrids., Acta Biomater. 9 (2013) 4457–4486. doi:10.1016/j.actbio.2012.08.023.

[106] F. Baino, G. Novajra, V. Miguez-Pacheco, A.R. Boccaccini, C. Vitale-Brovarone, Bioactive glasses: Special applications outside the skeletal system, J. Non. Cryst. Solids. 432, Part

(2016) 15–30. doi:http://dx.doi.org/10.1016/j.jnoncrysol.2015.02.015.

[107] L.L. Hench, Bioceramics, J. Am. Ceram. Soc. 81 (1998) 1705–1728. doi:10.1111/j.1151-2916.1998.tb02540.x.

[108] P. Ducheyne, Bioglass coatings and bioglass composites as implant materials, J. Biomed. Mater. Res. 19 (1985) 273–291. doi:10.1002/jbm.820190309.

[109] M. MačKović, A. Hoppe, R. Detsch, D. Mohn, W.J. Stark, E. Spiecker, A.R. Boccaccini, Bioactive glass (type 45S5) nanoparticles: In vitro reactivity on nanoscale and biocompatibility, J. Nanoparticle Res. 14 (2012). doi:10.1007/s11051-012-0966-6.

[110] A.R. Boccaccini, M. Erol, W.J. Stark, D. Mohn, Z. Hong, J.F. Mano, Polymer/bioactive glass nanocomposites for biomedical applications: A review, Compos. Sci. Technol. 70 (2010) 1764–1776. doi:10.1016/j.compscitech.2010.06.002.

[111] M. De, P.S. Ghosh, V.M. Rotello, Applications of Nanoparticles in Biology, Adv. Mater. 20 (2008) 4225–4241. doi:10.1002/adma.200703183.

[112] K. Kim, D. Dean, A. Lu, A.G. Mikos, J.P. Fisher, Early osteogenic signal expression of rat bone marrow stromal cells is influenced by both hydroxyapatite nanoparticle content and initial cell seeding density in biodegradable nanocomposite scaffolds, Acta Biomater. 7 (2011) 1249–1264. doi:10.1016/j.actbio.2010.11.007.

[113] N.M. Alves, I.B. Leonor, H.S. Azevedo, R.L. Reis, J.F. Mano, Designing biomaterials based on biomineralization of bone, J. Mater. Chem. 20 (2010) 2911. doi:10.1039/b910960a.

[114] N. Li, Q. Jie, S. Zhu, R. Wang, Preparation and characterization of macroporous sol-gel bioglass, Ceram. Int. 31 (2005) 641–646. doi:10.1016/j.ceramint.2004.05.011.

[115] P. Saravanapavan, L.L. Hench, Low-temperature synthesis, structure, and bioactivity of gel-derived glasses in the binary CaO-SiO2 system, J. Biomed. Mater. Res. 54 (2001) 608–6018.

[116] D. Bellucci, A. Sola, I. Cacciotti, C. Bartoli, M. Gazzarri, A. Bianco, F. Chiellini, V. Cannillo, Mg- and/or Sr-doped tricalcium phosphate/bioactive glass composites: Synthesis, microstructure and biological responsiveness, Mater. Sci. Eng. C. 42 (2014) 312–324. doi:http://dx.doi.org/10.1016/j.msec.2014.05.047.

[117] J. Isaac, J. Nohra, J. Lao, E. Jallot, J.M. Nedelec, A. Berdal, J.M. Sautier, Effects of strontium-doped bioactive glass on the differentiation of cultured osteogenic cells, Eur. Cells Mater. 21 (2011) 130–143. doi:10.22203/eCM.v021a11.

[118] A.M. El-Kady, A.F. Ali, R.A. Rizk, M.M. Ahmed, Synthesis, characterization and microbiological response of silver doped bioactive glass nanoparticles, Ceram. Int. 38 (2012) 177–188.

doi:http://dx.doi.org/10.1016/j.ceramint.2011.05.158.

[119] M. Bellantone, N.J. Coleman, L.L. Hench, Bacteriostatic action of a novel four-component bioactive glass, J. Biomed. Mater. Res. 51 (2000) 484–490. doi:10.1002/1097-4636(20000905)51:3<484::AID-JBM24>3.0.CO;2-4.

[120] M. Xiao, Y.M. Chen, M.N. Biao, X.D. Zhang, B.C. Yang, Bio-functionalization of biomedical metals, Mater. Sci. Eng. C. 70 (2017) 1057–1070. doi:10.1016/j.msec.2016.06.067.

[121] M. Geetha, A.K. Singh, R. Asokamani, A.K. Gogia, Ti based biomaterials, the ultimate choice for orthopaedic implants – A review, Prog. Mater. Sci. 54 (2009) 397–425. doi:https://doi.org/10.1016/j.pmatsci.2008.06.004.

[122] E.J. Szili, S. Kumar, R.S.C. Smart, N.H. Voelcker, Generation of a stable surface concentration of amino groups on silica coated onto titanium substrates by the plasma enhanced chemical vapour deposition method, Appl. Surf. Sci. 255 (2009) 6846–6850. doi:https://doi.org/10.1016/j.apsusc.2009.02.092.

[123] A. Eskelinen, V. Remes, L. Helenius, P. Pulkkinen, J. Nevalainen, P. Paavolainen, Uncemented total hip arthroplasty for primary osteoarthritis in young patients: A mid-to long-term follow-up study from the Finnish Arthroplasty Register, Acta Orthop. 77 (2006) 57–70. doi:10.1080/17453670610045704.

[124] S.L. Haddad, J.C. Coetzee, R. Estok, K. Fahrbach, D. Banel, L. Nalysnyk, Intermediate and Long-Term Outcomes of Total Ankle Arthroplasty and Ankle Arthrodesis. A Systematic Review of the Literature, J. Bone Jt. Surg. 89 (2007) 1899–1905. doi:10.2106/JBJS.F.01149.

[125] M.C. Dixon, R.R. Brown, D. Parsch, R.D. Scott, Modular fixed-bearing total knee arthroplasty with retention of the posterior cruciate ligament. A study of patients followed for a minimum of fifteen years, J Bone Jt. Surg Am. 87–A (2005) 598–603. doi:10.2106/JBJS.C.00591.

[126] F.E. Lambert, H.-P. Weber, S.M. Susarla, U.C. Belser, G.O. Gallucci, Descriptive analysis of implant and prosthodontic survival rates with fixed implant-supported rehabilitations in the edentulous maxilla., J. Periodontol. 80 (2009) 1220–1230. doi:10.1902/jop.2009.090109.

[127] B.E. Pjetursson, U. Br??gger, N.P. Lang, M. Zwahlen, Comparison of survival and complication rates of tooth-supported fixed dental prostheses (FDPs) and implant-supported FDPs and single crowns (SCs), Clin. Oral Implants Res. 18 (2007) 97–113. doi:10.1111/j.1600-0501.2007.01439.x.

[128] P. Simonis, T. Dufour, H. Tenenbaum, Long-term implant survival and success: A 10-16-year follow-up of non-submerged dental implants, Clin. Oral Implants Res. 21 (2010) 772–777.

doi:10.1111/j.1600-0501.2010.01912.x.

[129] A. Mahapatro, Bio-functional nano-coatings on metallic biomaterials, Mater. Sci. Eng. C. 55 (2015) 227–251. doi:10.1016/j.msec.2015.05.018.

[130] D. Duraccio, F. Mussano, M.G. Faga, Biomaterials for dental implants: current and future trends, J. Mater. Sci. 50 (2015) 4779–4812. doi:10.1007/s10853-015-9056-3.

[131] S.K. Mishra, S. Kannan, Development, mechanical evaluation and surface characteristics of chitosan/polyvinyl alcohol based polymer composite coatings on titanium metal, J. Mech. Behav. Biomed. Mater. 40 (2014) 314–324. doi:10.1016/j.jmbbm.2014.08.014.

[132] H. Ao, Y. Xie, H. Tan, S. Yang, K. Li, X. Wu, X. Zheng, T. Tang, Fabrication and in vitro evaluation of stable collagen/hyaluronic acid biomimetic multilayer on titanium coatings., J. R. Soc. Interface. 10 (2013) 1–9. doi:10.1098/rsif.2013.0070.

[133] N. Hou, H. Perinpanayagam, M. Mozumder, J. Zhu, Novel Development of Biocompatible Coatings for Bone Implants, Coatings. 5 (2015) 737–757. doi:10.3390/coatings5040737.

[134] S. Schweizer, T. Schuster, M. Junginger, G. Siekmeyer, A. Taubert, Surface modification of nickel/titanium alloy and titanium surfaces via a polyelectrolyte multilayer/calcium phosphate hybrid coating, Macromol. Mater. Eng. 295 (2010) 535–543. doi:10.1002/mame.200900347.

[135] Q. Wei, R. Haag, Universal polymer coatings and their representative biomedical applications, Mater. Horizons. 2 (2015) 567–577. doi:10.1039/c5mh00089k.

[136] C.J. Pan, L.Q. Pang, F. Gao, Y.N. Wang, T. Liu, W. Ye, Y.H. Hou, Anticoagulation and endothelial cell behaviors of heparin-loaded graphene oxide coating on titanium surface, Mater. Sci. Eng. C. 63 (2016) 333–340. doi:10.1016/j.msec.2016.03.001.

[137] M. Basiaga, W. Kajzer, W. Walke, A. Kajzer, M. Kaczmarek, Evaluation of physicochemical properties of surface modified Ti6Al4V and Ti6Al7Nb alloys used for orthopedic implants, Mater. Sci. Eng. C. 68 (2016) 851–860. doi:https://doi.org/10.1016/j.msec.2016.07.042.

[138] T. Boudou, T. Crouzier, K. Ren, G. Blin, C. Picart, Multiple functionalities of polyelectrolyte multilayer films: New biomedical applications, Adv. Mater. 22 (2010) 441–467. doi:10.1002/adma.200901327.

[139] J.L. Dalsin, B.-H. Hu, B.P. Lee, P.B. Messersmith, Mussel Adhesive Protein Mimetic Polymers for the Preparation of Nonfouling Surfaces, J. Am. Chem. Soc. 125 (2003) 4253–4258. doi:10.1021/ja0284963.

[140] X. Hu, K.-G. Neoh, Z. Shi, E.-T. Kang, C. Poh, W. Wang, An in vitro assessment of titanium

functionalized with polysaccharides conjugated with vascular endothelial growth factor for enhanced osseointegration and inhibition of bacterial adhesion, Biomaterials. 31 (2010) 8854–8863. doi:https://doi.org/10.1016/j.biomaterials.2010.08.006.

[141] T. Hryniewicz, R. Rokicki, K. Rokosz, Corrosion Characteristics of Medical-Grade AISI Type 316L Stainless Steel Surface After Electropolishing in a Magnetic Field, CORROSION. 64 (2008) 660–665. doi:10.5006/1.3279927.

[142] S. Sutha, K. Kavitha, G. Karunakaran, V. Rajendran, In-vitro bioactivity, biocorrosion and antibacterial activity of silicon integrated hydroxyapatite/chitosan composite coating on 316 L stainless steel implants, Mater. Sci. Eng. C. 33 (2013) 4046–4054. doi:https://doi.org/10.1016/j.msec.2013.05.047.

[143] M.B. González, S.B. Saidman, Electrodeposition of polypyrrole on 316L stainless steel for corrosion prevention, Corros. Sci. 53 (2011) 276–282. doi:https://doi.org/10.1016/j.corsci.2010.09.021.

[144] M. Jokar, S. Darvishi, R. Torkaman, M. Kharaziha, M. Karbasi, Corrosion and bioactivity evaluation of nanocomposite PCL-forsterite coating applied on 316L stainless steel, Surf. Coatings Technol. 307, Part (2016) 324–331. doi:https://doi.org/10.1016/j.surfcoat.2016.08.094.

[145] Y. Hu, C. Zhang, S. Zhang, Z. Xiong, J. Xu, Development of a porous poly(L-lactic acid)/hydroxyapatite/collagen scaffold as a BMP delivery system and its use in healing canine segmental bone defect, J. Biomed. Mater. Res. Part A. 67A (2003) 591–598. doi:10.1002/jbm.a.10070.

[146] K. Rezwan, Q.Z. Chen, J.J. Blaker, A.R. Boccaccini, Biodegradable and bioactive porous polymer/inorganic composite scaffolds for bone tissue engineering., Biomaterials. 27 (2006) 3413–31. doi:10.1016/j.biomaterials.2006.01.039.

[147] J. Degner, F. Singer, L. Cordero, A.R. Boccaccini, S. Virtanen, Electrochemical investigations of magnesium in DMEM with biodegradable polycaprolactone coating as corrosion barrier, Appl. Surf. Sci. 282 (2013) 264–270. doi:https://doi.org/10.1016/j.apsusc.2013.05.115.

[148] A.R. Boccaccini, I. Notingher, V. Maquet, R. Jérôme, Bioresorbable and bioactive composite materials based on polylactide foams filled with and coated by Bioglass® particles for tissue engineering applications, J. Mater. Sci. Mater. Med. 14 (2003) 443–450. doi:10.1023/A:1023266902662.

[149] F. Wu, J. Li, K. Zhang, Z. He, P. Yang, D. Zou, N. Huang, Multifunctional Coating Based on

Hyaluronic Acid and Dopamine Conjugate for Potential Application on Surface Modification of Cardiovascular Implanted Devices, ACS Appl. Mater. Interfaces. 8 (2016) 109–121. doi:10.1021/acsami.5b07427.

[150] A. Charlot, V. Sciannamea, S. Lenoir, E. Faure, R. Jerome, C. Jerome, C. Van De Weerdt, J. Martial, C. Archambeau, N. Willet, A.-S. Duwez, C.-A. Fustin, C. Detrembleur, All-in-one strategy for the fabrication of antimicrobial biomimetic films on stainless steel, J. Mater. Chem. 19 (2009) 4117–4125. doi:10.1039/B820832H.

[151] H. Lee, Y. Lee, A.R. Statz, J. Rho, T.G. Park, P.B. Messersmith, Substrate-independent layer-by-layer assembly by using mussel-adhesive-inspired polymers, Adv. Mater. 20 (2008) 1619–1623. doi:10.1002/adma.200702378.

[152] H. Ye, Y. Xia, Z. Liu, R. Huang, R. Su, W. Qi, L. Wang, Z. He, Dopamine-assisted deposition and zwitteration of hyaluronic acid for nanoscale fabrication of low-fouling surfaces, Royal Society of Chemistry, 2016. doi:10.1039/C6TB01022A.

[153] J. Xu, S. Strandman, J.X.X. Zhu, J. Barralet, M. Cerruti, Genipin-crosslinked catechol-chitosan mucoadhesive hydrogels for buccal drug delivery, Biomaterials. 37 (2015) 395–404. doi:10.1016/j.biomaterials.2014.10.024.

[154] K. Kim, K. Kim, J.H. Ryu, H. Lee, Chitosan-catechol: A polymer with long-lasting mucoadhesive properties, Biomaterials. 52 (2015) 161–170. doi:10.1016/j.biomaterials.2015.02.010.

[155] A. Ghadban, A.S. Ahmed, Y. Ping, R. Ramos, N. Arfin, B. Cantaert, R. V. Ramanujan, A. Miserez, Bioinspired pH and magnetic responsive catechol-functionalized chitosan hydrogels with tunable elastic properties, Chem. Commun. 52 (2016) 697–700. doi:10.1039/C5CC08617E.

[156] Z. Hong, R.L. Reis, J.F. Mano, Preparation and in vitro characterization of novel bioactive glass ceramic nanoparticles, J. Biomed. Mater. Res. - Part A. 88 (2009) 304–313. doi:10.1002/jbm.a.31848.

[157] G.M. Luz, J.F. Mano, Preparation and characterization of bioactive glass nanoparticles prepared by sol–gel for biomedical applications, Nanotechnology. 22 (2011) 494014. doi:10.1088/0957-4484/22/49/494014.

[158] J. Borges, J.F. Mano, Molecular interactions driving the layer-by-layer assembly of multilayers., Chem. Rev. 114 (2014) 8883–8942. doi:10.1021/cr400531v.

[159] K. Halasz, G. Grozdits, L. Csóka, Functional nanostructured coatings via layer-by-layer self-assembly, in: Anti-Abrasive Nanocoatings, Woodhead Publishing, 2015: pp. 249–281.

doi:https://doi.org/10.1016/B978-0-85709-211-3.00010-8.

[160] N.G. Hoogeveen, M.A. Cohen Stuart, G.J. Fleer, M.R. Böhmer, Formation and Stability of Multilayers of Polyelectrolytes, Langmuir. 12 (1996) 3675–3681. doi:10.1021/la951574y.

[161] M.M. de Villiers, D.P. Otto, S.J. Strydom, Y.M. Lvov, Introduction to nanocoatings produced by layer-by-layer (LbL) self-assembly, Adv. Drug Deliv. Rev. 63 (2011) 701–715. doi:http://dx.doi.org/10.1016/j.addr.2011.05.011.

[162] P.M. Martin, Deposition technologies: an overview, in: Handb. Depos. Technol. Film. Coatings, 3rd edn, Elsevier, 2010: pp. 1–31.

[163] M.D. Tyona, A theoritical study on spin coating technique, Adv. Mater. Res. 2 (2013) 195–208.

[164] N. Sahu, B. Parija, S. Panigrahi, Fundamental understanding and modeling of spin coating process: A review, Indian J. Phys. 83 (2009) 493–502.

[165] S. Vozar, Y.-C. Poh, T. Serbowicz, M. Bachner, P. Podsiadlo, M. Qin, E. Verploegen, N. Kotov, A.J. Hart, Automated spin-assisted layer-by-layer assembly of nanocomposites, Rev. Sci. Instrum. 80 (2009) 23903-1-5.

[166] P.T. Hammond, Engineering materials layer-by-layer: challenges and opportunities in multilayer assembly, AIChE J. 57 (2011) 2928–2940. doi:10.1002/aic.12769.

[167] Y. Li, X. Wang, J. Sun, Layer-by-layer assembly for rapid fabrication of thick polymeric films, Chem. Soc. Rev. 41 (2012) 5998–6009. doi:10.1039/C2CS35107B.

[168] P. Held, L. Buehrer, The Synergy ™ HT: A Unique Multi-Detection Microplate Reader for HTS and Drug Discovery, BioTek. (2003) 1–9. http://www.biotek.com.

[169] R.J. Anderson, D.J. Bendell, P.W. Groundwater, Organic Spectroscopic Analysis, The Royal Society of Chemistry, 2004. doi:10.1039/9781847551566.

[170] T.G. Mezger, The Rheology Handbook: For Users of Rotational and Oscillatory Rheometers, Vincentz Network, 2006. https://books.google.pt/books?id=N9Fdn0MEIDIC.

[171] G. Schramm, A practical approach to rheology and rheometry, 2nd ed., Karlsruhe: Haake, 1994.

[172] G. Tabilo-Munizaga, G. V Barbosa-Cánovas, Rheology for the food industry, J. Food Eng. 67 (2005) 147–156. doi:http://dx.doi.org/10.1016/j.jfoodeng.2004.05.062.

[173] P. Atkin, J. de Paula, Atkins' physical chemistry, 8th ed., Oxford University Press, 2006.

[174] A. Sze, D. Erickson, L. Ren, D. Li, Zeta-potential measurement using the Smoluchowski equation and the slope of the current-time relationship in electroosmotic flow, J. Colloid

Interface Sci. 261 (2003) 402–410. doi:10.1016/S0021-9797(03)00142-5.

[175] N. Schultz, G. Metreveli, M. Franzreb, F.H. Frimmel, C. Syldatk, Zeta potential measurement as a diagnostic tool in enzyme immobilisation, Colloids Surfaces B Biointerfaces. 66 (2008) 39–44. doi:10.1016/j.colsurfb.2008.05.004.

[176] A. Doostmohammadi, A. Monshi, R. Salehi, M.H. Fathi, Z. Golniya, A.U. Daniels, Bioactive glass nanoparticles with negative zeta potential, Ceram. Int. 37 (2011) 2311–2316. doi:10.1016/j.ceramint.2011.03.026.

[177] M.C. Dixon, Quartz crystal microbalance with dissipation monitoring: Enabling real-time characterization of biological materials and their interactions, J. Biomol. Tech. 19 (2008) 151–158.

[178] N.M. Alves, C. Picart, J.F. Mano, Self assembling and crosslinking of polyelectrolyte multilayer films of chitosan and alginate studied by QCM and IR spectroscopy., Macromol. Biosci. 9 (2009) 776–785. doi:10.1002/mabi.200800336.

[179] G.Z. Sauerbrey, Use of quartz vibration for weighing thin films on a microbalance, Z. Phys. 155 (1959) 206–222.

[180] M. V. Voinova, M. Rodahl, M. Jonson, B. Kasemo, Viscoelastic Acoustic Response of Layered Polymer Films at Fluid-Solid Interfaces: Continuum Mechanics Approach, Phys. Scr. 59 (1999) 391–396. doi:10.1238/Physica.Regular.059a00391.

[181] B.C. Smith, Fundamentals of Fourier Transform Infrared Spectroscopy, CRC press, 2011.

[182] B. Suart, Infrared Spectroscopy: Fundamental and Applications, Analytical Techniques in the Sciences, 2004.

[183] C. Peniche, W. Arguelles-Monal, N. Davidenko, R. Sastre, A. Gallardo, J. San Roman, Self-curing membranes of chitosan/PAA IPNs obtained by radical polymerization: preparation, characterization and interpolymer complexation., Biomaterials. 20 (1999) 1869–1878.

[184] J.W. Kuo, Practical aspects of hyaluronan based medical products, CRC Press, 2005.

[185] G. Lawrie, I. Keen, B. Drew, A. Chandler-Temple, L. Rintoul, P. Fredericks, L. Grøndahl, Interactions between alginate and chitosan biopolymers characterized using FTIR and XPS, Biomacromolecules. 8 (2007) 2533–2541.

[186] M. Kakudo, N. Kasai, X-ray diffraction by macromolecules, Springer, 2005.

[187] C. Suryanarayana, M.G. Norton, X-ray diffraction: a practical approach, Springer, 2013.

[188] M. Driver, Coatings for biomedical applications, Woodhead Publishing, 2012.

[189] Z. Ma, Z. Mao, C. Gao, Surface modification and property analysis of biomedical polymers used

for tissue engineering, Colloids Surfaces B Biointerfaces. 60 (2007) 137–157. doi:10.1016/j.colsurfb.2007.06.019.

[190] R. Williams, Surface modification of biomaterials: Methods analysis and applications, Woodhead publishing, 2010.

[191] K.L. Menzies, L. Jones, The Impact of Contact Angle on the Biocompatibility of Biomaterials, Optom. Vis. Sci. 87 (2010) 387–399.

[192] S. Kaur, S. Sundarrajan, D. Rana, R. Sridhar, R. Gopal, T. Matsuura, S. Ramakrishna, Review: the characterization of electrospun nanofibrous liquid filtration membranes, J. Mater. Sci. 49 (2014) 6143–6159.

[193] J. Goldstein, D.E. Newbury, P. Echlin, D.C. Joy, A.D. Romig Jr, C.E. Lyman, C. Fiori, E. Lifshin, Scanning electron microscopy and X-ray microanalysis: a text for biologists, materials scientists, and geologists, Springer Science & Business Media, 2012.

[194] A.V. Girão, G. Caputo, M.C. Ferro, Application of Scanning Electron Microscopy–Energy Dispersive X-Ray Spectroscopy (SEM-EDS), in: T.A.P. Rocha-Santos, A.C. Duarte (Eds.), Charact. Anal. Microplastics, Elsevier, 2017: pp. 153–168. doi:http://dx.doi.org/10.1016/bs.coac.2016.10.002.

[195] C.E. Lyman, D.E. Newbury, J. Goldstein, D.B. Williams, A.D. Romig Jr, J. Armstrong, P. Echlin, C. Fiori, D.C. Joy, E. Lifshin, Scanning electron microscopy, X-ray microanalysis, and analytical electron microscopy: a laboratory workbook, 2nd ed., Springer Science & Business Media, 2012.

[196] ASTM, Standard Test Method for Apparent Shear Strength of Single-Lap-Joint Adhesively Bonded Metal Specimens by Tension Loading (Metal-to-Metal), ASTM, 1999.

[197] B. Broughton, M. Gower, Preparation and testing of adhesive joints, (2001) 1–77.

[198] M. Kobayashi, M. Terada, A. Takahara, Reversible adhesive-free nanoscale adhesion utilizing oppositely charged polyelectrolyte brushes, Soft Matter. 7 (2011) 5717–5722.

[199] S. Vahabi, B. Nazemi Salman, A. Javanmard, Atomic Force Microscopy Application in Biological Research: A Review Study, Iran. J. Med. Sci. 38 (2013) 76–83. http://www.ncbi.nlm.nih.gov/pmc/articles/PMC3700051/.

[200] S. Liu, Y. Wang, Application of AFM in microbiology: a review, Scanning. 32 (2010) 61–73.

[201] A.M. Whited, P.S.-H. Park, Atomic force microscopy: a multifaceted tool to study membrane proteins and their interactions with ligands., Biochim. Biophys. Acta. 1838 (2014) 56–68. doi:10.1016/j.bbamem.2013.04.011.

[202] Y. Song, B. Bhushan, Atomic force microscopy dynamic modes: modeling and applications, J. Phys. Condens. Matter. 20 (2008) 1–29.

[203] V. Bellitto, Atomic Force Microscopy-Imaging, Measuring and Manipulating Surfaces at the Atomic Scale, Croatia, InTech, 2012.

[204] T. Kokubo, H. Takadama, How useful is SBF in predicting in vivo bone bioactivity?, Biomaterials. 27 (2006) 2907–2915. doi:http://dx.doi.org/10.1016/j.biomaterials.2006.01.017.

[205] G. Malich, B. Markovic, C. Winder, The sensitivity and specificity of the MTS tetrazolium assay for detecting the in vitro cytotoxicity of 20 chemicals using human cell lines., Toxicology. 124 (1997) 179–192.

3. CHAPTER 3 – THIN LBL COATINGS WITH SUPERIOR ADHESIVE AND BIOACTIVE PROPERTIES

Ana C. Almeida[1,2], Ana C. Vale[1,2], Natália M. Alves[1,2]

[1] 3B´s Research Group – Biomaterials, Biodegradables and Biomimetics, University of Minho, Headquarters of the European Institute of Excellence on Tissue Engineering and Regenerative Medicine. AvePark, 4806-909, Taipas, Guimarães, Portugal.

[2] ICVS/3B's PT Associate Laboratory, Guimarães, Portugal.

Abstract

Inspired by the marine mussel's adhesive proteins (MAPs) and the tough nacre-like structure, different configurations of nanostructured films were developed by layer-by-layer (LbL) assembly, using the dip-coating method. Multifunctional (MF) films were constructed using bioactive glass nanoparticles (BGNPs) as the inorganic phase and hyaluronic acid (HA) and chitosan (CHT) based polymers as the organic phase. Polymeric (CTR) films were also constructed using the same above mentioned polysaccharides. In addition, since the catechol groups are the main responsible for the outstanding adhesion in MAPs, their conjugation with both CHT and HA was carried out. The combined effect of the presence of catechol groups on both polymers is expected to result in coatings with enhanced adhesive properties, while the inclusion of BGNPs is expected to provide bioactivity. It was the first time that multilayered coatings containing both HA and CHT modified with catechol groups with or without BGNPs were developed. The substitution degrees of catechol-conjugated chitosan (CHT-C) and catechol-conjugated hyaluronic acid (HA-DN) were determined by ultraviolet-visible (UV-Vis) spectroscopy, showing that both modifications were successful. Prior to the LbL build-up, viscosity and zeta potential measurements of the polyelectrolytes (PE) were conducted. *In-situ* LbL growth of the films was monitored by quartz crystal microbalance with dissipation monitoring (QCM-D). It was found that the combination of CHT-C and HA-DN in a LbL assembly leads to the formation of a more compact structure than when this system has the presence of BGNPs. It was also shown that the developed coatings presented an improved adhesion. Bioactivity results evidenced the formation of a bone-like apatite layer onto the MF films after immersion in a simulated body fluid solution. Finally, *in-vitro* cellular tests confirmed an enhanced cell adhesion, proliferation, and viability for the developed biomimetic LbL films, demonstrating their potential to be used as coatings of a variety of implants.

Keywords: Biomimetic, Layer-by-Layer assembly, Catechol groups, Polysaccharides, Bioglass nanoparticles, Coatings, Dip-coating

3.1 Introduction

Mimicking structures and functions from natural organisms, as the marine mussels, to produce high-performing and environmentally friendly materials, has recently been a hot research topic due to their superior mechanical and biological properties compared to synthetic materials [1–6]. Systems inspired on the surface chemistry and the rough nacre structure of molluscs have attracted much attention, since they can provide a solution for creating robust layer-by-layer (LbL) films with improved adhesive properties [7–9]. Nacre is a natural composite of hard shells of molluscs with outstanding mechanical properties thanks to its hierarchical layered structure containing an inorganic matrix, 95 wt% aragonite (crystallographic form of $CaCO_3$), and an organic matrix, 5 wt% proteins and polysaccharides [6–8]. The combination of the layered organic and inorganic components provides structure with high mechanical resistance and toughness [7,8]. Toughness is essentially provided by the organic matrix that plays an important role in dissipating the mechanical energy, owing to its capability for undergoing inelastic deformations [8]. The strong underwater adhesion of marine mussels to almost all types of surfaces, have recently attracted much attention [1,9,10]. It has been confirmed that the ortho-dihydroxyphenyl (catechol) moiety of amino acid 3,4-dihydroxy-phenylalanine (DOPA) present in secreted mussel's adhesive proteins (MAPs), is responsible for this strong adhesion between adhesive pads of mussels and opposing surfaces [1,10–12]. The catechol group had an extremely strong affinity to various organic/inorganic surfaces such as metals, metal oxides, polymer surfaces, and even biomacromolecules, such as pig gastric mucin glycoprotein [13,14]. In addition, researchers have utilized catechol chemistry to modify several types of flat substrates [2,15], particles [16,17] and to improve the mechanical properties of polymer composites [6].

So, inspired by the inorganic–organic composites nacre-like and by MAPs, we propose new robust multifunctional (MF) LbL films developed by the alternate combination of inorganic nanoparticles with biopolymeric layers bearing catechol groups. In parallel, biopolymeric films containing catechol groups were also proposed for the sake of comparison. Dip-coating was the LbL deposition technique chosen for film build-up, since is relatively simple and suitable for coating substrates with complex geometries [18,19]. In this study, we select natural polyelectrolytes such as chitosan (CHT) and hyaluronic acid (HA) with catechol functionalities as the organic phase in the LbL assembly, with the aim of enhancing film stability and improving adhesion strength. By conjugating catechol groups to both CHT and HA, through

carbodiimide chemistry, we not only preserve the cationic and anionic characteristics of the polymers, but also the electrostatic interactions. For the inorganic phase of the MF LbL coatings, we used bioactive glass nanoparticles (BGNPs) produced by a sol-gel method, since it expected that its inclusion will not only improve the mechanical performance of the produced coatings, but will also confer a bioactive character. Bioactivity provides bone-bonding ability to the coatings, hence, improving osteoconductivity [20–24].

Previous works of our group [25–27], have already used dip-coating to prepare LbL coatings based on catechol-modified HA (HA-DN), CHT and BGNPs. It was found that the combination of these materials resulted in nanostructured films with enhanced adhesion properties, bioactivity and mechanical performance. In the current work, we hypothesized that the modification of both polymers, HA and CHT, with catechol groups can produce multilayer films with superior adhesive strength than the ones developed in these previous studies, as the content of catechol groups will be higher. We have optimized the modification of CHT with catechol groups, based on other works [28–30] to produce the catechol-modified CHT (CHT-C). We have also optimized HA-DN synthesis to achieve higher DS (%). Therefore, we believe that these biocompatible LbL films could be used as coatings on a variety of orthopaedic devices and scaffolds, to create an environment compatible with osteogenesis and promote a bone-friendly interface with improved adhesion properties. Thus, using MF films, a natural bonding junction between the implant and host's bone could be established in a simple and versatile way, avoiding the typical use of cements. On the other hand, an improved bonding between orthopaedic implants and other tissues could be achieved by using highly adhesive biopolymeric films, as an alternative to synthetic tissue adhesives.

3.2 Materials and Methods

3.2.1 Materials

Medium molecular weight chitosan (ref. 448877, Brookshield viscosity 200–800 cP, Mw = 190–310 kDa, 75–85% N-deacetylation degree), hyaluronic acid sodium salt from *Streptococcus equi* (ref. 53747, Mw = 1500–1800 kDa), dopamine hydrochloride (DN, ref. H8502, Mw = 189,64 Da), hydrocaffeic acid (ref. 102601, 98%, Mw = 182.17 Da), N-(3-(dimethylamino)propyl)-N′-ethylcarbodiimide hydrochloride (EDC, ref. 03450, purum, ≥98.0% (AT), Mw = 191.70 Da), dialysis tubing cellulose membrane (avg. flat width 33 mm), calcium nitrate tetrahydrate ($Ca(NO_3)_2 \cdot 4H_2O$ C_2H_6O, 99 %), citric acid

monohydrate (99%), ammonium phosphate dibasic ($(NH_4)_2HPO_4$, ≥98%), ethanol absolute, ammonium hydroxide solution (maximum of 33 % NH_3), sodium chloride (NaCl), magnesium chloride hexahydrate ($MgCl_2 \cdot 6H_2O$, ≥99.0%), sodium sulfate (Na_2SO_4 ≥99.0%), tris(hydroxymethyl)aminomethane (Tris buffer, $(CH_2OH)_3CNH_2$, 99%), hydrochloric acid (HCl), and polyethylenimine (PEI) were purchased from Sigma-Aldrich (St. Louis, Mo, USA). Tetraethyl orthosilicate (TEOS, 99.90%) was purchased from Merck KGaA (Darmstadt, Germany). Potassium chloride (KCl), acetone and 2-propanol were obtained from VWR International (UK). Sodium hydroxide (NaOH) was purchased from Fisher Chemical (Fisher Scientific UK, Leics, UK) and hydrogen peroxide 30% (w/v) was obtained from Panreac AppliChem (Darmstadt, Deutschland). Sodium of hydrogen carbonate ($NaHCO_3$), di-potassium hydrogen phosphate trihydrate ($K_2HPO_4 \cdot 3H_2O$) and calcium chloride ($CaCl_2$) were purchased from Merck (Merck Sharp & Dohme Corp., Kenilworth, NJ, USA). Standard gold QCM-D sensor crystals (QSX 301 Gold, Au 100 nm, 14 mm diameter) were purchased from Q-Sense (BiolinScientific, Stockholm, Sweden). For the cellular behaviour assays, the mouse fibroblast cell line L929 was obtained from European Collection of cell cultures (ECACC, UK). Dulbecco's modified minimum essential medium (D-MEM), fetal bovine serum (FBS), phalloidin–tetramethylrhodamine B isothiocyanate and DAPI (4',6-diamidino-2-phenylindole) were purchased from Sigma-Aldrich (St. Louis, MO, USA). MTS (3-(4,5-dimethylthiazol-2-yl)-5-(3-carboxymethoxyphenyl)-2-(4-sulfophenyl)-2H-tetrazolium) was obtained from VWR International (UK). CHT was the only reagent that was previously purified by recrystallization. Borosilicate glass plates (3 mm thickness), and circular coverglasses (Ø 18 mm, Agar Scientific, Stansted, UK), were used as substrates for deposition of LbL coatings by dip-coating method. Prior to coating deposition, all the substrates were cleaned in sequential ultrasonic baths to remove surface impurities: 1º - 15 minutes with acetone; 2º - 15 minutes with ethanol; 3º - 15 minutes in osmotized water; and finally, they were dried with a nitrogen flow.

3.2.2 HA-DN Synthesis

HA-DN was synthesized using the procedure proposed by Lee and co-workers [2], with some modifications. HA modification with catechol groups was performed by the carbodiimide chemistry using EDC as an activation agent of the carboxyl groups on HA chains. HA solution (10 $mg.mL^{-1}$) was prepared in phosphate buffered saline (PBS) solution and the pH was adjusted to 5.5 using 0.5 M HCl or 0.5 M NaOH aqueous solution under magnetic stirring. To limit the oxygen interaction with the solution, HA solution was purged with nitrogen for 30 min. Then, 338 mg of EDC and 474 mg of DN were added to the previous solution, and the pH was maintained at 5.5 at 4 °C. The resulting solution was divided in

two different solutions with different reaction times, i.e., HA-DN*$_{4h}$ and HA-DN*$_{36h}$. Unreacted chemicals and urea byproducts were removed by dialysis against an acidic osmotized water solution (pH 5.0, HCL solution) for 4 days and osmotized water for 1 day, using a dialysis membrane tube, at 4°C. Finally, the HA-DN conjugates were freeze-dried for 4 days and stored at -20°C. The entire procedure and storage of the produced HA-DN was performed at 4°C and protected from light to prevent oxidation of catechol groups.

3.2.3 CHT-C Synthesis

CHT-C synthesis was based on the procedure proposed by Kim *et al.* [28], Xu *et al.* [29] and Ghadban *et al.* [30]. As in HA-DN synthesis, CHT modification with catechol groups was accomplished by the carbodiimide chemistry using EDC as an activation agent. 1% (w/v) CHT solution was prepared in HCl solution at pH 2.5. Then, a HCA solution (59 mg.mL^{-1}) was prepared in osmotized water and an EDC solution (119 mg.mL^{-1}) was prepared in a mixture of osmotized water and ethanol. These two previous solutions were mixed and added to CHT solution, under stirring at 4° C, followed by the addition of 1M NaOH solution to obtain a final pH of 4.8. The reaction was allowed to continue for 18 h, under nitrogen atmosphere for 30 min. After that, the product, CHT-C*$_{18h}$, was purified by dialysis against an acidic osmotized water solution (pH 5.0, HCL solution) for 3 days and osmotized water for 4 hours, using a dialysis membrane tube, at 4°C. The resulting product was freeze-dried and stored at -20°C. Also, as in the HA-DN synthesis, the entire procedure and storage of the produced CHT-C was performed at 4°C and protected from light to prevent oxidation of catechol groups.

3.2.4 BGNPs Production

The procedure to obtain the ternary system of BGNPs with the composition SiO_2:CaO:P_2O_5 (mol.%) = 50:45:5, was based on the sol-gel method already optimized by two previous works [20,31]. First, a "solution A" was prepared through a mixture of precursor´s solutions. So, 6% (w/v) of calcium nitrate tetrahydrate, calcium precursor, was dissolved in osmotized water at room temperature. Then, 9.8353 mL of TEOS, silica precursor, together with 60 mL of ethanol absolute was added to the previous solution. The pH of solution A was adjusted to 2 with citric acid solution (10 % (w/v)), under stirring for 3 hours. After that, a "solution B" was also prepared by adding 0.07% (w/v) of ammonium phosphate dibasic, phosphorus precursor, to osmotized water. The pH of solution B was adjusted to 11.5 with ammonia hydroxide solution. Under stirring, the solution A was slowly added, drop-by-drop, to solution B and the

pH was maintained at 11.5 by continuous supplement of ammonia hydroxide solution. This reaction mixture was left under stirring during 48 h and then, under resting for 24 h to occur the gel particle precipitation. Afterwards, the gel precipitate was washed tree times with osmotized water and stored during 24 h at -80°C to be subsequently freeze-dried for 7 days. The obtained white gel powder was calcinated at 700°C for 3 h to get the BGNPs with improved bioactivity.

3.2.5 UV-Vis Spectroscopy Characterization

DS (%) of catechol groups in the conjugates were determined using a Synergy HT Multi-Mode Microplate Reader (BioTek Instruments, U.S.A.) with an absorbance measurement range of 200 to 350 nm, and a quartz microplate with 96 wells. Solutions of HA-DN*$_{4h}$, HA-DN*$_{36h}$ and CHT-C*$_{18h}$ with different concentrations, 0.5, 1, 2, 3, 4, 5 mg.mL^{-1} in 0.15 M NaCl, were prepared for the UV analysis. 100 µl of test solution was used in each well, and 0.15 M NaCl solution was used as blank.

3.2.6 Rheological Characterization

The viscosity of the different polyelectrolytes (PEs) used was determined on a Kinexus Pro Rheometer (Malvern Instruments Ltd, UK) fitted with cone-plate geometry. A cone with 40 mm diameter and 4° angle (CP4/40: SR 1772SS) and a plate with 65 mm diameter (PL65: S1425SS) were used. Rotational measurements of CHT, HA, CHT-C*$_{18h}$, HA-DN*$_{4h}$ and HA-DN*$_{36h}$ solutions at different concentrations of 0.5, 1, 2, 3 mg.mL^{-1}, in 0.15 M NaCl, were made. The steady-state flow measurements were performed under controlled-stress conditions, where the torque amplitude was imposed using a logarithmic ramp of shear rate ranging from 10 to 100 s^{-1}. All experiments were performed at a controlled temperature of 25 °C, and results represent the average of 3 measurements. Measured data were registered with rSpace for Kinexus Pro 1.7 software.

3.2.7 Zeta Potential (ζ) Characterization

The zeta potential of the different PEs was measured with a Zetasizer equipment (Nano ZS, Malvern, UK), at 25°C, and the results were given as an average of 3 measurements for each 0.5 mg.mL^{-1} solution in 0.15 M NaCl solution. Immediately prior to measurement, the BGNPs solution was dispersed for 15 minutes in an ultrasonic water bath (DT100H SONOREX, Bandelin electronic GmbH & Co. KG, Berlin, Deutschland) to prevent nanoparticle agglomeration and precipitation.

3.2.8 Quartz Crystal Microbalance with dissipation (QCM-D) Monitoring: Multilayer Films Modelling

The build-up of LbL coatings with different materials was monitored *in situ* by QCM-D (Q-sense, E4 system, Sweden) onto gold-coated quartz crystals (14 mm diameter, QSX301 Gold, Q-Sense). QCM-D is an accurate technique which make use of piezoelectric quartz crystals to detect adsorption of molecules, at nanoscale, by measuring frequency changes [32]. In addition, from the decay monitoring of the crystal's oscillation is quantified the dissipation which represents the viscoelastic properties of the adsorbed mass [33]. So, through the QCM-D monitoring it is possible to simultaneously measure the adsorbed amount, given by the normalized resonance frequency ($\Delta f/\nu$) of each overtone to the fundamental resonant, and the variation of the viscoelastic properties, given by energy dissipation (ΔD), of the multilayer film in real time [33].

Previously to QCM-D monitoring, the quartz crystals were cleaned in an ultrasonic water bath (DT100H SONOREX, Bandelin electronic GmbH & Co. KG, Berlin, Deutschland) with sequential sonication for 5-10 min in: 2% (v/v) acetic acid solution, mixture of osmotized water, ammonia hydroxide and hydrogen peroxide 30 % (w/v) at 75° C, acetone, isopropanol, ethanol, and ultrapure water. The crystals were then dried with flowing nitrogen gas and treated with UV/Ozone cleaner (Bioforce Nanoscience, ProCleaner 220) for 10 min.

To ensure that the crystals are perfectly clean (null frequency), all experiments started with a 0.15M NaCl baseline. The crystals were excited at multiple overtones, 3, 5, 7, 9, and 11, corresponding respectively, to 15, 25, 35, 45, and 55 MHz fundamental resonant *f*. Adsorption took place at 25 °C, and at a constant flow rate of 50 µL.min^{-1} using a peristaltic pump. LbL coatings were produced using fresh solutions prepared in 0.15 M NaCl and with the pH adjusted to 5.5 using 0.5 M HCl or 0.5 M NaOH aqueous solutions. LbL construction started with injection of CHT (1 mg.mL^{-1} with 2% (v/v) of acetic acid) or CHT-C*$_{18h}$ (1 mg.mL^{-1}) used as polycations, while HA (0.5 mg.mL^{-1}), HA-DN$_{4h}$* (0.5 mg.mL^{-1}), HA-DN$_{36h}$* (0.5 mg.mL^{-1}), and BGNPs (2.5 mg.mL^{-1}) acted as polyanions and were used as ended-polymer layer. Before the QCM experiments, the BGNPs suspension was dispersed in an ultrasonic water bath for 15 to 20 minutes to avoid agglomeration and precipitation of nanoparticles. The injection of the polymers was standing for 10 min and the nanoparticles for 20 min to allow the adsorption until the equilibrium was achieved in QCM-D monitoring. A rising step of 5 min, between the PE adsorptions, using 0.15M NaCl solution with the pH adjusted to 5.5 was included.

Distinct configurations, each with 22 layers, were developed, as shown in Figure 3.1: the MF LbL coatings containing [CHT/HA/CHT/BGNPs]$_5$ + [CHT/HA] (MF1), [CHT-C*$_{18h}$/HA/CHT-C*$_{18h}$/BGNPs]$_5$ + [CHT-C*$_{18h}$/HA] (MF2), [CHT/HA-DN*$_{4h}$/CHT/BGNPs]$_5$ + [CHT/HA-DN*$_{4h}$] (MF3), [CHT/HA-

DN*$_{36h}$/CHT/BGNPs]$_5$ + [CHT/HA-DN*$_{36h}$] (MF4), [CHT-C*$_{18h}$/HA-DN*$_{4h}$/CHT-C*$_{18h}$/BGNPs]$_5$ + [CHT-C*$_{18h}$/HA-DN*$_{4h}$] (MF5), [CHT-C*$_{18h}$/HA-DN*$_{36h}$/CHT-C*$_{18h}$/BGNPs]$_5$ + [CHT-C*$_{18h}$/HA-DN*$_{36h}$] (MF6), and respective controls (CTR) containing [CHT/HA]$_{11}$ (CTR1), [CHT-C*$_{18h}$/HA]$_{11}$ (CTR2), [CHT/HA-DN*$_{4h}$]$_{11}$ (CTR3), [CHT/HA-DN*$_{36h}$]$_{11}$ (CTR4), [CHT-C*$_{18h}$/HA-DN*$_{4h}$]$_{11}$ (CTR5), [CHT-C*$_{18h}$/HA-DN*$_{36h}$]$_{11}$ (CTR6).

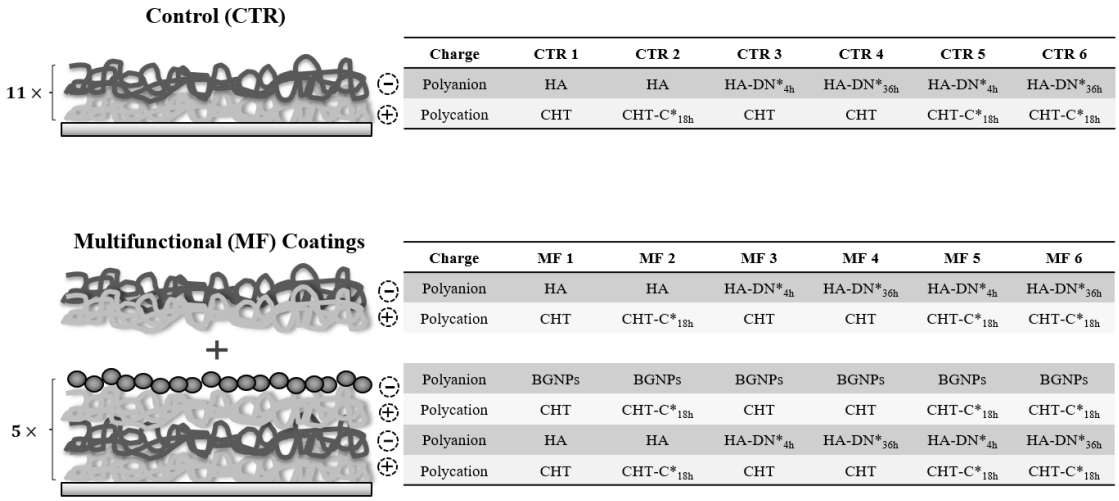

Charge	CTR 1	CTR 2	CTR 3	CTR 4	CTR 5	CTR 6
Polyanion	HA	HA	HA-DN*$_{4h}$	HA-DN*$_{36h}$	HA-DN*$_{4h}$	HA-DN*$_{36h}$
Polycation	CHT	CHT-C*$_{18h}$	CHT	CHT	CHT-C*$_{18h}$	CHT-C*$_{18h}$

Charge	MF 1	MF 2	MF 3	MF 4	MF 5	MF 6
Polyanion	HA	HA	HA-DN*$_{4h}$	HA-DN*$_{36h}$	HA-DN*$_{4h}$	HA-DN*$_{36h}$
Polycation	CHT	CHT-C*$_{18h}$	CHT	CHT	CHT-C*$_{18h}$	CHT-C*$_{18h}$
Polyanion	BGNPs	BGNPs	BGNPs	BGNPs	BGNPs	BGNPs
Polycation	CHT	CHT-C*$_{18h}$	CHT	CHT	CHT-C*$_{18h}$	CHT-C*$_{18h}$
Polyanion	HA	HA	HA-DN*$_{4h}$	HA-DN*$_{36h}$	HA-DN*$_{4h}$	HA-DN*$_{36h}$
Polycation	CHT	CHT-C*$_{18h}$	CHT	CHT	CHT-C*$_{18h}$	CHT-C*$_{18h}$

Figure 3.1 – Schematic illustration of the different multifunctional (MF) and control (CTR) LbL coatings.

During the entire monitoring, $\Delta f/\nu$ and ΔD shifts were continuously recorded as a function of time. The thickness of the multilayer films was estimated using the Voigt model in the Q-Tools software (Q-Sense). According to this model, the Δf and ΔD are given by equations (3.1) and (3.2), respectively [34]:

$$\Delta f \approx -\frac{1}{2\pi\rho_0 h_0}\left\{\frac{\eta_B}{\delta_B}+h_L\rho_L\omega-2h_L\left(\frac{\eta_B}{\delta_B}\right)^2\frac{\eta_L\omega^2}{\mu_L^2+\omega^2\eta_L^2}\right\} \quad (3.1)$$

$$\Delta D \approx \frac{1}{\pi f\rho_0 h_0}\left\{\frac{\eta_B}{\delta_B}+2h_L\left(\frac{\eta_B}{\delta_B}\right)^2\frac{\mu_L\omega}{\mu_L^2+\omega^2\eta_L^2}\right\} \quad (3.2)$$

Where ω is the angular frequency of the oscillation, ρ_0 and h_0 are the density and thickness of the crystal, respectively, η_B the solution viscosity, δ_B (=$(2\eta_B/\rho_B\omega)^{1/2}$) the viscous penetration depth of the shear wave in the solution, ρ_B the solution density, and h_L, ρ_L, η_L and μ_L the thickness, density, viscosity and elastic shear modulus of the adsorbed layer, respectively [33,34].

From the modelled results obtained by these equations, the QTools software from Q-Sense was used to compare them with Δf and ΔD experimental values and finds a best fit using a Simplex algorithm (Total ChiSqr) to find the minimum in the sum of the squares of the scaled errors. For this, ρ_B, η_B and ρ_L should be changed to get the lower error possible [33]. In this study, a fluid density of 1000 kg.m^{-3}, a fluid

viscosity of 1 mPa.s and a layer density of 1200 kg.m^{-3} was assumed. In addition, the $\Delta f/\nu$ and ΔD shifts were fitted to the 7th overtone.

3.2.9 Adhesion Tests

The adhesive strength of LbL coatings using glass plates with 3 mm thickness as the substrate was evaluated following an adaptation of the procedure described in the ASTM D1002 standard. Lap shear tests were performed using a universal mechanical testing machine (Instron 5543, USA) with a 1 kN load cell.

The LbL assembly of different LbL coatings was performed by dip-coating using fresh PE solutions prepared with 0.15 M NaCl solution, at room temperature. Seven different PE solutions, containing 1 mg.mL^{-1} CHT with 2% (v/v) of acetic acid, 0.5 mg.mL^{-1} HA, 1 mg.mL^{-1} CHT-C*$_{18h}$, 0.5 mg.mL^{-1} HA-DN*$_{4h}$, 0.5 mg.mL^{-1} HA-DN*$_{36h}$, 2.5 mg.mL^{-1} BGNPs and 5 mg.mL^{-1} PEI, were prepared. Except for PEI, the pH of the PE solutions was adjusted to 5.5 using 0.5 M NaOH or 0.5 M HCl aqueous solutions under magnetic stirring. To avoid BGNPs agglomeration, the solutions containing the nanoparticles were kept under stirring and periodically subjected to an ultrasonic treatment during 10 – 15 minutes. In this study, the HA, HA-DN*$_{4h}$, HA-DN*$_{36h}$ and BGNPs were used as polyanion, while CHT and CHT-C*$_{18h}$ were used as polycation. PEI was used as an initial layer precursor, by immersing each substrate for 20 min, prior to multilayer deposition. After immersion in PEI, the substrates were alternately dipped in the oppositely-charged PE solutions, to produce LbL coatings with 11 bilayers, i.e. 22 layers (see Figure 3.1), and to be able to compare the results with those obtained in previous works [81], [83]. A polycation was used to initiate alternating deposition between oppositely charged PE. All substrates used in the experiments were rinsed with acetone, ethanol and osmotized water and then dried with a nitrogen flow before each use. The dipping time for the CHT, HA and their respective conjugates (CHT-C and HA-DN) was 10 minutes, whereas for the BGNPs suspension it was 20 minutes. These dipping times were established after an optimization process in the two previously mentioned works [81], [83], where it was verified by a QCM-D study that these corresponded to the moment when the PE adsorption reached equilibrium. In addition, a rinsing step was included for 5 min with 0.15 M NaCl solution, between the adsorptions of each PE.

Immediately after the LbL deposition, pairs of glass plates were put in contact with an overlapping area of $15 \times 20\ mm^2$. The specimens were tightly clamped using metal binder clips, and maintained at 37°C overnight. To perform the adhesion experiments, each end of the specimens was placed in the grips of the mechanical testing machine. At the upper specimen edge an axial tensile load was applied, at a constant cross-head speed of 5 mm.min^{-1} to be pulled until the detachment of the specimens. Five

specimens of each condition were tested, at room temperature, to calculate the mean and standard deviation values of the ultimate adhesion strength.

The testing software used was the Bluehill2 (INSTRON Corporation), and stress-strain curves was obtained for each testing condition from the maximum tensile stress (σ_{Tmax}) and the maximum tensile strain (ε_{Tmax}) calculations. The σ_{Tmax} is the maximum stress that the film can support without detachment and is obtained from the load applied (F) data, acquired during the test, and the overlapping area (A_0), equation (3.3). The ε_{Tmax} corresponds to the strain value reached for the σ_{Tmax} and is obtained from the length change (ΔL) data, acquired during the test, and the initial length (L_0), equation (3.4) [27].

$$\sigma_{Tmax} = \frac{F(N)}{A_0\ (m^2)} \tag{3.3}$$

$$\varepsilon_{Tmax} = \frac{\Delta L(m)}{L_0\ (m)} \tag{3.4}$$

3.2.10 *In-Vitro* Bioactivity Studies

The bone-bonding ability of a material can be asserted *in-vitro* by evaluating the formation of apatite on its surface, when immersed in simulated body fluid (SBF). This solution contains ionic concentrations nearly equal to those of human blood plasma [35].

Thus, standard *in-vitro* bioactivity studies were performed by immersing the dip-coated LbL coatings in a pH adjusted SBF solution to 7.4, which was prepared by following the Kokubo and Takadama procedure [35], in order to simulate the concentration of ionic species and pH present in human blood plasma. Each dip-coated coverglass was immersed for 7 days in 13 mL of SBF solution at 37°C. Likewise, dip-coated coverglass pieces, with the same LbL coatings, were immersed for 14 days in 13 mL of SBF solution at 37°C. After removing from SBF solution, these coverglasses were cleaned three times with ultrapure water and dried at room temperature. The bone-like apatite layer formation was characterized by a surface analysis using the scanning electron microscopy (SEM, JSM-6010 LV, JEOL, Japan) coupled with energy dipersive X-ray spectroscopy (EDS, INCAx-Act, PentaFET Precision, Oxford Instruments) and X-ray diffraction (XRD, Bruker AXS D8, Discover, USA) technologies. Before SEM analysis the samples were sputtered with a thin platinum layer, using a sputter coater EM ACE600 (Leica Microsystems, Germany). The XRD experiments were performed at 40 kV and 40 mA using Cu Kα radiation (λ = 1.54060 Å). The XRD detector was scanned over a range of 2θ angles from 15° to 60° at a speed of 0.04°/1s.

The crystalline phases identification was achieved using an analytical software EVA and were indexed using the ICDD database (International Centre for Diffraction Data).

3.2.11 In-Vitro Biological Studies

Studies of morphology and cellular activity were performed with the aim of evaluating the *in-vitro* biological performance of the dip-coated LbL conditions build-up onto coverglasses.

The mouse fibroblast cell line L929, from European Collection of cell cultures (ECACC, UK), was chosen to perform direct contact tests with the developed LbL coatings. Before cell seeding, the samples were sterilized by ethylene oxide sterilization (EO) which takes approximately 12h, with 3h of EO exposure at 42°C and, then, they were washed twice with sterile PBS. Cells were cultured with Dulbecco's modified minimum essential medium (D-MEM) supplemented with 10% fetal bovine serum (FBS) and 1% antibiotic. The cultures were then incubated at 37°C, in humidified air atmosphere of 5% CO_2, and placed to grow until confluence. The culture medium was replaced every 2 days. When 90% of confluence was reached, the cells were seeded onto the LbL coatings, using 3 replicates (n=3), at a density of 1×10^4 cells per sample and then incubated at 37°C for one, three and seven days. After 4 hours, supplemented D-MEM was added to each well to nourish the adhered cells.

MTS Assays

After specific time points (1, 3 and 7 days) a MTS (3-(4,5-dimethylthiazol-2-yl)-5-(3-carboxymethoxyphenyl)-2-(4-sulfophenyl)-2H-tetrazolium) assay was performed to evaluate the cytotoxicity of the dip-coated LbL conditions, and to compare the relative cellular viability (%) between each condition and a positive control, the tissue culture polystyrene (TCPS).

The LbL coatings were immersed with a solution composed by a 1:5 ratio of MTS reagent and D-MEM culture medium without phenol red or FBS, and then incubated for period of 3 hours at 37 °C. All cytotoxicity tests were conducted by using three replicates (n=3). Finally, the optical density (OD) was read at 490 nm on a multiwell microplate reader (Synergy HT, BioTek Instruments, USA).

Phalloidin/DAPI Analysis

Phalloidin/DAPI fluorescent assays were performed at each time culture period, 1, 3 and 7 days, to obtain fluorescence images. Briefly, for each time point, the culture medium was removed, and 10% formalin was added to each well in three replicates (n=3) for 30 minutes. Then, formalin was removed, and the wells of the plate were washed with PBS. The samples were labelled with fluorescent stains:

Phalloidin (phalloidin-tetramethylrhodamine B isothiocyanate), which binds to actin filaments staining the cytoskeleton of the cells in red, and DAPI (4',6-diamidino-2-phenylindole), which binds to DNA regions staining cell nuclei in blue. For this, first, phalloidin was incubated with samples at 1:200 in PBS for 30 min and then, DAPI was added at 1:1000 in PBS for 5 min. This procedure was done at room temperature and protected from light. Finally, the samples were washed twice with PBS, left overnight, and then visualized in the dark using a fluorescence microscope (Transmitted and Reflected Light Microscope with Apotome 2, Zeiss, Germany). The images were acquired and processed using AxioVision software version: Zeiss 2012 (Zeiss, Germany).

3.2.12 Statistical Analysis

The results of all experiments were carried out at least in three replicates (n=3) and were presented as mean ± standard deviation (SD).

Statistical significance between groups was determined by One-way ANOVA with Turkey's Multiple comparison test, using Graph Pad Prism version 6.0 (GraphPad software, San Diego, CA). Statistical differences were represented and set to $p<0.05$(*), $p<0.01$(**), $p<0.001$(***), and $p<0.0001$(****).

3.3 Results and Discussion

3.3.1 Synthesis and Characterization of HA-DN and CHT-C conjugates

HA and CHT were modified with catechol groups as described at the experimental section. To confirm if the modification of HA and CHT was successful, solutions of HA-DN*$_{4h}$, HA-DN*$_{36h}$, and CHT-C*$_{18h}$ with different concentrations were analysed by UV-Vis spectroscopy.

The results obtained for both HA-DN conjugates are shown in Figure 3.2.

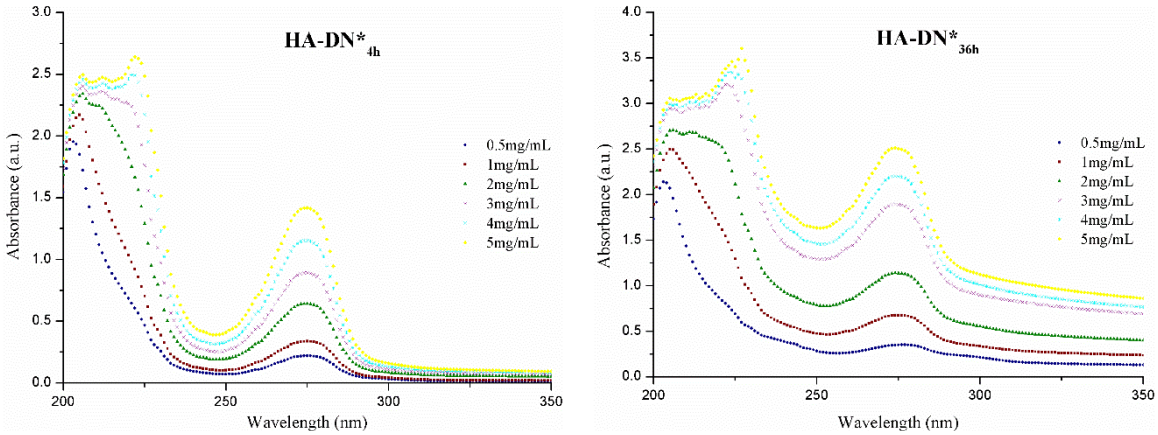

Figure 3.2 – UV-Vis spectra for different concentrations of HA-DN*$_{4h}$ and HA-DN*$_{36h}$.

Both spectra of the HA-DN conjugates exhibit a maximum absorbance peak for all concentrations at a wavelength of approximately 280 nm, which is more intense as the solution concentration increases. These results confirm the presence of the catechol groups in the modified HA, due to the presence of their characteristic peak at a wavelength of 280 nm [25,27], as opposed to the HA spectrum. In addition, the absence of additional peaks at wavelengths longer than 300 nm demonstrates that the synthesized conjugates were not oxidized [25,27,36].

Based on the results of Figure 3.2, the DS (%) of the HA-DN conjugates was estimated (see Appendix I) and their values were around 27% for HA-DN*$_{4h}$ and 54% for HA-DN*$_{36h}$. The DS (%) results obtained in this work were higher than those found in other works, which were only about 11 % [2,25,27]. These results can be explained by some different conditions that were employed in the HA-DN synthesis, such as the molecular weight of HA and/or the time of the reaction. Based on the present study, it was found that the increase in the reaction time from 4 to 36 hours contributed to an increase in the DS (%) from 27% to 54%.

Similarly, the UV-Vis characterization was performed for CHT-C*$_{18h}$ to confirm its successful modification and to obtain the DS (%). The experimental results are presented in Figure 3.3.

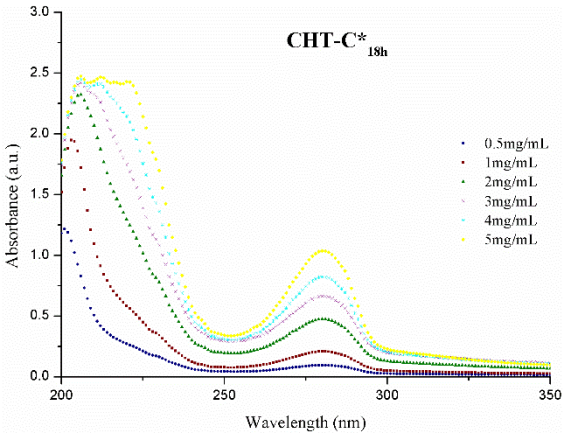

Figure 3.3 – UV-Vis spectra for different concentrations of CHT-C*$_{18h}$.

The CHT-C*$_{18h}$ spectrum also exhibits a maximum absorbance peak, which increases its intensity with the increase of the solution concentration, at a wavelength around 280 nm, confirming the presence of the catechol groups in the modified CHT. Likewise, the absence of additional peaks at wavelengths greater than 300 nm shows that the CHT-C*$_{18h}$ was not oxidized [28,29,37].

According to the DS (%) results obtained (see Appendix II), the estimated value for CHT-C*$_{18h}$ was approximately 9%. This value was lower than that found in other works [28–30]. However, in addition to the relative proportions of the reagents, and/or the molecular weight of CHT, and/or the reaction time used in the CHT-C*$_{18h}$ synthesis and that differ from those used in these studies, the conjugate was dissolved in 0.15 M NaCl.

3.3.2 Rheological Characterization of the PE used

To choose the best concentration for each PE used in the build-up of the LbL coatings, the viscosity of each one was evaluated by rotational measurements using a rheometer. The viscosity of different solutions of HA, HA-DN*$_{4h}$, HA-DN*$_{36h}$, CHT and CHT-C*$_{18h}$ at 0.5, 1, 2 and 3 mg.mL^{-1}, in 0.15 M NaCl, was measured to obtain a trend line. Figure 3.4 shows this trend line at different concentrations, obtained for each PE.

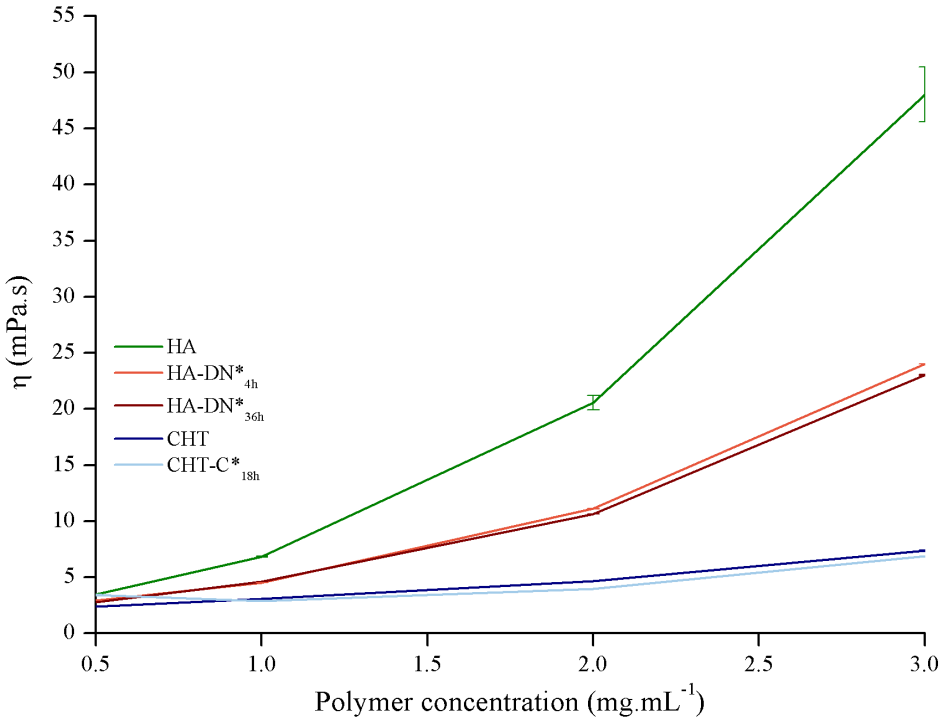

Figure 3.4 – Trend line of HA, HA-DN*$_{4h}$, HA-DN*$_{36h}$, CHT and CHT-C*$_{18h}$ solutions at different concentrations. Data are presented by means ± standard deviation (n = 3).

As can be seen in Figure 3.4, HA and HA-DN evidence an exponential trend line, i.e. their viscosities increase exponentially with increasing concentrations, while CHT and CHT-C show a near-linear trend

line, where viscosity increases almost linearly with concentration. The exponential character of HA has been reported in other studies [38,39], and this seems to happen not only with concentration but also with molecular weight. So, since the HA used in this study has a high molecular weight, its highly viscous properties can be explained. For CHT, the increase of its viscosity with the concentration, as well as with the increase of molecular weight, and deacetylation degree has also been reported elsewhere [40,41].

Furthermore, the viscosity of all conjugates is lower than the corresponding values of the unmodified polymers. This tendency seems to be more pronounced with increasing DS, since the viscosity reduction is higher for HA-DN. In the obtained UV-Vis results, it was shown that the HA-DN conjugates had a DS higher than CHT-C. In turn, this effect is also evidenced by the higher viscosity reduction in HA-DN*$_{36h}$ compared to HA-DN*$_{4h}$, which have a DS of 54 % and 27%, respectively.

So, the choice of concentration for each PE used was made considering these results. Similar viscosities were chosen for the build-up of LbL coatings. So, for HA and HA-DN a concentration value of 0.5 mg.mL^{-1} was used whereas for CHT and CHT-C a concentration value of 1 mg.mL^{-1} was chosen.

3.3.3 Zeta Potential (ζ) Characterization of PE used

The zeta potential of each PE used for the build-up of LbL coatings was measured - Table 3.1.

Table 3.1 – Zeta potential values for each PE solution with 0.5 mg.mL^{-1} concentration.

	CHT	**HA**	**HA-DN*$_{4H}$**	**HA-DN*$_{36H}$**	**CHT-C*$_{18H}$**	**BGNPs**
mV	19.2±1	-15.93±1.18	-19.47±1.70	-21.17±1.50	24.1±2.09	-20.5±0.76

By measuring the zeta potential, an indication of the degree of repulsion between adjacent particles, similarly charged, can be obtained. A value of ±25 mV can be taken as the arbitrary value to indicate whether the particles have low or high charge. Thus, for zeta potential values higher than ±25 mV, the particles tend to repel contributing to the stabilization of the dispersion, while for values below ±25 mV, the particles tend to aggregate leading to their precipitation [42].

As expected, zeta potential values for CHT and its derivates (CHT-C*$_{18h}$) were positive, whereas for HA and its derivates (HA-DN*$_{4h}$ and HA-DN*$_{36h}$) as well as for the BGNPs were negative, and in the same order of magnitude. Positive values for CHT and CHT-C are due to the positively charged amine groups present in their structures. On the other hand, negative charge values for HA and HA-DN are due to the negatively charged carboxylic groups present in their structures. The negative charge of the zeta potential for the BGNPs has already been reported in previous studies [27,43]. This value was -20.5±0.76 mV, which was similar to the value obtained for the same system in a previous work [21]. These results

indicated that the produced nanoparticles are stable and could better resist to aggregation and precipitation [42]. Lu *et al.* [44] demonstrated that a negative zeta potential on the BGNPs surface is crucial to promote the stable formation of an apatite layer. In addition, it has been suggested that surfaces with negative zeta potential values have more important biological effects *in-vivo* [45], promoting bone cell attachment and proliferation than surfaces with no or even positive electric charge [46,47].

Also, both HA and CHT polymers presented lower zeta potential values than their derivatives, HA-DN and CHT-C, respectively. In addition, HA-DN*$_{4h}$ showed a lower zeta potential (-19.47±1.70 mV) than HA-DN*$_{36h}$ (-21.17±1.50 mV). These results suggest that the polymer modification with catechol groups contributes to the zeta potential increase. Higher zeta potential values of these polymers could provide a more stable LbL assembly.

3.3.4 QCM-D Monitoring of the LbL Films Construction

The LbL assembly of multilayered films with CHT, CHT-C, HA, HA-DN, and BGNPs was monitored *in situ* using QCM-D. Through this technique it was possible to detect small changes in the mass and viscoelastic properties as the LbL films were adsorbed onto the quartz crystal surface.

The QCM-D results for the build-up of polymeric films (controls) are shown in Figure 3.5, and the results for their respective multilayered films with BGNPs are presented in Figure 3.6. These configurations were chosen to study the effect of the presence of BGNPs on the multilayer films, with or without conjugates on their final thickness, viscoelastic properties and on the success of the construction of stable LbL films.

The normalized frequency, $\Delta f/\nu$, where ν is the overtone, and the energy dissipation variation, ΔD, are shown in Figure 3.5 and Figure 3.6, as a function of the deposited layers for the different films. An $\Delta f/\nu$ decrease over time is observed after each layer deposition for each injection of CHT, HA, HA-DN*$_{4h}$, HA-DN*$_{36h}$, CHT-C*$_{18h}$ and BGNPs, indicating a successful multilayered film construction. However, a small increase of $\Delta f/\nu$ after each polymer adsorption can be observed, which is related to a desorption of a small fraction of free PE due to the rising step. On the other hand, each adsorbed layer is accompanied by a ΔD increase, due to the non-rigid layer structure of the film that is forming, typical of polymeric systems. Therefore, the multilayered films are expected to have higher damping properties as well as softer and more hydrated characteristics, which is also evidenced by the increase in overtones separation as the measurement evolves [25,48].

As can be seen in Figure 3.5 and Figure 3.6, the presence of the catechol groups appears to decrease the viscous component of the multilayered films. This ΔD decrease indicates that multilayered

films with catechol groups should probably be thinner, denser, more rigid, less water-rich and probably displaying a linear growth [25,48]. This effect was more pronounced in systems having CHT-C*$_{18h}$ (CTR2 and MF2) than in systems having one of the HA-DN conjugates (CTR3, CTR4, MF3 and MF4). Also, in the controls films where there was a combined presence of the two conjugates (CTR5 and CTR6) the ΔD decrease was noticeably more marked. On the other hand, when the BGNPs were included in the multilayered films having both conjugates present (MF5 and MF6), an opposite effect was observed, when compared with the respective controls (CTR5 and CTR6), showing a ΔD increase. Thus, when both conjugates are present, the addition of hydrophilic materials such as BGNPs seems to assist both in the hydration and in the viscoelastic properties of LbL films.

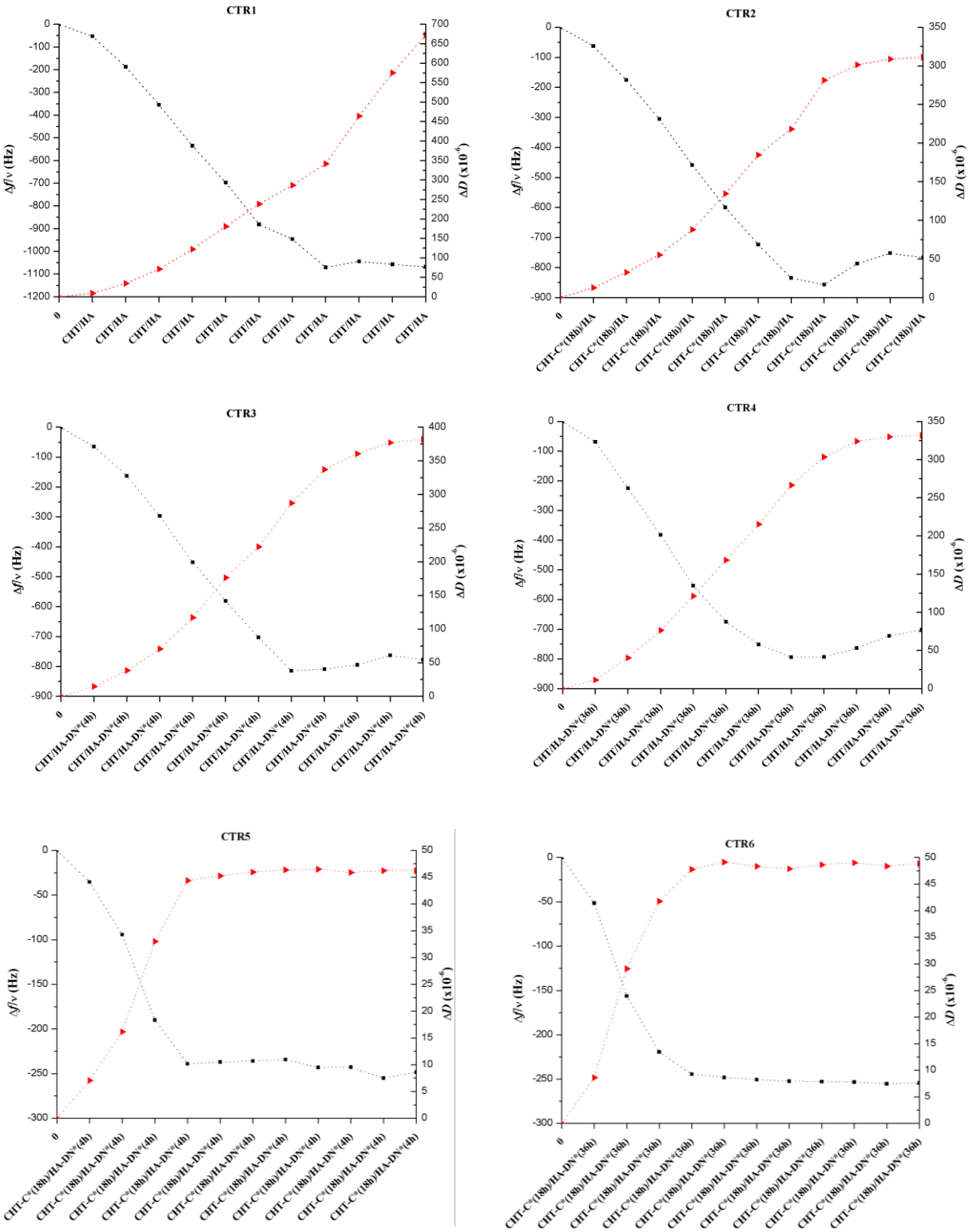

Figure 3.5 – QCM-D results representing the $\Delta f/\nu$ and ΔD variations at the 7th overtone as a function of the deposited layers in the build-up of polymeric films (CTR).

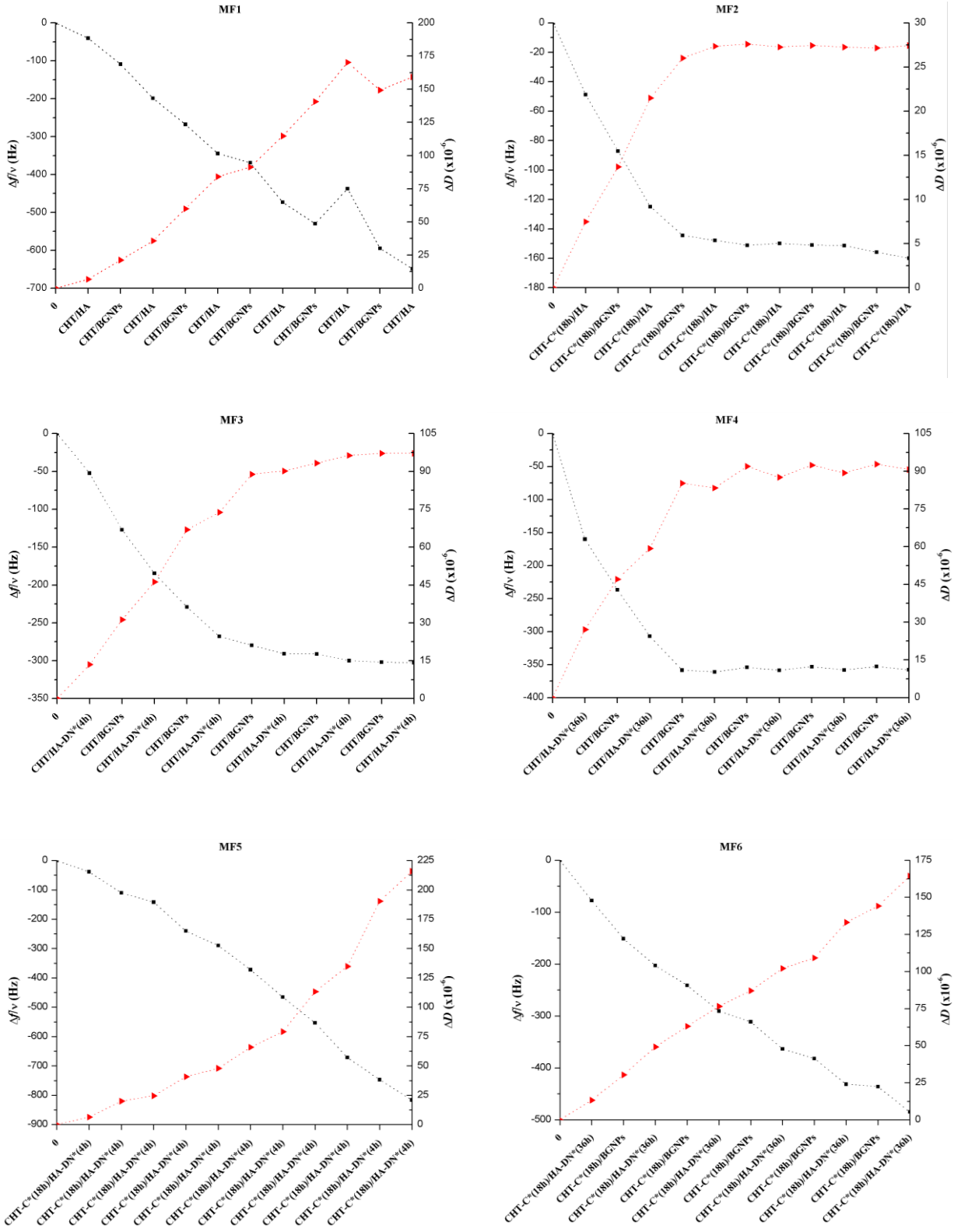

Figure 3.6 – QCM-D results representing the $\Delta f/\nu$ and ΔD variations at the 7th overtone as a function of the deposited layers in the build-up of the MF LbL coatings containing the BGNPs.

By applying a Voigt based model, it was possible to estimate the cumulative thickness evolution for all the studied conditions, as a function of the number of deposited layers, Figure 3.7.

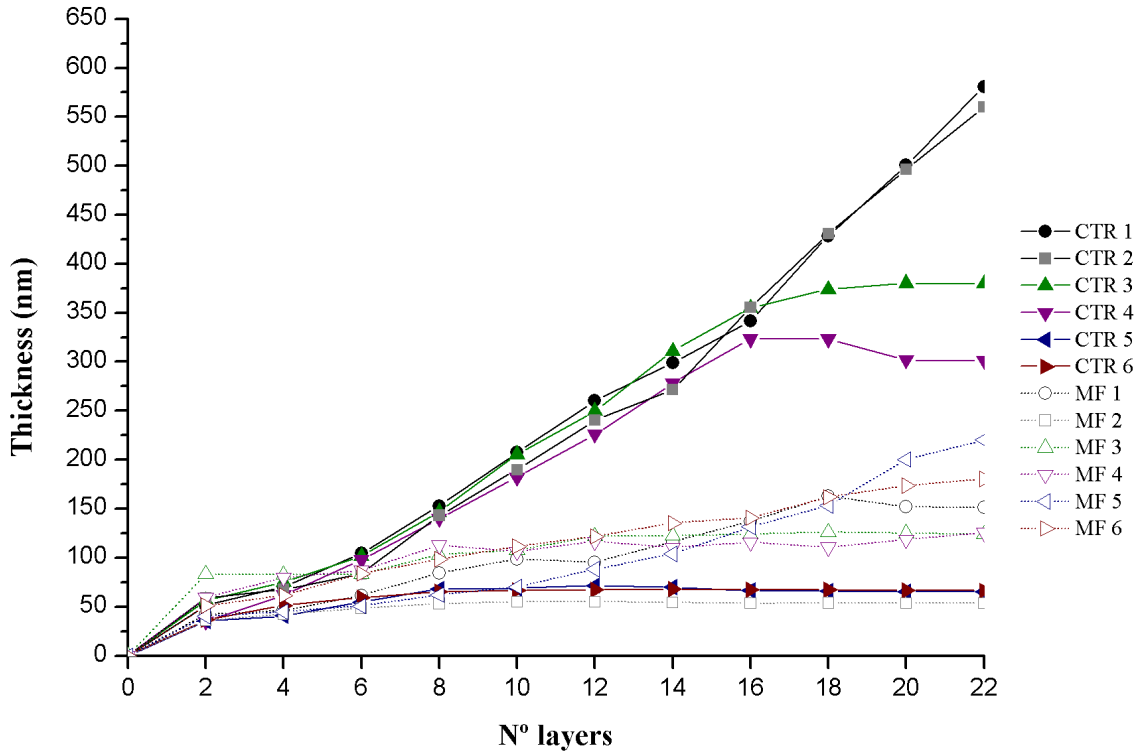

Figure 3.7 – Cumulative thickness evolution of the multilayered films constructed, as a function of the number of deposited layers.

As can be seen in Figure 3.7, the cumulative thickness evolution for CTR1 and CTR2 has a similar increase. Both demonstrate an exponential growth, which could explain the higher $\Delta f/\nu$ values for these two systems, with a final thickness for both around 500 nm. Other authors reported an exponential growth of multilayered films containing CHT and HA [25,49,50], which is in agreement with our results. Films with an exponential growth have been considered to occur by one of two general mechanisms: one attributed to the progressive increase in the film surface roughness upon successive deposition of each new layer, and one based on the ability of at least one PE component to diffuse "into" or "out" of a film during assembly [25,51]. Previous reports [51] have shown that this type of film growth can be caused by the molecular weight decrease of an anionic polymer, enhancing diffusion during assembly. On the other hand, as shown in Figure 3.7, the presence of the catechol groups seems to contribute to a linear film growth, revealing thinner and more rigid multilayered films. This linear trend line has already been reported for CTR3 and CTR4 films [25,48]. In particular, the DS increase of HA-DN seems to further promote the multilayered film compaction (CTR4>CTR3, MF4>MF3, and MF6>MF5). This effect was more pronounced in systems with both conjugates, CHT-C*$_{18h}$ and HA-DN*$_{4h}$ or HA-DN*$_{36h}$, (CTR5 and CTR6), having a final thickness of 65 and 66 nm, respectively. Here, the higher DS of CTR6 compared

to CTR5 did not show a considerable decrease in thickness, suggesting that multilayered films have probably reached their maximum compaction.

In a previous work [25], $[CHT/HA]_5$ and $[CHT/HA\text{-}DN]_5$ films with a final thickness of approximately 130 nm and 75 nm, respectively, were obtained. Comparing these results with those obtained in this work for 10 layers of $[CHT/HA]_{11}$ (CTR1), $[CHT/HA\text{-}DN^*_{4h}]_{11}$ (CTR3) and $[CHT/HA\text{-}DN^*_{36h}]_{11}$ (CTR4), it was found that these polymeric films had a higher thickness, 207 nm, 206 nm and 182 nm, respectively, than those previously obtained [25]. This can be explained by the differences in the concentrations of the polymers used, which in the case of ref. [25] was 0.5 $mg.mL^{-1}$ for all PE solutions, and in our work was 1 $mg.mL^{-1}$ for CHT and 0.5 $mg.mL^{-1}$ for both HA and HA-DN.

As expected from previous works [26,27], the inclusion of BGNPs in the multilayered films MF1, MF2, MF3 and MF4 led to a final thickness lower than their respective controls (CTR1, CTR2, CTR3 and CTR4).

It was previously reported the build-up of $[CHT/HA/CHT/BGNPs]_6$ and $[CHT/HA\text{-}DN/CHT/BGNPs]_6$ films [27], where for 22 layers they both had a final thickness around 190 nm, which in turn was slightly higher than the values obtained in this work. Thus, for 22 layers, a final thickness of 152 nm, 124 nm and 126 nm was obtained for MF1, MF3 and MF4, respectively. As expected from the ΔD values, the final thickness decreases with the combined presence of BGNPs and HA-DN as well as with the DS increase, (MF3 and MF4), when compared to their respective controls suggesting that these combinations should be responsible for obtaining more compact films. These results could also be due to the differences in the concentrations of the polymers used in ref. [27], which used concentration values of 0.5 $mg.mL^{-1}$ for all PE, and by the DS value (11 %), which is lower than the values obtained in this work, 27% and 54%, for $HA\text{-}DN^*_{4h}$ and $HA\text{-}DN^*_{36h}$, respectively. However, this behaviour was not verified for conditions MF5 and MF6, which also had both conjugates and BGNPs present. In these cases, the LbL assembly demonstrated a linear film growth and their final thicknesses were 220 nm for MF5 and 184 nm for MF6, being higher than the thickness values obtained for their respective controls, namely 65 nm for CTR5 and 66 nm for CTR6. These thicknesses were higher than the multilayered films containing only one of the two conjugates, CHT-C or HA-DN conjugates (MF2, MF3, and MF4), or having the combination of CHT, HA and BGNPs (MF1). Therefore, when both conjugates are present, it seems that the addition of the BGNPs contributes for obtaining a less compact, less rigid and more hydrated LbL film.

Overall, through these results, it was shown that the developed films could be successfully assembled by the LbL technique.

3.3.5 Adhesion tests

The adhesive strength results of the LbL films dip-coated on pairs of glass plates are shown in Figure 3.8. MF films ending with an adhesive layer were chosen since we found in a previous work [83] that they have higher adhesive strength than the MF films ending with BGNPs. These configurations were used to study the effect of the presence of BGNPs on the adhesive properties of multilayer films, with or without conjugates (CHT-C or/and HA-DN).

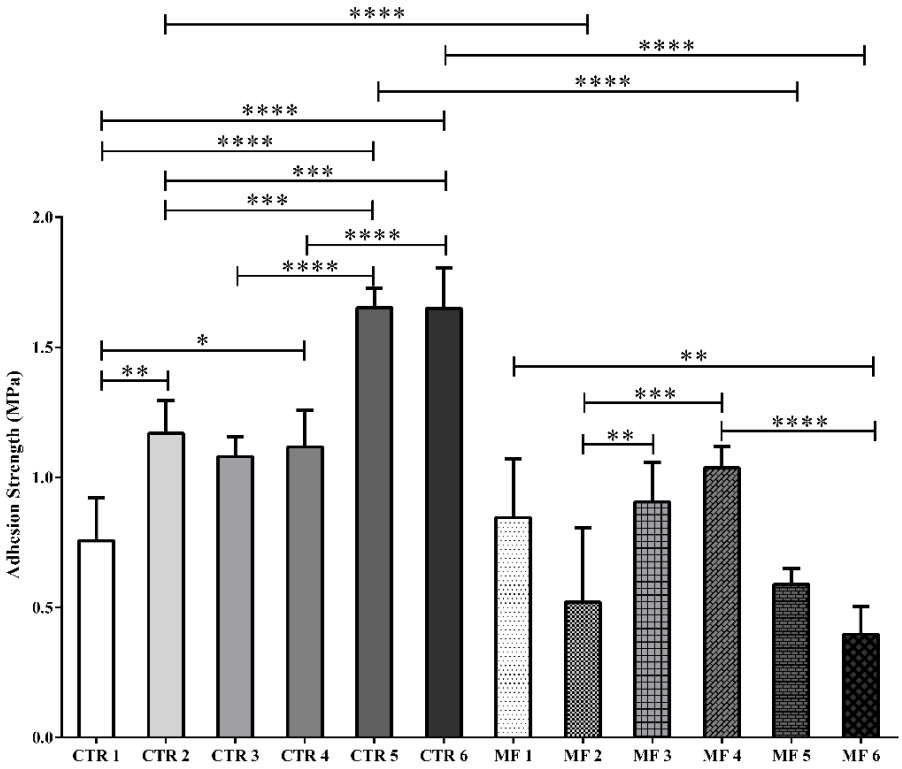

Figure 3.8 – Adhesion strength values (MPa) measured for each LbL coating. Data are presented by means ± standard deviation (n = 5; **** p<0.0001; *** p<0.001, ** p<0.01; * p<0.05) [One-way ANOVA with Turkey's Multiple comparison test].

As can be seen in Figure 3.8, polymeric films (controls) containing catechol groups in their compositions (CTR2, CTR3, CTR4, CTR5 and CTR6), had higher adhesive strength than the control film composed by unmodified polymers (CTR1). In fact, previous works [25,48] have already shown that the films containing HA-DN showed an increase in adhesive properties and that multilayers films containing higher amounts of catechol groups presented higher adhesive strength.

Adhesive strength results of $[CHT/HA\text{-}DN]_{11}$ coatings, represented by controls CTR3 and CTR4, were slightly higher than those obtained for the same system in a previous work [27]. These results could be explained by the DS differences which in the present work were higher, resulting in LbL coatings with enhanced adhesion properties. Moreover, when both conjugates were combined (CTR5 and CTR6) a statistically significant increase in the adhesion strength was observed compared to the formulations

containing only one of the modified polymers (CTR2, CTR3 and CTR4). By comparing CTR4 and CTR6 with CTR3 and CTR5, a slight increase of the adhesion properties of the controls with the DS increase of HA-DN can be seen.

Figure 3.8 also shows that the inclusion of BGNPs in the LbL assembly decreased the adhesion, except for MF1. As for the lamellar structure of nacre, the nanosized inorganic phase, BGNPs, arranged in a biopolymer matrix should exhibit inelastic deformations providing the stress redistribution around strain concentration sites and the elimination of stress concentration [27,52]. This was true for MF1 where the rotations and deformations in the BGNPs were helped by the biopolymer spacing composed by CHT and HA, resulting in an enhanced adhesion [27,53]. The adhesion increase with the presence of BGNPs was also observed in a previous work for CHT/HA based films [27]. However, for the remaining formulations containing BGNPs, the adhesive strength presented lower values than their respective polymeric films (controls). Probably, when the inorganic phase of BGNPs was included in the LbL coatings containing catechol groups, the increased stiffness of the films together with their compaction led to a lower interfacial adhesion between the multilayers.

Despite the already demonstrated adhesive properties of CHT-C in previous studies [28,29,37,54–57], the decrease in the adhesive strength in the presence of BGNPs appears to be more pronounced when CHT-C*$_{18h}$ was present in the multilayer system, for example in MF2, MF5 and MF6. As can be seen, in Figure 3.8, all these formulations have an adhesive strength lower than the respective controls. These effects could be explained by the lower content of adhesive polymers in the formulations that are replaced by BGNPs which, in turn, has been seen in this work to contribute to a lower adhesive strength.

Thus, through these mechanical tests, it was concluded that CTR5 and CTR6 were the configurations that demonstrated the best adhesive strength results. The increased strength of CTR5 and CTR6 could be explained by the unique feature of the catechol groups being able to effectively reduce the mobility of the polymer chains during LbL assembly [58]. Such decrease in the interdiffusion of PE leads to a linear growth behaviour of the LbL films and their consequent compaction. Thus, in addition to the intrinsic adhesive nature of the two polymers conjugated to catechol groups, CHT-C and HA-DN, this improved compaction probably confers increased stiffness to LbL coatings demonstrating a better response than the formulations containing BGNPs.

3.3.6 *In-Vitro* Bioactivity Analysis

In-vitro bioactivity of four LbL coatings configurations, namely CTR5, CTR6, MF5 and MF6 (see Figure 3.1), was assessed by analysing the apatite formation onto their surfaces under physiological-like

conditions. The choice of these conditions was based on the adhesive strength results, where the CTR5 and CTR6 formulations were the configurations that demonstrated the best values. MF5 and MF6 were chosen in parallel to evaluate their bioactive properties conferred by BGNPs. Figure 3.9 shows the SEM images and the respective EDS quantification, before and after immersion in SBF solution at 37 °C.

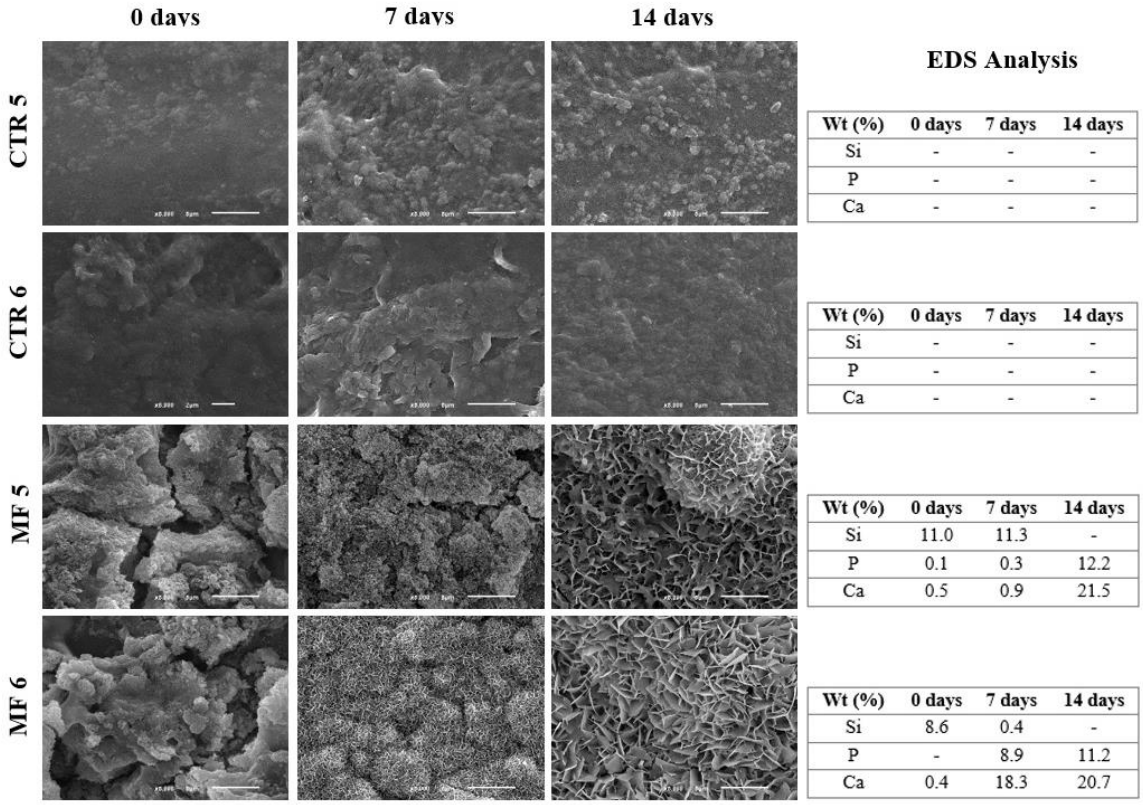

Wt (%)	0 days	7 days	14 days
Si	-	-	-
P	-	-	-
Ca	-	-	-

Wt (%)	0 days	7 days	14 days
Si	-	-	-
P	-	-	-
Ca	-	-	-

Wt (%)	0 days	7 days	14 days
Si	11.0	11.3	-
P	0.1	0.3	12.2
Ca	0.5	0.9	21.5

Wt (%)	0 days	7 days	14 days
Si	8.6	0.4	-
P	-	8.9	11.2
Ca	0.4	18.3	20.7

Figure 3.9 – *In-vitro* bioactivity studies. Representative SEM images and respective quantitative EDS analysis of four LbL coatings configurations (see Figure 3.1), before and after SBF immersion for 7 and 14 days. The scale bar represents 5 μm.

As expected from previous works [20,27,59], after immersion in SBF, only the formulations containing BGNPs (MF5 and MF6) were able to induce the formation of apatite-like structures with typical cauliflower morphology on their surfaces. After 7 days of immersion, nucleation and growth of apatite crystals were observed for both formulations. This was confirmed by the EDS analysis revealing changes in the elemental compositions related to silicon (Si), phosphorus (P) and calcium (Ca) on the film surface, as a result of BGNPs dissolution [20]. Particularly, changes in the elemental composition of MF6 remarkably greater than for MF5 were observed, demonstrating a decrease in Si concentration and an increase in Ca and P concentrations. After 14 days of immersion, both formulations evidenced well developed apatite-like structures and their respective EDS quantification showed similar results. On the other hand, the controls (CTR5 and CTR6), did not demonstrate significant morphological changes or presence of Si, P or Ca, as expected from previous works [20,27,59].

These results confirm the bioactive behaviour of the developed LbL configurations containing BGNPs, which proved to be potentially able of promoting the formation of a calcium phosphate (CaP) layer that would further crystallize in the form of carbonated apatite when interacting with bone tissue [21,60].

Figure 3.10 shows the XRD characterization of the LbL coatings, before and after immersion in SBF.

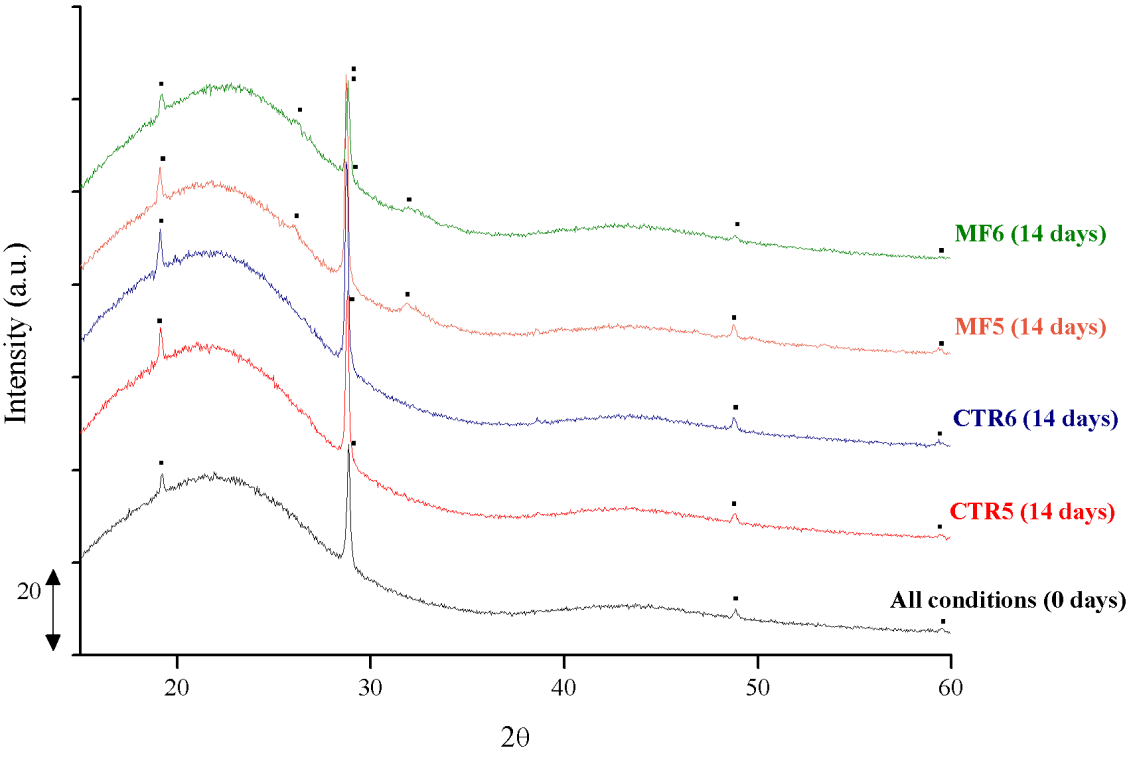

Figure 3.10 – XRD diffractograms obtained for each LbL coating configuration before and after immersion in SBF for 14 days.

Before the immersion in SBF, the XRD spectrum shows a crystalline profile for all LbL coatings. According to literature, the broad diffraction peak at around 2θ = 20° can be attributed to the presence of CHT, since its XRD pattern exhibited a characteristic peak around this value [61–65]. Meanwhile, the semi-crystalline structure of the natural CHT has been reported [65–68]. This characteristic is generally attributed to the intermolecular hydrogen bonding due to the presence of free NH_2 groups within the molecular structure, which results in the packing of the macromolecular polymeric chains [69]. In addition, some research works [62,70,71] have reported that the CHT modification with catechol groups substantially reduced the magnitude of the diffraction peak at 2θ = 20°, characteristic of CHT XRD pattern, indicating a marked decrease in the crystallinity of this compound. This decrease in crystallinity resulted from the partial breakage of the hydrogen bonds in the original CHT due to the grafting with catechol groups [62,70,71].

According to Nath el al. [64], the sharp diffraction peak around 2θ = 19° may confirm some complexation between CHT and HA. They also reported that the presence of this peak as well as others such as 2θ: 14.17°, 17.31°, and 22.56°, may be attributed to a change in crystallinity due to the interpenetrating polymer network structure as a result of complexation [64]. On the other hand, other authors [72,73] reported that diffraction peaks at around 2θ: 28°, 32°, 45° and 56° can be attributed to the presence of NaCl. In fact, since all PE solutions were dissolved in NaCl, this could explain the other additional peaks evidenced in the graph.

After 14 days of immersion in SBF, both formulations containing BGNPs exhibited typical crystalline peaks of hydroxyapatite, namely around 2θ: 26° and 32°, as previously reported in previous works [20,21,27]. As expected, control films without nanoparticles did not demonstrate these characteristic peaks of hydroxyapatite [27].

Therefore, these results confirmed the bioactivity of the LbL coatings containing BGNPs, supporting SEM/EDS results. Thus, such coatings could be potentially used for orthopaedic applications.

3.3.7 *In-Vitro* Biological Analysis

Cellular behaviour was evaluated performing a MTS assay. By the chemical reduction of the MTS compound into formazan, the metabolic activity of the cells could be determined. Figure 3.11 (a) shows the results obtained from MTS assay for 1, 3 and 7 days, where the highest absorbance value corresponds to higher metabolic cellular activity indicating higher number of cells. Four conditions were evaluated: CTR5, MF5, CTR6, MF6, and a positive control (TCPS), where cells were supposed to have a great proliferation.

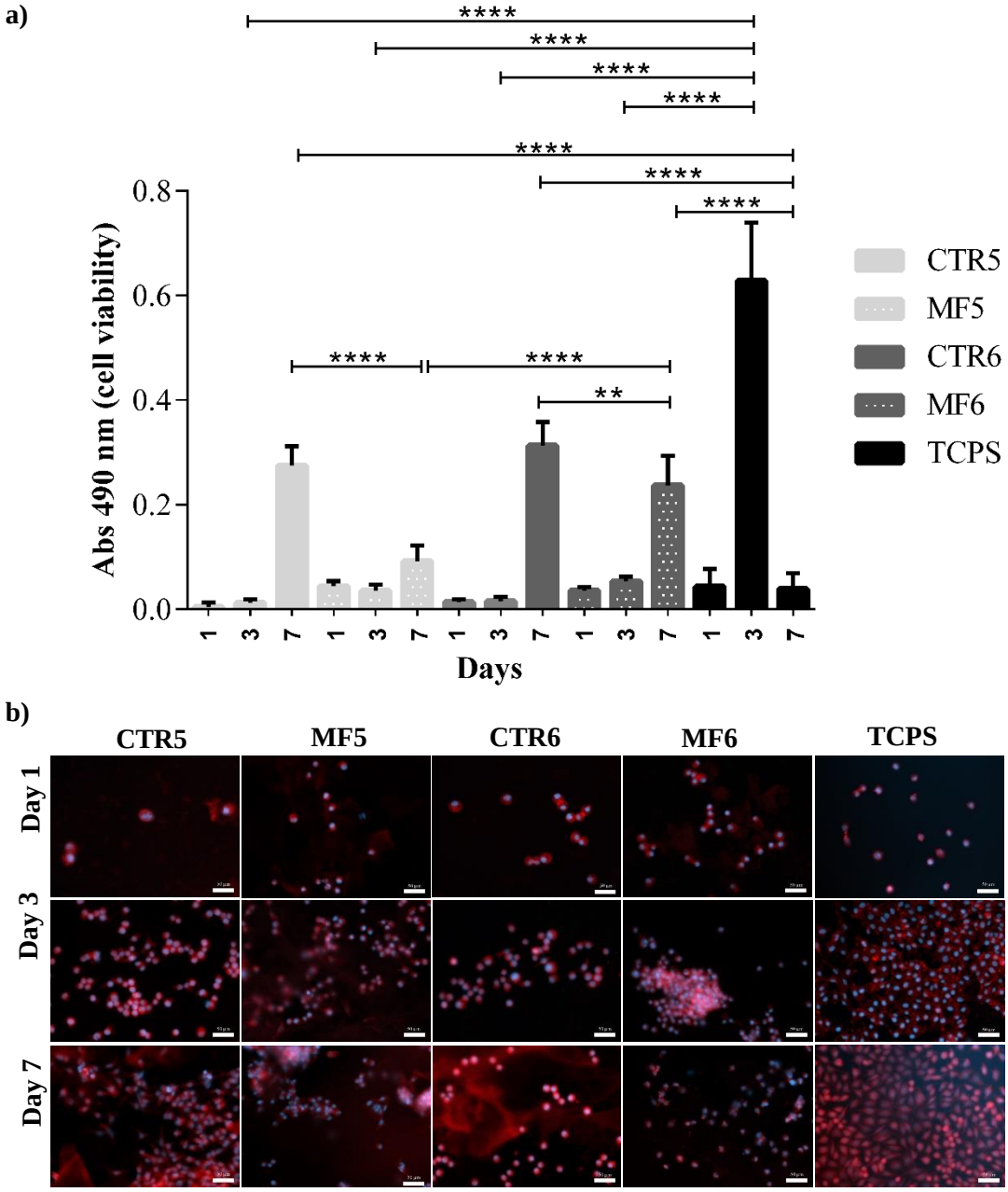

Figure 3.11– L929 viability results obtained through: a) MTS assay for 1, 3 and 7 days, where absorbance was read at 490 nm. Statistically significant differences between distinct samples by each time point were marked with ** and ***, which represents $p<0.01$ and $p<0.001$, respectively. Data are presented by means ± standard deviation (n = 3) [One-way ANOVA with Turkey's Multiple comparison test]; b) Fluorescence images of cells stained with DAPI (blue) and phalloidin (red) at 1, 3 and 7 days of culture on the different multilayer coatings (CTR5: $[CHT^*_{18h}/HA\text{-}DN^*_{4h}]_{11}$, MF5: $[CHT^*_{18h}/HA\text{-}DN^*_{4h}/CHT^*_{18h}/BGNPs]_5+CHT^*_{18h}/HA\text{-}DN^*_{4h}]$, CTR6: $[CHT^*_{18h}/HA\text{-}DN^*_{36h}]_{11}$, MF6: $[CHT^*_{18h}/HA\text{-}DN^*_{36h}/CHT^*_{18h}/BGNPs]_5+CHT^*_{18h}/HA\text{-}DN^*_{36h}]$): the nuclei of the cells were stained with blue and their cytoskeleton with red. All images are representative for each condition and time point. Scale bar represents 50 μm.

The MTS assay relatively evaluated cell proliferation, where it was observed that in the first 3 days there were no differences between the LbL conditions, as well as their cytotoxicity. Moreover, the results suggested that the presence of catechol groups in the last layer, conjugated to both CHT and HA polymers, had a great influence on the cellular response contributing for better cell viability and

proliferation. Similarly, other works have already reported better cellular responses on substrates modified with catechol groups [25–27,74,75].

At day 7, comparing with the previous time points, it was clear that the cell viability increased for all coatings, and particularly, CTR5 and CTR6 showed higher cell viability. These results evidenced that LbL coatings with higher catechol content, didn't have their cellular viability compromised. In fact, in our previous work [25], the cellular behaviour of CHT/HA and CHT/HA-DN multilayers was compared using two types of cells: L929 and SaOs-2. We concluded that the catechol groups conjugated to HA had a positive effect in terms of cell adhesion, proliferation, and cell viability comparing with the multilayer films without such groups. Several authors [1,13,25], have attributed the enhancement of the cellular response to the fact that catechol groups can play an active anchor between substrate surface and cells, allowing the formation of covalent and non-covalent bonds. On the other hand, the differences statistically significant of both MF5 and MF6 in relation to their respective controls should be related with the excess of BGNPs. This has already been observed in our previous work [27], being reported that this dissolution could increase the pH of the culture medium interfering with cell viability.

Furthermore, these MTS results were reinforced by the fluorescence images of L929 cells adhered on the surface of each LbL coating, at 1, 3 and 7 days, Figure 3.11 (b). Two fluorochromes, namely DAPI and phalloidin, were used to fix and stain the cells. Cell's nuclei were stained with blue (DAPI) and their cytoskeletons red (phalloidin). The fluorescence images presented were consistent with previously obtained cell behaviour results. As can be seen in Figure 3.11 (b), for both CTR5 and CTR6 conditions, after 3 days, the cells had the typical morphology of the L929 cells and, after 7 days, even developed a kind of fibroblastic network, where the adhered cells occupied large space of the LbL coatings due to their intense proliferative activity. On the other hand, for both MF5 and MF6, the rate of cell proliferation was lower. Generally, after 3 days, the cells appeared to stretch and gain the L929 morphology, being even more noticeable after 7 days of culture. Moreover, the morphology of the adhered cells was similar in both MF5 and MF6, where the presence of BGNPs appeared to lead to cell proliferation in cluster formations. This could be related to the typical heterogeneous distribution of BGNPs, already described by Couto *et al.* [21], and that might have been the reason for the presence of a higher number of cells in a certain area.

3.4 Conclusions

Nanostructured coatings inspired by MAPs and by the inorganic–organic nacre-like structure were successfully developed through the LbL assembly technique. Multifunctional films were constructed by alternate combination of inorganic BGNPs with biopolymeric layers of CHT and HA bearing catechol groups. Only-polymeric films containing catechol groups were also developed.

QCM-D results showed that the developed multilayered films were successfully assembled, producing stable LbL films. Polymeric films containing catechol groups showed a decrease in ΔD values, indicating that these films should be denser, more rigid, and less water-rich. In addition, it was observed that the presence of the catechol groups typically contributed to a linear film growth, revealing thinner multilayered films. Except for MF5 and MF6, all other multifunctional films containing catechol groups and BGNPs presented lower ΔD and thickness than the respective controls.

Adhesive strength results proved that the presence of both CHT-C and HA-DN conjugates in CTR5 and CTR6 conditions significantly improved their adhesion properties compared to the other CTR coatings. On the other hand, although the inclusion of BGNPs in these LbL systems, namely in MF5 and MF6, decreased the adhesion strength, they demonstrated bioactive potential after immersion in SBF

Finally, the evaluation of cell behaviour demonstrated that both polymeric and MF films were nontoxic, demonstrating enhanced cell adhesion, proliferation, and viability.

Overall, the LbL coatings produced could be used in a variety of applications as biocompatible interfaces between the implant and host tissues. So, MF films could be potentially used as adhesive coatings for orthopaedic implants to promote osteogenesis and hydroxyapatite deposition around the implant. On the other hand, highly adhesive polymeric coatings could be used to improve the junction between distinct implants and a variety of tissues in a simple and versatile way.

Acknowledgements

The authors acknowledge the Portuguese Foundation for Science and Technology (FCT) and the European program FEDER/COMPETE for the financial support through project LA ICVS/3Bs - 2015-2017.

3.5 References

[1] H. Lee, S.M. Dellatore, W.M. Miller, P.B. Messersmith, Mussel-Inspired Surface Chemistry for

Multifunctional Coatings, Science (80-.). 318 (2007) 426–430. doi:10.1126/science.1147241.

[2] H. Lee, Y. Lee, A.R. Statz, J. Rho, T.G. Park, P.B. Messersmith, Substrate-independent layer-by-layer assembly by using mussel-adhesive-inspired polymers, Adv. Mater. 20 (2008) 1619–1623. doi:10.1002/adma.200702378.

[3] Z. Tang, Y. Wang, P. Podsiadlo, N.A. Kotov, Biomedical Applications of Layer-by-Layer Assembly: From Biomimetics to Tissue Engineering, Adv. Mater. 18 (2006) 3203–3224. doi:10.1002/adma.200600113.

[4] E. Faure, C. Falentin-Daudré, C. Jérôme, J. Lyskawa, D. Fournier, P. Woisel, C. Detrembleur, Catechols as versatile platforms in polymer chemistry, Prog. Polym. Sci. 38 (2013) 236–270.

[5] J. Longo, T. Garnier, M. Mateescu, F. Ponzio, P. Schaaf, L. Jierry, V. Ball, Stable Bioactive Enzyme-Containing Multilayer Films Based on Covalent Cross-Linking from Mussel-Inspired Adhesives, Langmuir. 31 (2015) 12447–12454. doi:10.1021/acs.langmuir.5b03329.

[6] P. Podsiadlo, Z. Liu, D. Paterson, P.B. Messersmith, N.A. Kotov, Fusion of Seashell Nacre and Marine Bioadhesive Analogs: High-Strength Nanocomposite by Layer-by-Layer Assembly of Clay and L-3,4-Dihydroxyphenylalanine Polymer, Adv. Mater. 19 (2007) 949–955. doi:10.1002/adma.200602706.

[7] G.M. Luz, J.F. Mano, Biomimetic design of materials and biomaterials inspired by the structure of nacre, Philos. Trans. R. Soc. London A Math. Phys. Eng. Sci. 367 (2009) 1587–1605. doi:10.1098/rsta.2009.0007.

[8] J. Sun, B. Bhushan, Hierarchical structure and mechanical properties of nacre: a review, RSC Adv. 2 (2012) 7617–7632. doi:10.1039/C2RA20218B.

[9] J. Wu, L. Zhang, Y. Wang, Y. Long, H. Gao, X. Zhang, N. Zhao, Y. Cai, J. Xu, Mussel-Inspired Chemistry for Robust and Surface-Modifiable Multilayer Films, Langmuir. 27 (2011) 13684–13691. doi:10.1021/la2027237.

[10] S.K. Madhurakkat Perikamana, J. Lee, Y. Bin Lee, Y.M. Shin, E.J. Lee, A.G. Mikos, H. Shin, Materials from Mussel-Inspired Chemistry for Cell and Tissue Engineering Applications, Biomacromolecules. 16 (2015) 2541–2555. doi:10.1021/acs.biomac.5b00852.

[11] Y. Lee, H.J. Chung, S. Yeo, C.-H. Ahn, H. Lee, P.B. Messersmith, T.G. Park, Thermo-sensitive, injectable, and tissue adhesive sol–gel transition hyaluronic acid/pluronic composite hydrogels prepared from bio-inspired catechol-thiol reaction, Soft Matter. 6 (2010) 977–983. doi:10.1039/b919944f.

[12] Q. Lin, D. Gourdon, C. Sun, N. Holten-Andersen, T.H. Anderson, J.H. Waite, J.N. Israelachvili,

Adhesion mechanisms of the mussel foot proteins mfp-1 and mfp-3, Proc. Natl. Acad. Sci. U. S. A. 104 (2007) 3782–3786. doi:10.1073/pnas.0607852104.

[13] H. Lee, N.F. Scherer, P.B. Messersmith, Single-molecule mechanics of mussel adhesion, Proc. Natl. Acad. Sci. 103 (2006) 12999–13003. doi:10.1073/pnas.0605552103.

[14] J.H. Waite, M.L. Tanzer, Polyphenolic Substance of Mytilus edulis: Novel Adhesive Containing L-Dopa and Hydroxyproline., Science. 212 (1981) 1038–1040. doi:10.1126/science.212.4498.1038.

[15] J.H. An, N.T. Huynh, Y. Sil Jeon, J.-H. Kim, Surface modification using bio-inspired adhesive polymers based on polyaspartamide derivatives, Polym. Int. 60 (2011) 1581–1586. doi:10.1002/pi.3116.

[16] C.J. Ochs, T. Hong, G.K. Such, J. Cui, A. Postma, F. Caruso, Dopamine-Mediated Continuous Assembly of Biodegradable Capsules, Chem. Mater. 23 (2011) 3141–3143. doi:10.1021/cm201390e.

[17] E. Amstad, T. Gillich, I. Bilecka, M. Textor, E. Reimhult, Ultrastable Iron Oxide Nanoparticle Colloidal Suspensions Using Dispersants with Catechol-Derived Anchor Groups, Nano Lett. 9 (2009) 4042–4048. doi:10.1021/nl902212q.

[18] J. Borges, J.F. Mano, Molecular interactions driving the layer-by-layer assembly of multilayers., Chem. Rev. 114 (2014) 8883–8942. doi:10.1021/cr400531v.

[19] K. Halasz, G. Grozdits, L. Csóka, Functional nanostructured coatings via layer-by-layer self-assembly, in: Anti-Abrasive Nanocoatings, Woodhead Publishing, 2015: pp. 249–281. doi:https://doi.org/10.1016/B978-0-85709-211-3.00010-8.

[20] G.M. Luz, J.F. Mano, Preparation and characterization of bioactive glass nanoparticles prepared by sol–gel for biomedical applications, Nanotechnology. 22 (2011) 494014. doi:10.1088/0957-4484/22/49/494014.

[21] D.S. Couto, N.M. Alves, J.F. Mano, Nanostructured multilayer coatings combining chitosan with bioactive glass nanoparticles., J. Nanosci. Nanotechnol. 9 (2009) 1741–1748.

[22] Z. Hong, R.L. Reis, J.F. Mano, Preparation and in vitro characterization of scaffolds of poly(l-lactic acid) containing bioactive glass ceramic nanoparticles, Acta Biomater. 4 (2008) 1297–1306. doi:https://doi.org/10.1016/j.actbio.2008.03.007.

[23] Y. Abe, T. Kokubo, T. Yamamuro, Apatite coating on ceramics, metals and polymers utilizing a biological process, J. Mater. Sci. Mater. Med. 1 (1990) 233–238. doi:10.1007/BF00701082.

[24] M. Tanahashi, T. Yao, T. Kokubo, M. Minoda, T. Miyamoto, T. Nakamura, T. Yamamuro, Apatite

Coating on Organic Polymers by a Biomimetic Process, J. Am. Ceram. Soc. 77 (1994) 2805–2808. doi:10.1111/j.1151-2916.1994.tb04508.x.

[25] A.I. Neto, A.C. Cibrão, C.R. Correia, R.R. Carvalho, G.M. Luz, G.G. Ferrer, G. Botelho, C. Picart, N.M. Alves, J.F. Mano, Nanostructured polymeric coatings based on chitosan and dopamine-modified hyaluronic acid for biomedical applications, Small. 10 (2014) 2459–2469. doi:10.1002/smll.201303568.

[26] A.L. Carvalho, A.C. Vale, M. Sousa, A.M. Barbosa, E. Torrado, J. Mano, N.M. Alves, Antibacterial bioadhesive layer-by-layer coatings for orthopedic applications, J. Mater. Chem. B. 4 (2016) 5385–5393. doi:10.1039/C6TB00841K.

[27] S.J. Rego, A.C. Vale, G.M. Luz, J.F. Mano, N.M. Alves, Adhesive Bioactive Coatings Inspired by Sea Life, Langmuir. 32 (2016) 560–568. doi:10.1021/acs.langmuir.5b03508.

[28] K. Kim, K. Kim, J.H. Ryu, H. Lee, Chitosan-catechol: A polymer with long-lasting mucoadhesive properties, Biomaterials. 52 (2015) 161–170. doi:10.1016/j.biomaterials.2015.02.010.

[29] J. Xu, S. Strandman, J.X.X. Zhu, J. Barralet, M. Cerruti, Genipin-crosslinked catechol-chitosan mucoadhesive hydrogels for buccal drug delivery, Biomaterials. 37 (2015) 395–404. doi:10.1016/j.biomaterials.2014.10.024.

[30] A. Ghadban, A.S. Ahmed, Y. Ping, R. Ramos, N. Arfin, B. Cantaert, R. V. Ramanujan, A. Miserez, Bioinspired pH and magnetic responsive catechol-functionalized chitosan hydrogels with tunable elastic properties, Chem. Commun. 52 (2016) 697–700. doi:10.1039/C5CC08617E.

[31] Z. Hong, R.L. Reis, J.F. Mano, Preparation and in vitro characterization of novel bioactive glass ceramic nanoparticles, J. Biomed. Mater. Res. - Part A. 88 (2009) 304–313. doi:10.1002/jbm.a.31848.

[32] M.C. Dixon, Quartz crystal microbalance with dissipation monitoring: Enabling real-time characterization of biological materials and their interactions, J. Biomol. Tech. 19 (2008) 151–158.

[33] N.M. Alves, C. Picart, J.F. Mano, Self assembling and crosslinking of polyelectrolyte multilayer films of chitosan and alginate studied by QCM and IR spectroscopy., Macromol. Biosci. 9 (2009) 776–785. doi:10.1002/mabi.200800336.

[34] M. V. Voinova, M. Rodahl, M. Jonson, B. Kasemo, Viscoelastic Acoustic Response of Layered Polymer Films at Fluid-Solid Interfaces: Continuum Mechanics Approach, Phys. Scr. 59 (1999) 391–396. doi:10.1238/Physica.Regular.059a00391.

[35] T. Kokubo, H. Takadama, How useful is SBF in predicting in vivo bone bioactivity?, Biomaterials.

27 (2006) 2907–2915. doi:http://dx.doi.org/10.1016/j.biomaterials.2006.01.017.

[36] S. Hong, K. Yang, B. Kang, C. Lee, I.T. Song, E. Byun, K.I. Park, S.-W. Cho, H. Lee, Hyaluronic Acid Catechol: A Biopolymer Exhibiting a pH-Dependent Adhesive or Cohesive Property for Human Neural Stem Cell Engineering, Adv. Funct. Mater. 23 (2013) 1774–1780. doi:10.1002/adfm.201202365.

[37] K. Kim, J.H. Ryu, D.Y. Lee, H. Lee, Bio-inspired catechol conjugation converts water-insoluble chitosan into a highly water-soluble, adhesive chitosan derivative for hydrogels and LbL assembly, Biomater. Sci. 1 (2013) 783–790. doi:Doi 10.1039/C3bm00004d.

[38] T.C. Laurent, U.B.G. Laurent, J.R.E. Fraser, The structure and function of hyaluronan: An overview., Immunol. Cell Biol. 74 (1996) 1–7.

[39] M.K. Cowman, T.A. Schmidt, P. Raghavan, A. Stecco, Viscoelastic Properties of Hyaluronan in Physiological Conditions, F1000Research. 4 (2015) 622. doi:10.12688/f1000research.6885.1.

[40] H.Y. Zhou, X.G. Chen, M. Kong, C.S. Liu, D.S. Cha, J.F. Kennedy, Effect of molecular weight and degree of chitosan deacetylation on the preparation and characteristics of chitosan thermosensitive hydrogel as a delivery system, Carbohydr. Polym. 73 (2008) 265–273. doi:http://dx.doi.org/10.1016/j.carbpol.2007.11.026.

[41] W. Wang, D. Xu, Viscosity and flow properties of concentrated solutions of chitosan with different degrees of deacetylation, Int. J. Biol. Macromol. 16 (1994) 149–152.

[42] A. Doostmohammadi, A. Monshi, R. Salehi, M.H. Fathi, Z. Golniya, A.U. Daniels, Bioactive glass nanoparticles with negative zeta potential, Ceram. Int. 37 (2011) 2311–2316. doi:10.1016/j.ceramint.2011.03.026.

[43] G.M. Luz, J.F. Mano, Nanoengineering of bioactive glasses: hollow and dense nanospheres, J. Nanoparticle Res. 15 (2013) 1457. doi:10.1007/s11051-013-1457-0.

[44] H.H. Lu, S.R. Pollack, P. Ducheyne, Temporal zeta potential variations of 45 S 5 bioactive glass immersed in an electrolyte solution, J. Biomed. Mater. Res. 51 (2000) 80–87.

[45] R. Smeets, A. Kolk, M. Gerressen, O. Driemel, O. Maciejewski, B. Hermanns-Sachweh, D. Riediger, J.M. Stein, A new biphasic osteoinductive calcium composite material with a negative Zeta potential for bone augmentation, Head Face Med. 5 (2009) 13.

[46] J.J. Cooper, J.A. Hunt, The significance of zeta potential in osteogenesis, in: Trans. 31st Annu. Meet. Biomater., Society for Biomaterials, 2006: p. 592.

[47] N.C. Teng, S. Nakamura, Y. Takagi, Y. Yamashita, M. Ohgaki, K. Yamashita, A new approach to enhancement of bone formation by electrically polarized hydroxyapatite, J. Dent. Res. 80 (2001)

1925–1929.

[48] A.I. Neto, N.L. Vasconcelos, S.M. Oliveira, D. Ruiz-Molina, J.F. Mano, High-Throughput Topographic, Mechanical, and Biological Screening of Multilayer Films Containing Mussel-Inspired Biopolymers, Adv. Funct. Mater. 26 (2016) 2745–2755. doi:10.1002/adfm.201505047.

[49] L. Richert, P. Lavalle, E. Payan, X.Z. Shu, G.D. Prestwich, J.-F. Stoltz, P. Schaaf, J.-C. Voegel, C. Picart, Layer by Layer Buildup of Polysaccharide Films: Physical Chemistry and Cellular Adhesion Aspects, Langmuir. 20 (2004) 448–458. doi:10.1021/la035415n.

[50] O. Etienne, A. Schneider, C. Taddei, L. Richert, P. Schaaf, J.-C. Voegel, C. Egles, C. Picart, Degradability of Polysaccharides Multilayer Films in the Oral Environment: an in Vitro and in Vivo Study, Biomacromolecules. 6 (2005) 726–733. doi:10.1021/bm049425u.

[51] B. Sun, C.M. Jewell, N.J. Fredin, D.M. Lynn, Assembly of Multilayered Films Using Well-Defined, End-Labeled Poly(acrylic acid): Influence of Molecular Weight on Exponential Growth in a Synthetic Weak Polyelectrolyte System, Langmuir. 23 (2007) 8452–8459. doi:10.1021/la7010875.

[52] X. Li, Z.-H. Xu, R. Wang, In Situ Observation of Nanograin Rotation and Deformation in Nacre, Nano Lett. 6 (2006) 2301–2304. doi:10.1021/nl061775u.

[53] X. Li, W.-C. Chang, Y.J. Chao, R. Wang, M. Chang, Nanoscale Structural and Mechanical Characterization of a Natural Nanocomposite Material: The Shell of Red Abalone, Nano Lett. 4 (2004) 613–617. doi:10.1021/nl049962k.

[54] J.H. Ryu, Y. Lee, W.H. Kong, T.G. Kim, T.G. Park, H. Lee, Catechol-functionalized chitosan/pluronic hydrogels for tissue adhesives and hemostatic materials, Biomacromolecules. 12 (2011) 2653–2659. doi:10.1021/bm200464x.

[55] J. Xu, G.M. Soliman, J. Barralet, M. Cerruti, Mollusk Glue Inspired Mucoadhesives for Biomedical Applications, Langmuir. 28 (2012) 14010–14017. doi:10.1021/la3025414.

[56] J.H. Ryu, S. Hong, H. Lee, Bio-inspired adhesive catechol-conjugated chitosan for biomedical applications: A mini review, Acta Biomater. 27 (2015) 101–115. doi:10.1016/j.actbio.2015.08.043.

[57] J.H. Ryu, Y. Lee, W.H. Kong, T.G. Kim, T.G. Park, Bio-inspired tissue adhesive chitosan/pluronic composite hydrogel, J. Control. Release. 152 (2011) e236–e237. doi:http://dx.doi.org/10.1016/j.jconrel.2011.09.033.

[58] Y. Min, P.T. Hammond, Catechol-Modified Polyions in Layer-by-Layer Assembly to Enhance Stability and Sustain Release of Biomolecules: A Bioinspired Approach, Chem. Mater. 23 (2011) 5349–5357. doi:10.1021/cm201801n.

[59] J.R. Rodrigues, N.M. Alves, J.F. Mano, Biomimetic polysaccharide/bioactive glass nanoparticles multilayer membranes for guided tissue regeneration, RSC Adv. 6 (2016) 75988–75999.

[60] J. Shi, N.M. Alves, J.F. Mano, Thermally Responsive Biomineralization on Biodegradable Substrates, Adv. Funct. Mater. 17 (2007) 3312–3318. doi:10.1002/adfm.200601206.

[61] D. Nayak, A.P. Minz, S. Ashe, P.R. Rauta, M. Kumari, P. Chopra, B. Nayak, Synergistic combination of antioxidants, silver nanoparticles and chitosan in a nanoparticle based formulation: Characterization and cytotoxic effect on MCF-7 breast cancer cell lines., J. Colloid Interface Sci. 470 (2016) 142–152. doi:10.1016/j.jcis.2016.02.043.

[62] J. Liu, H.-T. Wu, J. Lu, X. Wen, J. Kan, C. Jin, Preparation and characterization of novel phenolic acid (hydroxybenzoic and hydroxycinnamic acid derivatives) grafted chitosan microspheres with enhanced adsorption properties for Fe(II), Chem. Eng. J. 262 (2015) 803–812. doi:https://doi.org/10.1016/j.cej.2014.10.041.

[63] C. Radhakumary, P.D. Nair, S. Mathew, C.P. Reghunadhan Nair, Synthesis, characterization, and properties of poly(vinyl acetate)- and poly(vinyl alcohol)-grafted chitosan, J. Appl. Polym. Sci. 104 (2007) 1852–1859. doi:10.1002/app.25841.

[64] S.D. Nath, C. Abueva, B. Kim, B.T. Lee, Chitosan-hyaluronic acid polyelectrolyte complex scaffold crosslinked with genipin for immobilization and controlled release of BMP-2., Carbohydr. Polym. 115 (2015) 160–169. doi:10.1016/j.carbpol.2014.08.077.

[65] T.S. Anirudhan, S.S. Nair, A.S. Nair, Fabrication of a bioadhesive transdermal device from chitosan and hyaluronic acid for the controlled release of lidocaine., Carbohydr. Polym. 152 (2016) 687–698. doi:10.1016/j.carbpol.2016.06.101.

[66] Y. Zhang, J.R. Venugopal, A. El-Turki, S. Ramakrishna, B. Su, C.T. Lim, Electrospun biomimetic nanocomposite nanofibers of hydroxyapatite/chitosan for bone tissue engineering, Biomaterials. 29 (2008) 4314–4322. doi:https://doi.org/10.1016/j.biomaterials.2008.07.038.

[67] J.-K. Francis Suh, H.W.T. Matthew, Application of chitosan-based polysaccharide biomaterials in cartilage tissue engineering: a review, Biomaterials. 21 (2000) 2589–2598. doi:https://doi.org/10.1016/S0142-9612(00)00126-5.

[68] B.W.S. Souza, M.A. Cerqueira, J.T. Martins, A. Casariego, J.A. Teixeira, A.A. Vicente, Influence of electric fields on the structure of chitosan edible coatings, Food Hydrocoll. 24 (2010) 330–335. doi:https://doi.org/10.1016/j.foodhyd.2009.10.011.

[69] T.-C. Chang, J.-W. Wang, M.-H. Hon, Synthesis of Nanosized Chitosan-Poly(acrylic acid) Particles by a Dropping Method, Macromol. Biosci. 4 (2004) 416–420. doi:10.1002/mabi.200300072.

[70] X. Huang, X. Bao, Y. Liu, Z. Wang, Q. Hu, Catechol-Functional Chitosan/Silver Nanoparticle Composite as a Highly Effective Antibacterial Agent with Species-Specific Mechanisms., Sci. Rep. 7 (2017) 1860. doi:10.1038/s41598-017-02008-4.

[71] Q.Y. Chen, J.B. Xiao, X.Q. Chen, X.Y. Jiang, H.Z. Yu, M. Xu, The Adsorption of Phenol, m-Cresol and m-Catechol on a β-Cyclodextrin Derivative-Grafted Chitosan and the Removal of Phenols from Industrial Wastewater, Adsorpt. Sci. Technol. 24 (2006) 547–558. doi:10.1260/026361706780810230.

[72] T. Tsuzuki, P.G. McCormick, Synthesis of Cr2O3 nanoparticles by mechanochemical processing, Acta Mater. 48 (2000) 2795–2801. doi:10.1016/S1359-6454(00)00100-2.

[73] R.A. and B.M. and A.M. and M. Tamizifar, ZnO Nanoparticles Synthesised by mechanochemical processing, J. Phys. Conf. Ser. 26 (2006) 312. http://stacks.iop.org/1742-6596/26/i=1/a=075.

[74] X. Zhang, Z. Li, X. Yuan, Z. Cui, X. Yang, Fabrication of dopamine-modified hyaluronic acid/chitosan multilayers on titanium alloy by layer-by-layer self-assembly for promoting osteoblast growth, Appl. Surf. Sci. 284 (2013) 732–737. doi:10.1016/j.apsusc.2013.08.002.

[75] S.-B. Lee, C. González-Cabezas, K.-M. Kim, K.-N. Kim, K. Kuroda, Catechol-Functionalized Synthetic Polymer as a Dental Adhesive to Contaminated Dentin Surface for a Composite Restoration, Biomacromolecules. 16 (2015) 2265–2275. doi:10.1021/acs.biomac.5b00451.

4. CHAPTER 4 – NEW ADHESIVE LBL COATINGS PRODUCED BY DIP- AND SPIN-COATING

Ana C. Almeida[1,2], Ana C. Vale[1,2], Ricardo A. Pires[1,2], Rui L. Reis[1,2], Natália M. Alves[1,2]

[1] 3B´s Research Group – Biomaterials, Biodegradables and Biomimetics, University of Minho, Headquarters of the European Institute of Excellence on Tissue Engineering and Regenerative Medicine. AvePark, 4806-909, Taipas, Guimarães, Portugal.
[2] ICVS/3B's PT Associate Laboratory, Guimarães, Portugal.

Abstract

Layer-by-layer (LbL) films were produced by dip- and spin-coating methods onto different substrates: glass, 316L stainless steel (SS) and titanium (Ti). Coatings with two distinct compositions, mimicking mussel adhesive properties were developed: Multifunctional (MF) and Polymeric (CTR) coatings. The films were composed of an organic phase of chitosan (CHT) and hyaluronic acid (HA) modified with catechol groups, similarly to the 3,4-dihydroxyphenyl-L-alanine (DOPA) amino-acid structure of the mussel's adhesive proteins (MAPs). Inspired by the inorganic-organic nacre structure, an inorganic phase of bioactive glass nanoparticles (BGNPs) was added to the organic phase of the MF films to impart additional improved bioactivity. It was the first time that both catechol-conjugated chitosan (CHT-C) and catechol-conjugated hyaluronic acid (HA-DN), combined or not with BGNPs, were used to construct LbL coatings onto different substrates and using distinct methods.

UV-Vis spectroscopy demonstrated that both CHT-C and HA-DN were successfully synthesised and their substitution degree was determined. Fourier transform infrared (FT-IR) imaging was used in an innovative way to analyse the interdiffusion of layers in the coatings. Further investigations on their morphology were conducted by scanning electron microscopy (SEM) and atomic force microscopy (AFM). Their wettability was also evaluated by water contact angle (WCA) measurements.

The results revealed differences in the structure and surface properties of the coatings assembled either by dip- or spin-coating. Smoother films with a more homogeneous structure and lower interdiffusion of polyelectrolytes layers were well observed in the spin-coated films, using glass as substrate, when compared with the dip-coated ones. Furthermore, it was concluded that the intrinsic surface roughness of 316L SS and Ti metals had a great influence on the results of both LbL methods.

Keywords: Biomimetic, Layer-by-Layer, Polysaccharides, Catechol groups, Bioglass nanoparticles, Dip-coating, Spin-coating

4.1 Introduction

Biomedical metals such as titanium (Ti) and its alloys, 316L stainless steel (SS) and Cobalt-Chromium (CoCr) alloys, have been widely used in orthopaedic and maxillofacial applications [1,2]. However, there are still few examples where these have been used successfully in clinic or have reported good *in-vivo* biocompatibility [3]. In most cases, after their implantation in the host bone, fibrous encapsulation occurs on the implant surface [4]. Therefore, since the mechanical and biological aspects of bone healing are closely interrelated, a biomedical metal must not only have adequate mechanical properties, but also possess other biological functions such as bioadhesiveness, bioactivity, and biocompatibility [2,3].

Current trends for improving osseointegration of orthopaedic implants consist on their surface modification with calcium phosphate-like coatings such hydroxyapatite [5,6] or other coatings containing bioactive glasses, for example 45S5 Bioglass® [7–9], or biomolecules such as proteins [10,11], growth factors [12–14], RGD peptides [15–17], and DNA molecules [18]. However, these approaches still have significant limitations and drawbacks [19].

So, driven by, these features, two new biocompatible layer-by-layer (LbL) coatings for orthopaedic applications were developed in this work: Multifunctional and Polymeric coatings. Multifunctional coatings combining adhesive properties and bioactivity were designed to promote bone-implant interaction, as an alternative option to bone cements. On the other hand, polymeric coatings with enhanced adhesive properties were designed to improve the adhesion between orthopaedic implants and other tissues where bioactivity is not a requirement, for instance as an alternative to synthetic tissue adhesives.

Both coatings were composed by two natural polymers, chitosan (CHT) and hyaluronic acid (HA). These biopolymers have received much attention due their numerous interesting properties such as biocompatibility, biodegradability, availability, processing, modification flexibility, among others [20–22]. Its assembly in polyelectrolytes multilayers (PEM) systems onto a huge diversity of substrates has already been reported in literature [23–25].

Based on previous studies [23–26], both polysaccharides were used in this work with their further modification with catechol groups to improve the adhesive properties of the coatings. Conjugation with catechol groups was inspired by the ortho-dihydroxyphenyl (catechol) moiety of 3,4-dihydroxyphenyl-L-alanine (DOPA) amino-acid present in the mussel's adhesive proteins (MAPs) [27–29]. Mussels present

strong adhesive properties to different substrates in wet environments [30]. This interesting property make them potential bioadhesives for diverse applications [31,32]. So far, previous works of our group [33,34] have only studied the adhesive properties of LbL coatings based on CHT and catechol-conjugated hyaluronic acid (HA-DN). Since those studies demonstrated that the presence of HA-DN had a positive effect on their adhesive properties, we hypothesized that the modification of both polysaccharides could further improve the adhesive ability of the previously developed coatings.

Furthermore, based on the interesting osteoconductive properties of bioactive glass nanoparticles (BGNPs) in the orthopaedic field [35–37], they were used in this work as an inorganic phase of the multifunctional coatings. BGNPs have already shown their binding potential to bone, stimulating new tissue growth by the precipitation of a calcium phosphate (CaP) layer on their surface while dissolving over time [8,9].

The combination of an inorganic phase of BGNPs and an organic phase of polysaccharides to develop multifunctional LbL coatings was inspired by the layered structure of nacre, which is present in the shell of some molluscs. This structure combines resistance to fracture provided by inorganic matrix of aragonite nanoplatelets (95% wt.) and toughness conferred by organic matrix (5% wt.) surrounding the inorganic materials [38,39]. However, unlike the nacre structure, in this study the content of inorganic phase was lower than the organic phase to develop flexible coatings.

Among the different processing techniques that have been proposed to develop nanostructured coatings, LbL deposition appears as one of the most attractive methods [40,41]. It allows the development of multilayer films with tailored thicknesses, compositions, structures, properties, and functions over any type of substrate [42]. Several deposition methods for the LbL build-up have been already reported in the literature, including dip-coating, spin-coating, spraying, and perfusion [42]. Among these, dip-coating is the LbL deposition technique most widely used due to the simplicity of its process and the low-cost of the equipment, as well as its suitability to coating substrates with complex geometries [42,43]. However, the need of a relatively large amount of materials for each deposition step and the time-consuming leads to choose alternative methods such as spin-coating [43,44]. Spin-coating appears as a good alternative to produce low-coat, rapid, and uniform thin films using the same materials of the dip-coating and allowing electrostatic self-assembly [43]. Additionally, spin-assisted films have demonstrated more highly ordered structures with less polyelectrolyte interpenetration between the layers leading a linear growth of film thickness, rather than the exponential growth, which is common in the dip-coated films [45–47]. Usually, the exponential growth is observed for weakly charged PEM systems and can be attributed to the reversible interdiffusion of at least one of the polyelectrolyte species that constitute the film [47].

In the present work, both polymeric and multifunctional coatings were produced on glass, 316L SS and Ti by two different LbL deposition methods: dip- and spin-coating. It was the first time that both CHT and HA modified with catechol groups, combined or not with BGNPs, were used to construct LbL coatings onto different substrates and by two different LbL techniques. Previous works of our group [33,34,48], have only used the dip-coating method to construct LbL coatings, based on CHT, HA-DN and BGNPs, onto glass substrates. The properties of the distinct coatings obtained by the two LbL methods on different substrates was analysed, envisaging their future use in orthopaedic applications. In particular, as far as we know, the polyelectrolyte interdiffusion of LbL coatings was analysed for the first time by FT-IR imaging.

4.2 Materials and Methods

4.2.1 Materials

Medium molecular weight chitosan (ref. 448877, Brookshield viscosity 200–800 cP, Mw = 190–310 kDa, 75–85% N-deacetylation degree), hyaluronic acid sodium salt from *Streptococcus equi* (ref. 53747, Mw = 1500–1800 kDa), dopamine hydrochloride (DN, ref. H8502, Mw = 189,64 Da), hydrocaffeic acid (HCA, ref. 102601, 98%, Mw = 182.17 Da), N-(3-dimethylamino)propyl)-N′-ethylcarbodiimide hydrochloride (EDC, ref. 03450, purum, ≥98.0% (AT), Mw = 191.70 Da), dialysis tubing cellulose membrane (avg. flat width 33 mm), calcium nitrate tetrahydrate ($Ca(NO_3)_2{\cdot}4H_2O$ C_2H_6O, 99 %), citric acid monohydrate (99%), ammonium phosphate dibasic ($(NH_4)_2HPO_4$, ≥98%), ethanol absolute, ammonium hydroxide solution (maximum of 33 % NH_3), sodium chloride (NaCl), hydrochloric acid (HCl), and polyethylenimine (PEI) were purchased from Sigma-Aldrich (St. Louis, Mo, USA). Tetraethyl orthosilicate (TEOS, 99.90%) was purchased from Merck KGaA (Darmstadt, Germany). Acetone and 2-propanol were obtained from VWR International (UK). Sodium hydroxide (NaOH) was purchased from Fisher Chemical (Fisher Scientific UK, Leics, UK) and hydrogen peroxide 30% (w/v) was obtained from Panreac AppliChem (Darmstadt, Deutschland).

CHT was the only reagent that was previously purified by recrystallization. Borosilicate coverglasses (Ø 18 mm, Agar Scientific, Stansted, UK), Ti (Ø 18 mm, 99.6 % purity, Goodfellow Metals Ltd, Cambridge, UK) and 316L SS (Ø 18 mm, Goodfellow Metals Ltd, Cambridge, UK) substrates were used for the deposition of LbL coatings by dip- and spin-coating methods. Ti substrates were manually polished with abrasive discs of P180, P320, P600 and P800 (Struers, France). Prior to deposition, all the substrates

were cleaned in sequential ultrasonic baths to remove surface impurities: 1° - 15 minutes with acetone; 2° - 15 minutes with ethanol; 3° - 15 minutes in osmotized water; and finally, they were dried with a nitrogen flow.

4.2.2 HA-DN Synthesis

HA-DN was synthesized from the procedure proposed by Lee and co-workers [23], with some modifications. HA modification with catechol groups was performed by the carbodiimide chemistry using EDC as an activation agent of the carboxyl groups on HA chains. HA solution (10 $mg.mL^{-1}$) was prepared in phosphate buffered saline (PBS) solution and the pH was adjusted to 5.5 using 0.5 M HCl or 0.5 M NaOH aqueous solution under magnetic stirring. To limit the oxygen interaction with the solution, HA solution was purged with nitrogen for 30 min. Then, 338 mg of EDC and 474 mg of DN were added to the previous solution. The reaction was allowed to continue for 36 hours, and the pH was maintained at 5.5 at 4 °C. Unreacted chemicals and urea byproducts were removed by dialysis against an acidic osmotized water solution (pH 5.0, HCL solution) for 4 days and osmotized water for 1 day, using a dialysis membrane tube, at 4°C. Finally, the HA-DN*$_{36h}$ conjugates were freeze-dried for 4 days and stored at -20°C. The entire procedure and storage of the produced HA-DN*$_{36h}$ was performed at 4°C and protected from light to prevent oxidation of catechol groups.

4.2.3 Catechol-conjugated chitosan (CHT-C) Synthesis

CHT-C synthesis was based on the procedure proposed by Kim *et al.* [24], Xu *et al.* [25] and Ghadban *et al.* [26]. As in the HA-DN synthesis, the CHT modification with catechol groups was accomplished by the carbodiimide chemistry using EDC as an activation agent. 1% (w/v) CHT solution was prepared in HCl solution at pH 2.5. Then, a HCA solution (59 $mg.mL^{-1}$) was prepared in osmotized water and a EDC solution (119 $mg.mL^{-1}$) was prepared in a mixture of osmotized water and ethanol. These two previous solutions were mixed and added to the CHT solution, under stirring at 4° C, followed by the addition of 1M NaOH solution to obtain a final pH of 4.8. The reaction was allowed to continue for 18 h, under nitrogen atmosphere for 30 min. After that, the product, CHT-C*$_{18h}$, was purified by dialysis against an acidic osmotized water solution (pH 5.0, HCL solution) for 3 days and osmotized water for 4 hours, using a dialysis membrane tube, at 4°C. The resulting product was freeze-dried and stored at -20°C. Also, as in the HA-DN synthesis, the entire procedure and storage of the produced CHT-C was performed at 4°C and protected from light to prevent oxidation of catechol groups.

4.2.4 BGNPs Production

The procedure to obtain the ternary system of BGNPs with the composition SiO_2:CaO:P_2O_5 (mol.%) = 50:45:5, was based on the sol-gel method already optimized by two previous works [49,50]. First, a "solution A" was prepared through a mixture of precursor´s solutions. So, 6% (w/v) of calcium nitrate tetrahydrate, calcium precursor, was dissolved in 120 mL of osmotized water at room temperature. Then, 9.8353 mL of TEOS, silica precursor, together with 60 mL of ethanol absolute was added to the previous solution. The pH of solution A was adjusted to 2 with citric acid solution (10 % (w/v)), under stirring for 3 hours. After that, a "solution B" was also prepared by adding 0.07% (w/v) of ammonium phosphate dibasic, phosphorus precursor, to osmotized water. The pH of solution B was adjusted to 11.5 with ammonia hydroxide solution. Under stirring, the solution A was slowly added, drop-by-drop, to solution B and the pH was maintained at 11.5 by continuous supplement of ammonia hydroxide solution. This reaction mixture was left under stirring during 48 h and then, under resting for 24 h to occur the gel particle precipitation. Afterwards, the gel precipitate was washed tree times with osmotized water and stored during 24 h at -80°C to be subsequently freeze dried for 7 days. The obtained white gel powder was calcinated at 700°C for 3 h to get the BGNPs with improved bioactivity.

4.2.5 UV-Vis Characterization of HA-DN and CHT-C

Before the construction of the LbL films, the polyelectrolytes used were characterized by UV-Vis to determine their substitution degree (DS (%)). A Synergy HT Multi-Mode Microplate Reader (BioTek Instruments, U.S.A.) with an absorbance measurement range of 200 to 350 nm, and a quartz microplate with 96 wells was used. Solutions of 0.5 $mg.mL^{-1}$ of $HA\text{-}DN^*_{36h}$, and 1 $mg.mL^{-1}$ of $CHT\text{-}C^*_{18h}$ were prepared in 0.15 M NaCl for the UV analysis. 100 µl of test solution was used in each well, and 0.15 M NaCl solution was used as blank. All experiments were performed at a controlled temperature of 25 °C, and results are represented as a mean of 3 measurements.

4.2.6 LBL Assembly of the Coatings

The LbL assembly of different coatings onto glass, 316L SS and Ti substrates was carried out using the two previously described methods, dip-coating, and spin-coating, at room temperature.

For such, four different solutions of $CHT\text{-}C^*_{18h}$ (1 $mg.mL^{-1}$), $HA\text{-}DN^*_{36h}$ (0.5 $mg.mL^{-1}$), BGNPs (2.5 $mg.mL^{-1}$) and PEI (5 $mg.mL^{-1}$) were prepared with 0.15 M NaCl solution, under magnetic stirring. Except for PEI, the pH of the solutions was adjusted to 5.5 using 0.5 M NaOH or 0.5 M HCl aqueous solutions.

To avoid BGNPs agglomeration, the solutions containing the nanoparticles were kept under magnetic stirring and periodically subjected to an ultrasonic treatment during 10 – 15 minutes.

HA-DN*$_{36h}$ and BGNPs were used as polyanion, while CHT-C*$_{18h}$ was used as polycation. PEI was used as an initial layer precursor, by immersing each substrate for 20 min, prior to multilayer deposition. Therefore, after immersion in PEI, the polycation CHT-C*$_{18h}$ was used to initiate alternating deposition between oppositely charged polyelectrolyte (PE).

LbL coatings with 11 bilayers, i.e. 22 layers, were developed, as shown in Figure 4.1: Multifunctional films containing [CHT-C*$_{18h}$/HA-DN*$_{36h}$/CHT-C*$_{18h}$/BGNPs]$_5$ + [CHT-C*$_{18h}$/HA-DN*$_{36h}$] (MF6); and polymeric films (control) containing [CHT-C*$_{18h}$/HA-DN*$_{36h}$]$_{11}$ (CTR6). MF films ending with an adhesive layer were chosen since we found in a previous work [83] that they have higher adhesive strength than those ending with BGNPs.

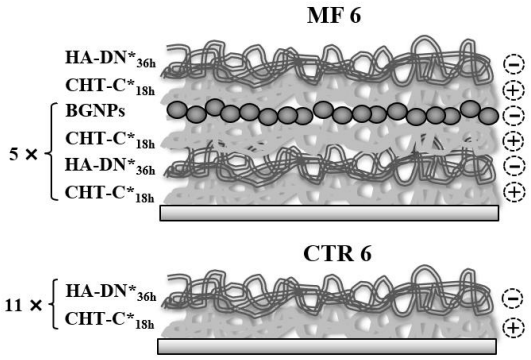

Figure 4.1 – Schematic illustration of the multifunctional (MF) and control (CTR) coatings.

Dip-coated films were build-up by alternating substrate immersion in the oppositely-charged PE solutions. The dipping times were established after an optimization process in previous works of our group [33,34], where 10 minutes were used for CHT-C*$_{18h}$ and HA-DN*$_{36h}$ and 20 minutes for BGNPs. In addition, a rinsing step was included for 5 min with 0.15 M NaCl solution, between the adsorptions of each PE.

Spin-coated films were prepared using a spin-coater (WS-650Hzb-23NPPB-UD-3, LAURELL, USA). A 300 µL PE solution was dropped for the first bilayer, 200 µL for the second bilayer and 100 µL for the remaining bilayers, so that the entire surface area of substrate was covered. PE solutions were alternatively spin-coated onto the substrates at a spinning speed of 3000 rpm for 10 seconds and at an acceleration of 1300 rmp^2. Additional rising steps between the layer depositions were excluded, since the concentration of PE solutions used was low.

At the end of each procedure, the coatings were subjected to 3 rising steps in ultrapure water to remove any salt deposition derived from the LbL process. Then, LbL coatings were allowed to dry at room temperature, overnight.

4.2.7 Surface Characterization

The surface morphology of LbL coatings was analysed by scanning electron microscopy (SEM, JSM-6010 LV, JEOL, Japan) and Fourier transform infrared (FT-IR) imaging (Perkin-Elmer Instruments, Shelton, CT, USA). Before SEM analysis, LbL coatings were sputtered with a thin platinum layer, using a sputter coater EM ACE600 (Leica Microsystems, Germany). SEM microphotographs were taken with a resolution of 500 μm and 10 μm. FT-IR imaging analysis was performed using a Perkin-Elmer Spectrum Spotlight 300 FT-IR Microscope System in reflectance mode. FT-IR maps were construct by a spectrum collected in continuous scan mode for a spectral range 4000–720 cm^{-1} and sample areas of 500×500 μm^2. Each spectrum was collected with an average of 15 repetitive scans with a spectral resolution of 16 cm^{-1}. FT-IR spectra were integrated by taking the areas under the curve between the limits of the peaks of interest. The peak ranges were chosen based on the characteristic peaks corresponding to specific vibrational bonds for all materials constituting the LbL coatings. A false colour was assigned to each material analysed. C=O stretching of amide I centred at approximately 1650 cm^{-1}, was the region chosen for CHT identification, and the C=O stretching of carboxylic acid at about 1730 cm^{-1} was chosen for HA, both depicted on the chemical maps by red and green, respectively [51,52]. The characteristic peak of CHT corresponding to the amine deformation vibration, N–H bending vibration, centred at 1590 cm^{-1} could not be used due to overlapping with the amide II peak present in both polysaccharides [53]. On the other hand, the region chosen for catechol groups identification corresponds to out-of-plane C–H bending vibration centred at 740 cm^{-1} and C–H stretching vibration centred at 3052 cm^{-1}, both belonging to the aromatic C–H group and represented on the chemical maps by blue [54–56]. The C=C vibrations peaks of the aromatic ring, approximately between 1466 and 1515 cm^{-1}, were not chosen due to overlapping with characteristic peaks of the polysaccharides [55,56]. Furthermore, for the BGNPs identification, the chosen region was the silicate absorption bands, Si–O–Si, assigned to the peaks 1085 and 800 cm^{-1} corresponding to asymmetric stretching and symmetric stretching vibration, respectively, and represented in the chemical maps by cyan [50,57].

The surface roughness of the LbL coatings was analysed by atomic force microscopy (AFM) using a JPK NanoWizard III AFM system (JPK Instruments AG, Berlin, Germany). Bio-AFM imaging was operated in air and performed on dried LbL coatings in tapping mode (AC mode) AFM. A commercial silicon probe (Acta probe) with Al coating on the cantilever backside, and with a spring constant of 40 N/m was used. The topography of the LbL coatings was analysed with a resolution of 512 x 512 $pixels^2$, at line rates of 0.5 to 1 Hz, and resonance frequency around 300 kHz. AFM images with 20 x 20 μm^2 were obtained

and at least three measurements of the surface roughness were performed, followed by R_q and R_a calculations.

The wettability of LbL coatings were also evaluated by the sessile drop method using an OCA15plus Goniometer equipment (DataPhysics, Germany). For each coating surface, 3 measurements were made, using 3 µL droplets of osmotized water dispensed by a motor-driven syringe. The water contact angle (WCA) measurements were performed at room temperature and the pictures taken immediately after the drop contacted the surface. The results were treated using the SCA20 software.

4.2.8 Statistical Analysis

The results of all experiments were carried out at least in three replicates (n=3) and were presented as mean ± standard deviation (SD).

Statistical significance between groups was determined by One-way ANOVA with Turkey's Multiple comparison test, using Graph Pad Prism version 6.0 (GraphPad software, San Diego, CA). Statistical differences were represented and set to $p<0.05$(+/*), $p<0.01$(++/**), $p<0.001$(+++/***), and $p<0.0001$(++++/****).

4.3 Results and Discussion

4.3.1 HA-DN and CHT-C Modified Polymers: DS (%) Analysis

To confirm if the modification of HA and CHT was successful, solutions of HA-DN*$_{36h}$ (0.5 mg.mL^{-1}) and CHT-C*$_{18h}$ (1 mg.mL^{-1}) were analysed by UV-Vis spectroscopy, Figure 4.2.

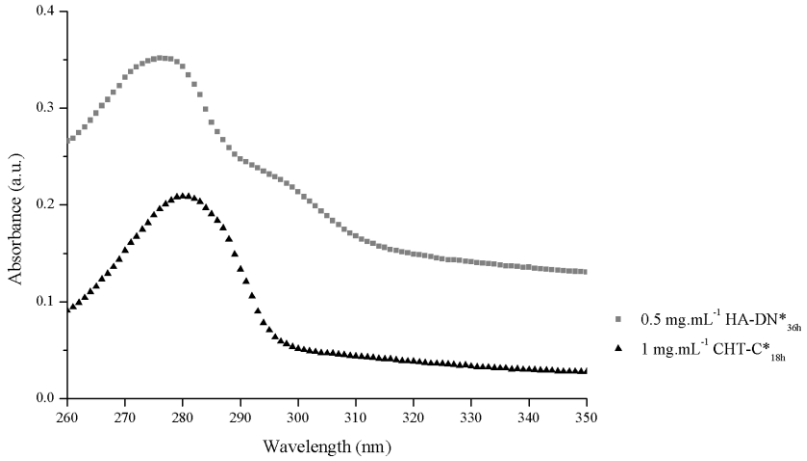

Figure 4.2 – UV-Vis spectra for HA-DN*$_{36h}$ and CHT-C*$_{18h}$.

The spectra of HA-DN*$_{36h}$ and CHT-C*$_{18h}$ exhibit a maximum absorbance peak at a wavelength around 280 nm, confirming the presence of the catechol groups in the modified CHT and HA polymers [24,25,33,34]. Moreover, the absence of additional peaks at wavelengths longer than 300 nm proves that the synthesized conjugates were not oxidized [24,25,33,34].

According to the experimental values (see Appendix I and II), the DS (%) obtained for HA-DN*$_{36h}$ and CHT-C*$_{18h}$ were around 54% and 9%, respectively. These DS (%) results obtained were different from those found in other works [23–26,33,34]. The DS (%) of HA-DN*$_{36h}$ was higher than the value of 11% obtained in our previous studies [33,34]. This feature could be explained by the different molecular weight of HA and/or the distinct reaction time. On the other hand, the DS (%) value of CHT-C*$_{18h}$ was lower than the one found in other works [24–26]. These results could be explained by different conditions used in this study, such as the relative proportions of the reagents, the molecular weight of CHT, the reaction time and the fact that the conjugate was dissolved in 0.15 M NaCl.

4.3.2 SEM and FT-IR Analysis

The morphology of the dip- and spin-coated LbL coatings was analysed by SEM. Figures 4.3-4.5 show the images of the produced coatings using glass, 316L SS and Ti as substrates, respectively.

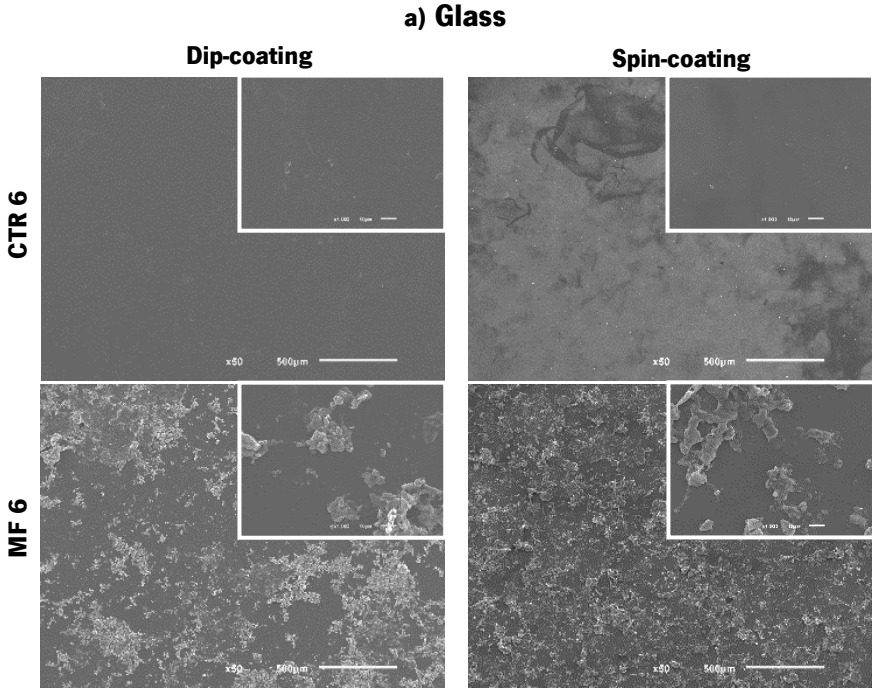

Figure 4.3 – SEM images of the two LbL coatings configurations (Figure 4.1) obtained by dip- and spin-coating methods, using glass as substrate. The scale bar of the main images represents 500 µm and the secondary ones 10 µm.

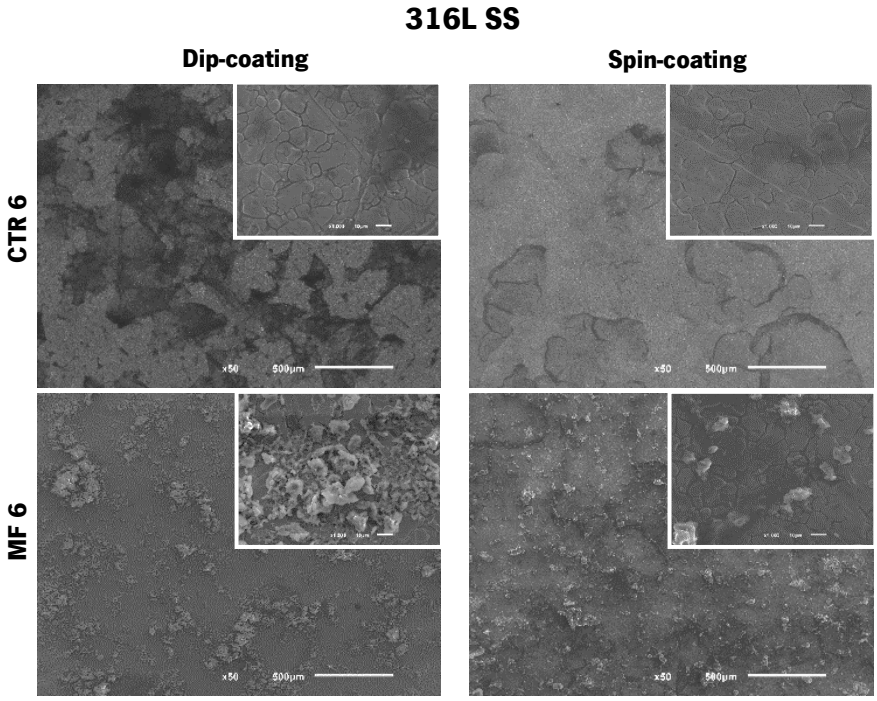

Figure 4.4 – SEM images of the two LbL coatings configurations (Figure 4.1) obtained by dip- and spin-coating methods, using 316L SS as substrate. The scale bar of the main images represents 500 µm and the secondary ones 10 µm.

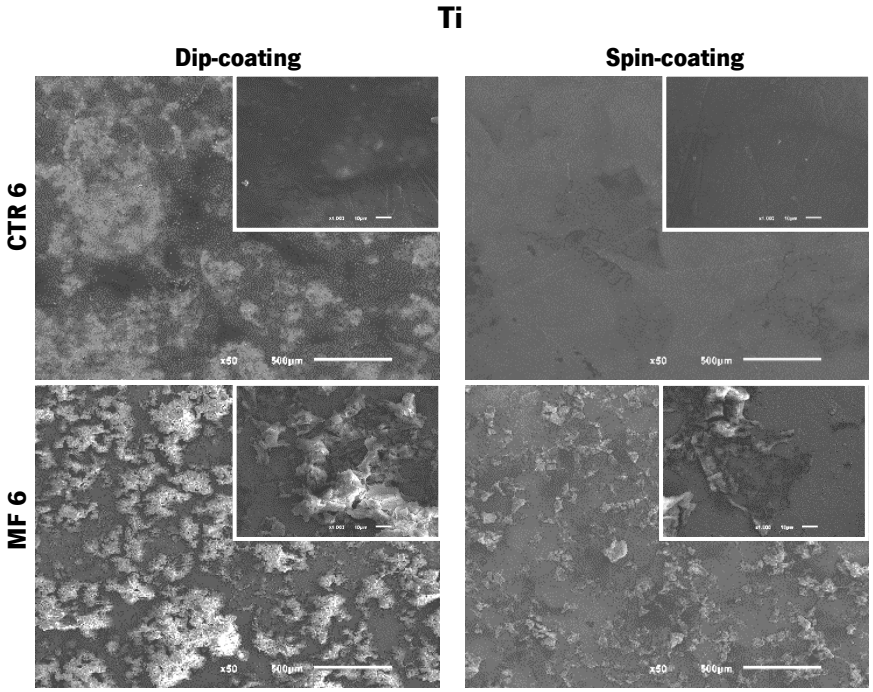

Figure 4.5 – SEM images of the two LbL coatings configurations (Figure 4.1) obtained by dip- and spin-coating methods, using Ti as substrate. The scale bar of the main images represents 500 µm and the secondary ones 10 µm.

As can be seen for the three types of substrates, there were differences in the morphology between the surfaces of the dip- and spin-coated LbL films. Independently of the substrate, all spin-coated formulations appear to be smoother and with a more homogeneous structure than the dip-coated ones. Herrera *et al.* [58] found the same result for nanocellulose coatings on porous cellulose substrates using

the dip- and spin-coating methods. They also found that the coating thickness was hundreds of nanometers for the spin-coated films whereas for the dip-coated ones was in the micrometers range [58].

MF6 films evidenced the presence of some particle agglomeration, when compared to CTR6 films. This difference in morphology is related to the presence of BGNPs in these films. Moreover, BGNPs distribution at the film surface seems to be more homogeneous in the spin-coated films than in the dip-coated ones. In addition to these particles, minor ones may be observed in almost all formulations. These are believed to be polymeric agglomerations of the coating components that were not completely removed in the centrifugation step, in the case of the spin-coating technique, or that resulted from the interlayer diffusion of PEs, in case of the dip-coating technique [47].

To further study the surface distribution of the various components of the LbL coatings obtained by dip- and spin-coating methods, namely CHT, HA, catechol groups and BGNPs, FT-IR imaging spectroscopy was performed.

Figures 4.6-4.8 show the FT-IR mapping for the produced LbL coatings using glass, 316L SS and Ti as substrates, respectively.

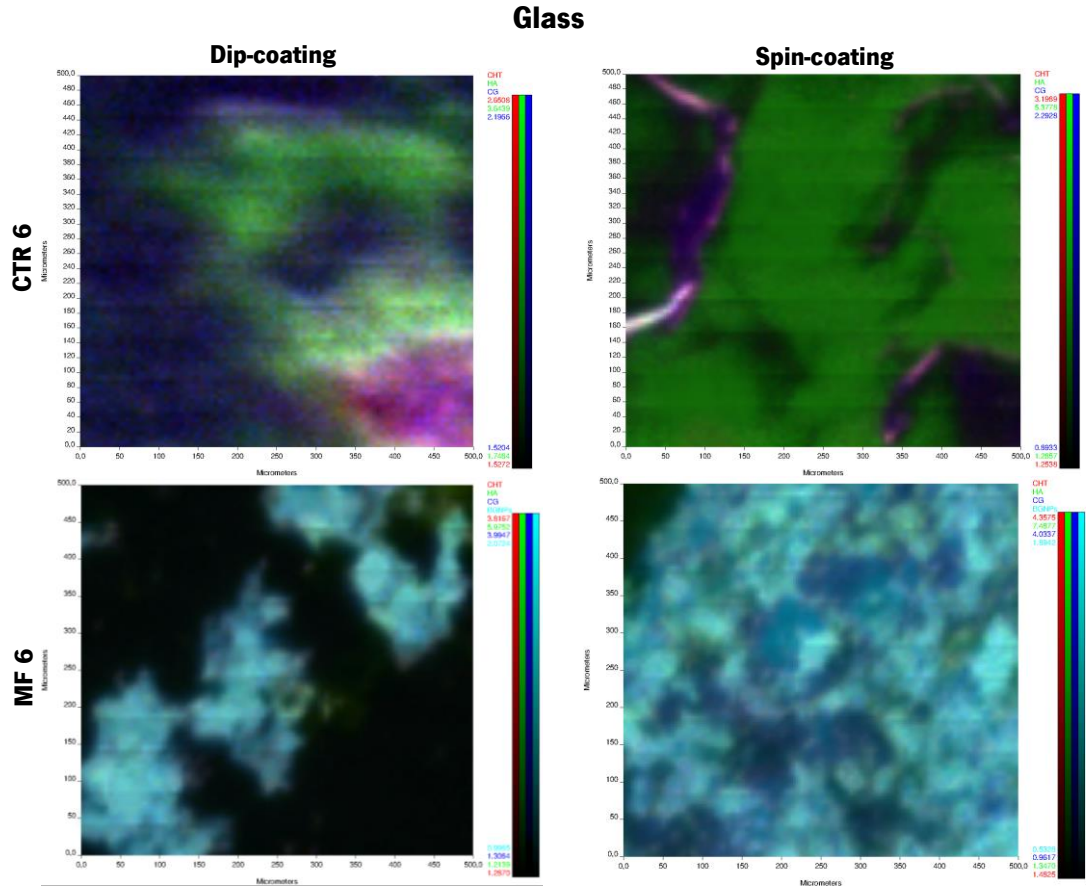

Figure 4.6 – Chemical maps of the two LbL coatings configurations (Figure 4.1) obtained by dip- and spin-coating methods, using glass as substrate. For the chemical map, red indicates the presence of CHT, green the presence of HA, blue the presence of catechol groups and cyan corresponds to the BGNPs. Note that the existence of regions with different intensities can be an indication of differences in thickness.

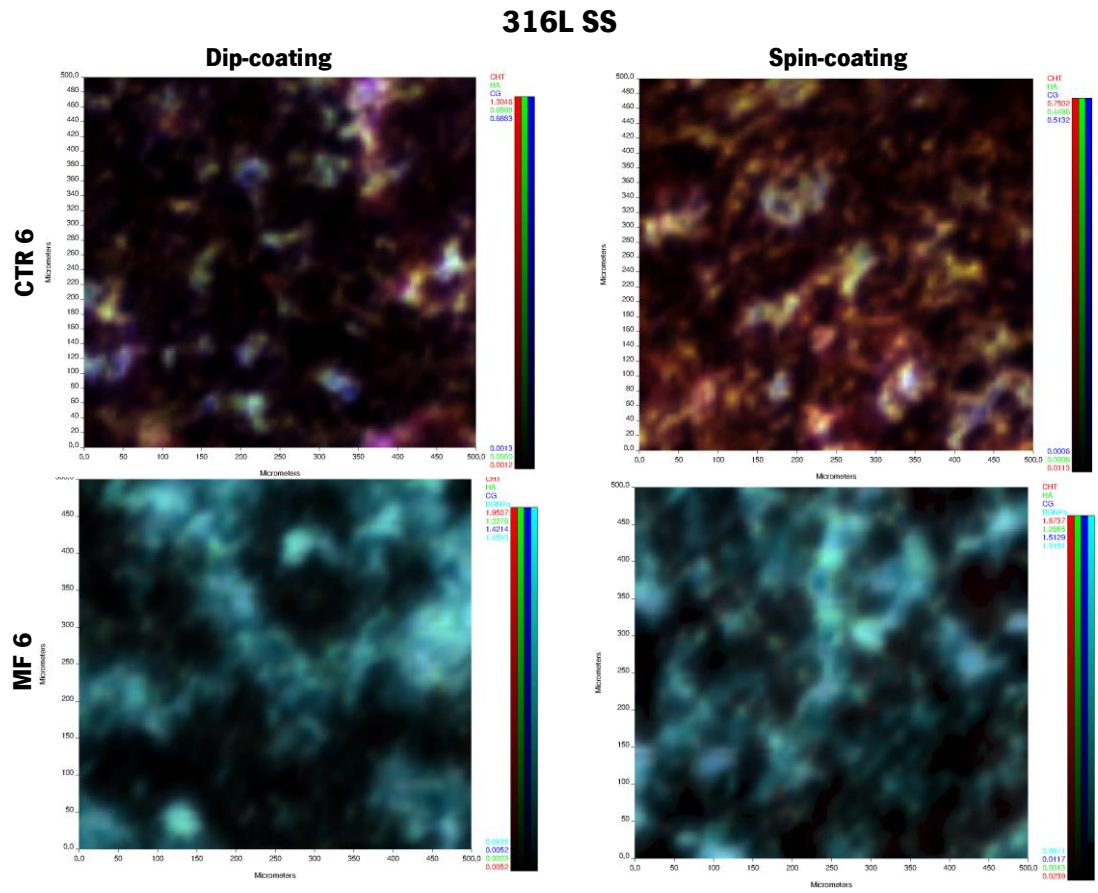

Figure 4.7 – Chemical maps of the two LbL coatings configurations (Figure 4.1) obtained by dip- and spin-coating methods, using 316L SS as substrate. For the chemical map, red indicates the presence of CHT, green the presence of HA, blue the presence of catechol groups and cyan corresponds to the BGNPs. Note that the existence of regions with different intensities can be an indication of differences in thickness.

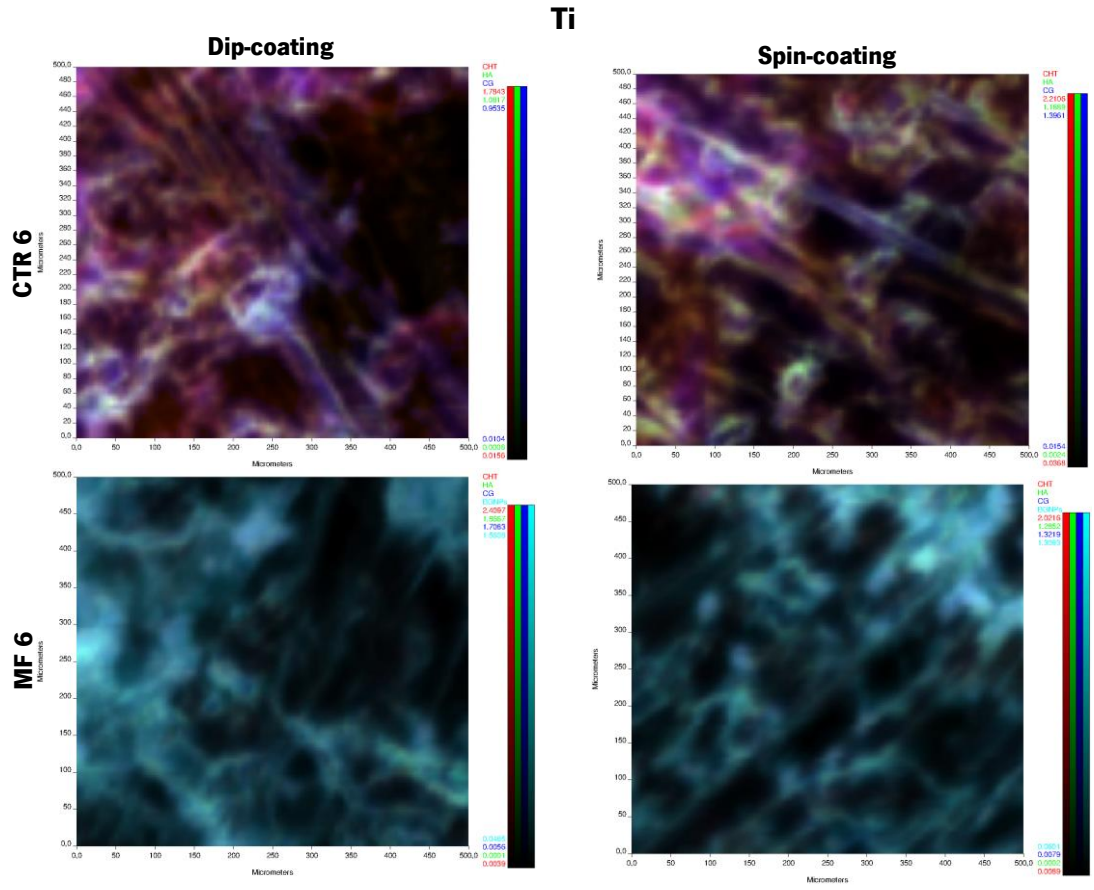

Figure 4.8 – Chemical maps of the two LbL coatings configurations (Figure 4.1) obtained by dip- and spin-coating methods, using Ti as substrate. For the chemical map, red indicates the presence of CHT, green the presence of HA, blue the presence of catechol groups and cyan corresponds to the BGNPs. Note that the existence of regions with different intensities can be an indication of differences in thickness.

Figure 4.6, shows that the CTR6 and MF6 spin-coated LbL configurations on the glass substrate appeared to have more uniform and ordered coating structures compared to those obtained by dip-coating. This finding is in agreement with the results of other authors [45,46]. Cho *et al.* [45], prepared spin- and dip-coated poly(allylamine hydrochloride)/poly(sodium 4-styrenesulfonate) films and the AFM analysis evidenced highly ordered structures for the spin-coated ones. Lee *et al.* [46], developed spin- and dip-coated linear polyethylenimine/poly(acrylic acid) films and, based on investigations of both the surface nanoroughness and the relative composition of constituting polyelectrolytes, concluded that films produced by spin-coating showed less PE interpenetration between the layers, producing a linear growth of the thickness, rather than the common exponential growth in the LbL assembly by dip-coating.

This characteristic was most clearly seen for the spin-coated CTR6 condition. In this configuration it was possible to identify the main presence of HA (green), which was the end-layer of all LbL coatings, indicating a more ordered coating structure. However, spots of a colour mixture were also detected in both dip- and spin-coated CTR6 films. As already evidenced in the SEM results, these spots probably resulted from the PE interpenetration between the layers or due to coating components that were not

completely removed during spinning. In the case of the dip- and spin-coated MF6 configurations, the presence of BGNPs (cyan) was easily visualized. Some HA (green) and catechol groups (blue) spots related to the end-layer of the LbL coatings were also observed in these formulations. In contrast to the dip- and spin-coated CTR6 configurations, the coatings containing BGNPs did not exhibit colour-mixed spots. This finding is quite relevant, indicating that the presence of BGNPs may act as barrier to the PE diffusion, facilitating the more uniform deposition of the polymer layers. Furthermore, in the both spin-coated CTR6 and MF6 configurations, a lower intensity difference was observed compared to the dip-coated ones, which may be an indication of a lower surface roughness.

For both metals, 316L SS and Ti (Figure 4.7 and Figure 4.8), these differences were not so obvious. Although differences in intensity were observed between the two LbL techniques, a similar colour mixture for dip- and spin-coated CTR6 conditions was noticed. Such feature may be due to the intrinsic surface roughness of these two metals, which can contribute to a higher PE interpenetration between the layers of the coatings obtained by the two LbL assembly methods. Nevertheless, it was also observed for the metals substrates that the dip- and spin-coated MF6 films did not present the PE colour-mixture, in agreement with the results found for the glass substrate.

4.3.3 AFM Analysis

The topography of the coatings produced on the three substrates was analysed by AFM. Figures 4.9-4.11 show the roughness results for each LbL coating produced on glass, 316L SS and Ti, respectively, by dip- and spin-coating techniques.

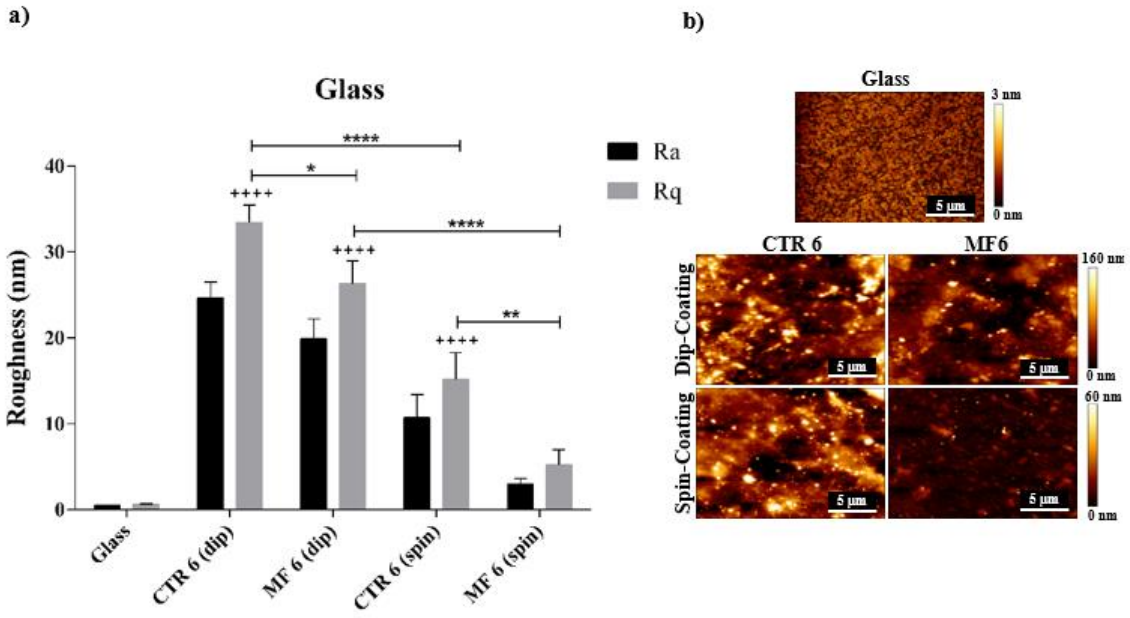

Figure 4.9 – a) Ra and Rq roughness values (nm) measured for the two LbL coatings configurations (Figure 4.1) produced on glass by dip- and spin-coating. Data are presented by means ± standard deviation (n = 3). Statistical differences were represented for Rq roughness values, where rows plus "*" indicate differences between the various conditions, and "+" (at the top of each bar) indicate their differences compared to the uncoated glass substrate (glass control) [++++/**** p<0.0001; ** p<0.01; * p<0.05; One-way ANOVA with Turkey's Multiple comparison test]. b) Representative AFM images for each LbL coating condition, with a scanned surface area of 20×20 µm².

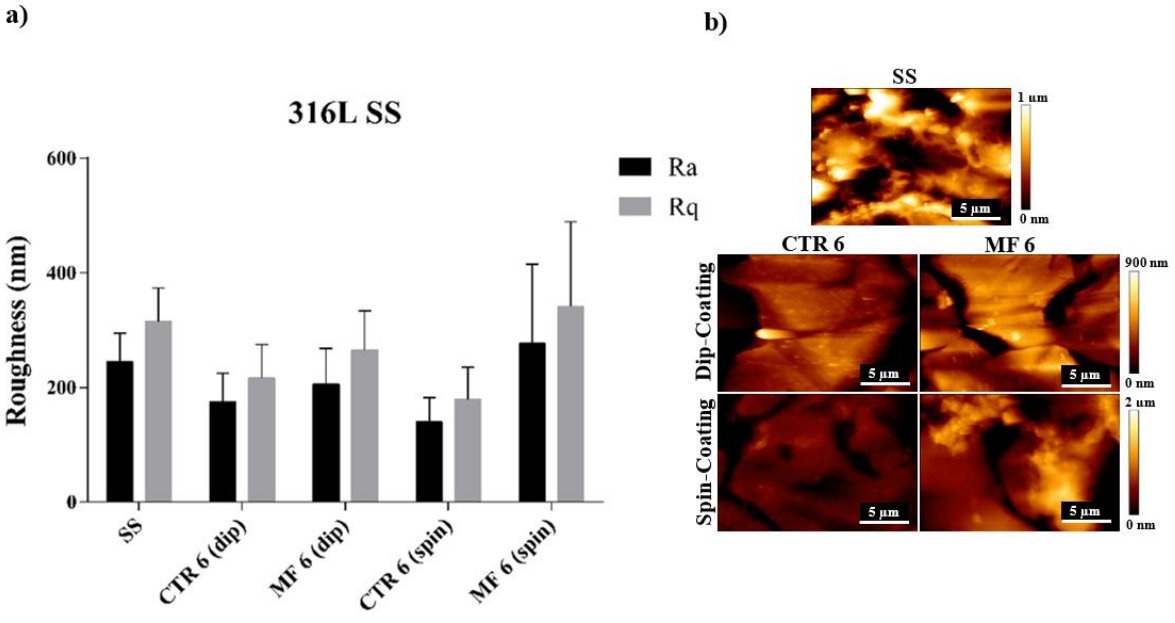

Figure 4.10 – a) Ra and Rq roughness values (nm) measured for the two LbL coatings configurations (Figure 4.1) produced on 316L SS by dip- and spin-coating methods. Data are presented by means ± standard deviation (n = 3) [One-way ANOVA with Turkey's Multiple comparison test]. b) Representative AFM images for each LbL coating condition, with a scanned surface area of 20×20 µm².

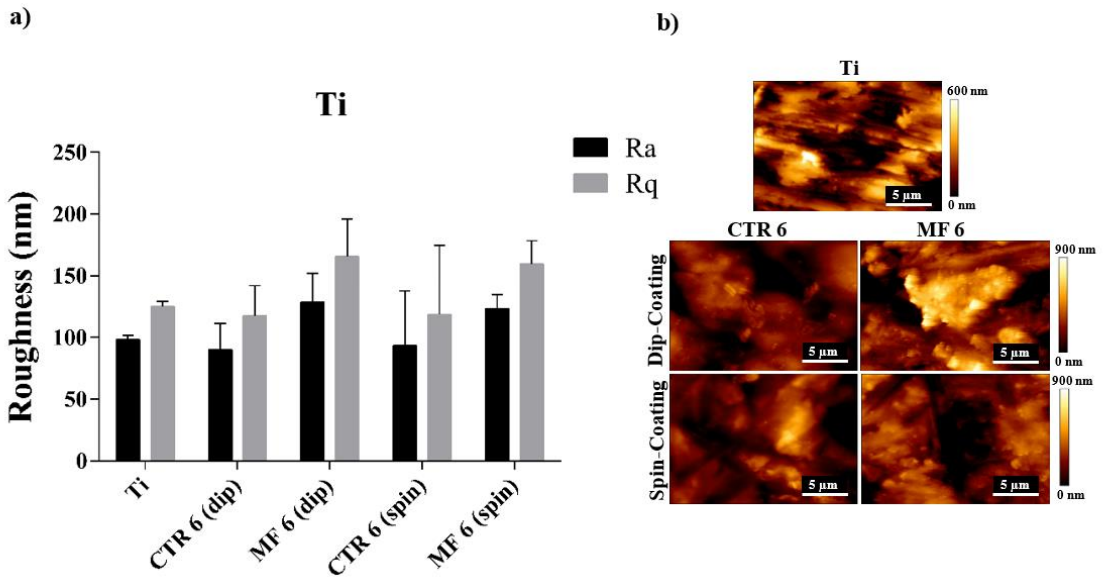

Figure 4.11 – a) Ra and Rq roughness values (nm) measured for the two LbL coatings configurations (Figure 4.1) produced on Ti by dip- and spin-coating methods. Data are presented by means ± standard deviation (n = 3) [One-way ANOVA with Turkey's Multiple comparison test]. b) Representative AFM images for each LbL coating condition, with a scanned surface area of 20×20 μm^2.

Figure 4.9 shows that the LbL coatings (CTR6 and MF6) obtained by spin-coating presented a statistically significant lower roughness (**** $p<0.0001$) than those produced by dip-coating. Marudova *et al.* [47], have also seen similar results. They observed that spin-coated CHT/xanthan multilayer films are smoother than the dip-coated ones. The low roughness of spin-coated coatings could be interpreted as a lack of PE interpenetration giving rise to more flat and clearly separated layers [47]. On the other hand, the rough surface topography of the dipping-assembled coatings could indicate the presence of higher loose interpenetrating structures [47].

Moreover, the surface roughness of the MF films containing BGNPs (MF6) decreases when compared to their respective controls (CTR6) - Figure 4.9. This trend was seen for MF films produced by both LbL assembly methods. This could be explained by the combined effect of catechol groups from CHT-C and HA-DN, which maintain the inorganic phase strongly bonded to the polymeric phase, acting as a glue [33,34].

As can be seen in Figure 4.10, the SS control exhibited a high surface roughness (Rq value around 315±58 nm). Indeed, the SS substrates were used without further surface treatment. Thus, despite changes in the surface roughness between the LbL conditions and the SS control were noted, due to the presence of the coatings, they did not present relevant differences. Except for the spin-coated MF6 condition, a tendency to decrease the surface roughness of the LbL conditions compared to the SS control can be observed, which indicates that the coatings contributed to greater uniformity of the SS substrates.

Although this decrease has not been observed for the spin-coated MF6 condition, it should be noted that it has a significant standard deviation value (Rq value around 340±147 nm). This may be due to the presence of BGNPs and to the thickness of the coating, which should be lower for the spin-coated conditions. Indeed, a comparison study between dip- and spin-coating techniques found that immersive-assembly prepared thicker, rougher films, whereas spinning resulted in thinner, smoother films [59]. As in the present study the SS substrate had a high surface roughness, such differences were not relevant. However, a slight decrease of the surface roughness of the spin-coated CTR6 condition was seen, when compared to the dip-coated one. Furthermore, unlike the AFM results of the glass, the presence of BGNPs in both dip- and spin-coated MF film appear to contribute to a greater surface roughness compared to their respective controls (CTR6).

Ti also presented a considerable surface roughness (Rq value around 125±4 nm) (Figure 4.11), although it was lower than the SS control. So, the roughness differences between Ti substrates and the LbL coatings were not evident. Nevertheless, it seems that CTR6 films present a lower roughness than the Ti control, whereas the MF6 films have a higher roughness. Furthermore, no significant differences between the two LbL techniques were noted. Also, similar to the 316L SS results, for both dip- and spin-coated MF films, the presence of BGNPs appears to contribute to a higher surface roughness than the one of their respective controls. These topographic results, as well as those obtained for 316L SS, appeared to have a significant interference of the intrinsic surface roughness of the metals. Hence, in a future work both substrates should be subjected to a more efficient polishing process.

4.3.4 WCA Analysis

The wettability of the developed LbL coatings was assessed by WCA analysis. Figures 4.12-4.14 show the wettability results for each LbL coating produced on glass, 316L SS and Ti, respectively, by dip- and spin-coating.

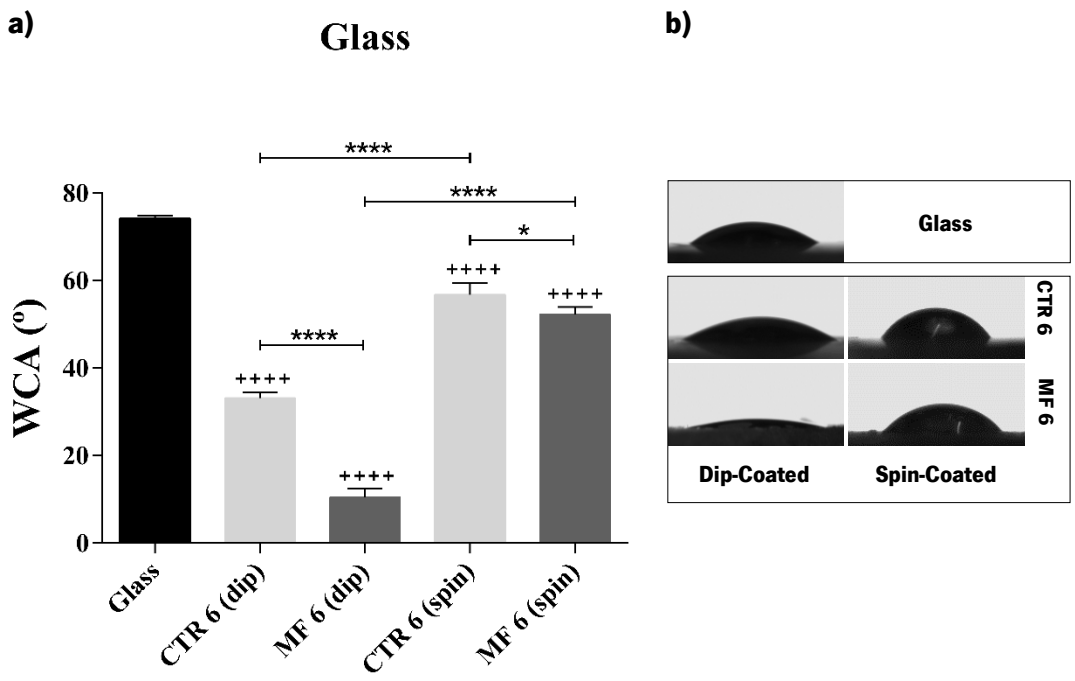

Figure 4.12 – a) WCA (°) values measured for the two LbL coatings configurations (Figure 4.1) produced on glass by dip- and spin-coating methods. Statistical differences between the various configurations are indicated by the rows plus "*", while their comparisons with the uncoated glass substrate (glass control) are indicated by "+" (at the top of each bar). Data are presented by means ± standard deviation (n = 3; ++++/**** p<0.0001; * p<0.05) [One-way ANOVA with Turkey's Multiple comparison test]; b) Representative image of water drops for each multilayered film surface.

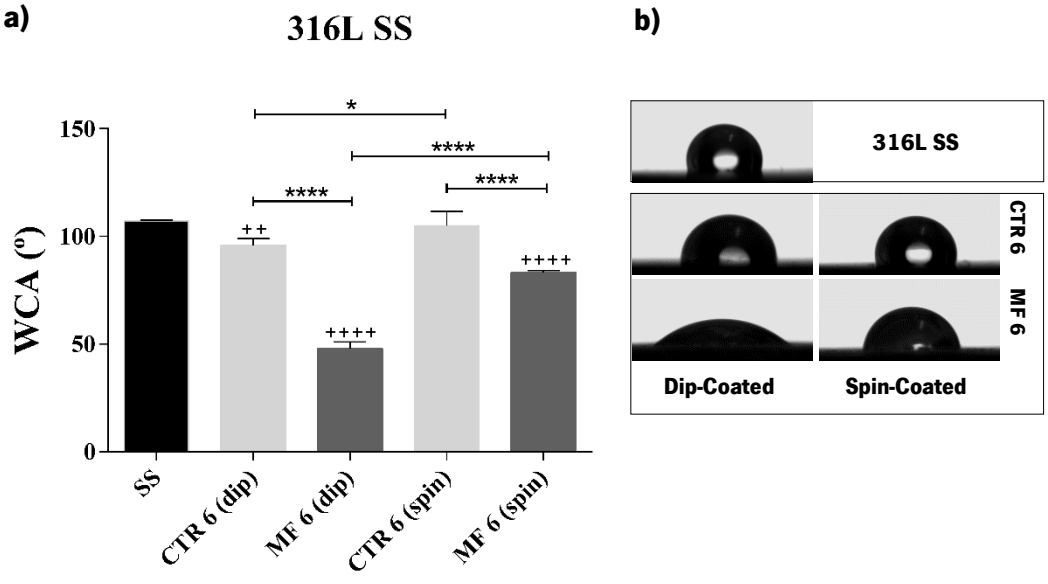

Figure 4.13 – a) WCA (°) values measured for the two LbL coatings configurations (Figure 4.1) produced on 316L SS by dip- and spin-coating methods. Statistical differences between the various configurations are indicated by the rows plus "*", while their comparisons with the uncoated SS substrate (SS control) are indicated by "+" (at the top of each bar). Data are presented by means ± standard deviation (n = 3; ++++/**** p<0.0001; ++ p<0.01; * p<0.05) [One-way ANOVA with Turkey's Multiple comparison test]; b) Representative image of water drops for each multilayered film surface.

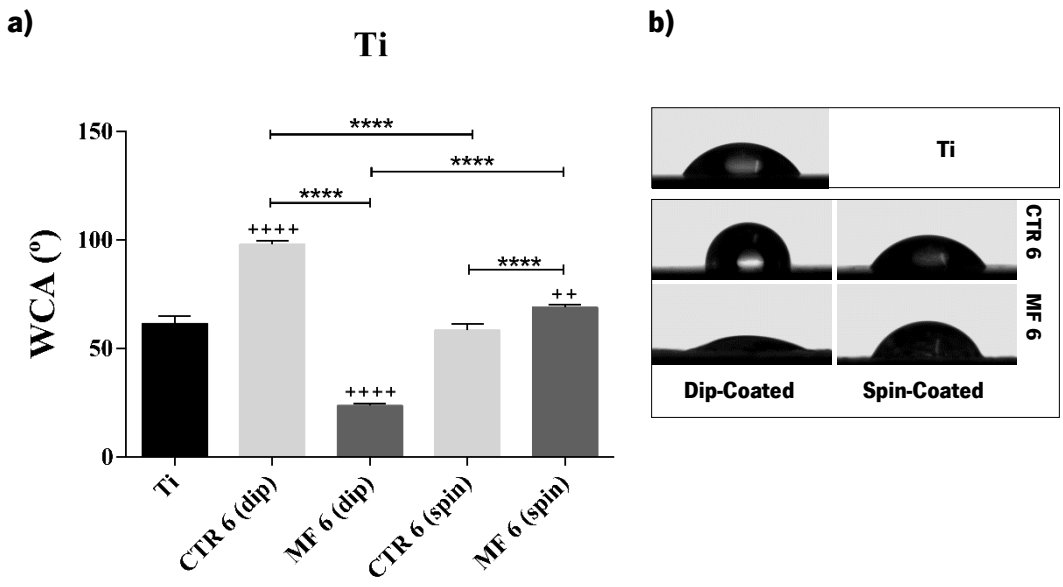

Figure 4.14 – a) WCA (°) values measured for the two LbL coatings configurations (Figure 4.1) produced on Ti by dip- and spin-coating methods. Statistical differences between the various configurations are indicated by the rows plus "*", while their comparisons with the uncoated Ti substrate (Ti control) are indicated by "+" (at the top of each bar). Data are presented by means ± standard deviation (n = 3; ++++/**** $p<0.0001$; ++ $p<0.01$) [One-way ANOVA with Turkey's Multiple comparison test]; b) Representative image of water drops for each multilayered film surface.

As expected from the AFM analysis, WCA changes between the various LbL conditions and the glass control were noticed in Figure 4.12. These changes were statistically significant for all conditions obtained by dip- and spin-coating methods. According to the Wenzel model [60], roughness affects the contact angle hysteresis. This model predicts that roughness will decrease the WCA if the angle on the smoother surface of the same material is lower than 90° (hydrophilic solid). On the other hand, the WCA will increase if the angle is higher than 90° (hydrophobic solid) [60]. Therefore, since the uncoated glass surface has a hydrophilic nature (WCA around 74°), the increased roughness of the dip-coated LbL conditions compared to the spin-coated ones resulted in a decrease in WCA values. This decrease in WCA values for the dip-coated conditions (CTR6 and MF6) showed statically significant differences (**** $p<0.0001$) compared to those spin-coated ones.

Moreover, it was found that the coatings obtained by the two LbL methods exhibit higher hydrophilicity than the glass control. These results could be explained by the presence of catechol groups in the modified CHT and HA polymers. In fact, the hydrophilicity increase of glass substrates after deposition of multilayer films containing HA modified with catechol groups has been reported [33,61–63]. For example, we found in a previous work [33] that $[CHT/HA\text{-}DN]_{10}$ dip-coated films showed lower WCA values (around 73°) compared to $[CHT/HA]_{10}$ dip-coated films (around 77°), using glass as substrate. These WCA results obtained for $[CHT/HA\text{-}DN]_{10}$ dip-coated films were higher than those

obtained in the present study. Such can be explained by the higher content of catechol groups in the LbL coatings, as both polymers were modified with catechol groups.

Furthermore, the inclusion of BGNPs in the dip- and spin-coated films seems to affect their wettability. In fact, the presence of BGNPs in the MF6 films were able to render their surfaces more hydrophilic, showing lower WCA values compared to those obtained for their respective controls (CTR6). These results are in agreement with previous works [64–66], where it was found that the presence of bioactive glass particles at the surface of a composite increases its hydrophilicity.

WCA changes between the various LbL conditions and the SS control were also observed in Figure 4.13. As with the glass wettability results, an increase of the hydrophilicity of the SS substrates was observed with the film deposition by the two LbL methods. In particular, a statistically significant WCA decrease was detected for the dip- and spin-coated MF6 conditions, while a less significant decrease was observed for the dip-coated CTR6 condition. On the other hand, the spin-coated CTR6 condition showed only a slight WCA decrease. Furthermore, a more pronounced WCA decrease was noted for both dip- and spin-coated MF6 conditions, when compared to their respective controls (CTR6). This decrease was related to the hydrophilic nature of BGNPs and was statistically significant for both dip- and spin-coated MF6 conditions. Unlike glass, the uncoated SS substrate showed a hydrophobic nature (107°). According to the Wenzel model [60], the increased roughness will increase the WCA if the angle is higher than 90° (hydrophobic solid) [60]. From Figure 4.13, higher WCA values were observed for both spin-coated CTR6 and MF6 conditions, when compared to those dip-coated ones. These differences were statistically significant for the MF6 and CTR6 condition. In fact, it was previously noticed through SS AFM analysis that the LbL conditions obtained by spin-coating seemed to present surface roughness values equal to or greater than those obtained by dip-coating.

WCA changes between the various LbL conditions and Ti control were also observed (Figure 4.14). Unlike the glass and SS wettability results, a WCA decrease was not seen for all conditions, when compared to the Ti control. In particular, a statistically significant WCA increase was observed for the dip-coated CTR6 and the spin-coated MF6. On the other hand, a statistically WCA significant decrease was detected for the dip-coated MF6 and insignificant for the spin-coated CTR6. Clearly, the Ti wettability results were affected by the intrinsic surface roughness of this metal.

According to the Wenzel model [67], since the uncoated Ti substrate showed a hydrophilic nature (about 61°), its greater roughness will decrease the WCA. As can be seen in Figure 4.14, the dip-coated CTR6 condition showed to induce a statistically significant decrease in the hydrophilicity of the Ti substrates compared to the spin-coated one. This can be explained by the increased surface roughness

in the spin-coated CTR6. Since the spin-coating technique produces thinner films, the intrinsic roughness of the metal can more easily affect the wettability results, showing WCA values similar to the Ti control. On the other hand, it can be observed that the dip-coated MF6 condition led to a statistically significant increase in the hydrophilicity of the Ti substrates, when compared to the spin-coated one. Unlike the spin-coating method, dip-assembly leads to a less homogeneous distribution of BGNPs. This less ordered distribution may contribute to the increase in surface roughness of MF6 films, explaining these differences in WCA values.

Furthermore, as for glass and SS results, a statistically significant WCA decrease was noted for the dip-coated MF6, when compared to its respective control.

4.4 Conclusions

Dip- and spin-coating techniques were successfully applied for the deposition of catechol-modified polysaccharides multilayered films with or without bioglass nanoparticles on glass, 316L SS and Ti substrates. SEM images of all substrates indicated that, at the microscale, the spin-coated formulations had a smoother and more homogeneous surface morphology than the dip-coated ones.

Further investigations with FT-IR imaging and AFM analysis proved that both spin-coated films on the glass substrate had a more uniform structure with lower surface roughness, when compared to those obtained by dip-coating. These results could be interpreted as a lack of PE interpenetration between the spin-coated layers, unlike those obtained by dip-assembly.

For the glass substrate, it was found that the incorporation of BGNPs in both dip- and spin-coated films contributed to a smoother cohesive structure with less diffusion of PEs, when compared to their respective controls. Such feature may result from the combined effect of catechol groups of both CHT-C and HA-DN polymers, acting as a glue between the inorganic and organic phase. Wettability analysis revealed that the coatings obtained by the two LbL methods exhibit higher hydrophilicity than the glass control. It was also found that the spin-coated films had higher WCA than the dip-coated ones.

However, for both metals, 316L SS and Ti, such differences were not so obvious. This feature was due to the intrinsic surface nanoroughness observed for the two metals by AFM. Nevertheless, from the FT-IR analysis we noticed that although the results of MF6 condition on both metals agreed with those found for the glass substrate, the CTR6 condition presented a PE colour-mixture for the two LbL methods, evidencing PE interpenetration between the layers of the coatings. Furthermore, unlike the AFM results of the glass, for both dip- and spin-coated MF6 films the presence of BGNPs appeared to contribute to a

higher surface roughness compared to their respective controls (CTR6). In general, for both metals the wettability increased when the coatings were deposited by both LbL methods.

Acknowledgements

The authors acknowledge the Portuguese Foundation for Science and Technology (FCT) and the European program FEDER/COMPETE for the financial support through project LA ICVS/3Bs - 2015-2017.

4.5 References

[1] M. Niinomi, M. Nakai, J. Hieda, Development of new metallic alloys for biomedical applications, Acta Biomater. 8 (2012) 3888–3903. doi:https://doi.org/10.1016/j.actbio.2012.06.037.

[2] S.B. Goodman, Z. Yao, M. Keeney, F. Yang, The future of biologic coatings for orthopaedic implants., Biomaterials. 34 (2013) 3174–3183. doi:10.1016/j.biomaterials.2013.01.074.

[3] M. Xiao, Y.M. Chen, M.N. Biao, X.D. Zhang, B.C. Yang, Bio-functionalization of biomedical metals, Mater. Sci. Eng. C. 70 (2017) 1057–1070. doi:10.1016/j.msec.2016.06.067.

[4] R.A. Gittens, R. Olivares-Navarrete, Z. Schwartz, B.D. Boyan, Implant osseointegration and the role of microroughness and nanostructures: Lessons for spine implants, Acta Biomater. 10 (2014) 3363–3371. doi:https://doi.org/10.1016/j.actbio.2014.03.037.

[5] R.A. Surmenev, M.A. Surmeneva, A.A. Ivanova, Significance of calcium phosphate coatings for the enhancement of new bone osteogenesis – A review, Acta Biomater. 10 (2014) 557–579. doi:https://doi.org/10.1016/j.actbio.2013.10.036.

[6] E. Mohseni, E. Zalnezhad, A.R. Bushroa, Comparative investigation on the adhesion of hydroxyapatite coating on Ti–6Al–4V implant: A review paper, Int. J. Adhes. Adhes. 48 (2014) 238–257. doi:https://doi.org/10.1016/j.ijadhadh.2013.09.030.

[7] J.R. Jones, Reprint of: Review of bioactive glass: From Hench to hybrids, Acta Biomater. 23 (2015) S53–S82. doi:https://doi.org/10.1016/j.actbio.2015.07.019.

[8] J.R. Jones, Review of bioactive glass: from Hench to hybrids., Acta Biomater. 9 (2013) 4457–4486. doi:10.1016/j.actbio.2012.08.023.

[9] F. Baino, G. Novajra, V. Miguez-Pacheco, A.R. Boccaccini, C. Vitale-Brovarone, Bioactive glasses: Special applications outside the skeletal system, J. Non. Cryst. Solids. 432, Part (2016) 15–30. doi:http://dx.doi.org/10.1016/j.jnoncrysol.2015.02.015.

[10] P. Korn, M.C. Schulz, V. Hintze, U. Range, R. Mai, U. Eckelt, M. Schnabelrauch, S. Möller, J. Becher, D. Scharnweber, B. Stadlinger, Chondroitin sulfate and sulfated hyaluronan-containing collagen coatings of titanium implants influence peri-implant bone formation in a minipig model, J. Biomed. Mater. Res. Part A. 102 (2014) 2334–2344. doi:10.1002/jbm.a.34913.

[11] M. Sartori, G. Giavaresi, A. Parrilli, A. Ferrari, N.N. Aldini, M. Morra, C. Cassinelli, D. Bollati, M. Fini, Collagen type I coating stimulates bone regeneration and osteointegration of titanium implants in the osteopenic rat, Int. Orthop. 39 (2015) 2041–2052. doi:10.1007/s00264-015-2926-0.

[12] W.-G. La, M. Jin, S. Park, H.-H. Yoon, G.-J. Jeong, S.H. Bhang, H. Park, K. Char, B.-S. Kim, Delivery of bone morphogenetic protein-2 and substance P using graphene oxide for bone regeneration, Int. J. Nanomedicine. 9 (2014) 107–116. doi:10.2147/IJN.S50742.

[13] N.J. Shah, M.N. Hyder, M.A. Quadir, N.-M. Dorval Courchesne, H.J. Seeherman, M. Nevins, M. Spector, P.T. Hammond, Adaptive growth factor delivery from a polyelectrolyte coating promotes synergistic bone tissue repair and reconstruction, Proc. Natl. Acad. Sci. . 111 (2014) 12847–12852. doi:10.1073/pnas.1408035111.

[14] E. Nyberg, C. Holmes, T. Witham, W.L. Grayson, Growth factor-eluting technologies for bone tissue engineering, Drug Deliv. Transl. Res. 6 (2016) 184–194. doi:10.1007/s13346-015-0233-3.

[15] J.-J. Ryu, K. Park, H.-S. Kim, C.-M. Jeong, J.-B. Huh, Effects of anodized titanium with Arg-Gly-Asp (RGD) peptide immobilized via chemical grafting or physical adsorption on bone cell adhesion and differentiation., Int. J. Oral Maxillofac. Implants. 28 (2013) 963–972.

[16] C.-Y. Chien, W.-B. Tsai, Poly(dopamine)-Assisted Immobilization of Arg-Gly-Asp Peptides, Hydroxyapatite, and Bone Morphogenic Protein-2 on Titanium to Improve the Osteogenesis of Bone Marrow Stem Cells, ACS Appl. Mater. Interfaces. 5 (2013) 6975–6983. doi:10.1021/am401071f.

[17] C.-Y. Chien, T.-Y. Liu, W.-H. Kuo, M.-J. Wang, W.-B. Tsai, Dopamine-assisted immobilization of hydroxyapatite nanoparticles and RGD peptides to improve the osteoconductivity of titanium, J. Biomed. Mater. Res. Part A. 101A (2013) 740–747. doi:10.1002/jbm.a.34376.

[18] K.M. Dupont, J.D. Boerckel, H.Y. Stevens, T. Diab, Y.M. Kolambkar, M. Takahata, E.M. Schwarz, R.E. Guldberg, Synthetic scaffold coating with adeno-associated virus encoding BMP2 to promote endogenous bone repair., Cell Tissue Res. 347 (2012) 575–588. doi:10.1007/s00441-011-1197-3.

[19] E.J. Tobin, Recent coating developments for combination devices in orthopedic and dental

applications: A literature review., Adv. Drug Deliv. Rev. 112 (2017) 88–100. doi:10.1016/j.addr.2017.01.007.

[20] I.-Y. Kim, S.-J. Seo, H.-S. Moon, M.-K. Yoo, I.-Y. Park, B.-C. Kim, C.-S. Cho, Chitosan and its derivatives for tissue engineering applications, Biotechnol. Adv. 26 (2008) 1–21. doi:10.1016/j.biotechadv.2007.07.009.

[21] A. Di Martino, M. Sittinger, M. V. Risbud, Chitosan: A versatile biopolymer for orthopaedic tissue-engineering, Biomaterials. 26 (2005) 5983–5990. doi:10.1016/j.biomaterials.2005.03.016.

[22] G. Kogan, L. Šoltés, R. Stern, P. Gemeiner, Hyaluronic acid: A natural biopolymer with a broad range of biomedical and industrial applications, Biotechnol. Lett. 29 (2007) 17–25. doi:10.1007/s10529-006-9219-z.

[23] H. Lee, Y. Lee, A.R. Statz, J. Rho, T.G. Park, P.B. Messersmith, Substrate-independent layer-by-layer assembly by using mussel-adhesive-inspired polymers, Adv. Mater. 20 (2008) 1619–1623. doi:10.1002/adma.200702378.

[24] K. Kim, K. Kim, J.H. Ryu, H. Lee, Chitosan-catechol: A polymer with long-lasting mucoadhesive properties, Biomaterials. 52 (2015) 161–170. doi:10.1016/j.biomaterials.2015.02.010.

[25] J. Xu, S. Strandman, J.X.X. Zhu, J. Barralet, M. Cerruti, Genipin-crosslinked catechol-chitosan mucoadhesive hydrogels for buccal drug delivery, Biomaterials. 37 (2015) 395–404. doi:10.1016/j.biomaterials.2014.10.024.

[26] A. Ghadban, A.S. Ahmed, Y. Ping, R. Ramos, N. Arfin, B. Cantaert, R. V. Ramanujan, A. Miserez, Bioinspired pH and magnetic responsive catechol-functionalized chitosan hydrogels with tunable elastic properties, Chem. Commun. 52 (2016) 697–700. doi:10.1039/C5CC08617E.

[27] J.J. Wilker, Marine bioinorganic materials: mussels pumping iron, Curr. Opin. Chem. Biol. 14 (2010) 276–283. doi:https://doi.org/10.1016/j.cbpa.2009.11.009.

[28] M. Yu, T.J. Deming, Synthetic Polypeptide Mimics of Marine Adhesives, Macromolecules. 31 (1998) 4739–4745. doi:10.1021/ma980268z.

[29] H. Lee, N.F. Scherer, P.B. Messersmith, Single-molecule mechanics of mussel adhesion, Proc. Natl. Acad. Sci. 103 (2006) 12999–13003. doi:10.1073/pnas.0605552103.

[30] B.K. Ahn, S. Das, R. Linstadt, Y. Kaufman, N.R. Martinez-Rodriguez, R. Mirshafian, E. Kesselman, Y. Talmon, B.H. Lipshutz, J.N. Israelachvili, J.H. Waite, High-performance mussel-inspired adhesives of reduced complexity, Nat. Commun. 6 (2015) 8663. http://dx.doi.org/10.1038/ncomms9663.

[31] H.J. Cha, D.S. Hwang, S. Lim, Development of bioadhesives from marine mussels., Biotechnol.

J. 3 (2008) 631–638. doi:10.1002/biot.200700258.

[32] C.R. Matos-Pérez, J.D. White, J.J. Wilker, Polymer Composition and Substrate Influences on the Adhesive Bonding of a Biomimetic, Cross-Linking Polymer, J. Am. Chem. Soc. 134 (2012) 9498–9505. doi:10.1021/ja303369p.

[33] A.I. Neto, A.C. Cibrão, C.R. Correia, R.R. Carvalho, G.M. Luz, G.G. Ferrer, G. Botelho, C. Picart, N.M. Alves, J.F. Mano, Nanostructured polymeric coatings based on chitosan and dopamine-modified hyaluronic acid for biomedical applications, Small. 10 (2014) 2459–2469. doi:10.1002/smll.201303568.

[34] S.J. Rego, A.C. Vale, G.M. Luz, J.F. Mano, N.M. Alves, Adhesive Bioactive Coatings Inspired by Sea Life, Langmuir. 32 (2016) 560–568. doi:10.1021/acs.langmuir.5b03508.

[35] M. MačKović, A. Hoppe, R. Detsch, D. Mohn, W.J. Stark, E. Spiecker, A.R. Boccaccini, Bioactive glass (type 45S5) nanoparticles: In vitro reactivity on nanoscale and biocompatibility, J. Nanoparticle Res. 14 (2012). doi:10.1007/s11051-012-0966-6.

[36] A.R. Boccaccini, M. Erol, W.J. Stark, D. Mohn, Z. Hong, J.F. Mano, Polymer/bioactive glass nanocomposites for biomedical applications: A review, Compos. Sci. Technol. 70 (2010) 1764–1776. doi:10.1016/j.compscitech.2010.06.002.

[37] M. De, P.S. Ghosh, V.M. Rotello, Applications of Nanoparticles in Biology, Adv. Mater. 20 (2008) 4225–4241. doi:10.1002/adma.200703183.

[38] J. Sun, B. Bhushan, Hierarchical structure and mechanical properties of nacre: a review, RSC Adv. 2 (2012) 7617–7632. doi:10.1039/C2RA20218B.

[39] J. Wang, Q. Cheng, Z. Tang, Layered nanocomposites inspired by the structure and mechanical properties of nacre, Chem. Soc. Rev. 41 (2012) 1111–1129. doi:10.1039/C1CS15106A.

[40] V. Gribova, R. Auzely-Velty, C. Picart, Polyelectrolyte Multilayer Assemblies on Materials Surfaces: From Cell Adhesion to Tissue Engineering, Chem. Mater. 24 (2012) 854–869. doi:10.1021/cm2032459.

[41] N.M. Alves, I. Pashkuleva, R.L. Reis, J.F. Mano, Controlling cell behavior through the design of polymer surfaces., Small. 6 (2010) 2208–2220. doi:10.1002/smll.201000233.

[42] J. Borges, J.F. Mano, Molecular interactions driving the layer-by-layer assembly of multilayers., Chem. Rev. 114 (2014) 8883–8942. doi:10.1021/cr400531v.

[43] K. Halasz, G. Grozdits, L. Csóka, Functional nanostructured coatings via layer-by-layer self-assembly, in: Anti-Abrasive Nanocoatings, Woodhead Publishing, 2015: pp. 249–281. doi:https://doi.org/10.1016/B978-0-85709-211-3.00010-8.

[44] M.M. de Villiers, D.P. Otto, S.J. Strydom, Y.M. Lvov, Introduction to nanocoatings produced by layer-by-layer (LbL) self-assembly, Adv. Drug Deliv. Rev. 63 (2011) 701–715. doi:http://dx.doi.org/10.1016/j.addr.2011.05.011.

[45] J. Cho, K. Char, J.-D. Hong, K.-B. Lee, Fabrication of Highly Ordered Multilayer Films Using a Spin Self-Assembly Method, Adv. Mater. 13 (2001) 1076–1078. doi:10.1002/1521-4095(200107)13:14<1076::AID-ADMA1076>3.0.CO;2-M.

[46] Y.M. Lee, D.K. Park, W.-S. Choe, S.M. Cho, G.Y. Han, J. Park, P.J. Yoo, Spin-assembled layer-by-layer films of weakly charged polyelectrolyte multilayer., J. Nanosci. Nanotechnol. 9 (2009) 7467–7472.

[47] M. Marudova, I. Bodurov, S. Sotirov, Y. Uzunova, B. Pilicheva, I. Avramova, A. Viraneva, I. Vlaeva, G. Exner, T. Yovcheva, Nanostructured polyelectrolyte multilayer drug delivery systems for buccal administration, Bulg. Chem. Commun. 48 (2016) 468–474.

[48] A.L. Carvalho, A.C. Vale, M. Sousa, A.M. Barbosa, E. Torrado, J. Mano, N.M. Alves, Antibacterial bioadhesive layer-by-layer coatings for orthopedic applications, J. Mater. Chem. B. 4 (2016) 5385–5393. doi:10.1039/C6TB00841K.

[49] Z. Hong, R.L. Reis, J.F. Mano, Preparation and in vitro characterization of novel bioactive glass ceramic nanoparticles, J. Biomed. Mater. Res. - Part A. 88 (2009) 304–313. doi:10.1002/jbm.a.31848.

[50] G.M. Luz, J.F. Mano, Preparation and characterization of bioactive glass nanoparticles prepared by sol–gel for biomedical applications, Nanotechnology. 22 (2011) 494014. doi:10.1088/0957-4484/22/49/494014.

[51] C. Peniche, W. Arguelles-Monal, N. Davidenko, R. Sastre, A. Gallardo, J. San Roman, Self-curing membranes of chitosan/PAA IPNs obtained by radical polymerization: preparation, characterization and interpolymer complexation., Biomaterials. 20 (1999) 1869–1878.

[52] J.W. Kuo, Practical aspects of hyaluronan based medical products, CRC Press, 2005.

[53] G. Lawrie, I. Keen, B. Drew, A. Chandler-Temple, L. Rintoul, P. Fredericks, L. Grøndahl, Interactions between alginate and chitosan biopolymers characterized using FTIR and XPS, Biomacromolecules. 8 (2007) 2533–2541.

[54] X. Huang, X. Bao, Y. Liu, Z. Wang, Q. Hu, Catechol-Functional Chitosan/Silver Nanoparticle Composite as a Highly Effective Antibacterial Agent with Species-Specific Mechanisms., Sci. Rep. 7 (2017) 1860. doi:10.1038/s41598-017-02008-4.

[55] M. Altmaier, B. Kienzler, V. Montoya, L. Duro, M. Grivé, 4th Annual Workshop Proceedings of the

Collaborative Project “Redox Phenomena Controlling Systems” (7th EC FP CP RECOSY) (KIT Scientific Reports; 7626), KIT Scientific Publishing, 2012.

[56] P.K. Jha, G.P. Halada, The catalytic role of uranyl in formation of polycatechol complexes, Chem. Cent. J. 5 (2011) 12. doi:10.1186/1752-153X-5-12.

[57] J. Ma, C.Z. Chen, D.G. Wang, X.G. Meng, J.Z. Shi, In vitro degradability and bioactivity of mesoporous CaO-MgO-P2O5-SiO2 glasses synthesized by sol–gel method, J. Sol-Gel Sci. Technol. 54 (2010) 69–76. doi:10.1007/s10971-010-2159-z.

[58] M.A. Herrera, J.A. Sirviö, A.P. Mathew, K. Oksman, Environmental friendly and sustainable gas barrier on porous materials: Nanocellulose coatings prepared using spin- and dip-coating, Mater. Des. 93 (2016) 19–25. doi:https://doi.org/10.1016/j.matdes.2015.12.127.

[59] J. Seo, J.L. Lutkenhaus, J. Kim, P.T. Hammond, K. Char, Effect of the Layer-by-Layer (LbL) Deposition Method on the Surface Morphology and Wetting Behavior of Hydrophobically Modified PEO and PAA LbL Films, Langmuir. 24 (2008) 7995–8000. doi:10.1021/la800906x.

[60] R.N. Wenzel, Surface Roughness and Contact Angle., J. Phys. Colloid Chem. 53 (1949) 1466–1467. doi:10.1021/j150474a015.

[61] X. Zhang, Z. Li, X. Yuan, Z. Cui, X. Yang, Fabrication of dopamine-modified hyaluronic acid/chitosan multilayers on titanium alloy by layer-by-layer self-assembly for promoting osteoblast growth, Appl. Surf. Sci. 284 (2013) 732–737. doi:10.1016/j.apsusc.2013.08.002.

[62] S. Hong, K. Yang, B. Kang, C. Lee, I.T. Song, E. Byun, K.I. Park, S.-W. Cho, H. Lee, Hyaluronic Acid Catechol: A Biopolymer Exhibiting a pH-Dependent Adhesive or Cohesive Property for Human Neural Stem Cell Engineering, Adv. Funct. Mater. 23 (2013) 1774–1780. doi:10.1002/adfm.201202365.

[63] W. Chen, X. Shen, Y. Hu, K. Xu, Q. Ran, Y. Yu, L. Dai, Z. Yuan, L. Huang, T. Shen, K. Cai, Surface functionalization of titanium implants with chitosan-catechol conjugate for suppression of ROS-induced cells damage and improvement of osteogenesis, Biomaterials. 114 (2017) 82–96. doi:http://dx.doi.org/10.1016/j.biomaterials.2016.10.055.

[64] X. Li, J. Shi, X. Dong, L. Zhang, H. Zeng, A mesoporous bioactive glass/polycaprolactone composite scaffold and its bioactivity behavior., J. Biomed. Mater. Res. A. 84 (2008) 84–91. doi:10.1002/jbm.a.31371.

[65] S.G. Caridade, E.G. Merino, N.M. Alves, V. de Z. Bermudez, A.R. Boccaccini, J.F. Mano, Chitosan membranes containing micro or nano-size bioactive glass particles: evolution of biomineralization followed by in situ dynamic mechanical analysis, J. Mech. Behav. Biomed. Mater. 20 (2013) 173–

183. doi:http://dx.doi.org/10.1016/j.jmbbm.2012.11.012.

[66] J.R. Rodrigues, N.M. Alves, J.F. Mano, Biomimetic polysaccharide/bioactive glass nanoparticles multilayer membranes for guided tissue regeneration, RSC Adv. 6 (2016) 75988–75999.

5. CHAPTER 5 – GENERAL CONCLUSIONS AND FUTURE WORK

5.1 General Conclusions

Many attempts have been made to produce multifunctional coatings with enhanced bioactive and adhesive properties to avoid the use of cements on the orthopaedic implants. As well, there is a growing need to develop biocompatible natural adhesive tissues as an alternative to those currently used in clinical practice.

In this work, different LbL coatings were successfully developed by using the LbL assembly method:

1) Multifunctional films (MF) containing sequential layers of an organic polysaccharide phase and an inorganic phase of BGNPs;
2) Polymeric films containing the same organic phase.

The organic phase was based on two natural biocompatible polymers, CHT and HA modified with catechol groups to impart adhesive properties. This modification was inspired by mussels and their strong adhesion in harsh environments. The addition of an inorganic phase of BGNPs in MF films was inspired by the inorganic-organic layered structure of nacre and was used to impart bioactivity properties.

Through the reaction of HA with dopamine and CHT hydrocaffeic acid was possible to successfully modify them. The *in-situ* build-up of films with these distinct compositions was monitored by QCM-D, indicating the successful formation of the MF and polymeric coatings by LbL. It has been shown that the presence of the catechol groups contributed to the linear film growth, revealing thinner multilayered films.

MF and polymeric films were produced by dip-coating and subjected to lap shear tests, which proved that the presence of both CHT-C and HA-DN conjugates in CTR5 ($[CHT\text{-}C^*_{18h}/HA\text{-}DN^*_{4h}]_{11}$) and CTR6 ($[CHT\text{-}C^*_{18h}/HA\text{-}DN^*_{36h}]_{11}$) polymeric conditions significantly improved their adhesion properties compared to the other CTR coatings. Moreover, it was observed that the CTR6 condition showed slightly higher adhesion properties than the CTR5 condition due to the higher content of catechol groups. On the other hand, although the inclusion of BGNPs in these LbL systems, namely in MF5 ($[CHT\text{-}C^*_{18h}/HA\text{-}DN^*_{4h}/CHT\text{-}C^*_{18h}/BGNPs]_5+[CHT\text{-}C^*_{18h}/HA\text{-}DN^*_{4h}]$) and MF6 ($[CHT\text{-}C^*_{18h}/HA\text{-}DN^*_{36h}/CHT\text{-}C^*_{18h}/BGNPs]_5+[CHT\text{-}C^*_{18h}/HA\text{-}DN^*_{36h}]$), decreased the adhesion strength, they demonstrated bioactive potential, developing a calcium phosphate layer after immersion in a SBF solution. Particularly, after 7 days of immersion in a SBF solution, changes in the elemental composition of MF6 remarkably greater than for MF5 were observed, demonstrating a decrease in Si concentration and an increase in Ca and P concentrations.

Furthermore, both polymeric (CTR5 and CTR6) and MF films (MF5 and MF6) showed good biocompatibility. In particular, polymeric films seemed to present an enhanced viability at the different time points.

Considering all these results, it was possible to conclude that the best configurations were the CTR6 and MF6 coatings.

Therefore, since the structure and topography play an important role in the functional performance of the CTR6 and MF6 films, two LbL assembly methods, dip- and spin-coating, were compared using three different substrates: glass, 316L stainless steel, and titanium.

Surface analysis by SEM, FT-IR imaging and AFM showed that both CTR6 and MF6 spin-coated formulations on glass substrate had a smoother, more homogeneous surface morphology and ordered coating structures than those dip-coated ones. Moreover, it was found that the incorporation of BGNPs in the dip- and spin-coated MF6 films on glass substrates contributed to a smoother cohesive structure compared to their respective controls (CTR6). These results suggested that the combined effect of catechol groups of both CHT-C*$_{18h}$ and HA-DN*$_{36h}$ polymers may act as a glue between the inorganic and organic phase.

Also, wettability analysis showed that CTR6 and MF6 obtained by the two LbL methods exhibit higher hydrophilicity than the glass control, evidencing the hydrophilic nature of LbL coatings provided by both modified polymers and BGNPs. In addition, spin-coated CTR6 and MF6 conditions demonstrated lower hydrophilicity than the dip-coated ones, revealing that the surface roughness had an impact in wettability results.

Furthermore, it was concluded that the intrinsic surface roughness of 316L SS and Ti metals had a great influence on the above mentioned results of both LbL methods, where no obvious differences were observed.

Attending all these results, MF6 films could be used to coat orthopaedic implants, contributing to a more successful implantation by enhancing their bioactive and adhesive properties as well as the cellular response. CTR6 film could be used to coat distinct implants, where bioactivity is not an important issue, by promoting a highly adhesive and biocompatible connection between the implant and a variety of tissues. In addition, spin-coating could be considered in their build-up, since it allows to control the inner and surface structure of the LbL films, enabling to manipulate their physical properties or chemical activity. In this way, tunable bioadhesiveness and BGNPs ions release properties could be achieved.

5.2 Future Work

Even though the results obtained in this work have been encouraging, further work is required to optimize the LbL coatings produced for the intended biomedical applications. Therefore, the following topics are suggested as future work:

1. To investigate the development of MF films with fewer BGNPs deposition steps, to find the optimum BGNPs concentration that results in coatings with higher adhesion performance, without compromising their bioactivity. As an example, the production of the following MF film system could be studied: [CHT-C/HA-DN/CHT-C/HA-DN/CHT-C/BGNPs]$_3$ + [CHT-C/HA-DN]$_2$.

2. To perform cellular studies with other cell types to assess the viability of the LbL coatings for the intended biomedical applications. As a suggestion, the viability of Saos-2 cell line could be studied, envisaging orthopaedic applications.

3. To evaluate the structure and topography of the LbL coatings on metal substrates as a function of the polishing process.

4. To investigate the thickness differences obtained by dip- and spin-coating. A spectroscopic ellipsometer could be used to characterize the thickness of the LbL coatings produced.

5. To explore the differences in adhesive strength, bioactivity, and cellular behaviour between dip- and spin-coated LbL conditions. As the lap shear test is not suitable for the spin-coated conditions, the AFM analysis could be used to measure the adhesive forces between the LbL coating surfaces and the AFM probe, thereby maintaining the same conditions between the different samples.

APPENDIX I – HA MODIFICATION WITH CATECHOL GROUPS

Study of HA-DN synthesis

To optimize the synthesis of HA-DN, the effect of the ratio between the activating agent (EDC) and the donor of catechol groups (dopamine), and the reaction time was studied. This modification of HA with catechol groups was based on two previous established methodologies by Lee *et al.* [1,2]. Further, to confirm the conjugation degree of catechol groups to polymer backbone was used an UV-Vis spectrophotometer.

Firstly, based on the procedure proposed in 2010 by Lee and co-workers [2], with some modifications, a HA solution (10 $mg.mL^{-1}$) was prepared in PBS solution and the pH was ajusted to 5.5 using 0.5M HCL or 0.5M NaOH aqueous solutions under magnetic stirring. This solution was purged with nitrogen for 30 min to limit the oxygen interaction with the solution. Then, 237 mg of EDC and 194 mg of DN were added to the previous solution with an acidic pH (5.5) at 4°C. This mixture was divided in two different solution with different reaction times i.e. **HA-DN$_{4h}$** and **HA-DN$_{36h}$**. The unreacted chemicals were removed by the dialysis against a pH 5.0 HCl solution for 4 days and osmotized water for 1 day, using a dialysis membrane tube, at 4°C and protected from the light. The final products were freeze-dried and stored at -20°C.

On the other hand, based on procedure proposed in 2008 by Lee and co-workers [1], additional HA-DN* were prepared using an experimental protocol similar to that described previously. So, a HA solution (10 $mg.mL^{-1}$) was prepared in PBS solution and the pH was adjusted to 5.5 using 0.5M HCL or 0.5M NaOH aqueous solutions under magnetic stirring. The solution was purged with nitrogen for 30 min and then, 338 mg of EDC and 474 mg of DN were added to the previous solution with an acidic pH (5.5) at 4°C. Likewise, the final solution was divided in two different solution with different reaction times i.e. **HA-DN*$_{4h}$** and **HA-DN*$_{36h}$**. The product was dialyzed against a pH 5.0 HCl solution for 4 days and osmotized water for 1 day, using a dialysis membrane tube, at 4°C and protected from the light. Finally, the final products were freeze-dried and stored at -20°C.

References:

[1] H. Lee, Y. Lee, A.R. Statz, J. Rho, T.G. Park, P.B. Messersmith, Substrate-independent layer-by-layer assembly by using mussel-adhesive-inspired polymers, Adv. Mater. 20 (2008) 1619–1623. doi:10.1002/adma.200702378.

[2] Y. Lee, H.J. Chung, S. Yeo, C.-H. Ahn, H. Lee, P.B. Messersmith, T.G. Park, Thermo-sensitive, injectable, and tissue adhesive sol–gel transition hyaluronic acid/pluronic composite hydrogels prepared from bio-inspired catechol-thiol reaction, Soft Matter. 6 (2010) 977–983. doi:10.1039/b919944f.

HA-DN conjugation degree: UV-Vis results

To perform HA-DN UV-Vis experiments, different concentrations of DN (1mM, 1.5mM, 2.5mM, 3mM, 3.3mM and 3.5mM) were firstly analysed using a 96 wells quartz plate. It was put 100 µL per well with triplicates and protecting from the light to avoid their oxidation.

Thus, the Abs spectra of DN solutions, at wavelengths between 200 nm and 350 nm, were obtained to get the linear regression line between the Abs and the DN concentration in mM.

According to the literature, the Abs of catechol group corresponds to λ=280nm by which it was quantified, and their respective values are shown in Table I.1.

Table I.1 – UV-Vis characterization of different concentrations of DN.

[DN] (mM)	Abs (λ=280 nm)
1.0	0.216
1.5	0.305
2.5	0.510
3.0	0.611
3.3	0.664
3.5	0.709

The relationship between the Abs at λ=280 nm and the concentration of DN, was given by equation (I.1).

$$[\mathrm{DN}](\mathrm{mM}) = \frac{\mathrm{Abs} - 0.0137}{0.1982} \quad \text{(I.1)}$$

Then, UV-Vis experiments were performed for different concentrations of **HA-DN$_{4h}$** and **HA-DN$_{36h}$** solutions, and the experimental results are presented in Figure I.1 and Table I.2.

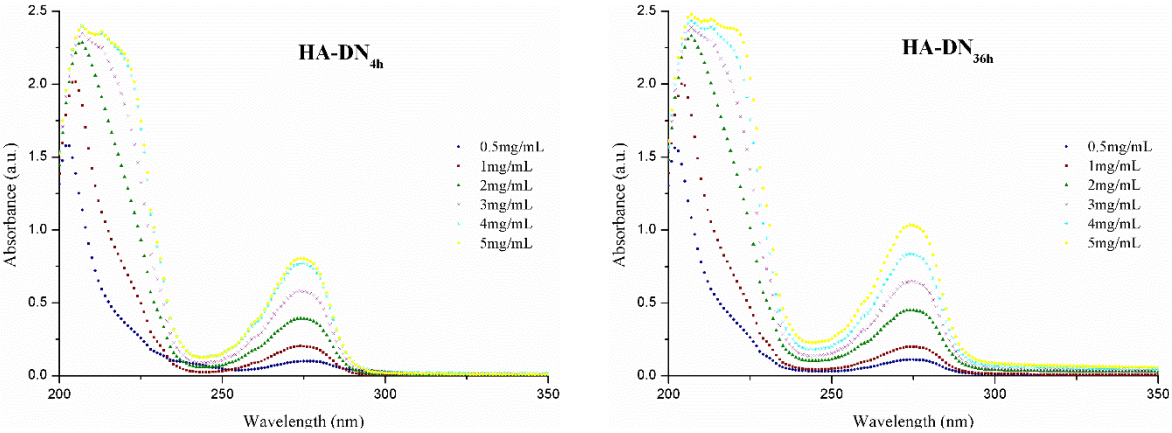

Figure I.1 – UV-Vis spectra for different concentrations of HA-DN_{4h} and HA-DN_{36h}.

Table I.2 – UV-Vis characterization of different concentrations of HA-DN_{4h} and HA-DN_{36h}.

[HA-DN_{4h}] [HA-DN_{36h}] (mg.mL^{-1})	**Abs (λ=280 nm) HA-DN_{4h}**	**Abs (λ=280 nm) HA-DN_{36h}**
0.5	0.095	0.100
1.0	0.176	0.176
2.0	0.340	0.398
3.0	0.501	0.568
4.0	0.666	0.733
5.0	0.696	0.907

From the results obtained, an Abs peak was observed for all concentrations at 280 nm, confirming the presence of the characteristic peak of catechol groups mentioned in the literature. Therefore, based on the experimental values, it is possible to estimate the substitution degree of catechol groups, DS (%), assuming that it can be given by equation (I.2).

$$DS(\%) = \frac{m_{DN}}{m_{HA-DN}} \times 100 \qquad (I.2)$$

Where,

$$m_{DN} = Equation\ I.1 \times V_{well} \times 10^{-3} \times M_W(DN)$$

m_{DN}: DN mass

V_{well}: Well volume

M_w: Molecular weight

According to these results, the DS (%)of **HA-DN$_{4h}$** and **HA-DN$_{36h}$** was around **15%** and **17%**, respectively.

Similarly, the UV-Vis characterization was performed for HA-DN* conjugates to confirm their synthesis and obtain their DS (%). The experimental results are presented in Figure I.2 and Table I.3.

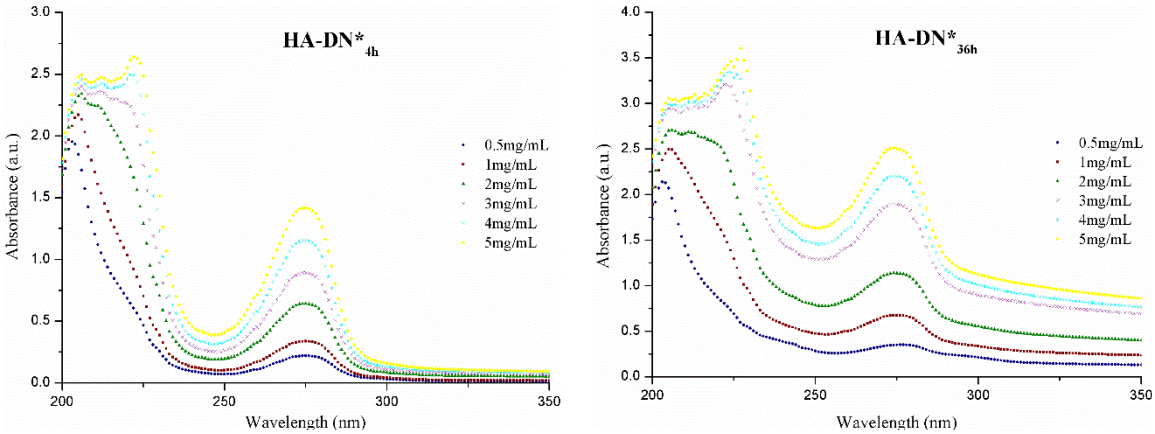

Figure I.2 – UV-Vis spectra for different concentrations of HA-DN*$_{4h}$ and HA-DN*$_{36h}$.

Table I.3 – UV-Vis characterization of different concentrations of HA-DN*$_{4h}$ and HA-DN*$_{36h}$.

[HA-DN*$_{4h}$] [HA-DN*$_{36h}$] (mg.mL^{-1})	**Abs (λ=280 nm) HA-DN*$_{4h}$**	**Abs (λ=280 nm) HA-DN*$_{36h}$**
0.5	0.198	0.343
1.0	0.303	0.641
2.0	0.572	1.073
3.0	0.794	1.770
4.0	1.024	2.057
5.0	1.263	2.337

According to these results, the DS (%) of **HA-DN*$_{4h}$** and **HA-DN*$_{36h}$** was around **27%** and **54%**, respectively.

APPENDIX II – CHT MODIFICATION WITH CATECHOL GROUPS

Study of CHT-C synthesis

Similarly, the synthesis of CHT-C was optimized. This modification of CHT with catechol groups was achieved through by activating agent (EDC) and the donor of catechol groups (hydrocaffeic acid). An UV-Vis spectrophotometer was also used to confirm the conjugation degree of catechol groups to polymer backbone.

Firstly, based on two previous established methodologies by Ryu *et al.* [1] and Xu and co-workers [2], 100 mL of 1% (w/v) medium molecular weight CHT solution was prepared in 1% HCl solution at pH 2.5.

Then, a HCA solution (10 $mg.mL^{-1}$) was prepared in ethanol and a EDC solution (24 $mg.mL^{-1}$) was prepared in osmotized water. These two previous solutions were mixed and added to CHT solution, under stirring at 4° C. After that, the pH of solution was adjusted to 5.5 by adding of 1M NaOH solution. This solution was divided in two different solution with different reaction times i.e. **CHT-C$_{18h}$** and **CHT-C$_{36h}$**.

After these timepoints, the products were purified by dialysis against an acidic osmotized water solution (pH 5.0, HCL solution) for 3 days and osmotized water for 4 hours, using a dialysis membrane tube, at 4°C and protected from the light. The resulting products were freeze-dried and stored at -20°C.

On the other hand, based on procedure proposed by Kim *et al.* [3], Xu *et al.* [2], Ghadban *et al.* [4], additional CHT-C* was prepared using an experimental protocol similar to that described previously. So, 1% (w/v) medium molecular weight CHT solution was prepared in HCl solution at pH 2.5.

Then, a HCA solution (59 $mg.mL^{-1}$) was prepared in osmotized water and a EDC solution (119 $mg.mL^{-1}$) was prepared in a mixture of osmotized water and ethanol. These two previous solutions were mixed and added to CHT solution, under stirring at 4° C, followed by the addition of 1M NaOH solution to obtain a final pH of 4.8.

The reaction was allowed to continue for 18 h, **CHT-C*$_{18h}$**, under nitrogen atmosphere for 30 min. After that, the product was purified by dialysis against an acidic osmotized water solution (pH 5.0, HCL solution) for 3 days and osmotized water for 4 hours, using a dialysis membrane tube, at 4°C and protected from the light. The resulting product was freeze-dried and stored at -20°C.

References:

[1] J.H. Ryu, Y. Lee, W.H. Kong, T.G. Kim, T.G. Park, H. Lee, Catechol-functionalized

chitosan/pluronic hydrogels for tissue adhesives and hemostatic materials, Biomacromolecules. 12 (2011) 2653–2659. doi:10.1021/bm200464x.

[2] J. Xu, S. Strandman, J.X.X. Zhu, J. Barralet, M. Cerruti, Genipin-crosslinked catechol-chitosan mucoadhesive hydrogels for buccal drug delivery, Biomaterials. 37 (2015) 395–404. doi:10.1016/j.biomaterials.2014.10.024.

[3] K. Kim, K. Kim, J.H. Ryu, H. Lee, Chitosan-catechol: A polymer with long-lasting mucoadhesive properties, Biomaterials. 52 (2015) 161–170. doi:10.1016/j.biomaterials.2015.02.010.

[4] A. Ghadban, A.S. Ahmed, Y. Ping, R. Ramos, N. Arfin, B. Cantaert, R. V. Ramanujan, A. Miserez, Bioinspired pH and magnetic responsive catechol-functionalized chitosan hydrogels with tunable elastic properties, Chem. Commun. 52 (2016) 697–700. doi:10.1039/C5CC08617E.

CHT-Cat conjugation degree: UV-Vis results

To perform CHT-C UV-Vis experiments, different concentrations of HCA (1mM, 1.5mM, 2.5mM, 3mM, 3.3mM and 3.5mM) were firstly analysed using a 96 wells quartz plate. It was put 100 µL per well with triplicates and protecting from the light to avoid their oxidation.

Thus, the Abs spectra of HCA solutions, at wavelengths between 200 nm and 350 nm, were obtained to get the linear regression line between the Abs and the HCA concentration in mM.

According to the literature, the Abs of catechol group corresponds to λ=280nm by which it was quantified, and their respective values are shown in Table II.1.

Table II.1– UV-Vis characterization of different concentrations of HCA.

[HCA] (mM)	Abs (λ=280 nm)
1.0	0.341
1.5	1.429
2.5	2.053
3.0	2.445
3.3	2.711
3.5	2.969

The relationship between the Abs at λ=280 nm and the concentration of HCA, was given by equation (II.1).

$$[\mathrm{HCA}](\mathrm{mM}) = \frac{\mathbf{Abs}+0.3236}{0.9384} \qquad \text{(II.1)}$$

Then, UV-Vis experiments were performed for different concentrations of **CHT-C$_{18h}$** and **CHT-C$_{36h}$** solutions, and the experimental results are presented in Figure II.1 and Table II.2.

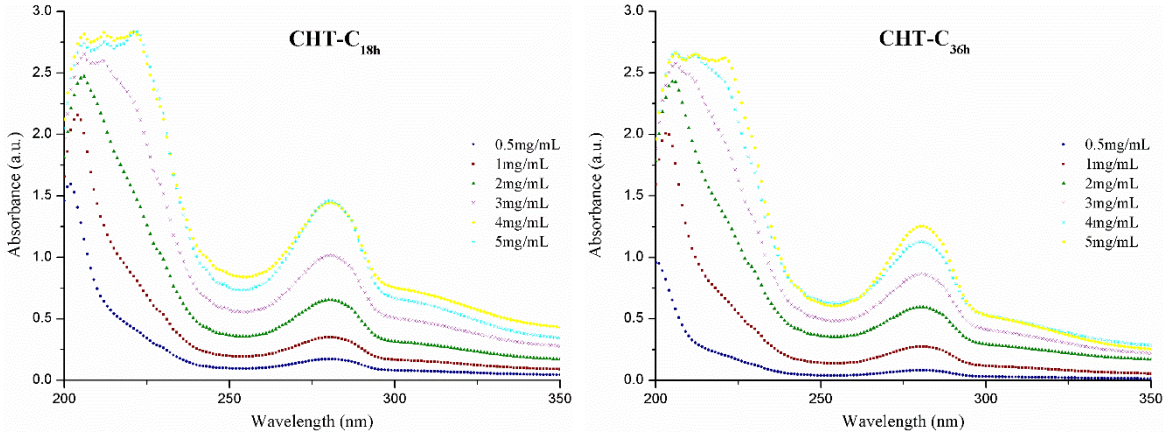

Figure II.1 – UV-Vis spectra for different concentrations of CHT-C$_{18h}$ and CHT-C$_{36h}$.

Table II.2– UV-Vis characterization of different concentrations of CHT-C$_{18h}$ and CHT-C$_{36h}$.

[CHT-C$_{18h}$] [CHT-C$_{36h}$] (mg.mL^{-1})	**Abs (λ=280 nm) CHT-C$_{18h}$**	**Abso (λ=280 nm) CHT-C$_{36h}$**
0.5	0.173	0.082
1.0	0.351	0.275
2.0	0.655	0.596
3.0	1.014	0.862
4.0	1.446	1.125
5.0	1.460	1.254

Based on the results obtained, an Abs peak was observed for all concentrations at 280 nm, confirming the presence of the characteristic peak of catechol groups mentioned in the literature. So, based on the experimental values, it is possible to estimate the DS (%) assuming that it can be given by equation (II.2).

$$DS(\%) = \frac{m_{HCA}}{m_{CHT-C}} \times 100 \quad \text{(II.2)}$$

Where,

$$m_{HCA} = Equation\ II.1 \times V_{well} \times 10^{-3} \times M_W(HCA)$$

m_{DN}: HCA mass

V_{well}: Well volume

M_w: Molecular weight

Attending these results, the DS (%)of **CHT-C$_{18h}$** and **CHT-C$_{36h}$** was around **11%** and **10%**, respectively.

Similarly, the UV-Vis characterization was performed for **CHT-C*$_{18h}$** conjugates to confirm their synthesis and obtain their DS (%). The experimental results are presented in Figure II.2 and Table II.3.

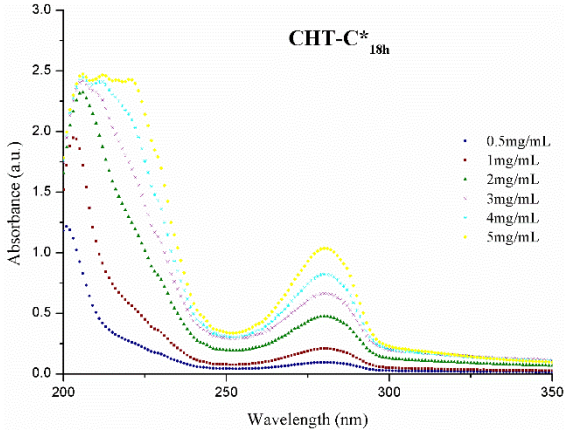

Figure II.2 – UV-Vis spectra for different concentrations of CHT-C*$_{18h}$.

Table II.3– UV-Vis characterization of different concentrations of CHT-C*$_{18h}$.

[CHT-C*$_{18h}$] (mg.mL^{-1})	**Abs (λ=280 nm) CHT-C*$_{18h}$**
0.5	0.096
1.0	0.209
2.0	0.475
3.0	0.663
4.0	0.882
5.0	1.037

According to these results, the DS (%) of **CHT-C*$_{18h}$** was around **9%**.
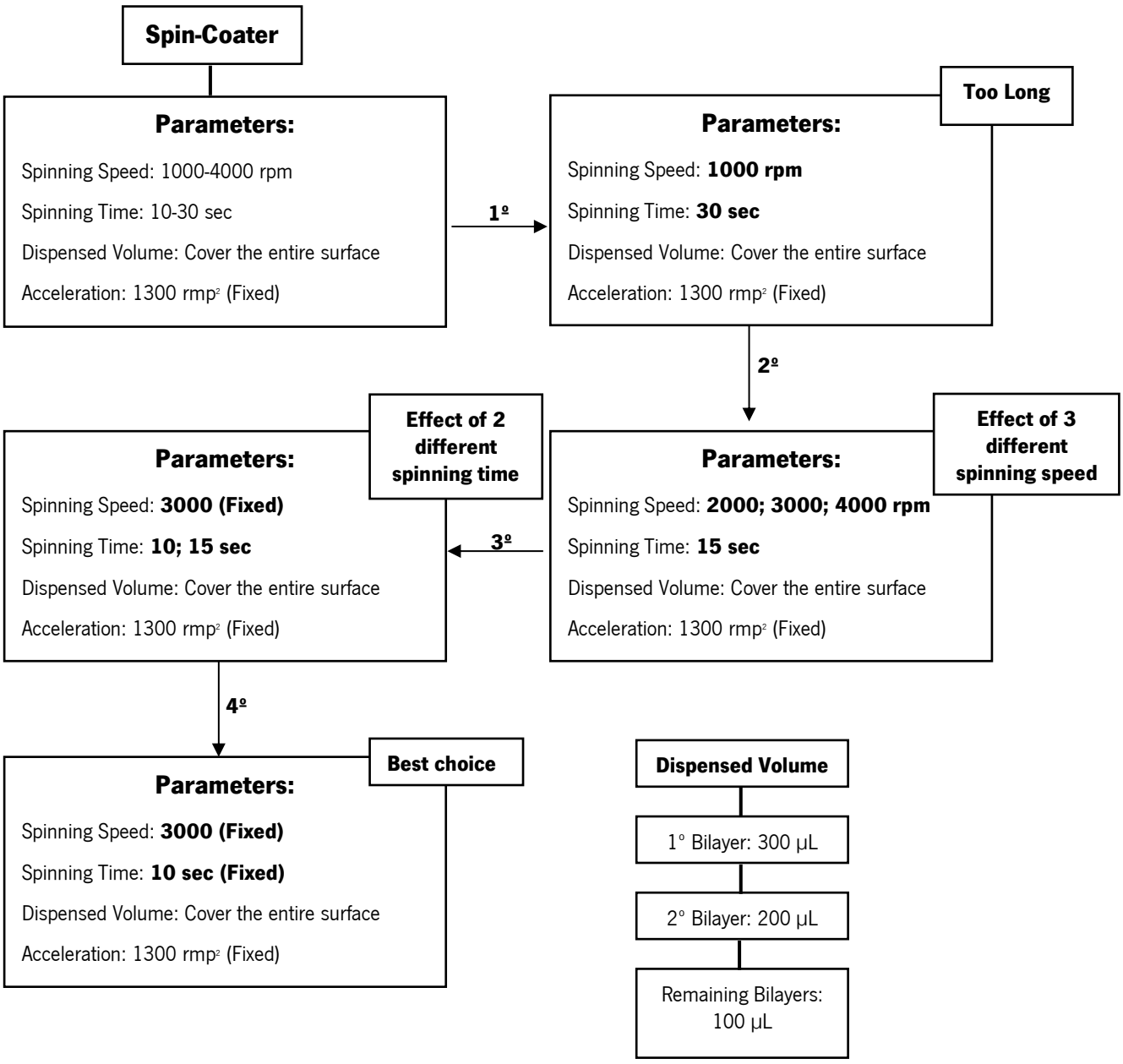
APPENDIX III – OPTIMIZATION WORK ON SPIN COATER